

## Solid state phase transformations in steels: a neutron and synchrotron radiation study

Fang, Haixing

**DOI**

[10.4233/uuid:ecd8e101-3164-4227-b47b-13a04bc4b8fb](https://doi.org/10.4233/uuid:ecd8e101-3164-4227-b47b-13a04bc4b8fb)

**Publication date**

2019

**Document Version**

Final published version

**Citation (APA)**

Fang, H. (2019). *Solid state phase transformations in steels: a neutron and synchrotron radiation study*. [Dissertation (TU Delft), Delft University of Technology]. <https://doi.org/10.4233/uuid:ecd8e101-3164-4227-b47b-13a04bc4b8fb>

**Important note**

To cite this publication, please use the final published version (if applicable). Please check the document version above.

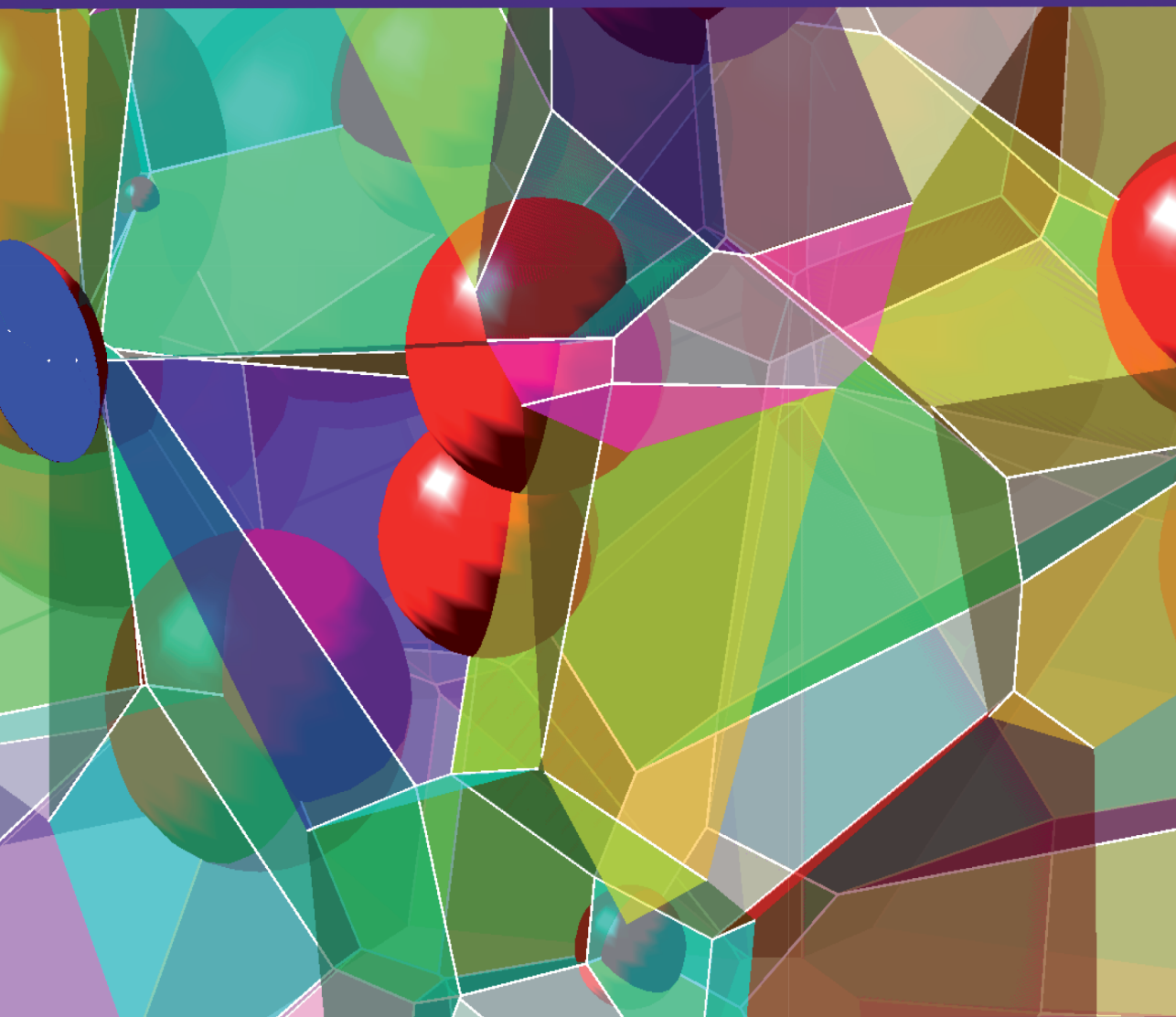
**Copyright**

Other than for strictly personal use, it is not permitted to download, forward or distribute the text or part of it, without the consent of the author(s) and/or copyright holder(s), unless the work is under an open content license such as Creative Commons.

**Takedown policy**

Please contact us and provide details if you believe this document breaches copyrights. We will remove access to the work immediately and investigate your claim.

Solid state phase transformations in steels:  
a neutron and synchrotron radiation study



Haixing Fang

方海星



# **Solid state phase transformations in steels:**

## a neutron and synchrotron radiation study

Proefschrift

ter verkrijging van de graad van doctor

aan de Technische Universiteit Delft,

op gezag van de Rector Magnificus Prof. dr. ir. T.H.J.J. van der Hagen,

voorzitter van het College voor Promoties,

in het openbaar te verdedigen op donderdag 10 januari 2019 om 10:00 uur

door

**Haixing FANG**

Master of Engineering in Metallurgical Engineering,

Chongqing University, Chongqing, China

geboren te Chenzhou, China



Dit proefschrift is goedgekeurd door de promotoren:

Prof. dr. ir. S. van der Zwaag, Prof. dr. E.H. Brück and Dr. ir. N.H. van Dijk

Samenstelling promotiecommissie bestaat uit:

Rector Magnificus, voorzitter

Prof. dr. ir. S. van der Zwaag Technische Universiteit Delft, promotor

Prof. dr. E.H. Brück Technische Universiteit Delft, promotor

Dr. ir. N.H. van Dijk Technische Universiteit Delft, promotor

Onafhankelijke leden:

Prof. dr. A. Borgenstam KTH Royal Institute of Technology, Sweden

Prof. dr. W. Ludwig European Synchrotron Radiation Facility, France

Prof. dr. ir. B.J. Kooij University of Groningen, The Netherlands

Prof. dr. ir. J. Sietsma Technische Universiteit Delft

Prof. dr. C. Pappas Technische Universiteit Delft, Reservelid

This research was financially supported by the China Scholarship Council (CSC) and the innovation oriented program (IOP) on self-healing materials of the Dutch Ministry of Economic Affairs, Agriculture and Innovation.

Keywords: Phase transformation, self healing, steel, neutron depolarization, mixed-mode model, X-ray tomography, synchrotron radiation.

ISBN 978-94-028-1285-5

Printed in the Netherlands by Ipskamp in the Netherlands

An electronic version of this dissertation is available at

<http://repository.tudelft.nl>

Copyright © 2018 by Haixing Fang

All rights reserved. No part of the material protected by this copyright notice may be reproduced or utilized in any form or by any means, electronic or mechanics, including photocopying, recording or by any information storage and retrieval system, without permission from the author.

Author email: H.Fang@tudelft.nl; haixingfang868@gmail.com

# Contents

<b>Introduction.....</b>	<b>1</b>
1.1. Cyclic partial austenite-ferrite ( $\gamma$ - $\alpha$ ) phase transformations.....	1
1.2. Self healing creep alloys.....	5
1.3. Aim of this thesis.....	7
1.4. Contents of this thesis.....	7
References.....	8
<b>Analysis of the grain size evolution for ferrite formation in Fe-C-Mn steels using a 3D model under a mixed-mode interface condition .....</b>	<b>11</b>
2.1. Introduction .....	12
2.2. Model description .....	12
2.2.1. Starting structure .....	13
2.2.2. Ferrite nucleation .....	14
2.2.3. Ferrite growth .....	15
2.2.4. Computational procedure .....	20
2.3. Results.....	23
2.3.1. Comparison between the present model and the phase-field model.....	23
2.3.2. Comparison between the simplified nucleation model (SNM) and the classical nucleation theory (CNT).....	27
2.3.3. Carbon diffusion and mixed-mode character .....	29
2.4. Discussion .....	30
2.5. Conclusions .....	32
References.....	33
<b>Modelling study on the three-dimensional neutron depolarisation response of the evolving ferrite particle size distribution during the austenite-ferrite phase transformation in steels.....</b>	<b>35</b>
3.1. Introduction .....	36
3.2. Neutron depolarisation .....	37
3.3. Microstructural magnetic model .....	39
3.4. Results and discussion .....	41
3.4.1. Influence of the size distribution .....	41
3.4.2. Influence of the volume fraction .....	43
3.5. Conclusions .....	47

References.....	48
<b>In-situ 3D neutron depolarization study of the transformation kinetics and grain size evolution during cyclic partial austenite-ferrite phase transformations in Fe-C-Mn steels.....</b>	<b>51</b>
4.1. Introduction.....	52
4.2. 3DND technique and experimental procedure.....	53
4.3. Results.....	57
4.3.1. Transformation kinetics in the whole ND experiment.....	57
4.3.2. Transformation kinetics and grain size evolution during individual cycles....	62
4.3.3. Comparison to DICTRA simulations.....	66
4.4. Discussion.....	68
4.4.1. Absence of new nucleation during cycling.....	68
4.4.2. Interface migration during cycling.....	71
4.5. Conclusions.....	73
References.....	74
<b>Autonomous filling of creep cavities in Fe-Au alloys studied by synchrotron X-ray nano-tomography.....</b>	<b>77</b>
5.1. Introduction.....	78
5.2. Materials and methods.....	79
5.2.1. Sample preparation and creep tests.....	79
5.2.2. Synchrotron X-ray nano-tomography.....	79
5.2.3. Data analysis.....	81
5.3. Results.....	82
5.3.1. Creep behavior and electron microscopy.....	82
5.3.2. Tomographic rendering.....	84
5.3.3. Shape classification of cavities and precipitates.....	87
5.3.4. Size distribution.....	89
5.3.5. Filling ratio of the creep cavities.....	91
5.4. Discussion.....	94
5.4.1. Growth modes of the creep cavities.....	94
5.4.2. Filling mechanism of the creep cavities.....	98
5.5. Conclusions.....	101
References.....	102
Supplementary Material for Chapter 5.....	105

<b>Autonomous filling of grain boundary cavities during creep loading in Fe-Mo alloys.....</b>	<b>109</b>
6.1. Introduction .....	110
6.2. Experimental .....	111
6.3. Results.....	112
6.3.2. Scanning electron microscopy .....	115
6.3.3. Transmission electron microscopy .....	119
6.3.4. Atom probe tomography .....	121
6.4. Discussion .....	123
6.4.1. Autonomous repair of creep damage.....	123
6.4.2. Requirements for the healing of creep damage .....	124
6.4.3. Solute reservoir for the healing of creep damage.....	125
6.4.4. Healing efficiency of creep damage.....	126
6.4.5. Effect of autonomous creep cavity filling on the macroscopic creep behavior	127
References .....	128
<b>Autonomous filling of creep cavities by dynamic precipitation in Fe-W alloys studied by synchrotron X-ray nanotomography .....</b>	<b>131</b>
7.1. Introduction .....	132
7.2. Experimental methods .....	133
7.2.1. Samples and creep tests .....	133
7.2.2. Synchrotron X-ray nano-tomography .....	134
7.2.3. Quantitative analysis .....	135
7.3. Results.....	135
7.3.1. Creep results .....	135
7.3.2. Tomographic rendering .....	137
7.3.3. Identification of isolated and linked cavities.....	140
7.3.4. Filling ratio of individual cavity by precipitation .....	142
7.4. Discussion .....	147
7.4.1. Autonomous filling of creep cavities by precipitation .....	147
7.4.2. Nucleation and growth of creep cavities and precipitates .....	148
7.4.3. Filling time for creep cavities.....	151
7.5. Conclusions .....	153
References .....	154
Supplementary Material for Chapter 7.....	156
<b>Summary.....</b>	<b>165</b>

<b>Samenvatting .....</b>	<b>169</b>
<b>Acknowledgements .....</b>	<b>173</b>
<b>List of publications .....</b>	<b>177</b>
<b>Curriculum Vitae .....</b>	<b>179</b>

---

# Chapter 1

## Introduction

Steel, the generic brand name for iron-based alloys containing carbon and a number of other alloying elements with a total concentration typically less than 25 weight percent, is an indispensable metallic material for modern society. With its increasing production reaching 1.69 billion tons in 2017, steel continues to play an important role as its versatile mechanical properties meet the different requirements for applications in a variety of sectors such as automotive, construction, packaging and rail [1]. One of the key factors that makes steel such a successful man-made material is that for a given chemical composition the microstructure of the steel can be tailored easily. The microstructures in steels, as defined by the spatial distribution of its constituent phases, are created via successive solid-state phase transformations during various stages of its production process. In this thesis, two solid state phase transformations, both requiring the most advanced physical characterization techniques currently available in the field, are studied: 1) cyclic phase transformations between two different allotropic forms of iron (*i.e.* austenite  $\gamma$  and ferrite  $\alpha$ ) to better understand nucleation and growth mechanisms in C-Mn steels and 2) high temperature precipitation at free internal surfaces in binary Fe-X alloys to explore the potential of autonomous healing of creep damage.

### 1.1. Cyclic partial austenite-ferrite ( $\gamma$ - $\alpha$ ) phase transformations

At temperatures of 1000 °C or higher, most steels will have a face-centered cubic (*fcc*) crystal structure, called austenite, into which all alloying elements are homogeneously dissolved, and all grains have the same chemical composition. Upon cooling down a solid state transformation takes place resulting in the formation of ferritic grains, which have the body-centered cubic (*bcc*) crystal structure, as well as other phases. Depending on the chemical composition and the cooling conditions the solid state transformations result in microstructures differing in grain size, phases present and their spatial arrangement [2]. The simplest picture for the austenite-ferrite phase transformations in the Fe-C system, which can be regarded as the purest model system for construction and engineering steels, shows two features: 1) ferrite needs to expel carbon to austenite as the solubility of carbon in ferrite is very low and 2) the atomic arrangement of the iron atoms needs to be reconstructed from the *fcc* to the *bcc* structure. In steels, *i.e.* iron alloys containing also containing alloying elements such as Mn, Si, Ni, Co, Mo etc., the alloying elements play an important role in the kinetics of the austenite-ferrite phase transformations. This important role is the result of the elements having different solubility in both phases and hence the transition of the *fcc* crystal structure into the *bcc* crystal structure also requires element partitioning at the interface separating both phases during the phase transformation. The austenite-to-ferrite transformation taking place during cooling from the hot-working temperatures is unavoidable in the production of most steel

grades and therefore has been studied extensively, both academically and industrially [3-6]. However, the ferrite-to-austenite transformation during heating and intercritical annealing is less well studied, and only recently has drawn more attention [7-9].

Whatever the transformation direction, both transformations proceed via a process of nucleation and growth of the newly formed phase, which in the end completely (or almost completely) consumes the original or parent phase. The driving force for the nucleation of a new phase from the parent phase is provided by the overall reduction in Gibbs free energy of the total system. At the same time the creation of new interfaces consumes energy. These two effects compete and result in a total Gibbs free energy  $\Delta G$  that depends on the number of atoms in the cluster  $n$ . Beyond a critical size  $n^*$  the Gibbs free energy of the cluster continuously decreases after the activation energy  $\Delta G^*$  at  $n^*$  is crossed. For  $n > n^*$  the cluster becomes a stable nucleus and rapidly grows into a larger particle [10, 11]. A generic description on the nucleation process from the thermodynamic point of view is addressed by Van Dijk and coworkers [12]. For a nucleation energy barrier  $\Delta G^*$  significantly larger than the kinetic energy, the nucleation rate becomes steady after an initial stage, as described accurately by the classical nucleation theory [13, 14]. For a nucleation energy barrier  $\Delta G^*$  comparable to the kinetic energy the nucleation rate starts to deviate from the predictions of the classical nucleation theory, while barrier-free nucleation could take place when  $\Delta G^*$  is smaller than the kinetic energy. As it is not yet possible to directly measure the nucleation of either ferrite or austenite at its embryonic state, the quantification of the nucleation kinetics involves a lot of uncertainties. These uncertainties challenge the accuracies of any modelling approach to describe and predict the overall transformation kinetics. Furthermore, as nucleation takes place preferentially at the (triple points of the) grain boundaries of the parent phase, the nucleation rate itself being dependent on the parent grain size, is responsible for the grain size of the product phase.

The growth of ferrite ( $\alpha$ ) in the austenite ( $\gamma$ ) involves the partitioning of carbon (and other alloying elements) between ferrite and austenite and the lattice reconstruction from the *fcc* to the *bcc* simultaneously. There are different assumptions for the rate-controlling mechanism. For an Fe-C alloy the diffusion-controlled model assumes that carbon concentrations at the interface between  $\gamma$  and  $\alpha$  are equal to the equilibrium concentrations for both phases at the actual temperature at any time and that the transformation kinetics is only controlled by the rate of carbon diffusion to and away from the actual interface. This implies that the interfacial reaction, *i.e.* the rearrangement of the iron atoms at the interface, occurs seemingly infinitely fast [15]. The interface-controlled model assumes that a finite interface mobility controls the transformation and that carbon diffuses fast enough such that both phases present have no gradient in their carbon concentration [16]. A more general model is the so-called mixed-mode model that takes into both carbon diffusion and interface reactions into account [17-20]. In the mixed-mode model both carbon diffusion and the finite interface mobility play a role. As a result the carbon concentrations at the ferritic and austenitic side of the interface are the result of the dynamics of interface migration and carbon diffusion. The diffusion-controlled and interface-controlled models thereby

become two extremes of the mixed-mode model. For Fe-C-X (X = Mn, Si, Ni, Co, Mo etc.) alloys, the partitioning of substitutional X element also needs to be considered. Historically there are two approaches to describe the kinetics of the Fe-C-X ternary alloy: the para-equilibrium (PE) model [21] and the local equilibrium (LE) model [15, 22]. In the PE model only carbon partitioning is considered and the X is not required to partition, hence the molar ratio of element X to Fe is constant across the interface. In the LE model all alloying elements can partition in the time of the transformation and the chemical potentials of each component are equal at the interface, *i.e.* the concentration of each alloying element at either side of the interface is equal to the equilibrium value at that temperature. For an Fe-C-X ternary alloy with the composition above the zero partition line at a given temperature, the transformation requires the redistribution of alloying elements in the bulk and the kinetics is controlled under local equilibrium with partitioning (LEP<sup>1</sup>). For the composition below the zero partition line at a given temperature, the transformation does not require the redistribution of alloying elements in the bulk and the kinetics is controlled under local equilibrium with negligible partitioning (LENP<sup>2</sup>). Here ‘negligible’ means that the partitioning of substitutional element X is restricted only to the interfacial region and thereby a ‘spike’ in the concentration profile of X is present at the interface. The width of the spike  $\varepsilon$  can be approximated to  $\varepsilon = 2D_X/v$  where  $D_X$  is the diffusivity of X and  $v$  is the interface velocity. The calculated width according to experimentally determined growth rate of ferrite is found to be smaller than the inter-atomic distance [23], which raises questions on the physical foundation for the LENP [24]. However, there is large amount of experimental evidence directly and indirectly supporting the existence of such a spike at the interface [6, 24, 25].

Over the years various experimental approaches, *i.e.* linear cooling and heating experiments, gradient experiments and decarburization experiments, have been carried out to study the austenite-to-ferrite and the ferrite-to-austenite transformation [6]. In contrast to these experiments in which nucleation and growth take place simultaneously, recently the concept of cyclic partial transformation was proposed [26]. This novel approach has been proven to be more informative processes taking place at the moving interfaces, as nucleation of new grains during the transformation is assumed not to occur and only the interface migration is supposed to affect the transformation kinetics. The assumption of no new nucleation during cycling is based on the fact that during every stage of the process both phases are present. The resulting abundance of austenite-ferrite interfaces means that the transformation can proceed energetically more favorably by moving the existing interface rather than via the creation of new grains. In the cyclic experiments the steel samples are first fully austenitized and then cooled down to  $\gamma/\alpha$  two-phase region, followed by an isothermal holding. Then the temperature is cycled without (Fig. 1.1a) or with isothermal holding (Fig. 1.1b) between the two extreme temperatures ( $T_1$  and  $T_2$ ) both located in the two-phase region. The behavior of the interface migration under non-equilibrium conditions is well illustrated in these cyclic experiments. As shown in Fig. 1.1c once a cycle is started, the interface stays stagnant (S) as the partitioning spike of the alloying

<sup>1</sup> In some texts PLE is used as abbreviation.

<sup>2</sup> In some texts NPLE is used as abbreviation.



elements needs to be diffused out, then migrates in line with the temperature change (the expected normal direction (N)), followed by moving in the same direction whilst the temperature change inverses its direction (I), reaches a stagnant stage again (S) and only with a substantial temperature change the interface will proceed in the ‘right’ direction (N). Over cycling the interface experiences all these stages, which modifies the composition locally and thereby influences the kinetics even during early stages of the final cooling. However, while the dilatometric observations during cyclic transformation can be fully explained by assuming the number of grains remaining more or less constant there is no actual proof for this. In a more general sense, the evolution of the grain size distribution of the product phase (ferrite during the cooling and austenite during heating) is generally ignored, not because it is not important but primarily because *in-situ* techniques to assess the grain size within the bulk of the sample during transformation are rare. In fact, the only technique known to us to give an indication of the grain size of (magnetic) ferrite during transformation is the three dimensional neutron depolarization (3DND) technique [27, 28], first used for that purpose by Te Velthuis [29, 30] for a high carbon steel transforming during slow isochronal cooling.

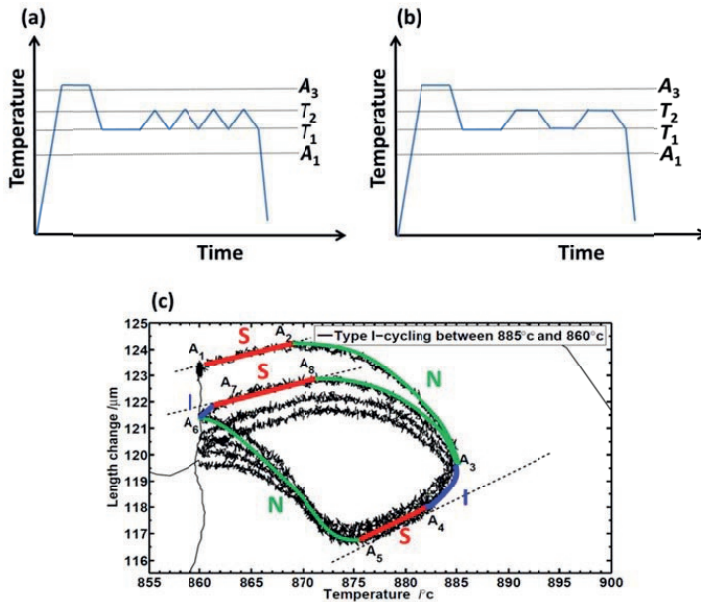


**Fig. 1.1.** Temperature profiles of cyclic partial transformations that show (a) a type I experiment where temperature rate switches instantaneously at the changing direction during cycling and (b) a type H experiment where temperature cycles with isothermal holding. (c) Dilatometer measurements on an Fe-0.023C-0.17Mn (wt.%) alloy subjected to the type I experiment [26].

## 1.2. Self healing creep alloys

Creep is a time-dependent deformation process occurring in materials subjected to elevated temperature and external stress. For metals the creep deformation can be observed in a realistic time scale above a temperature of  $0.4T_m$  where  $T_m$  is the melting temperature in kelvin under a constant load [31]. High temperature heat-resistant steels are widely used in fossil and nuclear power plants as turbine blades, boilers and pipes subjected to a temperature above 500 °C and a load above 22 MPa for an energy efficiency above 40% [32]. A key requirement for this type of steel is to have a good creep-resistance, which is normally defined as being able to withstand at the selected temperature a static stress of 100 MPa for  $10^5$  h without fracture [32]. Fracture during creep loading generally starts with the creation of cavities that preferentially nucleate and grow at grain boundaries perpendicular or inclined to the imposed stress [31]. The coalescence of creep cavities at the late stage of creep leads to the catastrophic failure of steels. The conventional approach to create better creep-resistant steels is to delay the occurrence of cavity formation. The effective means to do so is to strengthen the steels via solid-solution strengthening, precipitation hardening and work hardening. The strengthening approach generally works as demonstrated in the development of high-performance creep steels such as Ni containing austenitic steels, 9-12 wt.% Cr ferritic/martensitic steels and 12-29 wt.% Cr ferritic steels [33-35]. However, while these steels show a strong creep-resistance in the initial stage, inevitably the creep properties degrade over the service time and the initial creep damage, once formed, increases in severity in a continuous manner without any tendency to stop or slow down.

Given that the occurrence of the creep damage is unavoidable, an alternative approach has been proposed to autonomously heal the damage by the material itself. This so-called self-healing approach is inspired by nature and has been applied successfully to a wide range of materials such as polymers, coatings, concretes, asphalts, composites, ceramics and metals [36-38]. The common strategy to make a material self-healing is to enable 'local temporary mobility' [38]. This demands that the healing agent has sufficient mobility to arrive at the damage sites only when the damage appears. While the mobility of atoms in alloys is much smaller than those in other classes of materials *e.g.* molecules in polymers, there are a number of promising self-healing approaches for metals such as aluminum alloys, magnesium alloys and creep steels as presented in recent reviews on self-healing metals [39, 40].

For compositionally modified multi-component austenitic stainless steels Laha and coworkers [41] and Shinya [42] observed that the precipitation of either Cu or BN in the creep cavities resulted in a significant extension of the creep lifetime. Subsequently, extensive studies on the self-healing of creep damage in Fe-Cu [43] and Fe-Au [44-46] binary alloys, both serving as model systems for self healing steels and designed to facilitate the observation of damage and healing rather than aiming to obtain relevant creep strength values, have been made at the TU Delft. From these results the design criteria for metallic systems having the ability to autonomously heal early stage creep damage have been derived [44, 45]. As shown in Fig. 1.2a, the potential healing agent of solute X in the Fe-X alloys should be fully solutionizable at a

relatively high temperature and its solubility should be larger than that at the desired creep temperature. In this manner, a proper degree of super saturation at the creep temperature is created and this super-saturation provides the driving force for precipitation. To let the precipitation take place selectively at the damage sites (creep cavities), the nucleation energy barrier at the damage sites should be considerably smaller than that for precipitation in the *bcc* iron matrix. This requires the atomic size  $r$  of the X should be substantially larger than Fe atom. A good example to illustrate this requirement is a comparative study between Fe-Au and Fe-Cu alloys. As the atomic ratio  $r_{\text{Au}}/r_{\text{Fe}} = 1.13$  and  $r_{\text{Cu}}/r_{\text{Fe}} = 1.005$ , Au-rich precipitates are much more damage site selective than Cu-rich precipitates. As shown in Fig. 1.2b, the gold precipitates fill the empty space of the grain-boundary creep cavities, resulting in Au-depleted regions adjacent to the grain boundary. For Fe-Cu alloys the Cu-rich precipitation is less site selective *i.e.* precipitates form at damage sites as well as in the matrix. Nevertheless, the Cu-rich precipitation at creep cavities significantly extend the creep lifetime, as illustrated in the comparative study between an annealed Fe-Cu sample (without super saturated solute in the matrix) and an as-quenched Fe-Cu sample (with super saturated solute in the matrix) with the same composition. However, the site selective Au-precipitation prolongs the creep lifetime of an Fe-Au sample even more when subjected to the same creep condition (see Fig. 1.2c).

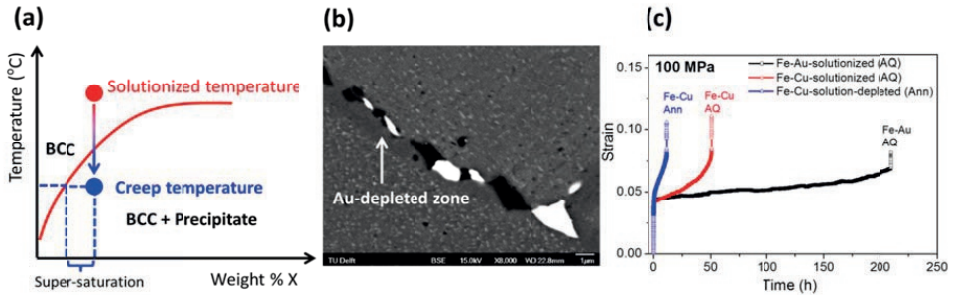


**Fig. 1.2.** (a) Schematic phase diagram of an Fe-X self-healing creep alloy. (b) SEM image of an Fe-0.83 at.% Au after creep at 550 °C and 100 MPa showing the filling of grain-boundary cavities (black features) by the gold-rich precipitates (white features) and the gold depleted zone [45]. (c) the creep curves of the fully annealed Fe-0.98 at.% Cu, the as-quenched (AQ) Fe-0.98 at.% Cu and the as-quenched Fe-0.83 at.% Au subjected to a temperature of 550 °C and a load of 100 MPa [45].

Although the Fe-Au alloys demonstrate a promising approach for self-healing creep steels, as an alloying element gold is too expensive to be a realistic option for the steel industry. Exploring more affordable and equally effective healing agents is thus of great interest. Some modelling studies using the first principles, Monte-Carlo and finite-element modelling provided useful guidelines [47-49]. The diffusivities for a wide

range of elements in *bcc* iron were computed by density functional theory (DFT) [48]. For the creep healing mechanism Versteyleen and coworkers [50] proposed that the diffusional flux of vacancies are counteracted by the diffusion flux of super saturated solutes, thereby the steady-state strain rate can be reduced resulting in an extension of the creep lifetime. To search for cost-effective and compatible solutes for self-healing creep steels, it is obvious that more experimental work should be done. To better understand the self-healing mechanism, it is apparent that a more detailed characterization of the interaction between the precipitates and the creep cavities is required.

### 1.3. Aim of this thesis

The aim of this study is to gain new insights into the evolution of the microstructure during austenite-ferrite phase transformations of carbon-manganese steels for automotive constructions with a specific interest in nucleation and ferrite grain size evolution. To this aim, the influence of the nucleation on the grain size distribution has been studied in detail with a computer model. The capability of the neutron depolarization technique for measuring ferrite grain size and the width of the ferrite grain size distribution was first analyzed theoretically. This technique has then been applied to study the kinetics of cyclic partial austenite-ferrite phase transformations together with a modelling approach to unravel the fine details of the transformation. To elucidate the self-healing mechanism, high resolution synchrotron X-ray nano-tomography has been adopted to study the co-locations of Au-rich precipitates and creep cavities in Fe-Au alloys. To search for more cost-effective self-healing agents than gold, the time resolved healing of creep damage in Fe-Mo and Fe-W alloys has been studied in detail.

### 1.4. Contents of this thesis

In Chapter 2 a 3D model that couples classical nucleation theory and the interface moving under mixed-mode interface condition is presented for predicting the average ferrite grain size and ferrite grain size distribution in Fe-C-Mn steels. The results of this model are compared to those of a published phase-field model to simulate the ferritic microstructure evolution during linear cooling of an Fe-0.10C-0.49Mn (wt.%) steel. The research aims to link the grain size distribution for different levels of ferrite fraction to accurate estimates of the key physical parameters, the nucleation temperature interval and the effective interface mobility for the  $\gamma$ - $\alpha$  phase transformation in this C-Mn steel. To link a ferritic-austenitic microstructure in 3D with the data as obtainable from three-dimensional neutron depolarization (3DND) technique, a modelling study has been conducted and this is presented in Chapter 3. The magnetic configurations of the ferromagnetic ferrite particles are directly linked to 3DND parameters. By computing the magnetic configurations for magnetic microstructures with mono- and poly-disperse magnetic particles in 3D space, the applicability of 3DND for determination of the average ferrite grain size is re-evaluated. Furthermore by exploring the field correlation function the 3DND technique not only yields the average ferrite grain size but also can give a good estimate of the relative width of the particle size distribution. The 3DND technique developed is then applied

to study the kinetics of cyclic partial phase transformations for an Fe-0.25C-2.1Mn (wt.%) steel in Chapter 4. The number density of the ferrite grains was estimated and the results demonstrate that during cycling nucleation is negligible or even absent. The experimental results also led to insights into slow interface velocity due to partitioning of Mn and unusual cyclic behavior compared to lean-alloyed steels.

In Chapter 5 synchrotron X-ray nano-tomography experiments to study the microstructure of the creep-failed Fe-Au alloy samples are described. Different stages in the filling process of individual creep cavities by gold precipitation were identified to characterize the self-healing mechanism in creep-resistant steels. The nucleation, growth and coalescence of both precipitates and creep cavities have been studied in detail. The time evolution for the filling ratio of individual creep cavities led to two distinct routes that are well explained by a simple model considering the absence and presence of linkage for neighboring creep cavities. The autonomous repair of creep damage by site-selective precipitation in a binary Fe-Mo alloy (6.2 wt.% Mo) is presented in Chapter 6. The precipitation of Laves  $\text{Fe}_2\text{Mo}$  phase at creep cavities has been studied in detail with scanning electron microscopy (SEM), electron back scattered diffraction (EBSD), transmission electron microscopy (TEM) and atom probe tomography (APT). The results show that  $\text{Fe}_2\text{Mo}$  precipitation can fill the grain-boundary creep cavities and this process is strongly temperature dependent. The demonstrated site-selective  $\text{Fe}_2\text{Mo}$  precipitation at creep cavity surfaces provides a new perspective on the role of Mo for creep steels in addition to its positive solid solution strengthening effect. Inspired by the self-healing  $\text{Fe}_2\text{Mo}$  alloy, the potential for self-healing of creep damage has also been evaluated for Fe-W alloys as discussed in Chapter 7. It is found that in Fe-W alloys W-rich precipitation occurs at the free surface of creep cavities. The synchrotron X-ray nano-tomography has been adopted to characterize the spatial distribution and the morphology of both the precipitates and the cavities at different stages of creep. The detailed statistics show two different trends for the cavity filling for isolated and linked cavities, respectively. The study on the nucleation and growth of precipitates and creep cavities led to a deeper understanding of the dependence of precipitate nucleation on the cavities and an estimate of the self-filling kinetics.

The main findings in this thesis are compiled in the Summary section.

## References

1. The World Steel Association: <https://www.worldsteel.org>.
2. D.A. Porter, K.E. Easterling, M. Sherif: *Phase Transformations in Metals and Alloys*, 3<sup>rd</sup> Edition, CRC press, 2009.
3. G. Purdy, J. Ågren, A. Borgenstam, Y. Bréchet, M. Enomoto, E. Gamsjager, M. Gouné, M. Hillert, C. Hutchinson, M. Militzer, H. Zurob, *ALEMI: Metall. Mater. Trans. A*, 2011, vol. 42, pp. 3703-18.
4. H.S. Zurob, C.R. Hutchinson, Y. Breché, H. Seyedrezai, G.R. Purdy: *Acta Mater.*, 2009, vol. 57, pp. 2781-92.

5. E. Novillo, D. Hernández, I. Gutiérrez, B. López: *Mater. Sci. Eng. A*, 2004, vol. 385, pp. 83-90.
6. M. Gouné, F. Danoix, J. Ågren, Y. Bréchet, C.R. Hutchinson, M. Militzer, G. Purdy, S. van der Zwaag, and H. Zurob: *Mater. Sci. Eng. R*, 2015, vol. 92, pp. 1-38.
7. V.I. Savran, S.E. Offerman, J. Sietsma: *Metall. Mater. Trans. A*, 2010, vol. 41, pp. 583-91.
8. M. Ollat, M. Militzer, V. Massardier, D. Fabregue, E. Buscarlet, F. Keovilay, M. Perez: *Comp. Mater. Sci.*, 2018, vol. 148, pp. 282-90.
9. M.G. Mecozzi, C. Bos, J. Sietsma: *Acta Mater.*, 2015, vol. 88, pp. 302-13.
10. H.I. Aaronson, M. Enomoto, and J.K. Lee: *Mechanisms of diffusional phase transformations in metals and alloys*, CRC Press, Boca Raton, 2010, pp. 49-245.
11. S. van der Zwaag: "Kinetics of phase transformations in steels", *Phase Transformations in Steels: Fundamentals and Diffusion-Controlled Transformations*, 2012, pp. 126-156.
12. N.H. van Dijk, S.E. Offerman, J. Sietsma, and S. van der Zwaag: *Acta Mater.*, 2007, vol. 55, pp. 4489-98.
13. K.F. Kelton: *Solid State Physics*, Vol. 45, H. Ehrenreich and D. Turnbull, eds., Academic Press, New York, NY, 1991, pp. 75.
14. D. Kashchiev: *Nucleation, basic theory with applications*, Butterworth-Heinemann, Oxford, OX, 2000, pp. 184-270.
15. C. Zener: *J. Apply. Phys.*, 1949, vol. 20, pp. 950-3.
16. J.W. Christian: *The theory of transformations in metals and alloys, 3<sup>rd</sup> Edition*, Pergamon, Oxford, 2002.
17. G.P. Krielaart, J. Sietsma, and S. van der Zwaag: *Mater. Sci. Eng. A*, 1997, vol. 237, pp. 216-23.
18. J. Sietsma and S. van der Zwaag: *Acta Mater.*, 2004, vol. 52, pp. 4143-52.
19. C. Bos and J. Sietsma: *Acta Mater.*, 2009, vol. 57, pp. 136-44.
20. C. Bos, J. Sietsma: *Acta Mater.*, 2009, vol. 57, pp. 136-44.
21. M. Hillert: *Report of the Swedish Institute for Metal Research*, Stockholm, Sweden, 1953.
22. J.S. Kirkaldy: *Can. J. Phys.*, 1958, vol. 36, pp. 907-16.
23. D.E. Coates: *Metall. Trans.*, 1973, vol. 3, pp. 2313-25.
24. H. Chen, S. van der Zwaag: *Philos. Mag. Lett.*, 2012, vol. 92, pp. 86-92.
25. C. Capdevila, J. Cornide, K. Tanaka, K. Nakanishi, E. Urones-Garrote: *Metall. Mater. Trans. A*, 2011, vol. 42, pp. 3719-28.
26. H. Chen, B. Appolaire, S. van der Zwaag: *Acta Mater.*, 2011, vol. 59, pp. 6751-60.
27. M.T. Rekveldt and F.J. van Schaik: *J. Appl. Phys.*, 1979, vol. 50, pp. 2122-7.
28. R. Rosman and M.T. Rekveldt: *Phys. Rev. B*, 1991, vol. 43, pp. 8437-49.
29. S.G.E. te Velthuis, N.H. van Dijk, M.Th. Rekveldt, J. Sietsma, and S. van der Zwaag: *Acta Mater.*, 2000, vol. 48, pp. 1105-14.
30. S.G.E. te Velthuis, N.H. van Dijk, M.Th. Rekveldt, J. Sietsma, and S. van der Zwaag: *Mater. Sci. Eng. A*, 2000, vol. 277, pp. 218-28.
31. J. Lemaitre, R. Desmorat: *Engineering damage mechanics: ductile, creep, fatigue and brittle failures*, Springer-Verlag Berlin 2005.
32. H.K.D.H. Bhadeshia: *ISIJ Int.*, 2001, vol. 41, pp. 626-640.
33. M. Taneike, F. Abe, K. Sawada: *Nature*, 2003, vol. 424, pp. 294-296.

34. Q. Lu, W. Xu, S. van der Zwaag: *Acta Mater.*, 2004, vol. 77, pp. 310-23.
35. R.L. Klueh: *Int. Mater. Rev.*, 2005, vol. 50, pp. 287-310.
36. S.R. White, N.R. Sottos, P.H. Geubelle, J.S. Moore, M.R. Kessler, S.R. Sriram, E.N. Brown, S. Viswanathan: *Nature*, 2001, vol. 409, pp. 794-7.
37. M.D. Hager, P. Greil, C. Leyens, S. van der Zwaag, U.S. Schubert: *Adv. Mater.*, 2010, vol. 22, pp. 5424-30.
38. S. van der Zwaag, E. Brinkman, eds., *Self healing materials: pioneering research in the Netherlands*, IOS Press, Amsterdam, 2015.
39. J. B. Ferguson, B.F. Schultz, P.K. Rohatgi: *JOM*, 2014, vol. 66, pp. 866-871.
40. N.H. van Dijk, S. van der Zwaag: *Adv. Mater. Inter.*, 2018, pp. 1800226.
41. K. Laha, J. Kyono, S. Kishimoto, N. Shinya: *Scr. Mater.*, 2005, vol. 52, pp. 675-8.
42. N. Shinya: *Adv. Sci. Tech.*, 2008, vol. 54, pp. 152-7.
43. S.M. He, N.H. van Dijk, H. Schut, E.R. Peekstok, S. van der Zwaag: *Phys. Rev. B*, 2010, vol. 81, pp. 094103.
44. S. Zhang, J. Kohlbrecher, F.D. Tichelaar, G. Langelaan, E. Brück, S. van der Zwaag, N.H. van Dijk: *Acta Mater.*, 2013, vol. 61, pp. 7009-19.
45. S. Zhang, C. Kwakernaak, W.G. Sloof, E. Brück, S. van der Zwaag, N.H. van Dijk: *Adv. Eng. Mater.*, 2015, vol. 17, pp. 598-603.
46. S. Zhang, C. Kwakernaak, F.D. Tichelaar, W.G. Sloof, M. Kuzmina, M. Herbig, D. Raabe, E. Brück, S. van der Zwaag, N.H. van Dijk: *Metall. Mater. Trans. A*, 2015, vol. 46, pp. 5656-70.
47. E.G. Karpov, M.V. Grankin, M. Liu, M. Ariyan: *J. Mech. Phys. Solids*, 2012, vol. 60, pp. 250-260.
48. C.D. Versteyleen, N.H. van Dijk, M.H.F. Sluiter: *Phys. Rev. B*, 2017, vol. 96, pp. 94105.
49. C.D. Versteyleen, N.K. Szymański, M.H.F. Sluiter, N.H. van Dijk: *Philos. Mag.*, 2018, vol. 98, pp. 864-77.
50. C.D. Versteyleen, M.H.F. Sluiter, N.H. van Dijk: *J. Mater. Sci.*, 2018, vol. 53, pp. 14758-73.



---

# Chapter 2

## **Analysis of the grain size evolution for ferrite formation in Fe-C-Mn steels using a 3D model under a mixed-mode interface condition**

A 3D model has been developed to predict the average ferrite grain size and grain size distribution for an austenite-to-ferrite phase transformation during continuous cooling of an Fe-C-Mn steel. Using a Voronoi construction to represent the austenite grains, the ferrite is assumed to nucleate at the grain corners and to grow as spheres. Classical nucleation theory is used to estimate the density of ferrite nuclei. By assuming a negligible partition of manganese, the moving ferrite-austenite interface is treated with a mixed-mode model in which the soft impingement of the carbon diffusion fields is considered. The ferrite volume fraction, the average ferrite grain size and the ferrite grain size distribution are derived as a function of temperature. The results of the present model are compared with those of a published phase-field model simulating the ferritic microstructure evolution during linear cooling of an Fe-0.10C-0.49Mn (wt.%) steel. It turns out that the present model can adequately reproduce the phase-field modelling results as well as the experimental dilatometry data. The model presented here provides a versatile tool to analyze the evolution of the ferrite grain size distribution at low computational costs.



## 2.1. Introduction

Fe-C-Mn steels hold and retain an important position in high-quality construction and automotive steels, and therefore, their transformation behavior receives a lot of attention in academia and industry [1-6]. Their mechanical properties, which are controlled by their microstructure, can be tuned relatively easily by thermomechanical processing. Ferrite is the first transformation product that forms during cooling as a result of austenite decomposition. Therefore understanding the decomposition of austenite ( $\gamma$ ) into ferrite ( $\alpha$ ) during cooling, is of central importance for predicting the development of the microstructure during thermomechanical processes. This is the reason why the austenite-to-ferrite transformation has been studied extensively, both experimentally and theoretically [7-12]. A recent detailed overview on all physical aspects of this transformation is presented by Gouné and coworkers [13].

During the austenite-to-ferrite phase transformation the volume fraction and the grain size distribution of the ferrite fraction play a key role in the development of the ferritic microstructure. Traditional in-situ experimental techniques, like dilatometry, only determine the total fraction transformed, but yield no information on the evolution of the ferrite grain size. Such complementary information can however be obtained by micro-beam X-ray diffraction [14-15] and three-dimensional neutron depolarization [16-17]. These in-situ techniques provide a more detailed view on the microstructure development, but cannot monitor the evolution in chemical composition profile. The aim of this work is to establish a concise 3D model to achieve a comprehensive description of the austenite-to-ferrite transformation and to obtain quantitative information on the ferrite volume fraction, grain size distribution and carbon diffusion profiles in the austenite at relatively low computational costs.

In the following we will first define the 3D austenite-to-ferrite transformation model. This model is inspired by the topological transformation models established by Te Velthuis and coworkers [18] and Offerman and coworkers [19]. The predictions of our new transformation model are presented for an Fe-0.10C-0.49Mn (wt.%) steel cooled at modest constant cooling rates starting from a single-phase austenite. These results are then compared to the previously presented predictions from a computationally more demanding phase-field model [20], as well as the experimental results obtained from dilatometry. Special attention is given to the predicted ferrite grain size distribution as a function of the assumed nucleation behavior, as advanced experimental methods, such as neutron depolarization, emerge which will enable the in-situ experimental determination of this grain size distribution during linear cooling.

## 2.2. Model description

In the following we present an analytical model for the ferritic microstructure evolution. The 3D microstructure model assumes that the new ferrite phase nucleates at Voronoi vertices (grain corners) and grows isotropically (as a sphere). The number of ferrite nuclei formed is calculated using classical nucleation theory (CNT) [21-23]. The moving austenite-ferrite interface is treated as progressing under mixed-mode [24] conditions. Analytical expressions for the carbon concentration at the interface and far

away from the interface are derived for non-overlapping and overlapping of diffusion fields (soft impingement). As the transformation proceeds, the growing ferrite grains may also get in contact with other ferrite grains (hard impingement). As local contact between neighboring ferrite grains does not exclude further growth of the ferrite by the motion of the non-pinned part of the interface, the further growth after the onset of hard impingement is also modelled.

### 2.2.1. Starting structure

The parent structure is fully austenite with a given number density  $\rho_\gamma$  of austenite grains represented in a cubic box of length  $L_b$  in which periodic boundary conditions are applied. The average austenite grain size corresponds to  $\bar{d}_\gamma = (6/\pi\rho_\gamma)^{1/3}$ . The austenite grain centers are generated randomly with a minimum distance  $d_{min}$  to control the grain size distribution. Voronoi cells are subsequently constructed to represent the austenite grains. The vertices of the Voronoi cells are assumed to be the potential nucleation sites for the forming ferrite phase as its nucleation is found to be predominantly taking place at grain corners [25]. In the present work the Voronoi cells are constructed by using the Multi-Parametric Toolbox [26] in the Matlab environment. An initial austenite structure is shown in Fig. 2.1a and a 3D view of the same domain after partial austenite transformation to a ferrite fraction of 0.59 is shown in Fig. 2.1b.

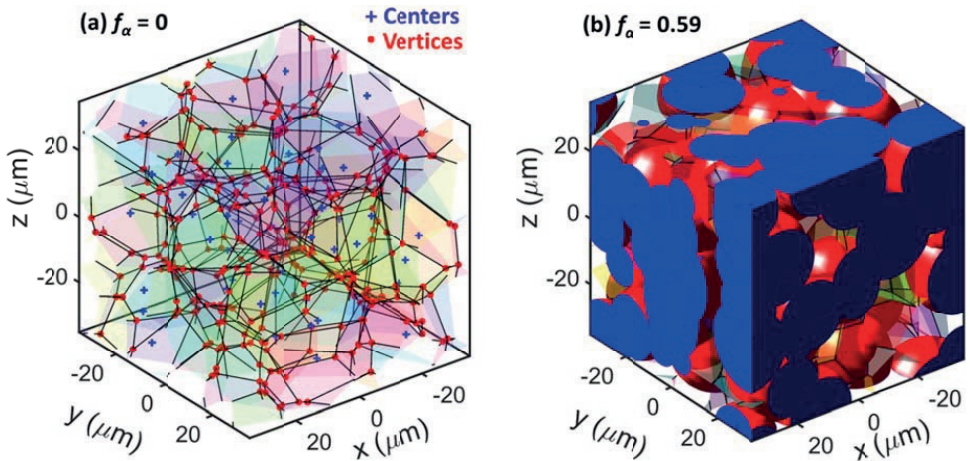


**Fig. 2.1.** (a) Initial austenite structure represented by Voronoi cells and (b) a 3D view of the transformed structure with a ferrite volume fraction of  $f_\alpha = 0.59$  in a cubic box with a length of  $L_b = 70 \mu\text{m}$  (spherical ferrites surface shown in red and their cut-off plane on the edge of the box is shown in blue).

### 2.2.2. Ferrite nucleation

The reduction in Gibbs free energy for the new ferritic phase with respect to the parent austenite phase provides the driving force for the austenite-to-ferrite transformation. At the same time, the creation of new interfaces requires a consumption of energy. The competition between these two effects results in a change in Gibbs free energy  $\Delta G$  that depends on the cluster size  $n$ . At a critical cluster size  $n^*$  the change in Gibbs free energy shows a maximum value  $\Delta G^*$ , which is the activation barrier for nucleation. When this activation barrier  $\Delta G^*$  is large compared to the thermal energy  $k_B T$  (where  $k_B$  is Boltzmann's constant and  $T$  the temperature in kelvin), then the Classical Nucleation Theory (CNT) describes the nucleation kinetics in polycrystalline materials [27-28]. Recently, Sharma and coworkers [29] estimated that  $\Delta G^* \approx 3 - 6 k_B T$  for the nucleation of austenite in ferrite. Similar small values are observed for the nucleation of ferrite in austenite [27]. According to the CNT, the steady-state nucleation rate per unit of volume  $\dot{N}$  can be expressed as [27]:

$$\dot{N} \propto Z N_p \beta^* \exp\left(-\frac{\Delta G^*}{k_B T}\right), \quad (2.1)$$

where  $Z$  is the Zeldovich factor,  $N_p$  the number density of potential nucleation sites,  $\beta^*$  the frequency factor,  $k_B$  the Boltzmann constant and  $T$  the temperature in kelvin. The Zeldovich factor is nearly constant ( $Z \approx 0.05$ ) and accounts for the width of the nucleation barrier on the effective number of clusters that become supercritical.  $N_p$  is decreasing during the austenite-to-ferrite transformation due to the consumption of potential nucleation sites by (i) the nucleation itself and (ii) by ferrite growth. As the density of potential nucleation sites is relatively high,  $N_p$  is assumed to be proportional to the untransformed volume fraction. The frequency factor can be expressed as  $\beta^* \propto \nu \exp[-Q_D/(k_B T)]$ , where  $Q_D$  is the energy barrier for diffusion,  $\nu \approx k_B T/h$  is the attempt frequency and  $h$  is Planck's constant. The energy barrier for nucleation  $\Delta G^*$  is given by:

$$\Delta G^* = \frac{\Psi}{(\Delta G_V - \Delta G_S)^2}, \quad (2.2)$$

where  $\Psi$  is a constant that comprises all the information of the shape of the critical nucleus and interfacial energies between the nucleus and the surrounding parent grains. A value of  $\Psi \approx 5 \times 10^{-8} \text{ J}^3 \text{ m}^{-6}$  [14] is used in the present work.  $\Delta G_V$  is the difference in Gibbs free energy per unit volume between ferrite and austenite, which is calculated with Thermo-Calc under para-equilibrium conditions.  $\Delta G_S$  is the misfit strain energy due to the difference in volume between ferrite and austenite and is estimated to be  $\Delta G_S \approx 1 \times 10^7 \text{ J m}^{-3}$  [30]. In the present work  $\Delta G_S$  is assumed to be  $0.7 \times 10^7 \text{ J m}^{-3}$  to adjust the starting nucleation temperature. The nucleation rate can thus be written as:

$$\dot{N} = AZN_0(1-f_a)\left(\frac{k_B T}{h}\right) \exp\left(-\frac{Q_D}{k_B T}\right) \exp\left(-\frac{\Psi}{k_B T(\Delta G_V(T) - \Delta G_S)^2}\right), \quad (2.3)$$

where  $A$  is a constant and  $N_0$  represents the number of potential nucleation sites at the austenite grain corners at the start of the transformation.

### 2.2.3. Ferrite growth

After nucleation the ferrite grains are assumed to grow isotropically, hence to grow as spheres. Using the mixed-mode concept [24], the interface velocity  $v$  is proportional to product of the local chemical driving force  $\Delta G$  and the interface mobility  $M$

$$v = M \Delta G. \quad (2.4)$$

The interface mobility  $M$  is temperature dependent:

$$M = M_0 \exp\left(-\frac{Q_M}{RT}\right), \quad (2.5)$$

where  $M_0$  is a constant and  $Q_M = 140 \text{ kJmol}^{-1}$  [31] is the activation energy for atomic motion. It should be noted that  $M_0$  in Eq. 2.5 corresponds to an effective interface mobility, which accounts for the lattice reconstruction, solute drag effect due to substitutional alloying elements [32], pinning effects of precipitates at the grain boundary [33] and the direction of the transformation [34].

The local driving force  $\Delta G$  depends on the solute concentrations at the interface. In this model, it is assumed that the carbon concentration in the ferrite is homogeneous and equal to the equilibrium value  $C_{eq}^{\alpha\gamma}$ . Therefore,  $\Delta G$  can be formulated as

$$\Delta G = \chi \left( C_{eq}^{\gamma\alpha} - C^\gamma \right), \quad (2.6)$$

where  $\chi$  is a proportionality factor (that can be calculated with Thermo-Calc),  $C_{eq}^{\gamma\alpha}$  is the equilibrium carbon concentration in austenite and  $C^\gamma$  is the carbon concentration at the interface at the austenite side. To calculate the interface velocity  $v$  the value of  $C^\gamma$  is required. For each ferrite grain, the growth velocity is expected to be different at each time step as the time since nucleation and the distance to neighboring ferrite grain differs. In the following the treatment used to calculate the interface velocity at distinctly different stages of the transformation is discussed.

#### (a) Non-overlapping of diffusion fields

As illustrated in Fig. 2.2a, at an early stage of ferrite growth the diffusion fields surrounding these ferrite grains do not overlap. In this case the carbon concentration far away from the  $\gamma/\alpha$  interface ( $C_\infty$ ) equals the nominal concentration ( $C_0$ ):  $C_\infty = C_0$ . In such a condition, the carbon concentration profile surrounding the ferrite grains,  $C(r)$ , can be approximated by a second-order polynomial [35], where the carbon concentration as a function of the distance  $r$  from the interface ( $r = 0$  at the  $\gamma/\alpha$  interface) is given by:

$$C(r) = C_0 + (C^\gamma - C_0) \left(1 - \frac{r}{L}\right)^2 \quad (0 \leq r \leq L), \quad (2.7)$$

where  $L$  is the diffusion length. This concentration profile fulfills the following boundary conditions:

$$C(r=0) = C^\gamma, \quad (2.8)$$

$$C(r=L) = C_0. \quad (2.9)$$

There is no concentration gradient at the position of diffusion length  $L$ :

$$\left. \left( \frac{\partial C}{\partial r} \right) \right|_{r=L} = 0, \quad (2.10)$$

Considering a ferrite grain radius of  $R_\alpha$ , the mass conservation of carbon can be expressed as:

$$\int_0^{R_\alpha} (C_0 - C_{eq}^{\alpha\gamma}) 4\pi r^2 dr = \int_0^L (C(r) - C_0) 4\pi (r + R_\alpha)^2 dr, \quad (2.11)$$

Combining Eqs. 2.7-11 results in:

$$\begin{aligned} (C_0 - C_{eq}^{\alpha\gamma}) V_\alpha &= 4\pi \int_0^L (C(r) - C_0) (r + R_\alpha)^2 dr \\ &= -\frac{4\pi (C_0 - C^\gamma) (L^3 + 5L^2 R_\alpha + 10L R_\alpha^2)}{30}, \end{aligned} \quad (2.12)$$

where  $V_\alpha = 4\pi R_\alpha^3/3$  is the ferrite grain volume. During the ferrite growth there is no carbon accumulation at the interface. Then, the following equation can be derived:

$$v(C^\gamma - C_{eq}^{\alpha\gamma}) = M \chi (C_{eq}^{\gamma\alpha} - C^\gamma) (C^\gamma - C_{eq}^{\alpha\gamma}) = -D \left. \left( \frac{\partial C}{\partial r} \right) \right|_{r=0}, \quad (2.13)$$

where  $D$  the carbon diffusivity in austenite calculated according to [36]. The mixed-mode nature of the transformation, quantified by the mode parameter  $S = (C^{\gamma\alpha} - C^\gamma) / (C^{\gamma\alpha} - C_0)$ , is controlled by parameter  $z = (D / M \chi) (A_\alpha / V_\alpha)$ , where  $A_\alpha$  is the interfacial area of the growing ferrite grain [37]. The extreme cases correspond to (i) diffusion control for  $z = 0$  and (ii) interface control for  $z = \infty$  [24]. Taking the derivative of  $C(r)$  at  $r = 0$  from Eq. 2.7 and inserting it into Eq. 2.13 results in:

$$\frac{2D}{LM \chi} (C_0 - C^\gamma) = (C_{eq}^{\gamma\alpha} - C^\gamma) (C_{eq}^{\alpha\gamma} - C^\gamma), \quad (2.14)$$

with an interface velocity  $v = 2D/L$ . One can now derive the interfacial carbon concentration  $C^\gamma$  and the diffusion length  $L$  by solving the set of Eqs. 2.12 and 2.14. Theoretically there is more than one solution for  $C^\gamma$  and  $L$  for this set of functions.

However, one can only find one unique real solution for  $C^\gamma$  with  $C_0 \leq C^\gamma \leq C_{eq}^{\gamma\alpha}$  and  $L > 0$ .

The condition of non-overlapping carbon diffusion fields around two neighboring growing ferrite grains is then given by:

$$R_{\alpha,i} + L_i + R_{\alpha,j} + L_j < r_{ij} \quad (i \neq j), \quad (2.15)$$

where  $i$  and  $j$  refer to specific ferrite grains,  $r_{ij}$  is the distance between ferrite grain  $i$  and  $j$  and  $R_\alpha$  and  $L$  are the radius and diffusion length, respectively. Fig. 2.2a schematically illustrates the case in which the carbon diffusion profiles around two neighboring ferrite grains do not overlap and the growth of one grain does not influence the growth of the other.

### (b) Soft impingement

With the progression of the austenite-to-ferrite transformation, the diffusion field surrounding a growing ferrite grain may start to overlap with that of a neighboring one. In Fig. 2.2b, the diffusion profile around grain 1 starts to intersect the profile around grain 2 at point  $m$ . This happens when the following condition is fulfilled:

$$R_{\alpha,i} + L_i + R_{\alpha,j} + L_j = r_{ij} \quad (i \neq j), \quad (2.16)$$

Assuming that the carbon outside the soft impingement region can diffuse fast enough in the matrix of the austenite grain to let the bulk carbon concentration be homogenous, we have  $C_\infty = C_m$  where  $C_m$  is the carbon concentration at the soft impingement point. At this stage the carbon concentration profile can be written as:

$$C(r) = C_m + (C^\gamma - C_m) \left(1 - \frac{r}{L}\right)^2 \quad (0 \leq r \leq L), \quad (2.17)$$

which fulfills the following conditions:

$$C(r=0) = C^\gamma, \quad (2.18)$$

$$C(r=L) = C_m, \quad (2.19)$$

$$\left. \frac{\partial C}{\partial r} \right|_{r=L} = 0. \quad (2.20)$$

Similar to the non-overlapping stage, mass conservation of carbon results in:

$$\begin{aligned} (C_0 - C_{eq}^{\alpha\gamma})V_\alpha &= 4\pi \int_0^L \left[ (C_m - C_0) + (C^\gamma - C_m) \left(1 - \frac{r}{L}\right)^2 \right] (r + R_\alpha)^2 dr \\ &= \frac{2\pi L \left( 9L^2 C_m - 10L^2 C_0 + L^2 C^\gamma + 20R_\alpha^2 C_m - 30R_\alpha^2 C_0 + 10R_\alpha^2 C^\gamma + 25LR_\alpha C_m - 30LR_\alpha C_0 + 5LR_\alpha C^\gamma \right)}{15} \end{aligned} \quad (2.21)$$

Eq. 2.13 also applies for this stage due to the absence of carbon accumulation at the interface:

$$\frac{2D}{\chi ML}(C_m - C^\gamma) = (C_{eq}^{\gamma\alpha} - C^\gamma)(C_{eq}^{\alpha\gamma} - C^\gamma). \quad (2.22)$$

During the ferrite grain growth, the diffusion field is first treated without soft impingement to derive the diffusion length  $L$ . When the derived diffusion length fulfills Eq. 2.16 for a specific ferrite grain, soft impingement happens at that moment and one could regard this diffusion length  $L$  as the maximum distance that carbon can diffuse for that grain. By combining Eqs. 2.21 and 2.22, one can derive the unique solution for  $C^\gamma$  and  $C_m$ . In Fig. 2.2b, the diffusion fields for ferrite grains 1 and 2 intersect at point  $m$ . This means that the diffusion length for grain 1 cannot extend beyond point  $m$  (and similarly for grain 2). Soft impingement further results in  $C_\infty = C_m$ , which slows down the growth of other ferrite grains nucleated at other sites of the same austenite grain although they may not show soft impingement with any grain (see for example grain 3 in Fig. 2.2b).

### (c) Hard impingement

After soft impingement has set in, further growth of the ferrite grains reduces the diffusion length until the grains are in physical local contact with each other, that means:

$$R_{\alpha,i} + R_{\alpha,j} = r_{ij} \quad (i \neq j). \quad (2.23)$$

At this stage, due to the hard impingement the diffusion length of the ferrite grains locally decreases to zero and the carbon concentration in the austenite matrix becomes homogeneous and equal to the interfacial concentration (see Fig. 2.2c). Then the remaining average carbon concentration in the remaining austenite fraction of the original austenite grain can be calculated with

$$C_\infty = \frac{C_0 - C_{eq}^{\alpha\gamma} f_\alpha^\gamma}{1 - f_\alpha^\gamma}. \quad (2.24)$$

where  $f_\alpha^\gamma$  is the volume fraction of ferrite in a specific austenite grain. It is assumed that available angular space for ferrite grain growth is equally distributed over the number of surrounding austenite grains. After correcting the intersection volume of ferrite spheres,  $f_\alpha^\gamma$  for a specific austenite grain can be derived by:

$$f_\alpha^\gamma = \frac{1}{V_{\gamma 0}} \sum_{i=1}^n \frac{V_{\alpha,i}}{n_i}, \quad (2.25)$$

where  $V_{\alpha,i}$  is the actual ferrite volume after subtracting the volume intersection,  $n_i$  is the number of austenite grains surrounding ferrite  $\alpha_i$  and  $V_{\gamma 0}$  is the initial volume of the austenite grain. The method to correct the volume for two and three impinging

spheres is explained in [18, 38]. As the transformation proceeds, it is possible that a grain may impinge with three (or more) ferrite grains at a later stage. When this happens, it becomes much more complex to analytically calculate the intersecting volume, resulting in an extensive increase in computational costs. When a ferrite grain impinges with more than two other ferrite grains, we derive its corrected volume  $V_{\alpha,i}$  with the following approach [39]:

$$V_{\alpha,i} = V_{local,i} \tanh\left(\frac{V_{\alpha,i}^e}{V_{local,i}}\right), \quad (2.26)$$

where  $V_{local,i}$  is the combined ferrite grain volume ( $V_{\alpha,i}$ ) with the available untransformed surrounding austenite grain volume,  $V_{\alpha,i}^e$  the extended volume of grain  $i$  (before correcting for hard impingement). With this method the volume of each ferrite grain can be corrected explicitly for the impingement of four or more ferrite grains.

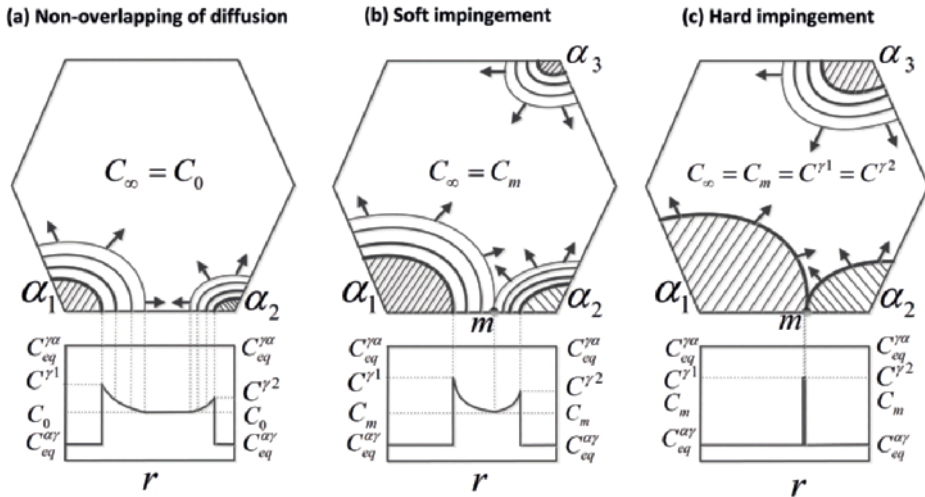


**Fig. 2.2.** Sketch of the development of carbon diffusion profiles during the growth of the  $\alpha$  phase into the  $\gamma$  phase in the (a) early stage without overlap of diffusion fields; (b) middle stage where diffusion fields starts to overlap (soft impingement) and (c) late stage where neighboring  $\alpha$  grains start to show direct contact with each other (hard impingement). For clarity, these stages in ferrite growth are only shown within one  $\gamma$  grain. Arrows indicate the growth direction of the  $\alpha$  phase. The shaded parts are the  $\alpha$  phase and the surrounding curves indicate the diffusion fields with a gradient in carbon concentration.



### 2.2.4. Computational procedure

The length of the cubic sample box is set as  $L_b = 70 \mu\text{m}$  and the average austenite grain size is  $\bar{d}_\gamma = 20 \mu\text{m}$  ( $\rho_\gamma = 2.4 \times 10^{14} \text{m}^{-3}$ ) with  $d_{min} = 12 \mu\text{m}$ . This results in 82 austenite grains in the starting structure and 392 vertices of Voronoi cells as potential nucleation sites for the ferrite phase. For a specific Fe-C-Mn steel, the para-equilibrium  $A_3$  temperature is calculated with Thermo-Calc. The phase boundary lines of  $(\alpha+\gamma)/\gamma$  and  $\alpha/(\alpha+\gamma)$  are also calculated and fitted in the temperature range of interest with a second-order polynomial to define the equilibrium carbon concentrations  $C_{eq}^{\alpha\gamma}$  and  $C_{eq}^{\gamma\alpha}$  and the equilibrium ferrite volume fraction:

$$f_\alpha^{eq} = \frac{C_{eq}^{\gamma\alpha} - C_0}{C_{eq}^{\gamma\alpha} - C_{eq}^{\alpha\gamma}}. \quad (2.27)$$

The difference in Gibbs free energy per unit of volume between the ferrite phase and austenite phase  $\Delta G_V$  is calculated as described by Mecozzi and coworkers [20]. The proportionality factor  $\chi$  is first calculated with Thermo-Calc (under para-equilibrium conditions) and then fitted as a function of temperature. The value for the pre-factor of the interface mobility expression  $M_0$  is pre-defined to match the phase field simulations and is close to the experimental value determined by Krielaart and coworkers [31]. It should be noted that there are many values of  $M_0$  reported in literature. Hillert and Höglund [40] reviewed these values and confirmed that the value reported in [31] was consistent with the experimental measurements for Fe-X (X = Mn, Co or Ni) alloys containing low amounts of carbon. In a recent publication by Zhu and coworkers [41] accurate values for the intrinsic mobility of the austenite-ferrite interface for interstitial-free Fe-X alloys are presented.

An iterative process with a time step  $\Delta t$  is adopted to predict the evolution of the ferrite transformation. At the start of the transformation the initial parameters are:  $t = 0$ ,  $T = A_3$  and  $f_\alpha = 0$ . The temperature  $T$  is then assumed to decrease at a constant cooling rate. For each time step the number of nuclei is derived from CNT with the local driving force at each potential nucleation site. At each time step, new nuclei will attempt to form at the potential nucleation sites, provided that the distance to a nucleated ferrite grain is bigger than a preset distance  $d_{shield}$ , which is defined as a quarter of the average spacing between ferrite grains ( $d_{shield} = \rho_\alpha^{-1/3} / 4$ ). Moreover, new nuclei are assumed to be formed preferably at the site where the local driving force (based on the carbon concentration on that site) is most favorable for nucleation. This means that the nucleation process is influenced by the pre-formed nuclei in terms of both spatial correlation and carbon distribution. The interface velocity for each ferrite grain is calculated by deriving the carbon concentration at the austenite/ferrite interface ( $C^\gamma$ ) and in the bulk of austenite grain ( $C_\infty$ ), as discussed in Section 2.3. As a result, the ferrite grain radius of grain  $i$  at time  $t$  is calculated from the previous interface position and velocity by:

$$R_{\alpha,i}(t) = R_{\alpha,i}(t - \Delta t) + v_i(t - \Delta t)\Delta t. \quad (2.28)$$

When this specific grain  $i$  starts to show hard impingement with other grains, an effective radius is derived from the ferrite grain volume corrected for the overlap volume  $V_i$ . After each time step, the microstructural characteristics including the ferrite volume fraction  $f_\alpha$ , the effective ferrite grain radius  $R_{\alpha,i}$ , the average grain radius  $\delta_s$  and the standard deviation  $\sigma_p$  for the ferrite grain radius are calculated:

$$f_\alpha = L_b^{-3} \sum_{i=1}^N V_{\alpha,i} \quad (2.29)$$

$$R_{\alpha,i} = (3V_{\alpha,i} / 4\pi)^{1/3} \quad (2.30)$$

$$\delta_s = \langle R_{\alpha,i} \rangle \quad (2.31)$$

$$\sigma_p = \left[ \frac{1}{N-1} \sum_{i=1}^N (R_{\alpha,i} - \langle R_{\alpha,i} \rangle)^2 \right]^{1/2} \quad (2.32)$$

Furthermore, the interfacial and remote matrix carbon concentration, the diffusion length for each ferrite grain and the chemical composition of the surrounding austenite grains are calculated after each time step. The iterative process continues until either the equilibrium ferrite fraction  $f_\alpha^{eq}$  or the  $A_1$  temperature is reached.

The present model is employed to simulate the ferrite transformation in a Fe-0.10C-0.49Mn (wt.%) steel during continuous cooling. The steel composition and transformation conditions were chosen equal to those in a previous computational study using a 3D phase-field model [20, 42] which used the MICRESS (MICrostructure Evolution Simulation Software) code developed by Steinbach and coworkers [43-44]. The  $A_3$  and  $A_1$  temperature of this steel are calculated to be 1116 K (843 °C) and 984 K (711 °C), respectively. A comparison is made between the results of the present model and those of the phase field simulations, where the nuclei were allowed to form over a nucleation temperature range,  $\delta T$ , with a constant nucleation rate. These phase field simulations employed a simplified linear, fixed temperature interval nucleation model (SNM).

To allow a better comparison between the results of our model and those of the phase field model, we adjusted the nucleation parameters in the classical nucleation theory (CNT) to achieve two types of nucleation kinetics: i) the final nuclei number density is the same as obtained for the SNM; ii) the onset nucleation rate is the same as obtained for the SNM. The two different conditions are shown in Fig. 2.3. The nucleation for the CNT starts at the same temperature as for the SNM. The simulation conditions are summarized in Table 2. 1. The goal of the simulations is to investigate the effect of the nucleation temperature range on the transformation kinetics, with an emphasis on the evolution of the ferrite grain size distribution.

**Table 2.1.** Selected simulation parameters with the cooling rate  $dT/dt = 0.4 \text{ K s}^{-1}$ , the nuclei density  $\rho_{\max}$ , the interface mobility  $M_0$ , the nucleation temperature range  $\delta T$  and the final averaging spacing of ferrite grains  $\rho_{\max}^{-1/3}$  for a comparison with the results from previous phase field modelling [20]. The results of the current transformation model are compared to those from the to the phase field model. For the current model two different nucleation models (SNM and CNT) are applied. The results of the current transformation model are compared to those from the phase-field model.

Model Trans.	Domain Size ( $\mu\text{m}^3$ )	Austenite Grains	$\rho_{\max}$ ( $\times 10^{15} \text{ m}^{-3}$ )	$\rho_{\max}^{-1/3}$ ( $\mu\text{m}$ )	Model Nucl.	$M_0$ ( $\times 10^{-6} \text{ m}^4 \text{ J}^{-1} \text{ s}^{-1}$ )	$\delta T$ (K)
							0
						0.24	12
Phase field	45×45×45	12	0.17	18.0	SNM		24
						0.35	18
						0.38	24
							0
						0.24	12
							24
Present model	70×70×70	82	0.17	18.0	SNM	0.15	0
						0.26	18
						0.3	24
			0.17	18.0	CNT	0.3	24
			0.25	15.8		0.3	24

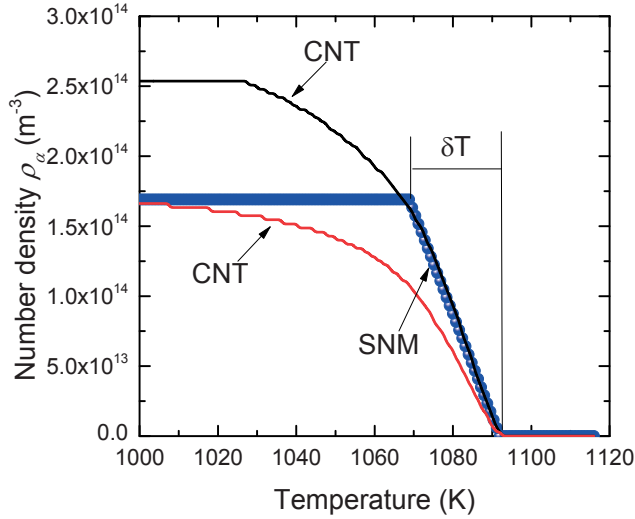


**Fig. 2.3.** Effect of the nucleation temperature range  $\delta T$  on the number density of ferrite grains  $\rho_a$ . The spheres show the data for the simple nucleation model (SNM), while solid curves represent the corresponding data for the classical nucleation theory (CNT) when (i) the final density of ferrite grains is equal (red line) or (ii) when the initial ferrite nucleation rate is equal (black line).

## 2.3. Results

### 2.3.1. Comparison between the present model and the phase-field model

The initial calculations of the transformation kinetics with the present model use exactly the same parameters for the simplified nucleation model as used in the reference phase-field model. Fig. 2.4 shows the ferrite grain microstructure and ferrite grain size distribution at different transformation stages during cooling for  $\delta T = 0$  and 24 K. For  $\delta T = 0$  K, a total number of 58 nuclei form at the same time (site saturation), which results in a single ferrite grain size at  $f_a = 0.01$ , while a small spread in grain size is present at  $f_a = 0.25$  due to hard impingement. Notably there are some ferrite grains that grow out of the edge of the cubic box so that they partially appear at different locations due to the periodic boundary conditions. For  $\delta T = 24$  K, the ferrite nuclei continuously form in a temperature range of 24 K, which results in an increase of the spread in ferrite grain size distribution during the transformation. The ferrite grains that nucleate earlier grow to bigger sizes than the ones that nucleate later. This is reflected in the broad ferrite grain size distribution of Fig. 2.4g originating from the spread in nucleation time. In the early growth stage soft impingement hardly occurs and therefore the ferrite grain growth is not significantly influenced by other grains at this stage. In later stages the size distribution becomes more irregular due to a progressive soft and hard impingement, as shown in Fig. 2.4d and 2.4h. The earlier formed ferrite grains with bigger grain sizes impinge with neighboring grains causing their growth to slow down, whereas the grains that nucleate later and have smaller

sizes are still growing relatively fast without impediment. In Fig. 2.4h a wide grain size distribution is observed in which all grain sizes up to 11  $\mu\text{m}$  are present.

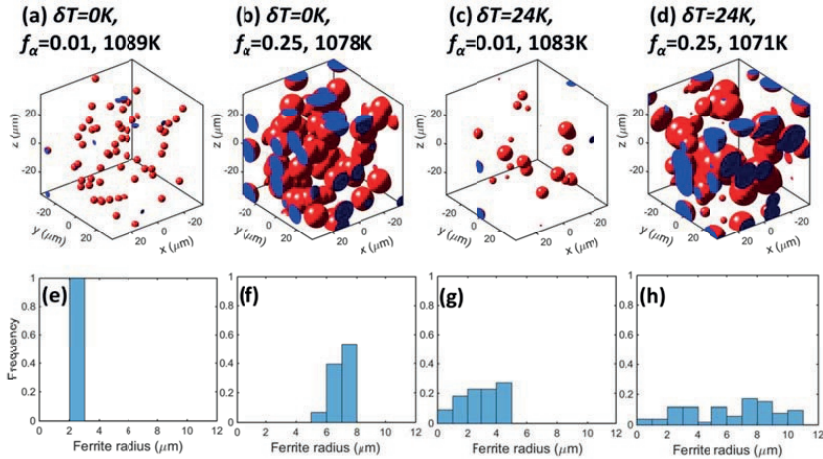


**Fig. 2.4.** Development of the formed ferrite grains for  $\rho_0 = 0.17 \times 10^{15} \text{ m}^{-3}$  and  $M_0 = 0.24 \times 10^{-6} \text{ m}^4 \text{ J}^{-1} \text{ s}^{-1}$  at a constant cooling rate of 0.4 K/s for (a)  $\delta T = 0 \text{ K}$  and  $f_a = 0.01$ ; (b)  $\delta T = 0 \text{ K}$  and  $f_a = 0.25$ ; (c)  $\delta T = 24 \text{ K}$  and  $f_a = 0.01$ ; (d)  $\delta T = 24 \text{ K}$  and  $f_a = 0.25$ . Below the corresponding ferrite grain size distribution is shown (e)-(h). For clarity, the austenite structure is not shown.

Fig. 2.5a compares the kinetics of the austenite-to-ferrite transformation for different values of  $\delta T$  using the present model and the phase-field model. Both use the simplified nucleation model. The equilibrium ferrite fraction of Fe-0.10C-0.49Mn (wt.%) as calculated by the Thermo-Calc package under para-equilibrium condition is also added. In both models, increasing the nucleation temperature range delays the transformation kinetics; this is because more nuclei can form and grow to a larger size for a smaller  $\delta T$  at the same transformation time (and corresponding temperature during continuous cooling). The total fraction transformed ultimately approaches the same equilibrium fraction,  $f_a \approx 0.7$ . However, the present model predicts a faster kinetics than the phase-field model for simulations with the same  $\delta T$ . The kinetics of the phase-field simulation with  $\delta T = 0 \text{ K}$  is in between the simulations of the present model with  $\delta T = 12$  and 24 K. This difference cannot be caused by model inputs such as nucleation parameters, thermodynamic and carbon diffusivity data, as these are effectively the same. Instead, the reason could be the difference in computational approach. The present model assumes isotropic growth, whilst the phase-field model allows different morphologies to form and takes into account the capillarity effect ( $2\sigma_{a\gamma}/R_a$  in 3D where  $\sigma_{a\gamma}$  is the  $a/\gamma$  interface energy), which consumes part of the chemical driving force during the growth of the ferrite. This capillarity effect, though decreases with increasing  $R_a$ , plays a non-negligible role, particularly in the early stage of the phase transformation, which slows down the ferrite growth in the phase-field simulation. However, the resulting geometrical differences between the present model

and phase-field simulation are small as ferrite grains also grow more or less spherically in the phase-field simulations when  $f_a < 0.3$  [42].

Although a considerable difference is observed in the transformation kinetics for these two models, the average grain size  $\delta_s$  and the standard deviation  $\sigma_p$  of the grain size distribution, show a comparable evolution as a function of  $f_a$ . The value of  $\delta_s$  increases nearly at the same speed for both models in the intermediate transformation stage ( $0.2 < f_a < 0.6$ ). For the size distribution, an increase in  $\delta T$  causes an increase in  $\sigma_p$  in the present model. For  $\delta T = 24$  K the distribution width  $\sigma_p$  reaches a broad maximum around  $f_a = 0.3$ , where the phase-field model indicates saturation. The reason for this difference is believed to be the geometrical difference between these two models. In the later transformation stage with severe hard impingements, the phase-field simulation allows the ferrite grains to alter their curvature to make the 'best' use of the untransformed parent structure to grow. As a result, the ferrite grains become less spherical, while they show more anisotropic growth, and thus the spread in grain size remains constant. In contrast, our present model assumes spherical growth throughout the whole transformation. The space for ferrite grains formed early in the process is limited by the continuous hard impingement, which provides the possibility for later formed ferrite grains to catch up in size. Therefore, a decrease in  $\sigma_p$  is observed at  $\delta T = 24$  K and a weaker decrease in  $\sigma_p$  can be seen for  $\delta T = 12$  K. Nevertheless, in general a good consistency is observed between the calculated values of  $\delta_s$  and  $\sigma_p$  for the phase-field model and the present model.

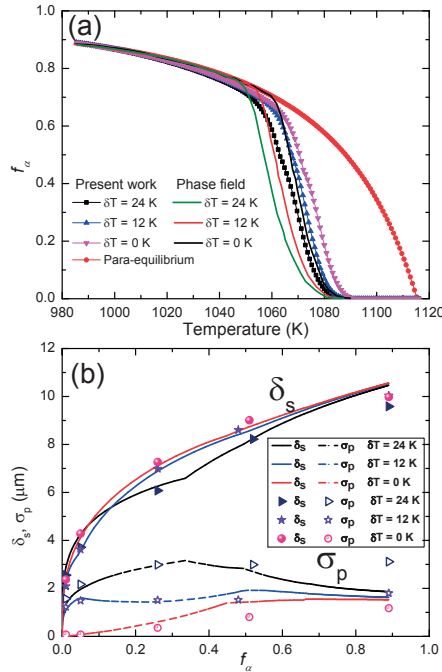


**Fig. 2.5.** Effect of the nucleation temperature range  $\delta T$  on (a) the transformation kinetics and (b) average grain radius  $\delta_s$  and the standard deviation  $\sigma_p$  of ferrite grain size for an interface mobility of  $M_0 = 0.24 \times 10^{-6} \text{ m}^4 \text{ J}^{-1} \text{ s}^{-1}$  at a constant cooling rate of 0.4 K/s. In (b) the phase-field simulation results are indicated by the symbols and the present modelling results correspond to the curves. The results from the phase-field model are from Mecozzi and coworkers [20].

Fig. 2.6 shows that by simultaneously tuning  $\delta T$  and  $M_0$  both models are able to replicate the experimental dilatometry data. The phase-field simulations show the best comparison for  $\delta T = 0 \text{ K}$  and  $M_0 = 2.4 \times 10^{-7} \text{ m}^4 \text{ J}^{-1} \text{ s}^{-1}$ . Using the present model it is found that  $\delta T = 0 \text{ K}$  and  $M_0 = 1.5 \times 10^{-7} \text{ m}^4 \text{ J}^{-1} \text{ s}^{-1}$  show good agreement with the measurements. By increasing  $\delta T$ , an increase in the value of  $M_0$  is required to achieve a good correspondence with the dilatometry data. Studying the influence of  $M_0$  at constant  $\delta T$ , indicates that the present model shows a smaller effective mobility than the phase-field model to achieve the same kinetics. As shown in Fig. 2.5 both models show a comparable evolution of  $\delta_s$  and  $\sigma_p$  as a function of  $f_a$ .

It is interesting to note that for the same time evolution of the ferrite fraction  $f_a$  during the phase transformation, the resulting ferrite grain size distribution can be distinctly different, depending on the assumptions regarding the nucleation process and the value of the interface mobility. Therefore, experimental information on the ferrite grain size distribution, as well as the ferrite fraction during the transformation will allow new insights into the nucleation and growth processes not obtainable from measurements of the ferrite fraction only.

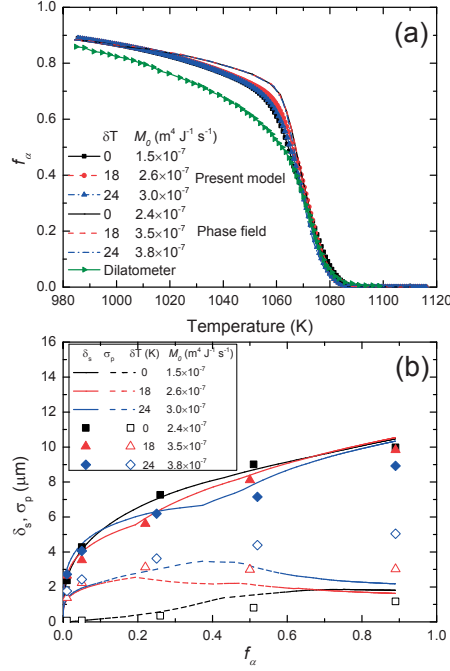


**Fig. 2.6.** Effect of nucleation temperature range  $\delta T$  and interface mobility  $M_0$  on (a) the volume fraction of ferrite (lines are from the present model and the symbols are from the phase-field simulation [20]) and (b) the average grain size (lines are from the present model and the solid symbols are from the phase-field simulations) and standard deviation (dashed curves are from the present model and the open symbols from the phase-field simulation [20]) at a constant cooling rate of 0.4 K/s.

### 2.3.2. Comparison between the simplified nucleation model (SNM) and the classical nucleation theory (CNT)

In the previous sections we compared the predictions for ferrite fraction and ferrite grain size (and distribution) for our present model and the earlier phase-field model, while employing the simplified nucleation model (SNM). Although SNM captures the important experimental finding that nucleation only occurs in a certain temperature range [14], it is unrealistic to assume that the actual nucleation rate is constant over a fixed temperature window and zero outside this region. Therefore, we incorporate the nucleation rate as predicted by the CNT into our present model to investigate the difference between SNM and CNT.



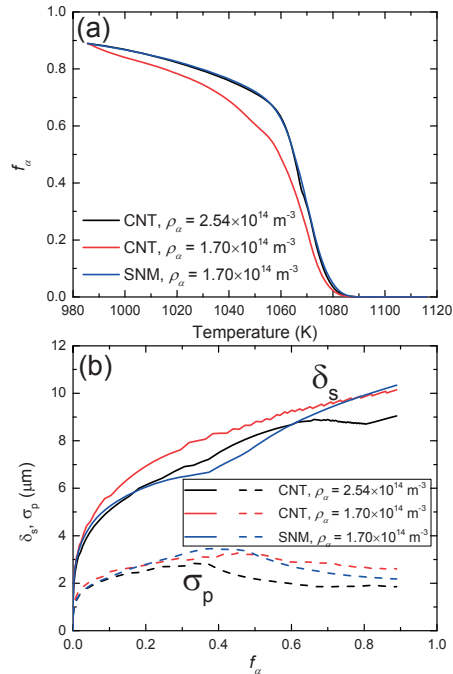


**Fig. 2.7.** Comparison of the transformation kinetics using SNM and CNT for  $\delta T = 24$  K with an interface mobility of  $M_0 = 3.0 \times 10^{-7} \text{ m}^4 \text{ J}^{-1} \text{ s}^{-1}$  at a constant cooling rate of 0.4 K/s. (a) The volume fraction as a function of temperature and (b) the average grain size and standard deviation as a function of ferrite fraction.

Fig. 2.7 compares the evolution of the ferrite fraction and grain size between SNM and CNT. Taking the model SNM predictions for  $\delta T = 24$  K, the parameter  $A$  in the CNT model as defined in Eq. 2.3 is adjusted to achieve two different effects: (i) the same final ferrite grain density and (ii) the same initial ferrite nucleation rate. As shown in Fig. 2.7a, the predicted value of  $f_\alpha$  for CNT with  $\rho_\alpha = 2.54 \times 10^{14} \text{ m}^{-3}$  overlaps with the simulation using SNM with  $\delta T = 24$  K and  $\rho_\alpha = 1.70 \times 10^{14} \text{ m}^{-3}$ . Hence for conditions at which the nucleation rate is the same at the lowest temperature of the SNM model (1068 K, 795 °C) the same development of  $f_\alpha$ , as well as  $\delta_s$  and  $\sigma_p$ , is observed. Below 1068 K (795 °C), new nuclei continue to form for the CNT until  $\rho_\alpha$  reaches a maximum value of  $2.54 \times 10^{14} \text{ m}^{-3}$  at 1027 K (754 °C, at which stage  $f_\alpha = 0.80$ ). During this stage the increase in  $f_\alpha$  in the CNT-based simulations is due to both the continuous growth of earlier formed ferrite grains and the formation of new nuclei. However, for the newly formed nuclei the average spacing between ferrite grains is much lower, resulting in a higher chance of soft and/or hard impingement compared to that in the SNM. Therefore the development of  $f_\alpha$  in the CNT simulation with  $2.54 \times 10^{14} \text{ m}^{-3}$  is comparable to the simulation with the SNM. The transformation kinetics for the CNT with  $\rho_\alpha = 1.70 \times 10^{14} \text{ m}^{-3}$  is considerably delayed because of the slower nucleation kinetics.

### 2.3.3. Carbon diffusion and mixed-mode character

As the present model is not a true 3D model, it only approximately predicts the carbon concentration in the austenite in the simulated volume. However, it contains relevant information on the interfacial carbon concentration, the effective remaining matrix carbon concentration, the diffusion length and the moment when soft and hard impingement happens for individual neighboring ferrite grains.

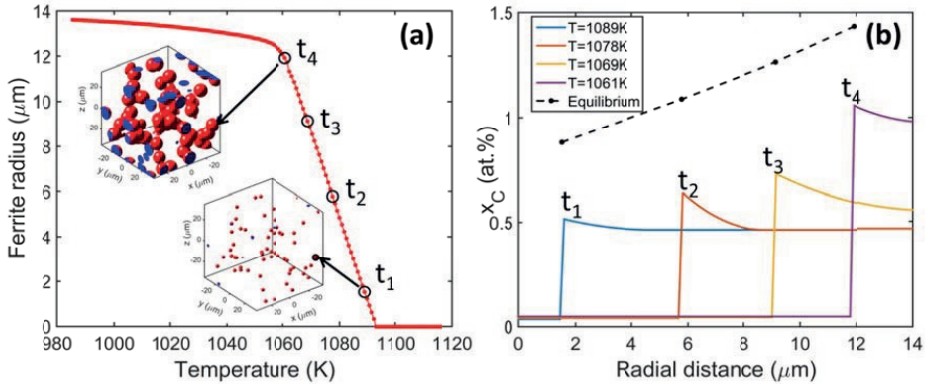


**Fig. 2.8.** Evolution of (a) a single ferrite grain radius as a function of temperature with a spatial position indicated in the inserted 3D structures and (b) diffusion profiles at four different temperatures with the times  $t_1$ ,  $t_2$ ,  $t_3$  and  $t_4$  indicated by open circles in (a). This structure is modelled with  $\rho_0 = 1.7 \times 10^{14} \text{ m}^{-3}$ ,  $\delta T = 0 \text{ K}$  and  $M_0 = 1.5 \times 10^{-7} \text{ m}^4 \text{ J}^{-1} \text{ s}^{-1}$  at a constant cooling rate of  $0.4 \text{ K/s}$ .

Fig. 2.8 illustrates the evolution of the radial carbon diffusion profile during the austenite-to-ferrite phase transformation as a function of temperature for a selected representative ferrite grain. The spatial position of the monitored single ferrite grain is shown in the inserts in Fig. 2.8a. Fig. 2.8b shows that up to time  $t_2$  (at which  $T \geq 1078 \text{ K}$ ,  $805 \text{ }^\circ\text{C}$ ) the carbon diffusion field of this grain does not show overlap with surrounding diffusion fields and therefore the growth of this ferrite is not influenced by its local environment. At a time  $t_3$  (corresponding to  $T = 1069 \text{ K}$ ,  $796 \text{ }^\circ\text{C}$ ) the carbon diffusion field for this ferrite grain starts to show overlap with the diffusion field of one of the neighboring grains, resulting in an increase of the carbon concentration in the bulk of the austenite grain. At a time  $t_4$  ( $T = 1061 \text{ K}$ ,  $788 \text{ }^\circ\text{C}$ ) the carbon diffusion profile shows hard impingement of this ferrite grain with the nearest ferrite grain. This hard impingement leads to a dramatic increase in the interfacial carbon concentration, as shown in Fig. 2.8b. As a result, a pronounced transition in the grain growth velocity takes place, as indicated in Fig. 2.8a. As the transformation proceeds, the interfacial carbon concentration keeps increasing and finally approaches the local equilibrium concentration indicated by the dashed curve in Fig. 2.8b.

The carbon diffusion profiles of the other ferrite grains show similar features as indicated above. All ferrite grains show an interface-controlled growth at the start of the transformation and then develop more and more into a diffusion-controlled growth until the interfacial carbon concentration approaches the equilibrium value. These detailed predictions indicate that the mixed-mode character of the moving interface is well captured in the present model, as is the case in several other mixed-mode models [24, 37, 45].

## 2.4. Discussion

The model as presented here provides a computationally cheap tool to monitor the microstructural development and local carbon profiles in a realistic austenitic microstructure for a simple Fe-C-Mn steel during continuous cooling for various assumed nucleation conditions. The ferrite grain size distribution is a crucial output parameter of this model. Although experimental information on the grain size distribution has traditionally been restricted to destructive techniques (imaging analysis on quenched samples), recent advances in radiation techniques like micro-beam synchrotron X-ray diffraction [14-15] and neutron depolarization [17-18] can provide in-situ time-resolved information on the ferrite grain size during the transformation. The present model may bridge (at relatively limited computationally efforts) the gap between the experimental ferrite fraction, ferrite grain density, average ferrite grain size and the ferrite grain size distribution and its metal physical interpretation in key microstructural processes. Below the time evolution of the ferrite grain size distribution at an identical overall ferrite fraction evolution is elaborated in more detail, in order to demonstrate the added-value of this new transformation model.

In Fig. 2.9 the ferrite grain size distribution is shown at specific transformation levels  $f_a$ , for three assumed simulations. Although these simulations show the same transformation kinetics (measurable in conventional experiments such as dilatometry), obtained by adjusting the interface mobility value and nucleation rate, significant differences in the evolution of the ferrite size distribution are observed. For an SNM simulation with  $\delta T = 0$  K the width of the size distribution is relatively small, although it increases with increasing  $f_a$  due to the increased occurrence of hard impingement. For an SNM simulation with  $\delta T = 24$  K or a CNT simulation with  $\delta T = 65$  K the size distributions are comparable but only up to a transformation fraction of  $f_a = 0.05$ . For higher ferrite fractions the size distribution for  $\delta T = 24$  K with SNM shows a wider grain size distribution. This is due to hard impingement to set in later in the SNM simulation than for the case for the CNT simulation with  $\delta T = 65$  K.

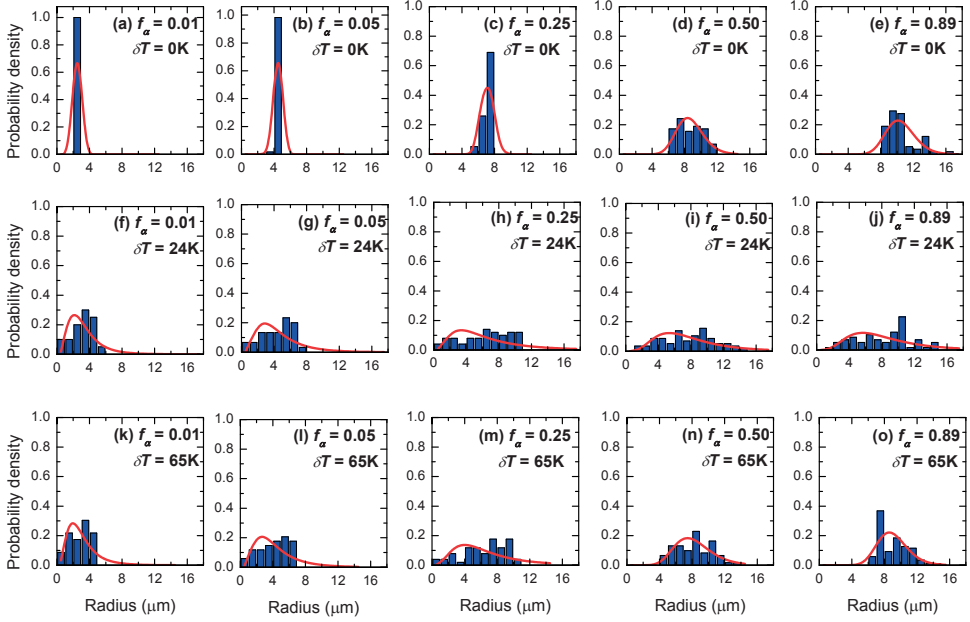


**Fig. 2.9.** Effect of the nucleation temperature range  $\delta T$  on the grain size distribution at a ferrite phase fraction of  $f_a = 0.01, 0.05, 0.25, 0.50$  and  $0.89$ , respectively. (a)-(e) is modelled with  $\rho_0 = 1.7 \times 10^{14} \text{ m}^{-3}$ ,  $\delta T = 0 \text{ K}$  and  $M_0 = 1.5 \times 10^{-7} \text{ m}^4 \text{ J}^{-1} \text{ s}^{-1}$ ; (f)-(j) is modelled with  $\rho_0 = 1.7 \times 10^{14} \text{ m}^{-3}$ ,  $\delta T = 24 \text{ K}$  and  $M_0 = 3.0 \times 10^{-7} \text{ m}^4 \text{ J}^{-1} \text{ s}^{-1}$  using SNM and (k)-(o) is modelled with  $\rho_0 = 2.5 \times 10^{14} \text{ m}^{-3}$ ,  $\delta T = 65 \text{ K}$  and  $M_0 = 3.0 \times 10^{-7} \text{ m}^4 \text{ J}^{-1} \text{ s}^{-1}$  using CNT. Lognormal fits are shown in solid curves. All simulations show the name transformation kinetics as the dilatometer measurement for a constant cooling rate of  $0.4 \text{ K/s}$ .

**Table 2.2.** The mean ( $E$ ) and standard deviation ( $SD$ ) of the effective ferrite grain size distribution derived from lognormal fits to the modelling results in three different conditions.

$f_a$	$\delta T = 0 \text{ K, SNM}$		$\delta T = 24 \text{ K, SNM}$		$\delta T = 65 \text{ K, CNT}$	
	$E$ ( $\mu\text{m}$ )	$SD$ ( $\mu\text{m}$ )	$E$ ( $\mu\text{m}$ )	$SD$ ( $\mu\text{m}$ )	$E$ ( $\mu\text{m}$ )	$SD$ ( $\mu\text{m}$ )
0.01	2.4(1)	0.0007(3)	3.2(9)	2.0(9)	2.9(8)	1.9(8)
0.05	4.2(1)	0.07(2)	4.6(8)	3.0(9)	4.3(9)	2.9(7)
0.25	7.1(2)	0.6(2)	6.7(9)	5.4(9)	6.7(9)	4.5(6)
0.50	8.7(5)	1.6(4)	8.0(4)	4.5(8)	8.3(9)	2.3(5)
0.89	10.5(5)	1.7(5)	8.4(8)	4.8(6)	9.0(5)	1.8(4)

Based on the above results it is clear that the ferrite grain size distribution is a valuable link to the system characteristics  $\delta T$  and  $M_0$ . The solid curves in Fig. 2.9 present the fittings of the simulated data to a lognormal grain size distribution:

$$F(R_a | \mu, \sigma) = \frac{1}{R_a \sigma \sqrt{2\pi}} \exp \left[ -\frac{(\ln R_a - \mu)^2}{2\sigma^2} \right] \quad (2.33)$$

where  $R_a$  is the effective ferrite grain radius and  $\mu$  and  $\sigma$  are the parameters of the lognormal distribution. For the lognormal distribution the mean corresponds to  $E = \exp(\mu + \sigma^2/2)$  and the variance  $VAR = SD^2 = \exp(2\mu + \sigma^2)[\exp(\sigma^2) - 1]$ , with the standard deviation  $SD$ . The derived parameters from the fits are given in Table 2.2. For  $\delta T = 0$  K the average ferrite grain radius  $E$  differs significantly from the other two nucleation modes, especially at the later transformation stages. This difference is less pronounced in the standard deviation of the ferrite grain radius  $SD$ . The fitting parameters for  $\delta T = 24$  K with SNM and  $\delta T = 65$  K with CNT are in close agreement with each other for  $f_a < 0.25$  and only start to show differences for higher ferrite fractions.

The above analysis suggests that from experimentally determined values for both the ferrite fraction and the average grain size at a particular stage of the transformation, it is possible to derive accurate estimates for the underlying physical parameters  $\delta T$  and  $M_0$ . However, given the  $E$  and  $SD$  values, there are multiple solutions for specific combinations of  $\delta T$ ,  $M_0$  and nucleation to describe the ferrite grain size distribution for one specific  $f_a$  level. Only by analyzing the ferritic grain size data for different  $f_a$  levels it is possible to derive accurate estimates of the key physical parameters.

## 2.5. Conclusions

A 3D model that couples classical nucleation theory and the interface moving under mixed-mode interface condition has been developed for ferrite formation in Fe-C-Mn steels during continuous cooling. This model predicts a comparable transformation kinetics as a published phase-field model and matches the experimental dilatometric data for linear cooling of an Fe-0.10C-0.49Mn (wt.%) steel. The influence of the increased nucleation temperature range on the  $\gamma$ - $\alpha$  transformation kinetics can be counteracted by increasing interface mobility. However, the evolution of the ferrite grain size distribution would be distinctly different, which cannot be undone by tuning the modelling parameters. A comparison between the simplified nucleation model and the classical nucleation theory shows that a close similarity in nucleation behavior in the early stage results in a similar evolution of ferrite fraction for the entire transformation process. Analyzing grain size distribution for different  $f_a$  levels is required to derive accurate estimates of the key physical parameters, the nucleation temperature interval and the effective interface mobility for the  $\gamma$ - $\alpha$  phase transformation in this C-Mn steel.

## Acknowledgements

H. Fang acknowledges the financial support from the China Scholarship Council (CSC).

## References

1. W. Bleck: *JOM*, 1996, vol. 48, pp. 26-30.
2. D.V. Edmonds, K. He, F.C. Rizzo, B.C. De Cooman, D.K. Matlock, and J.G. Speer: *Mater. Sci. Eng. A*, 2006, vol. 438, pp. 25-34.
3. S. Winkler, A. Thompson, C. Salisbury, M. Worswick, I. Van Riemsdijk, and R. Mayer: *Metall. Mater. Trans. A*, 2008, vol. 39, pp. 1350-8.
4. O. Bouaziz, H. Zurob and M. Huang: *Steel Res. Inter.*, 2013, vol. 84, pp. 937-47.
5. H.S. Zurob, C.R. Hutchinson, Y. Breché, H. Seyedrezai, and G.R. Purdy: *Acta Mater.*, 2009, vol. 57, pp. 2781-92.
6. X. Zhong, D.J. Rowenhorst, H. Beladi, and G.S. Rohrer: *Acta Mater.*, 2017, vol. 123, pp. 136-45.
7. E. Novillo, D. Hernández, I. Gutiérrez, and B. López: *Mater. Sci. Eng. A*, 2004, vol. 385, pp. 83-90.
8. A. Phillion, H.W. Zurob, C.R. Hutchinson, H. Guo, D.V. Malakhov, J. Nakano, and G.R. Purdy: *Metall. Mater. Trans. A*, 2004, vol. 35, pp. 1237-42.
9. F. Barbe and R. Quey: *Inter. J. Plast.*, 2011, vol. 27, pp. 823-40.
10. E. A. Jäggle and E.J. Mittemeijer: *Acta Mater.*, 2011, vol. 59, pp. 5775-86.
11. B. Zhu, Y. Zhang, C. Wang, P.X. Liu, W.K. Liang, and J. Li: *Metall. Mater. Trans. A*, 2014, vol. 45, pp. 3161-71.
12. G. Purdy, J. Ågren, A. Borgenstam, Y. Bréchet, M. Enomoto, E. Gamsjager, M. Gouné, M. Hillert, C. Hutchinson, M. Militzer, and H. Zurob: *Metall. Mater. Trans. A*, 2011, vol. 42, pp. 3703-18.
13. M. Gouné, F. Danoix, J. Ågren, Y. Bréchet, C.R. Hutchinson, M. Militzer, G. Purdy, S. van der Zwaag, and H. Zurob: *Mater. Sci. Eng. R*, 2015, vol. 92, pp. 1-38.
14. S.E. Offerman, N.H. van Dijk, J. Sietsma, S. Grigull, E.M. Lauridsen, L. Margulies, H.F. Poulsen, M.Th. Rekveldt, and S. van der Zwaag: *Science*, 2002, vol. 298, pp. 1003-5.
15. M. Militzer: *Science*, 2002, vol. 298, pp. 975-6.
16. S.G.E. te Velthuis, N.H. van Dijk, M.Th. Rekveldt, J. Sietsma, and S. van der Zwaag: *Acta Mater.*, 2000, vol. 48, pp. 1105-14.
17. S.E. Offerman, L.J.G.W. van Wilderen, N.H. van Dijk, M.Th. Rekveldt, J. Sietsma, and S. van der Zwaag: *Acta Mater.*, 2003, vol. 51, pp. 3927-38.
18. S.G.E. te Velthuis, N.H. van Dijk, M.Th. Rekveldt, J. Sietsma, and S. van der Zwaag: *Mater. Sci. Eng. A*, 2000, vol. 277, pp. 218-28.
19. S.E. Offerman, N.H. van Dijk, J. Sietsma, E.M. Lauridsen, L. Margulies, S. Grigull, H.F. Poulsen, and S. van der Zwaag: *Acta Mater.*, 2004, vol. 52, pp. 4757-66.
20. M.G. Mecozzi, M. Militzer, J. Sietsma, and S. van der Zwaag: *Metall. Mater. Trans. A*, 2008, vol. 39, pp. 1237-47.
21. K.F. Kelton: *Solid State Physics*, Vol. 45, H. Ehrenreich and D. Turnbull, eds., Academic Press, New York, NY, 1991, pp. 75.
22. D. Kashchiev: *Nucleation, basic theory with applications*, Butterworth-Heinemann, Oxford, OX, 2000, pp. 184-270.

23. H.I. Aaronson, M. Enomoto, and J.K. Lee: *Mechanisms of diffusional phase transformations in metals and alloys*, CRC Press, Boca Raton, 2010, pp. 49-245.
24. J. Sietsma and S. van der Zwaag: *Acta Mater.*, 2004, vol. 52, pp. 4143–52.
25. W. Huang and M. Hillert: *Metall. Mater. Trans. A*, 1996, vol. 27, pp. 480-3.
26. M. Herceg, M. Kvasnica, C.N. Jones, and M. Morari: *Multi-Parametric Toolbox 3.0*, In Proc. of the European Control Conference, Zurich, Switzerland, July 17–19, 2013, pp. 502–10, <http://control.ee.ethz.ch/~mpt>.
27. N.H. van Dijk, S.E. Offerman, J. Sietsma, and S. van der Zwaag: *Acta Mater.*, 2007, vol. 55, pp. 4489–98.
28. H. Song and J.J. Hoyt: *Phys. Rev. Lett.*, 2016, vol. 117, pp. 238001-5.
29. H. Sharma, J. Sietsma, and S. E. Offerman: *Sci. Rep.*, 2016, vol. 6, pp. 30860.
30. K.M. Lee, H.C. Lee, and J.K. Lee: *Phil. Mag.*, 2010, vol. 90, pp. 437-59.
31. G.P. Krielaart, J. Sietsma, and S. van der Zwaag: *Mater. Sci. Eng. A*, 1997, vol. 237, pp. 216-23.
32. M. Hillert and B. Sundman: *Acta Metall.*, 1976, vol. 24, pp. 731-43.
33. H. Buken and E. Kozeschnik: *Metall. Mater. Trans. A*, 2017, vol. 48A, pp. 2812-8.
34. E. Gamsjäger, M. Wiessner, S. Schider, H. Chen, and S. van der Zwaag: *Phil. Mag.*, 2015, vol. 95, pp. 2899-917.
35. H. Chen and S. van der Zwaag: *J. Mater. Sci.*, 2011, vol. 46, pp. 1328-36.
36. J. Ågren: *Scrip. Metall.*, 1986, vol. 20, pp. 1507-10.
37. C. Bos and J. Sietsma: *Scrip. Mater.*, 2007, vol. 57, pp. 1085-8.
38. K.D. Gibson and H.A. Scheraga: *J. Phys. Chem.*, 1987, vol. 91, pp. 4121-2.
39. E.J. Mittemeijer and F. Sommer: *Z. Metallkd.*, 2002, vol. 93, pp. 352-61.
40. M. Hillert and L. Höglund: *Scrip. Mater.*, 2006, vol. 54, pp. 1259-63.
41. J. Zhu, H. Luo, Z. Yang, C. Zhang, S. van der Zwaag, and H. Chen: *Acta Mater.*, 2017, vol. 133, pp. 258-68.
42. M. Militzer, M.G. Mecozzi, J. Sietsma, and S van der Zwaag: *Acta Mater.*, 2006, vol. 54, pp. 3961-72.
43. I. Steinbach, F. Pezzolla, B. Nestler, M. Seeßelberg, R. Prieler, G.J. Schmitz, and J.L.L. Rezende: *Physica D: Nonlin. Phenom.*, 1996, vol. 94, pp. 135-47.
44. L.Q. Chen: *Annu. Rev. Mater. Res.*, 2002, vol. 32, pp. 113-40.
45. C. Bos and J. Sietsma: *Acta Mater.*, 2009, vol. 57, pp. 136-44.

---

# Chapter 3

## **Modelling study on the three-dimensional neutron depolarisation response of the evolving ferrite particle size distribution during the austenite-ferrite phase transformation in steels**

The magnetic configuration of a ferromagnetic system with mono-disperse and poly-disperse distribution of magnetic particles with inter-particle interactions has been computed. The analysis is general in nature and applies to all systems containing magnetically interacting particles in a non-magnetic matrix, but has been applied to steel microstructures, consisting of a paramagnetic austenite phase and a ferromagnetic ferrite phase, as formed during the austenite-to-ferrite phase transformation in low-alloyed steels. The characteristics of the computational microstructures are linked to the correlation function and determinant of depolarisation matrix, which can be experimentally obtained in three-dimensional neutron depolarisation (3DND). By tuning the parameters in the model used to generate the microstructure, we studied the effect of the (magnetic) particle size distribution on the 3DND parameters. It is found that the magnetic particle size derived from 3DND data matches the microstructural grain size over a wide range of volume fractions and grain size distributions. A relationship between the correlation function and the relative width of the particle size distribution is proposed to accurately account for the width of the size distribution. This evaluation shows that 3DND experiments can provide unique in-situ information on the austenite-to-ferrite phase transformation in steels.



### 3.1. Introduction

Three-dimensional neutron depolarisation (3DND) is a powerful technique to characterise the magnetic microstructure of polycrystalline bulk materials on the (sub)micron scale [1-3]. In such measurements a polarised neutron beam interacts with the local magnetic induction in a magnetised sample, which results in a change of the polarisation vector of the neutron beam upon transmission through the (magnetised) sample. This change in polarisation is characterised by a rotation angle and by a shortening of the polarisation vector with respect to the initial polarisation. The mean magnetisation causes a net rotation of the polarisation vector and the magnetic inhomogeneities result in a decrease in polarisation. For a sample containing ferromagnetic particles (grains) in a paramagnetic matrix, the rotation angle monitors the phase fraction of the ferromagnetic phase inside the sample. The shortening of the polarisation determines magnetic correlation length, and thereby a mean magnetic particle (grain) size along the neutron beam.

This technique has successfully been used to study static and dynamic properties of magnetic microstructures in a wide range of materials such as magnetic recording materials, superconductors, amorphous metals and steels [4-9]. In low-alloyed steels the austenite-to-ferrite [10] and the austenite-to-pearlite [11] phase transformations have been studied using in-situ 3DND measurements. In such steels the high temperature austenite phase, which has an *fcc* lattice structure and is paramagnetic, transforms into ferrite with a *bcc* structure below a characteristic transformation temperature ( $A_3$ ). Below the Curie temperature  $T_C$  ( $= 1043$  K for pure Fe) the equiaxed ferritic phase becomes ferromagnetic. At a transformation temperature below the so-called  $A_1$  temperature the remaining austenite, being enriched in carbon, transforms into a lamellar structure composed of ferrite and cementite  $Fe_3C$  plates, the so-called pearlite. In this study we focus on the microstructure evolution for a two-phase austenite-ferrite mixture, in which the equiaxed austenite grains form the continuous parent phase and the equiaxed ferrite grains are the emerging product phase.

Key parameters to characterise the microstructure evolution during the austenite-to-ferrite transformation in steels for this magnetically inhomogeneous ferromagnetic system are the ferritic volume fraction and the ferritic particle size. Rosman and Rekveldt [1] derived the theoretical framework for the determination of the magnetic phase fraction and the (spherical) particle size in the case of monodisperse ferromagnetic particles in a dilute non-magnetic medium from neutron depolarisation experiments. Te Velthuis and coworkers [12] investigated the magnetic particle size obtained by neutron depolarisation and compared it to the ferrite grain size using a numerical model. The results showed that the magnetic particle size calculated from the neutron depolarisation is in good agreement (within of 10-20 %) with the actual average ferrite grain size. Simultaneous measurements of the (magnetic) volume fraction and the average (magnetic) particle size by in-situ neutron depolarisation measurements provides unique insight in the austenite-to-ferrite transformation in steels, as it is one of the few physical characterisation techniques known to determine both the volume fraction and the average particle size on a micron length scale in a single experiment. Such information makes it possible to separate nucleation and

growth effects during the solid state phase transformation and to reconstruct important details of the progression of this important solid-state phase transformation. However, the analysis of the 3DND data has not yet been brought to a level that makes it possible to capture not only the average ferritic particle size but also the width of the particle size distribution. The ferrite grain size distribution holds even more detailed information on the ferrite grain nucleation and growth rate and this information is crucial for accurate modelling of the austenite decomposition in low-alloyed steels during cooling. It is the aim of the present work to extend the 3DND data analysis in this direction.

To investigate the influence of the particle size distribution on the interpretation of 3DND data we developed a model to compute the magnetic configuration for a given 3D microstructure. From this microstructure the 3DND parameters were derived. By tuning the phase transformation parameters the microstructure can be varied. We thereby investigated the effect of size distribution on the particle size derived from the 3DND analysis by a comparison to the mean particle size of the actual distribution. This theoretic study provides the foundation for the 3DND analysis of evolving ferromagnetic microstructures starting from a fully paramagnetic parent phase.

### 3.2. Neutron depolarisation

Two approaches have been developed to describe the neutron depolarisation due to the interaction of a polarised neutron beam with a collection of magnetic particles: (i) the Larmor and (ii) the scattering approach. Rosman and Rekveldt [13] found that both approaches are fully equivalent as long as all scattered neutrons enter the analyser during the measurement. Here we will just briefly present the neutron depolarisation in Larmor approach. A detailed overview of the neutron depolarisation theory can be found elsewhere [1, 2, 7, 13].

As shown in Fig. 3.1, the neutron depolarisation technique measures the change of the polarisation for a polarised neutron beam after transmission through a magnetic material. The relationship between the initial polarisation vector ( $\vec{P}^0$ ) and the polarisation vector after transmission ( $\vec{P}'$ ) can be expressed as  $\vec{P}' = \hat{D}\vec{P}^0$ , where  $\hat{D}$  is a depolarisation matrix that contains 3×3 elements. Generally, the depolarisation matrix can be expressed in terms of a rotation of the beam polarisation and a reduction in beam polarisation (described by a matrix  $\hat{D}'$ ) [1, 2]. This reduction in beam polarisation is directly related to the field correlation matrix  $\hat{\alpha}$  of the sample volume  $V_w$  with components  $\alpha_{ij}$  ( $i, j = x, y$  or  $z$ ):

$$\alpha_{ij} = \int_{V_w} d^3\vec{r} \int_0^x \Delta B_i(x, y, z) \Delta B_j(x', y, z) dx', \quad (3.1)$$

where  $\vec{r} = (x, y, z)$  is a spatial vector, 0 is the position where neutrons enter the sample,  $(x, y, z)$  and  $(x', y, z)$  are two different arbitrary points in the sample volume,  $\Delta B_i(\vec{r})$  is the  $i$ -component of  $\Delta\vec{B}(\vec{r})$  that corresponds to the variation in magnetic induction with the mean magnetic induction  $\langle\vec{B}\rangle$  expressed as  $\Delta\vec{B}(\vec{r}) = \vec{B}(\vec{r}) - \langle\vec{B}\rangle$  (see Fig. 1 for the coordinate system). In the absence of correlations between the variations in the field

components  $\Delta B_i(\vec{r})$  and  $\Delta B_j(\vec{r})$  ( $i \neq j$ ) along the neutron path this correlation matrix  $\hat{\alpha}$  is diagonal. The correlation function  $\xi$ , which is proportional to the correlation length of  $|\Delta \vec{B}(\vec{r})|^2$  along the neutron beam, can be expressed as

$$\xi = \sum_i \alpha_{ii}. \quad (3.2)$$

In the absence of a net polarisation rotation the elements of the correlation matrix  $\hat{\alpha}$  and the depolarisation matrix  $\hat{D}'$  are related as:

$$D_{ij}' = \delta_{ij}(1 - c_1 L_w \xi) + c_1 L_w \alpha_{ij}, \quad (3.3)$$

where  $\delta_{ij}$  is the Kronecker delta and  $c_1 = 2.15 \times 10^{29} \lambda^2 \text{ T}^{-2} \text{ m}^{-4}$  with  $\lambda$  the neutron wavelength and  $L_w$  is the sample length along the neutron beam. Rosman and Rekveldt [13] showed that in the Fourier space  $\hat{\alpha}$  is directly related to the magnetization of the sample  $\vec{M}(\vec{r})$ :

$$\alpha_{ij} = \frac{8\pi^4}{V_w} \int_S B_i(\vec{s}) B_j(-\vec{s}) d^2 \vec{s} - \frac{L_w}{2} \langle B_i \rangle \langle B_j \rangle, \quad (3.4)$$

where  $\vec{B}(\vec{s}) = \frac{\mu_0}{(2\pi)^3} \int_{V_w} (\vec{s} \times [\vec{M}(\vec{r}) \times \vec{s}]) e^{i\vec{s} \cdot \vec{r}} d^3 \vec{r}$ ,  $\mu_0$  is the permeability of vacuum,  $\vec{s}$  is the reciprocal lattice vector and  $\hat{s} = \vec{s}/|\vec{s}|$  its unit vector. As described in Ref. [12] for a distribution of uncorrelated ferromagnetic particles the diagonal elements of the matrix  $\hat{\alpha}$  have the following analytical solutions:

$$\alpha_{xx} = f(\mu_0 M_s)^2 \left( \frac{6 \langle m_x^2 \rangle \langle R^4 \rangle}{8 \langle R^3 \rangle} - \frac{2}{3} c_2 \langle m_x \rangle^2 \langle R^3 \rangle^{\frac{1}{3}} \right), \quad (3.5)$$

$$\alpha_{yy} = f(\mu_0 M_s)^2 \left( \frac{3 \left( \frac{3}{4} \langle m_y^2 \rangle + \frac{1}{4} \langle m_z^2 \rangle \right) \langle R^4 \rangle}{8 \langle R^3 \rangle} - \frac{2}{3} c_2 \langle m_y \rangle^2 \langle R^3 \rangle^{\frac{1}{3}} \right), \quad (3.6)$$

$$\alpha_{zz} = f(\mu_0 M_s)^2 \left( \frac{3 \left( \frac{1}{4} \langle m_y^2 \rangle + \frac{3}{4} \langle m_x^2 \rangle \right) \langle R^4 \rangle}{8 \langle R^3 \rangle} - \frac{2}{3} c_2 \langle m_z \rangle^2 \langle R^3 \rangle^{\frac{1}{3}} \right), \quad (3.7)$$

where  $f$  is the volume fraction of the ferromagnetic phase,  $\mu_0$  is the permeability of vacuum,  $\vec{m} = \vec{M}/M_s$  is the reduced magnetisation scaled to the saturation magnetisation  $M_s$  of the ferromagnetic phase,  $c_2 = (4\pi f^2/81)^{1/3}$  is a constant and  $R$  is the radius of the ferromagnetic particle. According to Eq. 3.2, the correlation function  $\xi$  then corresponds to

$$\xi = \frac{2f(\mu_0 M_s)^2 \langle R^4 \rangle}{3c_3 \langle R^3 \rangle} \left( 1 - c_2 c_3 m^2 \frac{\langle R^3 \rangle^{\frac{4}{3}}}{\langle R^4 \rangle} \right), \quad (3.8)$$

where  $m = |\langle \vec{m} \rangle|$  and  $c_3$  is a constant that depends on the shape, orientation and spatial distribution of the ferromagnetic particles. For identical spheres this constant is  $c_3 = 16/[9(1 + \langle m_x^2 \rangle)]$ . Eq. 3.8 shows that  $\xi$  depends on the ratio of the higher order averages of the particle sizes, which suggests that  $\xi$  includes the information of both the average particle radius  $\langle R \rangle$  and the spread in radius. By writing  $\delta = \frac{\langle R^4 \rangle}{\langle R^3 \rangle}$  and assuming  $\frac{\langle R^3 \rangle^{\frac{4}{3}}}{\langle R^4 \rangle} \rightarrow 1$ , Eq. 3.8 is transformed to give the relationship between  $\delta$  and  $\xi$ :

$$\delta = \frac{3c_3\xi}{2f(\mu_0M_s)^2(1-c_2c_3m^2)}. \quad (3.9)$$

These equations show that one can derive the neutron depolarisation parameters  $\hat{\alpha}$ ,  $\xi$ , and  $\hat{D}$  by computing the orientation of the magnetic moments for all magnetic particles in a particulate system. Furthermore, the characteristic particle size  $\delta$  can be obtained with Eq. 3.9 from the magnetic correlation length. In a 3DND measurement one measures the transmission of the polarisation components to derive the depolarisation matrix  $\hat{D}$  and then calculate  $f$  and  $\delta$  [10-11]. However, it should be noted that several approximations have been made in the derivation of Eq. 3.9. The goal of the present work is to evaluate how the particle size distribution influences the analysis of the neutron depolarisation data and how large the potential deviations are for our system of interest in the case of ferrous phase transformations.

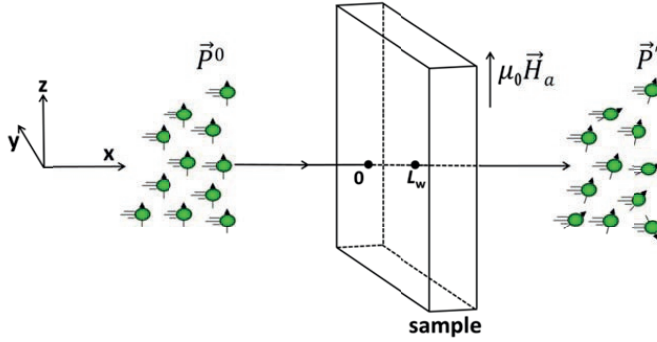


**Fig. 3.1.** Sketch of the neutron depolarisation method shows that a polarised neutron beam ( $\vec{P}^0$ ) is partly depolarised ( $\vec{P}'$ ) after transmitting through a magnetised sample subjected to an external applied magnetic field  $\mu_0 \vec{H}_a$  along  $z$  direction. The positions where neutrons enter and leave the sample are denoted as 0 and  $L_w$ , respectively. The sample volume is  $V_w$ .

### 3.3. Microstructural magnetic model

The present model was developed on the basis of the austenite-ferrite microstructural model by Te Velthuis and coworkers [12] in which spherical (ferromagnetic) ferritic particles nucleate and grow in a fully (paramagnetic) austenitic microstructure that is generated by a Voronoi construction. A given 3D microstructure with a preset ferrite size distribution was generated first and its magnetic configuration was computed. The resulting 3DND characteristics were then calculated using Eqs. 3.4-7. After the 3DND parameters were obtained, Eq. 3.9 was used to back calculate the magnetic particle size, which should be identical to the given particle size if all the used approximations are valid. Otherwise, a deviation will be generated, which can be evaluated subsequently. The present work is generic in nature, but has been applied to the magnetic microstructure evolution during the austenite-ferrite phase transformation in steels. In this phase transformation the high-temperature

austenite phase is nonmagnetic (paramagnetic), while the low-temperature ferrite phase is magnetic (ferromagnetic) below the Curie temperature  $T_C$  [10-12].

To start the simulations, a 3D microstructure comprising a nonmagnetic phase and a magnetic phase was created in a cubic box with a length  $L_b$ . The magnetic particles are assumed to be spherical and centred at the grain corners of the nonmagnetic phase, as discussed in [14]. For the austenite-ferrite microstructure in low-alloyed steels, the parent austenite grain corners, edges and surface are the preferred nucleation sites for the ferrite particles [15]. For isothermal transformations at a low undercooling or for transformations at a slow continuous cooling austenitic grain corners are the most probable sites for the nucleation of ferrites [16-17]. The geometry of the ferrite particles depends largely on the specific transformation conditions. Although ferrite can grow into allotriomorphic plate-like particles along grain boundaries [18-20], most experimental [17] and modelling [21-22] studies showed relatively isotropic equiaxed ferrite in the early stages of the phase transformation when coalesce of particles has not yet appeared. In the present modelling the geometry of the magnetic particles has been simplified to a spherical shape as this shape is close to the most frequently observed equiaxed ferrite particles. The collection of the magnetic particles closely resembles a log-normal size distribution. Each magnetic particle is then assigned with a radius, a spatial location and a randomly chosen magnetic anisotropy (referred to as the *easy axis*). The magnetisation of each magnetic particle  $\vec{M} = M_s \vec{m}$  is assumed to be homogeneous with a magnitude  $M_s$  and an orientation  $\vec{m}$ . The orientation for each magnetic particle was computed by extending the original Stoner-Wohlfarth model [23] to include the mean field and the magnetic interaction with neighbouring particles. To compute the magnetic configuration the total energy of all magnetic particles is minimised.

For a domain  $i$ , the local field  $\vec{H}_{l,i}$  is the summation of the applied field  $\vec{H}_a$ , the total magnetic dipole field  $\sum \vec{H}_{d,ji}$  (sum over  $j$ ) and the mean field  $\alpha \vec{M}$ :

$$\vec{H}_{l,i} = \vec{H}_a + \sum \vec{H}_{d,ji} + \alpha \vec{M}, \quad (3.10)$$

where  $\alpha$  is the mean field parameter [24], which has a fixed value of  $\alpha = 1/3$  in the present study. The magnetic dipole field accounts for the total field originating from all neighbouring magnetic particles [25]. The dipole field for particle  $i$  from another particle  $j$  is expressed as

$$\vec{H}_{d,ij} = \frac{1}{4\pi} \frac{3\vec{r}_{ji}(\vec{r}_{ji} \cdot \vec{M}_j) - \vec{M}_j}{|\vec{r}_{ji}|^3} V_j, \quad (3.11)$$

where  $\vec{r}_{ji}$  is the displacement vector from particle  $j$  to  $i$ ,  $\vec{M}_j$  is the magnetisation and  $V_j$  is the volume of particle  $j$ . When the magnitude of the dipole field  $H_{d,ij}$  (which depends on  $r_{ij}$  and  $V_j$ ) becomes smaller than 0.5%  $M_s$ , it is considered to be negligible and is ignored in the calculations. This threshold corresponds to:  $r_{ij}/(3V_j/4\pi)^{1/3} > 5.2$ .

The magnetic energy  $E_i$  of a particle  $i$  is the sum of the magnetostatic energy  $E_{H,i}$  and the anisotropy energy  $E_{a,i}$

$$E_i = E_{H,i} + E_{a,i}, \quad (3.12)$$

with  $E_{H,i} = -\mu_0 H_{l,i} M_s \cos \varphi_i$  and  $E_{a,i} = \frac{1}{2} \mu_0 N_s M_s^2 \sin^2(\theta_i - \varphi_i)$ , where  $\varphi_i$  is the angle between  $\vec{H}_{l,i}$  and  $\vec{M}_j$ ,  $\theta_i$  is the angle between  $\vec{H}_{l,i}$  and the easy axis and  $N_s$  is the shape anisotropy factor, chosen to be  $N_s = 0.1$  to reflect the sample geometries used in the ND

experiments. To derive the minimum of  $E_i$  expressed in Eq. 3.12, one can get a unique solution for  $\varphi_i$  by applying the constraints  $\frac{dE_i}{d\varphi_i} = 0$  and  $\frac{d^2E_i}{d\varphi_i^2} > 0$  [26]. Once the minimum energy is derived for all particles, the total energy of the whole system is calculated and compared to the one derived in the previous calculation until the difference between them is less than 0.5%. By this iterative process a stable magnetic configuration can be achieved. The mean magnetisation  $\langle \vec{M} \rangle$ , the reduced magnetisation  $m$  and the values of  $\langle m_i^2 \rangle$  are calculated in the same way as in [12].

The 3DND parameters are then calculated as a function of applied magnetic field from the computed magnetic configuration. The magnetic particle size  $\delta_{ND}$  is estimated from the 3DND data with Eq. 3.9 and compared to the known structural particle size  $\delta_s$  derived from the computed magnetic microstructure. To study the influence of grain size distribution, computations are carried out for a series of given microstructures, composed of (paramagnetic) austenite and (ferromagnetic) ferrite, that evolved as a function of temperature [14]. The saturation magnetisation of ferrite  $M_s$  is calculated with the formula proposed by Arrott and Heinrich [27]. The starting austenite structure is generated in a cubic box with  $L_b = 70 \mu\text{m}$  containing quasi isotropic austenite grain cells with an average diameter of  $d_\gamma = 20 \mu\text{m}$  and a minimum value of  $d_{min} = 12 \mu\text{m}$  constructed via a conventional Voronoi construction method. The ferrite is generated at the corners of the austenite grains and allowed to grow isotropically once nucleated, resulting in a ferrite grain number density  $\rho_a$ , volume fraction  $f$ , average grain radius  $\langle R \rangle$  and a standard deviation  $\sigma$ . The ferrite grain size distribution is produced in such a way that both  $f$  and  $\langle R \rangle$  are kept constant, whilst  $\rho_a$  is adjusted to ensure a constant ratio of  $\sigma/\langle R \rangle$ .

### 3.4. Results and discussion

#### 3.4.1. Influence of the size distribution

Fig. 3.2a shows the microstructure generated for  $f = 0.10$ ,  $\rho_a = 2.45 \times 10^{14} \text{m}^{-3}$ ,  $\langle R \rangle = 4.4 \mu\text{m}$  and  $\sigma/\langle R \rangle = 0.25$  and the corresponding magnetisation for each particle. By representing the particles by magnetic dipoles (of strength  $V M_s \vec{m}$  with  $V$  the volume of the particle) located at their centres, we can directly visualise the orientations of the magnetisation for each particle at different applied fields, as shown in Fig. 3.2b.

At a positive field of  $\mu_0 H_a = 0.39 \text{T}$ , the  $\vec{M}$  of all particles tend to incline towards the direction of the applied field. However, due to the magnetic interactions of the particles the local magnetisation inside the particles is not perfectly aligned, which results in  $\langle m_z \rangle = 0.97$  (with  $\langle m_x \rangle \approx \langle m_y \rangle \approx 0$ ). When  $\mu_0 H_a$  decreases to  $0.0075 \text{T}$ , the local magnetisation shows more orientational disorder resulting in  $\langle m_z \rangle = 0.57$ . When  $\mu_0 H_a$  is reversed to  $-0.39 \text{T}$ , most magnetisation vectors rotate to align with the negative applied field. As shown in Fig. 3.2c, the overall change in magnetisation shows a magnetic hysteresis loop. As in the actual 3DND experiment the magnetic field is aligned along the  $z$ -axis the magnitude of  $\langle m_x \rangle$  and  $\langle m_y \rangle$  is expected to be very small. We will therefore only focus on  $\langle m_z \rangle$  in the remainder of the analysis.

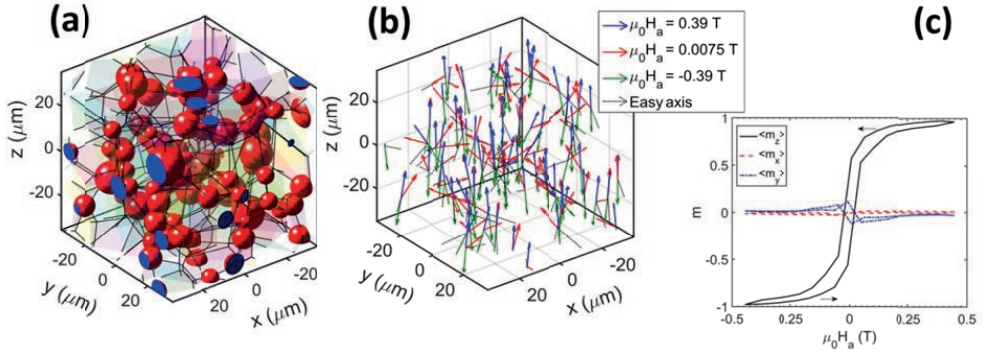


**Fig. 3.2.** (a) 3D visualization of the microstructure with  $f = 0.10$ ,  $\rho_a = 2.45 \times 10^{14} \text{ m}^{-3}$ ,  $\langle R \rangle = 4.4 \mu\text{m}$  and  $\sigma/\langle R \rangle = 0.25$  and (b) the computed magnetisation for each particle illustrated by the orientation of the arrows with easy axis shown in dashed lines. (c) The calculated  $\langle m_x \rangle$ ,  $\langle m_y \rangle$  and  $\langle m_z \rangle$  as a function of the applied field (arrows indicate the changing direction of applied field) for a magnetic hysteresis loop.

The first calculation was done for different microstructures with a fixed magnetic fraction  $f$ . Table 3.1 gives the configuration of the magnetic microstructure with  $f = 0.10$  for different values of  $\sigma/\langle R \rangle$ . Fig. 3.3 shows the characteristic 3DND parameters: the rotation angle  $\varphi$ , the determinant of depolarisation matrix  $\det(\hat{D})$ , the correlation function  $\xi$  and the particle radius  $\delta_{ND}$  as a function of the applied field. By increasing  $\sigma/\langle R \rangle$  from 0 to 0.25, the curves for  $\varphi$  hardly change. Only when  $\sigma/\langle R \rangle$  is increased to 0.50 the hysteresis increases and the saturation levels decreases. The value of  $\det(\hat{D})$  is more sensitive to  $\sigma/\langle R \rangle$  as it probes the variations in local magnetic induction. As shown in Fig. 3.3b, the magnitude of  $\det(\hat{D})$  decreases with increasing  $\sigma/\langle R \rangle$ . This indicates that for identical values of  $f$  and  $\langle R \rangle$ , the polarisation is reduced more strongly when the spread in size distribution increases. The lowest values for  $\det(\hat{D})$  are observed for the smallest applied fields ( $|\mu_0 H_a| < 0.1$  T), whereas a saturation is found for higher applied fields. In Fig. 3.3c the corresponding values for the magnetic correlation function  $\xi$  are shown. As  $\xi$  probes the product of the correlation length and the average variation in magnetic induction  $\langle |\Delta \vec{B}(\vec{r})|^2 \rangle$ , a more disordered magnetic configuration present at small applied fields (as shown in Fig. 3.2b) results in a bigger value of  $\xi$ . Fig. 3.3d compares  $\delta_{ND}$  to  $\delta_s$ . A very good consistency is found for the whole range of applied fields, although a small but growing deviation is found for increasing values of  $\sigma/\langle R \rangle$ .



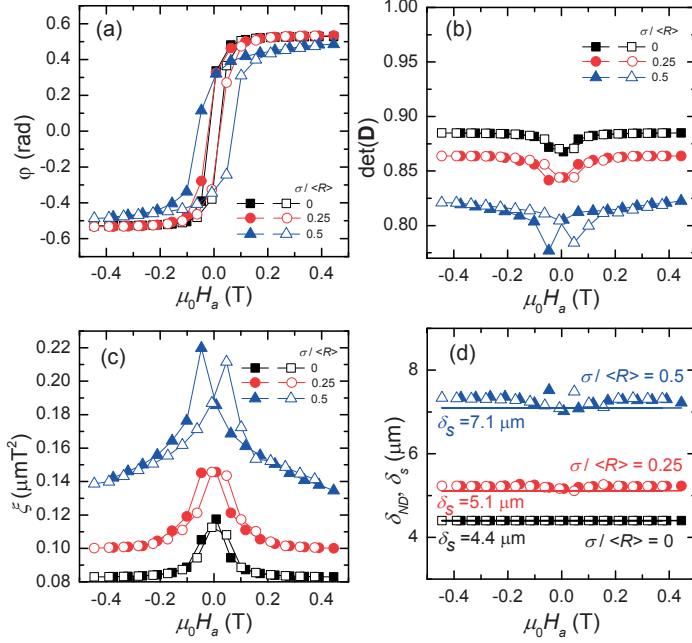


**Fig. 3.3.** Derived 3DND parameters as a function of the applied field  $\mu_0 H_a$  for microstructures with a constant magnetic fraction  $f = 0.10$  and different values of the distribution width  $\sigma/\langle R \rangle$ : (a) rotation angle  $\varphi$ , (b) determinant of depolarisation matrix  $\det(\mathbf{D})$ , (c) correlation function  $\xi$  and (d) average particle radius  $\delta_{ND}$ . In (d) the average particle radius  $\delta_s$  calculated directly from the microstructures computationally generated is plotted as solid lines. The relevant particle size characteristics are indicated in each figure. Note that the closed symbols correspond to a decreasing applied magnetic field, while the open symbols correspond to an increasing applied magnetic field.

**Table 3.1.** The configuration of the ferrite microstructure at an identical magnetic fraction.

$f$	$\rho_a$ ( $\times 10^{14} \text{ m}^{-3}$ )	$\langle R \rangle$ ( $\mu\text{m}$ )	$\sigma/\langle R \rangle$
0.10	2.80	4.4	0
0.10	2.45	4.4	0.25
0.10	1.75	4.4	0.50

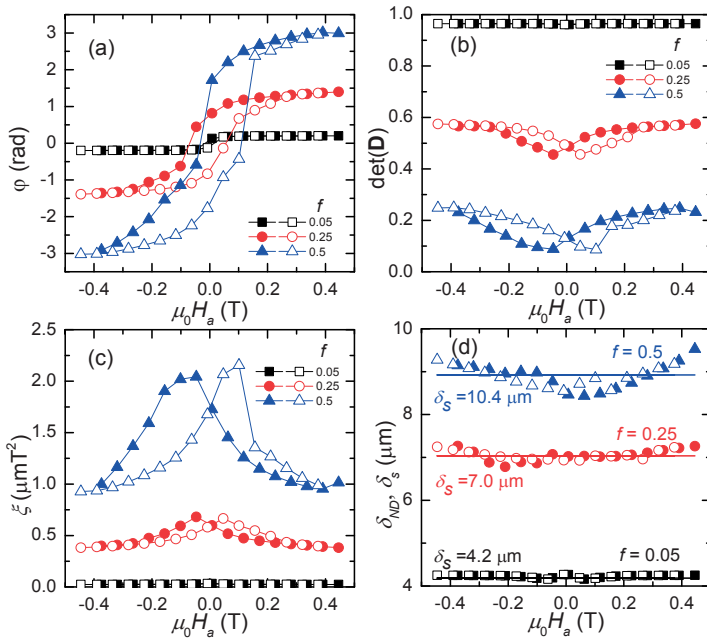
### 3.4.2. Influence of the volume fraction

Fig. 3.4 shows the characteristic 3DND parameters as a function of the applied field for different magnetic fractions  $f$  with a constant relative distribution width of  $\sigma/\langle R \rangle = 0.25$ . It can be seen from Fig. 3.4a that the value of  $f$  indeed has a significant effect on the rotation angle  $\varphi$  as the saturation level roughly scales with the magnetic



fraction. Similarly the saturation level of  $\det(\bar{D})$  is very sensitive to the magnetic fraction (see Fig. 3.4b) in comparison with the effect of varying  $\sigma\langle R \rangle$  (see Fig. 3.3b). It is interesting to note that for  $f = 0.05$  the derived  $\det(\bar{D})$  shows a negligible dependence on the applied field. However, the sensitivity of  $\det(\bar{D})$  to the applied magnetic field increases significantly for increasing values of  $f$ . For increasing values of  $f$  the difference between  $\delta_{ND}$  and  $\delta_s$  becomes more pronounced. At small applied fields  $\delta_{ND}$  underestimate  $\delta_s$ , whereas at higher fields  $\delta_{ND}$  is larger than  $\delta_s$ .

Similar results for  $\xi$  as a function of applied field are found for a value of constant  $\sigma\langle R \rangle$  (Fig. 3.4c) and a constant value of  $f$  (Fig. 3.3c). As the magnetic fraction  $f$  increases, the effect of magnetic inter-particle interactions becomes more pronounced, resulting in an increasing hysteresis.



**Fig. 3.4.** Derived 3DND parameters as a function of the applied field  $\mu_0 H_a$  for microstructures with a constant  $\sigma\langle R \rangle = 0.25$  and different values of the magnetic fraction  $f$ : (a) rotation angle  $\varphi$ , (b) determinant of depolarisation matrix  $\det(\bar{D})$ , (c) correlation function  $\xi$  and (d) average particle radius  $\delta_{ND}$ . For comparison in (d) the average particle radius  $\delta_s$  calculated directly from the microstructure is shown as solid lines. The values are indicated in the figure. Note that the closed symbols correspond to a decreasing applied magnetic field, while the open symbols correspond to an increasing applied magnetic field.

The simulations of Figs. 3.3 and 3.5 show that an increase in the width of the particle size distribution enhances the difference between  $\delta_{ND}$  and  $\delta_s$ . The main reason for this difference is that magnetic correlations were assumed to be negligible when

Eqs. 3.5-9 were derived. However, in the present numerical calculations these magnetic correlations are explicitly included. In addition, parameter  $c_3 = 16/[9(1 + \langle m_x^2 \rangle)]$  in Eq. 3.8 and 3.9 has been derived for identical spheres, but was applied for poly-dispersed spheres.

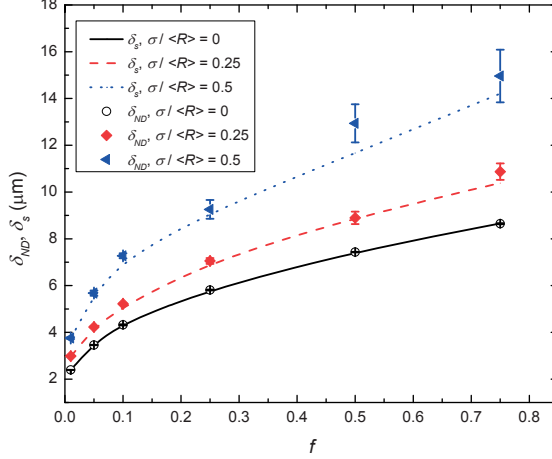


**Fig. 3.5.** Comparison between the particles radius  $\delta_{ND}$  derived by an 3DND analysis and the actual particle radius  $\delta_s$  for different size distributions with  $\sigma/\langle R \rangle = 0, 0.25$  and  $0.50$  as a function of the magnetic fraction  $f$  at applied fields ranging from  $-0.39$  to  $+0.39$  T.

In Fig. 3.5 a comparison between  $\delta_{ND}$  and  $\delta_s$  as a function of  $f$  is made for different values of  $\sigma/\langle R \rangle$  at applied magnetic fields ranging from  $-0.39$  to  $+0.39$  T. In general  $\delta_{ND}$  is in good agreement with  $\delta_s$  over the range of magnetic fractions and size distributions studied. However, the difference increases with increasing  $f$  and  $\sigma/\langle R \rangle$ . As explained earlier, this difference is mainly attributed to the limited validity of the assumptions made in the original 3DND analysis. As can be seen in Fig. 3.5, the maximum difference between  $\delta_{ND}$  and  $\delta_s$  is about 13%, which is satisfactory for most experiments. Based on this analysis, it was possible to deduce the number density  $\rho$  of magnetic particles. A simple relation based on the assumption of identical spherical particles yields  $\rho = 3f/4\pi\delta^3$  with an estimated number density that is found to be within a factor 5 compared to the real magnetic particle number density.

To accurately determine the average particle size an accurate relationship between  $\xi$  and  $\delta$  is required. Te Velthuis and coworkers [12] analysed the dependence of  $\xi$  on the magnetic configuration. They generalised Eq. 3.8 as:

$$\xi = \delta f (\mu_0 M_s)^2 (a_1 (1 + \langle m_x^2 \rangle) - a_2 m^2). \quad (3.13)$$

In the previous analysis the constants were equal to  $a_1 = 3/4$  and  $a_2 = 4/3(4\pi f^2/81)$ . In their numerical study it was found that the parameters  $a_1$  and  $a_2$  were sensitive to (1) the ferrite grain size distribution and (2) the spatial homogeneity of the ferrite grains.

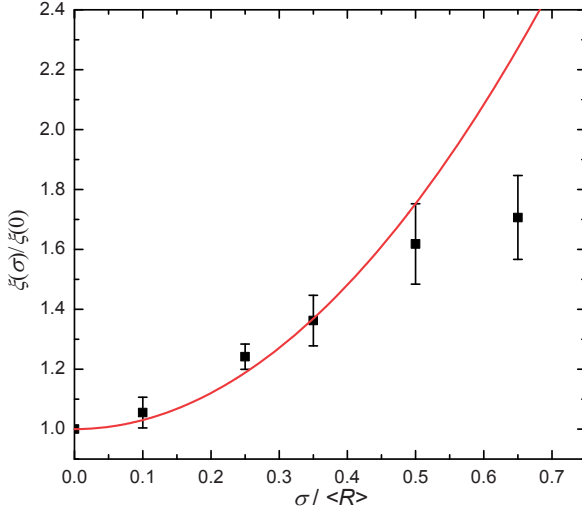


**Fig. 3.6.** Normalised field correlation function  $\xi(\sigma)/\xi(0)$  as a function of  $\sigma/\langle R \rangle$ . The solid line shows the fit to the relationship  $\frac{\xi(\sigma)}{\xi(0)} = 1 + 3.0(3) \left(\frac{\sigma}{\langle R \rangle}\right)^2$  for  $\sigma/\langle R \rangle \leq 0.5$ .

Since the analytical solution of Eq. 3.4 was derived for monodisperse particle distributions, it is not straightforward to include the effect of the size distribution on  $\xi$ . An alternative approach is to compare the numerical results for poly-disperse particle distributions to those for identical particles to investigate its influence. To this aim we calculated the ratio of  $\xi(\sigma)/\xi(0)$  for different values of  $f$ . The results show that  $\xi(\sigma)/\xi(0)$  is nearly independent of both the applied field and the magnetic fraction  $f$  at a fixed value of  $\sigma/\langle R \rangle$ . However,  $\xi(\sigma)/\xi(0)$  increases with increasing  $\sigma/\langle R \rangle$ . When we plot the parameter  $\xi(\sigma)/\xi(0)$  as a function of  $\sigma/\langle R \rangle$ , as shown in Fig. 3.6, a power law dependence  $\frac{\xi(\sigma)}{\xi(0)} - 1 \propto \left(\frac{\sigma}{\langle R \rangle}\right)^p$  with  $p = 2$  is observed for  $\sigma/\langle R \rangle \leq 0.5$ . This relation suggests that the effect of the size distribution on  $\xi$  can be described by an additional factor. We can therefore conclude that the relation

$$\frac{\xi(\sigma)}{\xi(0)} = 1 + \chi \left(\frac{\sigma}{\langle R \rangle}\right)^2, \quad (3.14)$$

with  $\chi = 3.0(3)$  can be used to describe the correlation function for poly-disperse particle size distributions. The variable  $\xi(0)$  can be calculated with Eq. 3.8. The newly derived equation (3.14) is now a very useful addition to analyse experimental 3DND data. For an identical particle system (mono-disperse), the average particle size can be calculated with Eq. 3.9. For a poly-disperse system,  $\xi(\sigma > 0)$  can be expressed as a function of  $\sigma/\langle R \rangle$  with Eq. 3.14, as shown in Fig. 3.6. The effective size  $\delta$  can then be calculated with Eq. 3.9. Since  $\delta$  now directly depends on  $\sigma/\langle R \rangle$ , the additional relation of Eq. 3.14 provides an accurate estimate for  $\delta$ . For a lognormal distribution  $f(R) =$

$\frac{1}{R\omega\sqrt{2\pi}} \exp\left(-\frac{(\ln(R)-\mu)^2}{2\omega^2}\right)$  one can derive the moments of the radius  $\langle R^n \rangle = \exp(n\mu + n^2\omega^2/2)$  and  $\omega^2 = \ln\left(1 + \left(\frac{\sigma}{\langle R \rangle}\right)^2\right)$ . Combining these relations yields  $\frac{\langle R^4 \rangle}{\langle R^3 \rangle \langle R \rangle} = \left(1 + \frac{\sigma^2}{\langle R \rangle^2}\right)^3$ . For  $\sigma/\langle R \rangle \ll 1$ , this results in  $\frac{\langle R^4 \rangle}{\langle R^3 \rangle \langle R \rangle} \approx 1 + 3\left(\frac{\sigma}{\langle R \rangle}\right)^2$ , which is fully consistent with the fitted relationship shown in Fig. 3.6. Hence the relationship between  $\xi(\sigma)/\xi(0)$  and  $\sigma/\langle R \rangle$  found in the present study is suitable to determine both the particle size and the width of the size distribution, particularly for  $\sigma/\langle R \rangle \leq 0.5$ . The average particle size now corresponds to  $\langle R \rangle \approx \frac{\delta}{1+3(\sigma/\langle R \rangle)^2}$ .

In the above simulations the value of  $\sigma/\langle R \rangle$  is set as a constant. During the austenite-to-ferrite phase transformations in steels  $\sigma/\langle R \rangle$  is found to vary between 0 and 0.7 [14, 28], but once nucleation is completed  $\sigma/\langle R \rangle$  tends to fluctuate around a constant value. This behaviour simplifies the above 3DND analysis to obtain a reliable experimental estimate of the magnetic particle size (ferrite grain size) and size distribution during phase transformations in steels. The newly established relationship between  $\xi(\sigma > 0)$  and  $\xi(\sigma = 0)$  thereby sheds new light on the analysis of size distributions of magnetic particles from the 3DND data. It should be noted that the geometry of the ferrite particles has been simplified in the present modelling to a spherical shape. Under most conditions, the simplified geometry used here reflects the ferrite growth reasonably well in the initial stages of the transformation. The conclusion drawn from this study are thereby very useful to link the 3DND parameters to the microstructural characteristics.

### 3.5. Conclusions

We have computed magnetic configurations for magnetic microstructures with mono- and poly-disperse magnetic particles in 3D space and translated those to the characteristic 3DND parameters. The correlation function and the determinant of the depolarisation matrix is found to be very sensitive not only on the magnetic phase fraction and average particle size, but also on the particle size distribution. The correlation function increases with increasing volume fractions and with the width of the particle size distribution of the magnetic particles. The magnetic particle size derived from 3DND data is found to be in very good agreement with the computed microstructural particle size over a wide range of volume fractions and grain size distributions. Deviations in the estimated particle size from 3DND data are found to originate from the spread in particle size. A relationship between the field correlation function and the relative width of the particle size distribution is found that accurately describes the deviations. The present simulations shed new light on the analysis of 3DND data from magnetic particle systems with a poly-disperse particle size distribution and are extremely useful to deepen the analysis of the austenite-ferrite transformation in low-alloyed steels.

## Acknowledgements

The authors appreciate many clarifying discussions with Dr. Theo Rekveldt. Haixing Fang is grateful to the financial support provided by the China Scholarship Council (CSC).

## References

1. R. Rosman and M.T. Rekveldt: *Phys. Rev. B*, 1991, vol. 43, pp. 8437-49.
2. M.T. Rekveldt, N.H. van Dijk, S.V. Grigoriev, and W.G. Bouwman: *Rev. Sci. Instr.*, 2006, vol. 77, pp. 073902.
3. A. Kumar: *Magnetic correlations at domain/cluster length scales using neutron depolarization*, Proceedings of the sixth conference on neutron scattering, 21-23 Nov. 2016, Mumbai, India.
4. M.T. Rekveldt and F.J. van Schaik: *J. Appl. Phys.*, 1979, vol. 50, pp. 2122-7.
5. S. Mitsuda and Y. Endoh: *J. Phys. Soc. Japan*, 1985, vol. 54, pp. 1570-80.
6. I. Mirebeau, S. Itoh, S. Mitsuda, T. Watanabe, Y. Endoh, M. Hennion, and R. Papoular: *Phys. Rev. B*, 1990, vol. 41, pp. 11405-16.
7. R. Rosman and M.T. Rekveldt: *J. Magn. Magn. Mater.*, 1991, vol. 95, pp. 319-40.
8. Ö. Çakr, M. Acet, M. Farle, and A. Wilders: *J. Phys.: Condens. Matter*, 2016, vol. 28, pp. 13LT02.
9. K. Manna, D. Samal, A.K. Bera, S. Elizabeth, S.M. Yusuf, and P.S. Anil Kumar: *J. Phys.: Condens. Matter*, 2013, vol. 26, pp. 016002.
10. S.G.E. te Velthuis, N.H. van Dijk, M.Th. Rekveldt, J. Sietsma, and S. van der Zwaag: *Acta Mater.*, 2000, vol. 48, pp. 1105-14.
11. S.E. Offerman, L.J.G.W. van Wilderen, N.H. van Dijk, M.Th. Rekveldt, J. Sietsma, and S. van der Zwaag: *Acta Mater.*, 2003, vol. 51, pp. 3927-38.
12. S.G.E. te Velthuis, N.H. van Dijk, M.T. Rekveldt, J. Sietsma, and S. van der Zwaag: *J. Appl. Phys.*, 2001, vol. 89, pp. 1275-80.
13. R. Rosman and M.T. Rekveldt: *Z. Phys. B: Condens. Matter*, 1990, vol. 79, pp. 61-8.
14. H. Fang, M.G. Meozzi, E. Brück, S. van der Zwaag, and N.H. van Dijk: *Metall. Mater. Trans. A*, 2018, vol. 48, pp. 41-53.
15. M. Enomoto, H.I. Aaronson: *Metall. Mater. Trans. A*, 1986, vol. 17, pp. 1385-97.
16. W. Huang, M. Hillert: *Metall. Mater. Trans. A*, 1996, vol. 27, pp. 480-3.
17. M. Militzer, R. Pandi, E.B. Hawbolt: *Metall. Mater. Trans. A*, 1996, vol. 27, pp. 1547-56.
18. E. Gamsjäger, M. Militzer, F. Fazeli, J. Svoboda, F. D. Fischer: *Comp. Mater. Sci.*, 2006, vol. 37, pp. 94-100.
19. E. Gamsjäger, R.E. Werner, W. Schiller, B. Buchmayr: *Steel Res. Int.*, 2014, vol. 85, pp. 131-42.
20. E. Gamsjäger, M. Wiessner, S. Schider, H. Chen, S. van der Zwaag: *Philos. Mag.*, 2015, vol. 95, pp. 2899-917.
21. Y.J. Lan, D.Z. Li, Y.Y. Li: *Acta Mater.*, 2004, vol. 52, pp. 1721-9.
22. M. Militzer, M.G. Meozzi, J. Sietsma, S. van der Zwaag: *Acta Mater.*, 2006, vol. 54, pp. 3961-72.
23. E.C. Stoner and E.P. Wohlfarth: *Philos. Trans. R. Soc. London Ser. A.*, 1948, vol. 240, pp. 599-642.

24. D.C. Jiles and D.L. Atherton: *J. Magn. Magn. Mater.*, 1986, vol. 61, pp. 48-60.
25. J.D. Jackson, *Classical electrodynamics, Third Edition*, Wiley, New York, 1999.
26. B.F. Phelps, F. Liorzou, and D.L. Atherton: *IEEE Trans. Magn.*, 2002, vol. 38, pp. 1326-32.
27. A.S. Arrott and B. Heinrich: *J. Appl. Phys.*, 1981, vol. 52, pp. 2113-15.
28. M.G. Meozzi, M. Miltzer, J. Sietsma, and S. van der Zwaag: *Metall. Mater. Trans. A*, 2008, vol. 39, pp. 1237-47.



---

# Chapter 4

## **In-situ 3D neutron depolarization study of the transformation kinetics and grain size evolution during cyclic partial austenite-ferrite phase transformations in Fe-C-Mn steels**

We have analyzed the evolution of the ferrite fraction and average ferrite grain size during partial cyclic austenite-to-ferrite and ferrite-to-austenite phase transformations in an Fe-0.25C-2.1Mn (wt.%) steel using three-dimensional neutron depolarization (3DND). In the 3DND experiments, the ferrite fraction is derived from the rotation angle of the neutron polarization vector and the average grain size is determined from the shortening of the polarization vector. From these the number density of ferrite grains is derived, which indicates that grain nucleation is negligible during partial cycling in the intercritical regime and that all transformation kinetics can be attributed to growth processes only. In the multiple successive cyclic partial transformations the interface migration rate was found to be sluggish due to Mn partitioning. The transformation kinetics determined with 3DND was compared to the predicted behaviors for diffusion-controlled simulations under local equilibrium and para-equilibrium interfacial conditions. It was found that the simulation predictions under local equilibrium only qualitatively capture the transformation kinetic with a difference of one order of magnitude in the variation in the ferrite fraction during cycling. The cyclic behavior of this Fe-0.25C-2.1Mn (wt.%) steel shows that the austenite-ferrite interface indeed migrates back and forth during cycling, while at the same time there is a gradual increase in both the ferrite fraction and the average ferrite grain size over subsequent cycles. The intrinsic cyclic behavior is only visible after subtracting the effect of the progressive interfacial migration into austenite. The present study demonstrates the advantage of 3DND in studying partial cyclic phase transformations over conventional experimental approaches.



## 4.1. Introduction

The kinetics of the austenite-to-ferrite ( $\gamma$ - $\alpha$ ) and the ferrite-to-austenite ( $\alpha$ - $\gamma$ ) transformation in low-alloyed steels has attracted extensive attention due to its practical importance and scientific challenges [1-5]. During the austenite-to-ferrite transformation the ferrite first nucleates at preferred nucleation sites and subsequently grows into the austenite grains. As observed with synchrotron X-ray diffraction, ferrite nucleation occurs in a certain temperature (or time) range, where new nuclei continuously form until a maximum density is reached [6]. Once nucleated, the growth of a ferritic grain, *i.e.* the interface migration, is controlled by interface mobility and diffusion of solute elements in the vicinity of the moving interface. To explore the effect of the alloying elements  $M$  ( $=$  Mn, Ni, Co, *etc.*) on interface migration in Fe-C-M steels, extensive studies have been performed using conventional isothermal or continuous heating and cooling experiments [7-10]. However, in such experiments where nucleation and interface migration take place simultaneously, the impossibility to determine the nucleation rate during the entire transformation process unavoidably leads to non-negligible uncertainties in the derivation of the interface mobility and investigating the effect of the alloying elements. To avoid the effect of nucleation on the transformation kinetics, the concept of cyclic partial austenite-ferrite transformation, where the temperature is varied cyclically within the  $\gamma/\alpha$  two phase region, was recently proposed [11]. This cyclic approach has proven to be more informative in studying the effect of interface mobility and alloying elements on the rate of the interface migration as a result of the (assumed) absence of new nucleation events from the moment of the first inverse transformation cycle. This assumption is physically realistic and has been verified ex-situ by 2D metallographic cross sections [12]. A large number of dilatometric cyclic partial phase transformation measurements [11, 12] and various modelling approaches such as DICTRA [11], 1D mixed-mode [13] and 1D phase-field [14] and 2D phase-field [15] modelling have been used to study the effect of alloying element  $M$  on the austenite decomposition rate and to obtain the interface mobility. These cyclic partial phase transformation studies reveal unexpected phenomena such as inverse and stagnant transformations as a result of various degrees of local partitioning of substitutional alloying elements at the moving austenite-ferrite interface. However, the key assumption behind the cyclic partial phase transformation approach that there are no, or only negligible, new nucleation events during cycling has not been verified by in-situ experiments yet. To resolve this, we use three-dimensional neutron depolarization (3DND) to simultaneously measure the ferrite fraction and grain size during cyclic partial phase transformations in a low-alloyed construction steel. In the present work the ferrite number density can be determined in situ during the cyclic partial phase transformation. The 3DND method also allows the in-situ determination of the average grain size during the transformation, which can hardly be obtained from other physical in-situ characterization techniques.

3DND is a powerful technique to characterize magnetic induction inside bulk materials at (sub)micron scale [16, 17]. In a 3DND measurement polarized neutrons demonstrate Larmor precession around a local magnetic field within a magnetized

sample. After transmission through the sample, the mean magnetization causes a net rotation of the polarization vector while a field variation due to magnetic inhomogeneities results in the decrease of the polarization vector. Therefore, the rotation angle measures the ferromagnetic phase fraction inside bulk materials. The shortening of the polarization vector determines the magnetic correlation length and thereby the mean size of the magnetic regions along the neutron path. A quantitative description of the relation between the correlation and the size of the magnetic particles in 3DND experiments was derived by Rosman and Rekveldt [16]. For the austenite-to-ferrite transformation in steels, the newly formed ferritic grains become magnetic below the Curie temperature (1043 K for pure iron), while the surrounding austenitic matrix remains paramagnetic and thereby effectively non-magnetic. This enables 3DND to determine the key microstructural features of the ferrite phase, i.e. the ferrite volume fraction and the average ferrite grain size. Te Velthuis and coworkers [18] further developed the formulation of the 3DND method and applied it to study the austenite-to-ferrite transformation in medium carbon steels. In a recent study we computationally analyzed the effect of the size distribution on the 3DND derived microstructural parameters and found that the 3DND method under certain conditions may even yield information on the ferrite grain size distribution [19]. Therefore, the 3DND technique provides a powerful tool to simultaneously measure the ferrite fraction and the grain size within the bulk of steel samples. This technique has been used successfully to study austenite-to-ferrite [20] and austenite-to-pearlite [21] phase transformations in steels for isothermal conditions and during continuous cooling conditions.

In the present work we carried out in-situ 3DND measurements on cyclic partial phase transformations in an Fe-0.25C-2.1Mn (wt.%) steel. The ferrite fraction and the average grain size were derived explicitly as a function of time and temperature during cycling. The derived nuclei density and interface migration rate provide detailed information on the austenite-ferrite transformation behavior.

## 4.2. 3DND technique and experimental procedure

In a 3DND measurement, a  $3 \times 3$  depolarization matrix  $\hat{D}$  expresses the relationship between the polarization vector before ( $\vec{P}^0$ ) and after ( $\vec{P}'$ ) transmission through the sample by  $\vec{P}' = \hat{D}\vec{P}^0$  [16, 22]. The components of the polarization vector are determined by the corresponding intensities detected by a  $^3\text{He}$  detector parallel or anti-parallel to the  $x$ ,  $y$  and  $z$  axis as expressed by

$$D_{ij} = \frac{I_s - I_{ij}}{I_s P_0}, \quad (4.1)$$

where  $i, j = x, y$  or  $z$  axis represent the analyzed and initial polarization direction, respectively.  $P_0$  is the degree of polarization of the incoming neutron beam and  $I_s$  the shim intensity, which is given by  $I_s = (I_{zz} + I_{zz})/2$ . The capital  $Z$  indicates a negative  $z$  direction. For the case with a net magnetization along the  $z$  axis, the neutron precession is around the plane perpendicular to the magnetization, resulting in a rotation angle of the polarization vector, that can be expressed as

$$\varphi = \arctan\left(\frac{D_{xy}-D_{yx}}{D_{xx}+D_{yy}}\right). \quad (4.2)$$

This rotation of the polarization vector is related to the mean magnetization of the sample [20, 21]

$$\varphi = \eta\sqrt{c}L_x f\langle m_z \rangle \mu_0 M_s, \quad (4.3)$$

where  $\eta$  is a geometric factor that accounts for the stray fields,  $c = 2.15 \times 10^{29} \lambda^2 T^{-2} \text{m}^{-4}$  is a constant with  $\lambda$  the neutron wavelength,  $L_x$  is the sample thickness,  $f$  is the volume fraction of the ferromagnetic phase,  $\langle m_z \rangle$  is the average reduced magnetization in the direction of the applied magnetic field ( $z$  direction),  $\mu_0$  is the permeability of vacuum and  $M_s$  is the saturation magnetization of the ferromagnetic phase. In the present work, ferrite is the only ferromagnetic phase in the temperature range of interest. The  $\langle m_z \rangle$  value was determined by fitting the magnetization hysteresis curves, which were obtained by varying the applied magnetic field at a constant temperature. In the present work  $\langle m_z \rangle = 1.0$  for temperatures above 1022 K (749 °C),  $\langle m_z \rangle = 0.7$  for temperatures below 955 K (682 °C), and a linear temperature dependence  $\langle m_z \rangle = 1 - 0.3(749 - T)/67$  with  $T$  in degrees Celcius was found between 1022 and 955 K (749 and 682 °C).  $M_s$  is calculated with the method proposed by Arrott and Heinrich [23].  $\eta$  can be expressed as  $\eta = (1 - f)\eta^P + \eta^M$  with  $\eta^P = 0.5$  for spherical magnetic particles and  $\eta^M = \frac{2}{\pi} \arctan\left(\frac{L_z}{L_y}\right)$  determined by the sample dimensions perpendicular to the neutron beam [24]. Hence the ferrite volume fraction can be determined.

The correlation function  $\xi$ , which is proportional to the correlation length of  $|\vec{B}(\vec{r})|^2$  along the neutron beam, measures the size of the magnetic particles. Assuming that there are no correlations between  $\Delta\vec{B}_i(\vec{r})$  and  $\Delta\vec{B}_j(\vec{r})$  ( $i \neq j$ ) along the neutron path, the relation between the correlation function and the determinant of the depolarization matrix can be expressed as  $\xi = -\frac{\ln(\det(\hat{D}))}{2cL_x}$ . The effective radius of the magnetic particle that characterizes the average particle size  $\delta$  is related to the correlation function  $\xi$  as

$$\delta = \frac{3c_3\xi}{2f(\mu_0 M_s)^2(1 - c_2 c_3 \langle m_z \rangle^2)}, \quad (4.4)$$

where the constants  $c_2$  and  $c_3$  are calculated according to [18]. For a given particle size distribution the average particle size  $\delta$  corresponds to  $\delta = \frac{\langle R^4 \rangle}{\langle R^3 \rangle}$  where  $R$  is the particle radius [18]. The validity of the analysis was recently evaluated by simulated particle size distribution [19]. The influence of the particle size distribution was characterized in detail. The previous simulations confirm that Eq. 4.4 provides a reliable estimate for the ferrite grain size. More detailed information about the 3DND theory can be found elsewhere [16, 17, 22].

**Table 4.1.** The chemical composition of the studied steel (wt.%).

C	Mn	Si	P	Al	N	S
0.247	2.060	0.098	0.023	0.021	0.0033	<0.002

Steel samples for the 3DND measurements with dimensions  $L_x \times L_y \times L_z = 1.5 \times 15 \times 100 \text{ mm}^3$  were cut from a cold rolled steel sheet ( $1.5 \times 150 \times 200 \text{ mm}^3$ ) provided by Arcelor Mittal. The middle area ( $\Delta L_y \times \Delta L_z = 15 \times 20 \text{ mm}^2$ ) of the plate samples was thinned down to 0.4 mm by spark wire erosion. The chemical composition of the samples is given in Table 4.1. The 3DND experiments were performed on the PANDA instrument at the nuclear reactor at the Reactor Institute Delft using a polarized neutron beam with a fixed wave wavelength of  $2.06 \text{ \AA}$  and a spread of about 2%. The degree of polarization of the empty beam is 98%. The samples were mounted in a sample holder sandwiched by two BN blocks. Three K-type thermocouples were welded onto the sample with an identical spacing to monitor the temperature homogeneity along the vertical axis of the sample. The sample was mounted into a furnace, which was placed on the PANDA instrument, under a vacuum environment (with a pressure  $< 10^{-3} \text{ Pa}$ ). In the present study, neutron beam is in the  $x$  direction and applied magnetic field is along the  $z$  direction. During the time-dependent 3DND experiments the applied magnetic field was  $B_{\text{appl}} = 6.2 \text{ mT}$ .

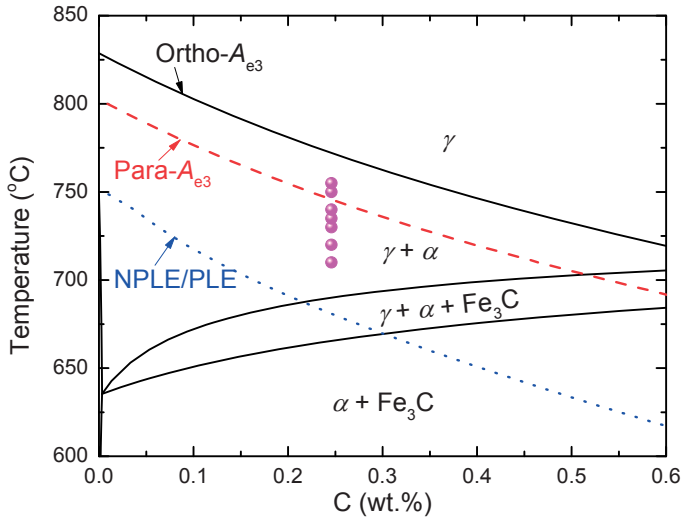


**Fig. 4.1.** Phase diagram of Fe-C-2.06 wt.% Mn steel with the composition and the cycling temperatures studied shown as solid circles. The phase boundaries calculated under ortho-equilibrium conditions are shown as solid lines. The  $A_{e3}$  line calculated under para-equilibrium is shown as dashed line, while the dotted line indicates the NPLE/PLE transition temperature between negligible partitioning local equilibrium (NPLE) and partitioning local equilibrium (PLE).

In-situ 3DND measurements were carried out to investigate the microstructure evolution in the sample during cycling between  $T_1$  and  $T_2$  in the  $\gamma/a$  two-phase region. The sample was first annealed at 1073 K (800 °C) for at least one hour and subsequently cooled to  $T_1$  at a rate of 3 K min<sup>-1</sup>. After holding at  $T_1$  for 20 min in order to reach an (quasi-)equilibrium state, the temperature was raised to  $T_2$  and lowered back to  $T_1$  and cycled between these values at a constant rate. After a preset number of cycles, the sample was cooled down to room temperature. During the test the temperature difference over the sample region probed by the neutron beam was within 2 K. The cycling temperatures and the corresponding equilibrium ferrite fraction calculated with Thermo-Calc software using the TCFE8 database are given in Table 4.2. The sample composition and the cycling temperatures of the Fe-C-2.06 wt.% Mn alloy are shown in the phase diagram in Fig. 4.1.

**Table 4.2.** The cyclic experimental conditions. Characteristic temperatures are ortho- $A_{e3}$  = 1045 K (772 °C), para- $A_{e3}$  = 1020 K (747 °C), NPLe/PLe = 954 K (681 °C),  $A_1$  = 939 K (666 °C) and  $T_C$  = 1034 K (761 °C).

Experiments	$T_1$ (K)	$f_{eq}^a(T_1)$	$T_2$ (K)	$f_{eq}^a(T_2)$	$\langle T \rangle$ (K)	$\Delta T$ (K)	Cycling rate (K min <sup>-1</sup> )
S720A	983	0.537	1003	0.417	993 (720 °C)	20	1
S720B	983	0.537	1003	0.417	993 (720 °C)	20	2
S730	993	0.482	1013	0.341	1003 (730 °C)	20	1
S740	1003	0.417	1023	0.253	1013 (740 °C)	20	1
S745	1008	0.381	1028	0.204	1018 (745 °C)	20	1

The cycling temperatures were chosen such that the equilibrium ferrite fraction is not too small to form a significant amount of the ferrite phase and is not too large to avoid extensive hard impingement of the ferrite grains. Therefore, the cycling temperatures were chosen to show an equilibrium ferrite fraction between 0.2 and 0.6. The cycling temperature window was set to be constant  $\Delta T = 20$  K. As the ferrite formation in this steel is relatively slow according to previous studies [2, 7], we chose a relatively slow cycling rate to ensure that a sizable variation of the ferrite fraction can be observed. As neutron experiments are rate limited too, this low cycling rate matches the relatively long measurement times required for the 3DND measurements: for the current installation 45 seconds were required to complete the determination of a whole depolarization matrix. Fig. 4.1 shows that the temperature is cycled across the  $A_{e3}$  under para-equilibrium condition (para- $A_{e3}$ ) for the tests of S740 and S750, while for the other tests the temperature is cycled below para- $A_{e3}$  and above the NPLe/PLe transition temperature between negligible partitioning local equilibrium (NPLe) and partitioning local equilibrium (PLe). The ferromagnetic Curie temperature of the

sample is determined from the 3DND measurements as  $T_C = 1034$  K (761 °C). Micrographs of the samples after the multi cyclic partial transformation 3DND measurements were taken to evaluate the final ferrite grain size. To corroborate the 3DND results, rectangular samples with dimensions of  $1.5 \times 1.5 \times 10$  mm<sup>3</sup> were heat treated in a DIL805D/T dilatometer with the same temperature profiles as used in the 3DND experiments, but quenched at various stages during multi-cycling. The samples were etched with 2% nital to distinct the ferrite and the martensite that was transformed from the austenite during quenching. Both optical and electron microscopy (JEOL JSM 6500F) were used to examine the microstructures of the quenched samples. The ferrite volume fraction was determined using the point-counting method. The 3D ferrite grain radius  $R_{3D}$  was derived from the 2D spherical equivalent radius  $R_{2D}$  with  $R_{3D} = 4R_{2D}/\pi$  [25].

### 4.3. Results

#### 4.3.1. Transformation kinetics in the whole ND experiment

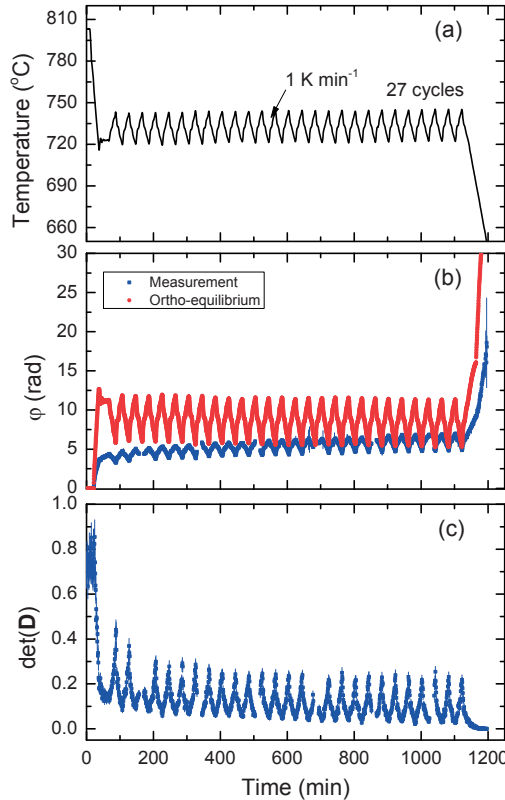


**Fig. 4.2.** The temperature profile (a) of the cycling experiment between 993 and 1013 K (720 and 740 °C) for sample S730. Derived 3DND parameters: (b) rotation angle  $\varphi$  and (c) determinant of depolarization matrix  $\det(\bar{D})$  as a function of time.

Fig. 4.2 shows the polarization rotation angle  $\varphi$  and the determinant of the depolarization matrix  $\det(\hat{D})$  derived from the 3DND data as a function of the temperature for cycling between 993 and 1013 K (720 and 740 °C). The corresponding ferrite volume fraction  $f_a$  and average grain radius  $\delta$  are presented in Fig. 4.3. In addition to the experimentally determined rotation angle measured with the 3DND, the rotation angle for the ortho-equilibrium ferrite fraction has been calculated with Eq. 4.3 and is shown in Fig. 4.2b. Fig. 4.3b compares the measured and equilibrium ferrite fractions calculated under ortho-equilibrium, para-equilibrium (PE) and negligible partitioning local equilibrium (NPLE) using the Thermo-Calc. During continuous cooling from the fully austenitic state at 1073 K (800 °C), an increase in rotation angle and a decrease in polarization was observed at 1034 K (761 °C), (i.e. the Curie temperature), which suggests that the ferrite started to form at or above this temperature. As shown in Fig. 4.3b, the presence of ferrite could be confirmed from 1034 K (761 °C) onwards. The values of  $\delta$  at the earliest stage of ferrite formation are not shown in Fig. 4.3c. This is because both the ferrite fraction and the derived correlation function are small, resulting in large uncertainties in  $\delta$ .

During the cooling step and the isothermal holding (20 min at  $T = 993$  K (720 °C)), the rotation angle grows until the corresponding ferrite fraction has reached a constant value of  $f_a \approx 0.20$ . This experimental fraction is still far away from the ortho- or para-equilibrium value predicted from thermodynamics. As the ferrite under NPLE is predicted to only form below 954 K (681 °C), the NPLE condition is not likely to be triggered until the temperature is well below the NPLE/PLE transition temperature. In the cycling region  $\varphi$  goes up and down with decreasing and increasing temperature while  $\det(\hat{D})$  varies in an opposite sense. Over the successive cycles both the ferrite fraction and the average ferrite grain size increase with respect to the starting moment of the cycling. However, the ferrite fraction after 27 cycles remains below the ortho-equilibrium value, whereas the amplitude of the variation in ferrite fraction during cycling is much smaller than that of PE, indicating a slow transformation kinetics under this condition. With further cooling, the ferrite fraction increases, while the derived magnetic particle radius  $\delta$  decreases. This does not necessarily reflect a decrease in the real grain size, but is probably due to the formation of magnetic multi domains within in one grain. Especially, the formation of pearlite in the low temperature region entered during the slow final cooling stage after the end of the cycling enhances the formation of magnetic domain walls inside individual grains. Moreover, at this stage the ferrite grains grow more anisotropic due to the higher chance of soft and hard impingement, which compromises the assumption that ferrite grain are quasi-spherical. As a result, using Eq. 4.4 (which assumes that ferrite grains remain spherical at all times) the grain size may lead to some deviations in the 3DND estimate of the ferrite grain size in the later stage of the transformation. As shown in Fig. 4.4, the micrograph of this sample indicates that about 25% of pearlite is present after cooling at the end of the partial transformation cycles. The metallographically determined final ferrite grain radius is about  $5 \pm 1$   $\mu\text{m}$ , which is comparable to the  $\delta = 4.6$   $\mu\text{m}$  obtained at the end of the cycling at 1003 K (720 °C). The value of  $\delta = 3.1$   $\mu\text{m}$  obtained at 923 K (650 °C) is however significantly lower, as shown in Fig. 4.3c. This indicates that the decrease of  $\delta$  in the final cooling stage after cycling is not reflecting

the decrease of the ferrite grain size, but due to the formation of magnetic multi domains in individual ferrite grains.

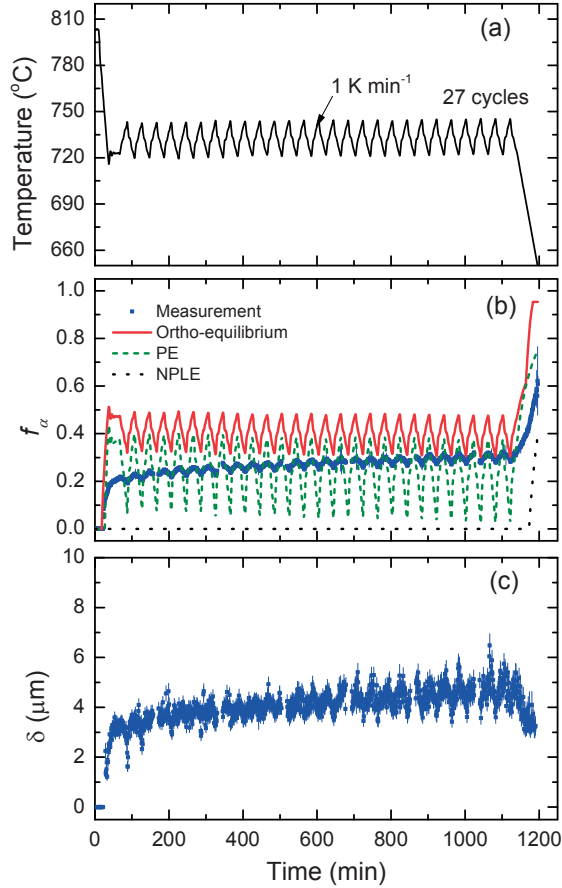


**Fig. 4.3.** The temperature profile (a) of the cycling experiment between 993 and 1013 K (720 and 740 °C) for sample S730, (b) ferrite volume fraction  $f_\alpha$  and (c) average ferrite grain radius  $\delta$  derived from the 3DND measurements shown in Fig. 4.2 as a function of time. The equilibrium ferrite fractions calculated under ortho-equilibrium, PE and NPLE are also shown in (b) for comparison.

As shown in Fig. 4.5, the transformation kinetics in the other cyclic experiments shows a similar behavior. All transformations are detectable below the Curie temperature of 1034 K (761 °C). The transformation proceeds with a relatively high speed during the first cooling stage and then slows down in the isothermal stage. The ferrite fraction is enhanced by a decrease in the minimum transformation temperature and the ferrite grain size grows to higher values in samples that are cycled at lower



temperature ranges. For cycling tests between 1003 and 1023 K (730 and 750 °C, S740) and 1008 and 1028 K (735 and 755 °C, S745), the ferrite fraction is nearly the same and also the ferrite grain size is changing around a comparable value of about 2.5  $\mu\text{m}$ . By decreasing the cycling temperature range, the average ferrite grain size  $\delta$  increases and the change in each cycle is more distinct. The rate of change in both the ferrite fraction and the ferrite grain size is slightly more enhanced at a higher cycling rate, as can be seen the cycling tests between 983 and 1003 K (710 and 730 °C) at a rate of 2  $\text{K min}^{-1}$  (S720B) compared to that at a rate of 1  $\text{K min}^{-1}$  (S720A).

The ferrite fraction and the average ferrite grain size determined by imaging analysis on the quenched samples are also plotted in Figs. 4.5b and 4.5c to compare with the 3DND results. The data are in good agreement with each other, only  $f_{\alpha}$  is slightly smaller for the image analysis than for the 3DND. Fig. 4.6 shows the micrographs of the quenched samples where both the ferrite and the martensite, which was transformed from the austenite during quenching, are present.

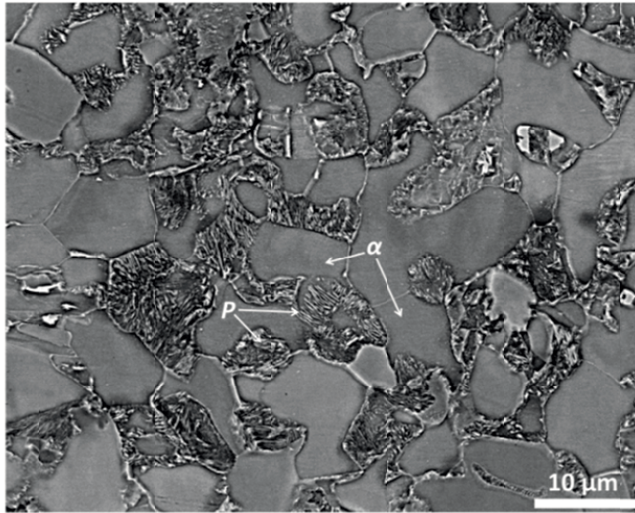


**Fig. 4.4.** SEM graph of the S730 sample showing ferrite ( $\alpha$ ) and pearlite ( $P$ ) after the 3DND measurement.

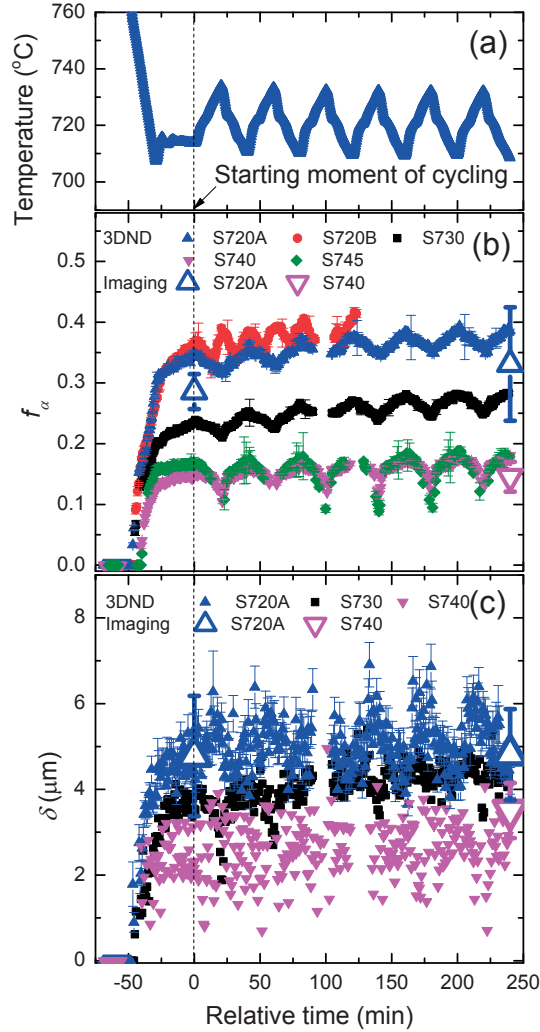


**Fig. 4.5.** (a) The temperature profile of the cycling experiment between 983 and 1003 K (710 and 730  $^{\circ}\text{C}$ ) at a rate of 1 K  $\text{min}^{-1}$  (sample S720A), which resembles the temperature profiles of all other tests. Comparison of (b)  $f_{\alpha}$  and (c)  $\delta$  derived from the 3DND measurements for the first 6 cycles. The reference time ( $t = 0$ ) is selected to be the start of the cycling. Only the error bars of grain radius for the cycling experiment between 983 and 1003 K (710 and 730  $^{\circ}\text{C}$ ) at a rate of 1 K  $\text{min}^{-1}$  (sample S720A) are shown for clarity in (b). The grain radius for the other tests show comparable error bars. For clarity, the grain size is only shown for the S720A, S730 and S740 samples. The values for  $f_{\alpha}$  and  $\delta$  derived from image analysis on quenched samples are also plotted in (b) and (c).

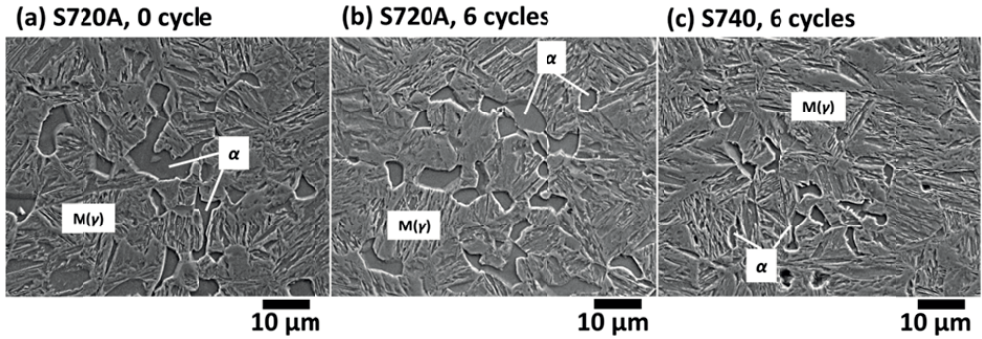


**Fig. 4.6.** Secondary electron images of the samples quenched after (a) 0 cycle and (b) 6 cycles for S720A and (c) 6 cycles for S740. M( $\gamma$ ): martensite;  $\alpha$ : ferrite.

#### 4.3.2. Transformation kinetics and grain size evolution during individual cycles

A closer look at the transformation behavior during individual cycles is shown in Fig. 4.7 for cycling between 993 and 1013 K (720 and 740 °C, S730) and in Fig. 4.8 for cycling between 983 and 1003 K (710 and 730 °C, S720A), respectively. As explained in [26], the kinetics in initial cycling stage is most relevant to the physical properties of the interface, *e.g.* interface mobility and partitioning of substitutional alloy elements, as there is less chance of soft or hard impingement. Therefore, we show the details of the first several cycles in Fig. 4.7 and Fig. 4.8.

A net increase in ferrite fraction after heating and cooling in each cycle is observed in both Fig. 4.7 and Fig. 4.8. The transition from decreasing  $f_a$  during heating to increasing  $f_a$  during cooling coincides with the moment of switching from heating to cooling and *vice versa*. Little inverse transformation, where the transformation does not proceed in line with the temperature change, is seen. However, the average grain size shows a more complicated behavior than  $f_a$ . In Fig. 4.7,  $\delta$  monotonically decreases and increases over changing temperature in the first cycle followed by more variations in the following cycles. By looking at the overall changes in each heating and cooling segments for each cycle, one finds there is a decrease of  $\delta$  in the heating part and an increase of  $\delta$  in the cooling part, which is in line with the change of  $f_a$  as one would generally expect. A larger variation in  $\delta$  can be seen in Fig. 4.8 for the cycling experiment between 983 and 1003 K (710 and 730 °C). The  $\delta$  even partially tends to increase as temperature goes up and decrease as temperature cools down. This unexpected change of  $\delta$  is not accidental because a similar behavior of  $\delta$  is also found in the cycling experiment between 983 and 1003 K (710 and 730 °C) at a higher rate of 2 Kmin<sup>-1</sup>. At first thought, one may think this is a contradictory trend because an increase in  $f_a$  must be associated with an increase in grain size if there are no new nuclei formed. However, it should be noted that the  $\delta$  derived from the 3DND technique is a measurement of the average grain size and its estimate is dominated by the bigger grains as  $\delta = \langle R^4 \rangle / \langle R^3 \rangle$ . For cycling between 983 and 1003 K (710 and 730 °C), a bigger grain size exists in the initial cycling stage compared to the other

cycling experiments (see Fig. 4.4b), which implies the concentrations of C and Mn are more likely to be higher in the untransformed austenite. When the temperature change switches direction, the bigger ferrite grains respond slower because of the higher concentrations of solute Mn atoms at the surrounding interface boundaries of the larger grains. This slower response may cause the hysteretic response of  $\delta$  to the temperature change, which can result in the more disordered change of  $\delta$  shown in Fig. 4.8.

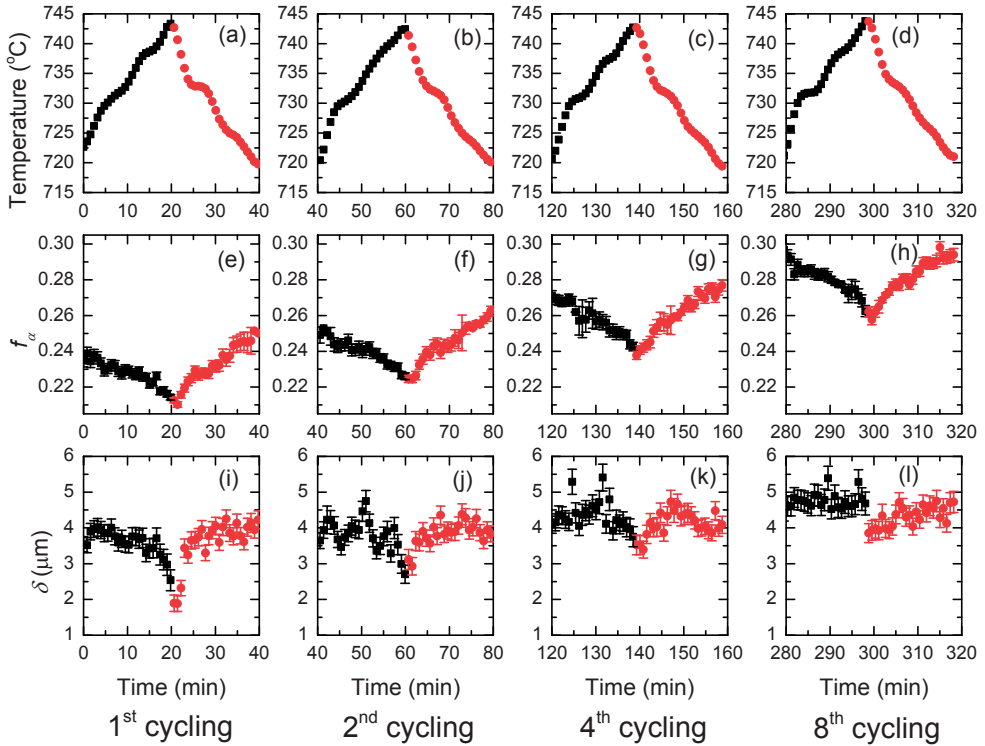


**Fig. 4.7.** Measured  $f_\alpha$  and  $\delta$  as a function of time for individual cycling experiments between 993 and 1013 K (720 and 740 °C) at a rate of 1 K min<sup>-1</sup> (S730). The reference time  $t = 0$  indicates the start of the cycling. The data obtained during heating are shown in black squares and in red circles during cooling.

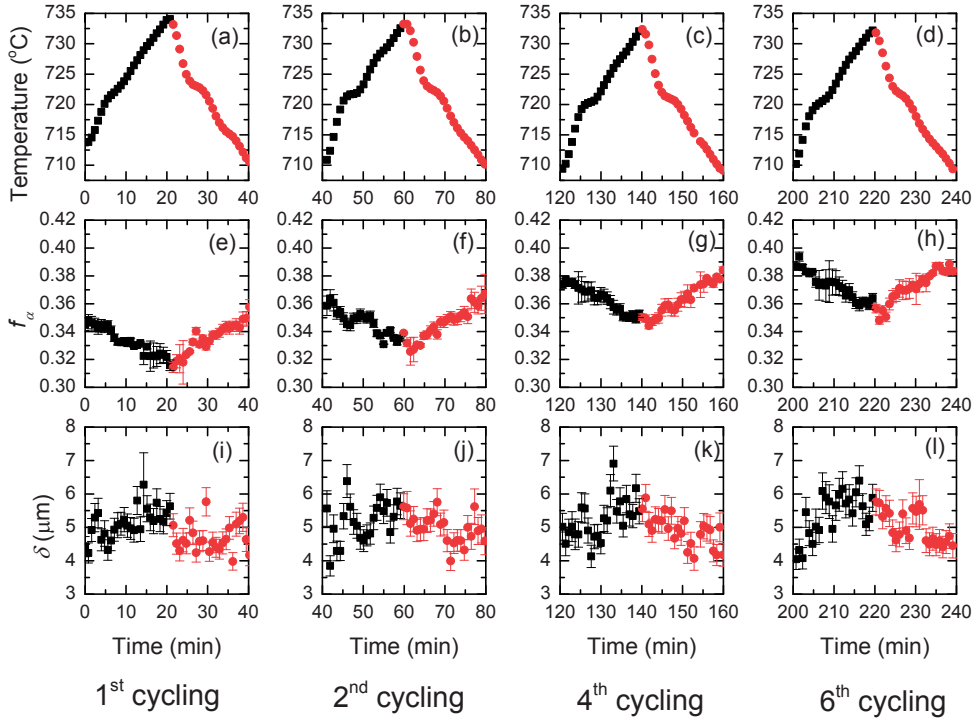


**Fig. 4.8.** Measured  $f_a$  and  $\delta$  as a function of temperature for individual cycling experiments between 983 and 1003 K (710 and 730 °C) at a rate of 1 K min<sup>-1</sup> (S720A). The reference time  $t = 0$  indicates the start of the cycling. The data obtained during heating are shown in black squares and in red circles during cooling.

For each heating and cooling part of an individual cycle, we calculate the average rate of change for the ferrite fraction  $\langle df_a/dt \rangle$  and the ferrite grain size  $\langle d\delta/dt \rangle$ , which are summarized in Table 4.3. A positive sign indicates that the austenite transforms to ferrite and a negative sign that ferrite transforms to austenite. The experimental data suggest that the interface migration is very sluggish, which was also found in several other works on isothermal transformations in steels with a similar Mn concentration [2, 7, 27-29]. As mentioned earlier, the tendency for  $f_a$  is in line with the temperature change for all cycling tests, whilst a more disordered behavior is found for  $\delta$  in the cycling experiments between 983 and 1003 K (710 and 730 °C). To quantify the net increase in  $f_a$  and  $\delta$  for an increasing number of cycles, we plot the average of  $f_a$  and  $\delta$  for the heating and cooling part of each cycle as a function of the cycle number in Fig. 4.9. The rate at which  $f_a$  and  $\delta$  increase is clearly found to increase for a decrease in cycling temperature for most of the cycling experiments, except for the rate of  $\delta$  for cycling between 993 and 1013 K (720 and 740 °C, S730) which is even larger than that for the cycling between 983 and 1003 K (710 and 730 °C, S720A). Although there is a considerable variation in behavior for  $\delta$  when cycling between 1008 and 1028 K (735

and 755 °C, S745) compared to cycling between 1003 and 1023 K (730 and 750 °C, S740), the net increase in  $f_a$  is very limited.

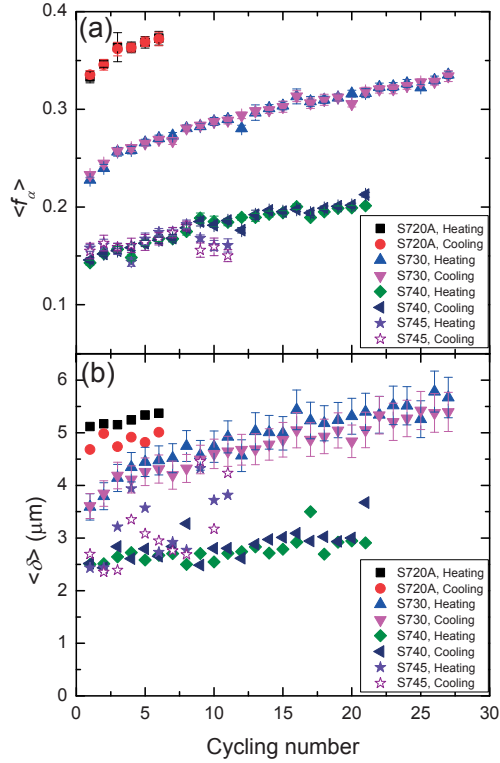


**Fig. 4.9.** Average (a) ferrite fraction  $f_a$  and (b) ferrite particle radius  $\delta$  obtained for heating and cooling segments in individual cycles as a function of the cycling number.

Since the interface migrates slowly in the present samples, the ferrite fraction is still far from equilibrium at the end of the cycling (see Fig. 4.3 as an example). There are two coupled effects in the cycling behavior of this 2 wt.% Mn steel: i) the intrinsic cycling behavior which moves the  $\gamma/\alpha$  interface back and forth; ii) the net increase in  $f_a$  and  $\delta$  over continued cycling. In particular the second phenomenon makes the cycling behavior quite different from a previously reported work [11] on a lean, low Mn steel (Fe-0.023C-0.17Mn in wt.%).

**Table 4.3.** The average rate of change  $df_a/dt$  and  $d\delta/dt$  during heating and cooling segments of the studied cycles.

Experiments	$\langle df_a/dt \rangle$		$\langle d\delta/dt \rangle$		$ D_{Mn}^{int}/v $		$\left  \frac{D_{Mn}^{int}}{v} / \frac{C_{Mn}^{\gamma*} - C_{Mn}^{\alpha*}}{C_{Mn}^{\gamma*} - C_{Mn}^{\alpha*}} \right $	
	$(\times 10^{-5} \text{ s}^{-1})$		$(\times 10^{-3} \text{ } \mu\text{m s}^{-1})$		(nm)		(nm)	
	Heating	Cooling	Heating	Cooling	Heating	Cooling	Heating	Cooling
S720A	-2.3(5)	3.2(2)	1.0(3)	-0.7(3)	5.2(9)	7.4(8)	4.1(9)	5.9(9)
S720B	-5.8(9)	7.6(2)	2.9(7)	-2.4(6)	1.8(6)	2.2(6)	1.3(6)	1.6(6)
S730	-2.7(5)	3.2(6)	-0.5(4)	0.5(4)	13.9(9)	14.0(9)	9.2(9)	9.2(9)
S740	-3(1)	3(1)	-1.8(8)	1.3(9)	5.2(9)	7.2(9)	3.1(9)	4.2(9)
S745	-5(2)	5(2)	-2.0(6)	1.8(6)	5.4(8)	6.0(9)	5.3(8)	5.8(9)

### 4.3.3. Comparison to DICTRA simulations

To further analyze the cycling behavior for the current steel and cycling condition, the experimental transformation kinetics is compared to the kinetics predicted by DICTRA (linked to the TCFE7 and MOB2 databases) simulations [29]. In the simplified (1-D) DICTRA simulation we start with a planar austenite phase with a length of 10  $\mu\text{m}$  and a thin ferrite phase of 10 nm growing from one side. The same temperature profile as used in 3DND experiments is applied to the simulation. The starting composition of the bulk austenite is Fe-0.247C-2.06Mn (wt.%). Two interfacial conditions are assumed: local equilibrium (LE) and para-equilibrium (PE) [30].

Fig. 4.10 shows the comparison of the ferrite fraction derived from 3DND for cycling experiment between 993 and 1013 K (720 and 740  $^{\circ}\text{C}$ , S730) and the ferrite fraction derived from the DICTRA simulations. The ortho equilibrium values of ferrite fraction calculated from phase diagrams are also shown. The experimental  $f_a$  is located in between the DICTRA predictions under LE condition and ortho equilibrium while it intertwines with the predictions under PE condition. None of the simulations directly corresponds to the transformation kinetics derived from the 3DND experiment. This is not surprising as Mn diffusion normally shows an intermediate behavior located between the LE and PE predictions [29, 31-32]. The tendency for  $f_a$  is qualitatively consistent with the simulation under LE, although the absolute values of  $f_a$  differ more than one order of magnitude. Similar to the 3DND results, the simulations under LE also show a slight increase of  $f_a$  in the isothermal stage followed by a cyclic decrease and increase, in line with the effect of the temperature change with an overall net increase in  $f_a$  built up over cycling. This behavior is not found in the simulations under PE.



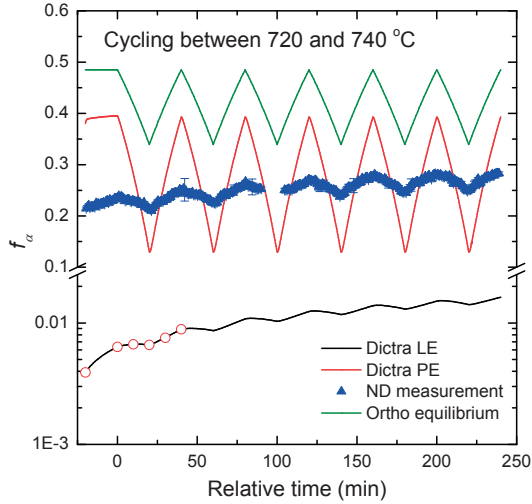


**Fig. 4.10.** Ferrite fraction  $f_\alpha$  during cycling between 993 and 1013 K (720 and 740 °C, S730) derived from the 3DND (triangles) compared to the calculated values derived from DICTRA simulations imposing local equilibrium (LE) and para-equilibrium (PE) conditions. For reference the ortho equilibrium is also indicated.

Regarding the cyclic behavior of  $f_\alpha$ , shown in both the 3DND experimental data and the simulation results under LE, one question arises: why does  $f_\alpha$  decrease during heating in each cycle while the fraction is still far away from its ortho equilibrium value? One would expect that  $f_\alpha$  does not decrease during heating, but continues to increase with a slower rate than that during cooling, which is thermodynamically favored. The observed behavior is however related to the relative speed of the Mn diffusion and the interface velocity. Fig. 4.11 shows the diffusion profiles of C and Mn for the first cycle for the simulation under LE, which is assumed to qualitatively represent the development of the C and Mn profiles in the 3DND experiment. After the primary cooling, diffusion spikes in C and Mn are formed at the interface and move forward until the start of the heating in the first cycle. During heating, the interfacial concentrations of C and Mn are decreasing, which drives the solutes into the austenite or diffuse back to the ferrite. In the early stages of heating the solutes are still able to diffuse into austenite, whereas with increasing temperature more and more solutes need to be diffused out, which decreases the interfacial concentration gradients in austenite and ultimately change the direction of the concentration gradient. This change triggers a reversion in the direction the transformation proceeds. However, since only part of the solutes in the original spike can diffuse back into the ferrite during heating, the interface moves back to form ferrite, resulting in a weaker back transformation than the forward transformation during cycling. This is why we also observed a net increase in  $f_\alpha$  over cycling. The essential reason for the reversion in transformation is attributed to the partitioning of Mn and the slow diffusion rate of Mn in austenite (or inside the interface depending on the length scale of the Mn diffusion



length). At these temperatures,  $D_{Mn}^{\gamma}/D_C^{\gamma} \approx 10^{-6}$  and as a result there is no depletion of Mn at the ferrite side. The reversion of the transformation direction due to Mn diffusion was previously analyzed by Vitek and coworkers [33]. They showed that a reversion may happen when a transition from the PE mode to the LE mode occurred during an isothermal at 983 K (700 °C) of Fe-0.1C-3Mn (wt.%). They did however not find experimental evidence from dilatometer measurements. With our 3DND measurements during cycling transformations, we experimentally observed a reversion of the transformation direction, which is probably caused by the diffusion of the substitutional element.

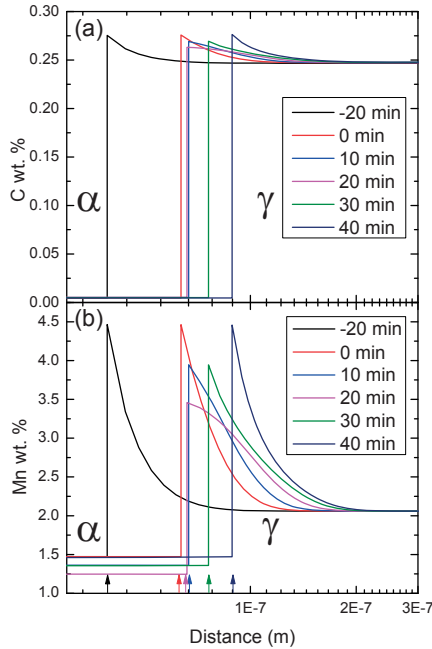


**Fig. 4.11.** (a) C and (b) Mn diffusion profiles derived from DICTRA simulations under LE conditions with arrows indicating the position of the interface. The times correspond to those indicated by the red circles in Fig. 4.10.

## 4.4. Discussion

### 4.4.1. Absence of new nucleation during cycling

The 3DND technique provides a unique way to simultaneously measure the ferrite fraction and the average ferrite grain size. Assuming that the ferrite grains are spherical, we can estimate the number density  $\rho_a$  of ferrite grains from the following equation:

$$\rho_\alpha = \frac{3f_\alpha}{4\pi\delta^3}. \quad (4.5)$$

To clarify the evolution of  $\rho_\alpha$ , we plotted the average of  $\rho_\alpha$  for the heating and cooling part of each cycle as a function of the cycling number in Fig. 4.12. It is clearly observed that the number density is constant over cycling with fluctuations within the experimental uncertainty. These results are distinct evidence that ferrite nucleation is indeed negligible during the cyclic transformation and that the transformation is therefore only controlled by ferrite growth. In Fig. 4.12b, there is a slight monotonic decrease of  $\rho_\alpha$  over cycling. This suggests that in this cycling experiment some coarsening of ferrite grains is taking place.

For the cycling data of Fig. 4.12b plotting  $\delta^3 - \delta_0^3$  as a function of time in Fig. 4.13a clearly shows a linear relationship  $\delta^3 - \delta_0^3 = kt$  with a coarsening rate of  $k = 0.129(4) \mu\text{m}^3\text{min}^{-1}$ . Fig. 4.13b directly shows that the number of ferrite grains decreases over time, confirming the coarsening behavior at this temperature range.

For cycling at other temperatures the ferrite grain coarsening is not significant as  $\rho_\alpha$  is constant during the whole cycling process shown in Fig. 4.12. The reduction of ferrite grain boundary area, *i.e.* coarsening, can take place by full hard impingement on the austenite grain boundaries and/or coalescence of ferrite grains [34, 35]. The significance of coarsening is most directly related to the spacing of the ferrite grains, the degree of transformation with respect to the equilibrium and the ferrite grain boundary mobility.

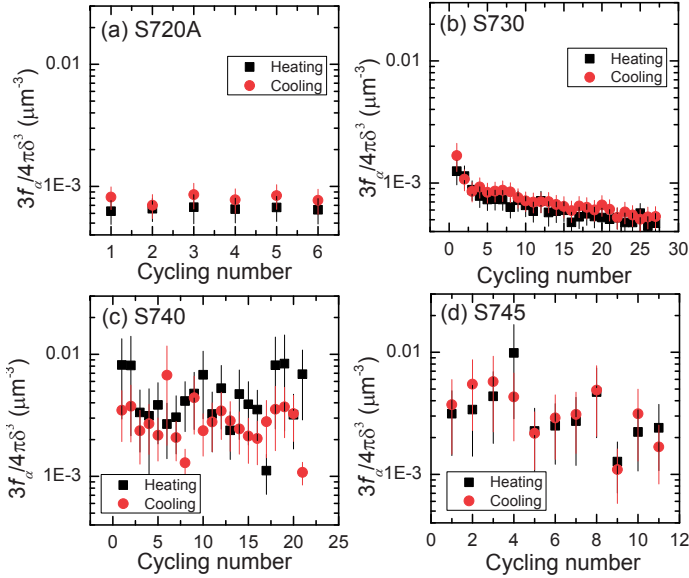


**Fig. 4.12.** Evolution of the number density of ferrite grains  $3f_\alpha/4\pi\delta^3$  as a function of the cycling number. The sample name indicates the average temperature during cycling with a temperature span of  $\Delta T = 20$  K.

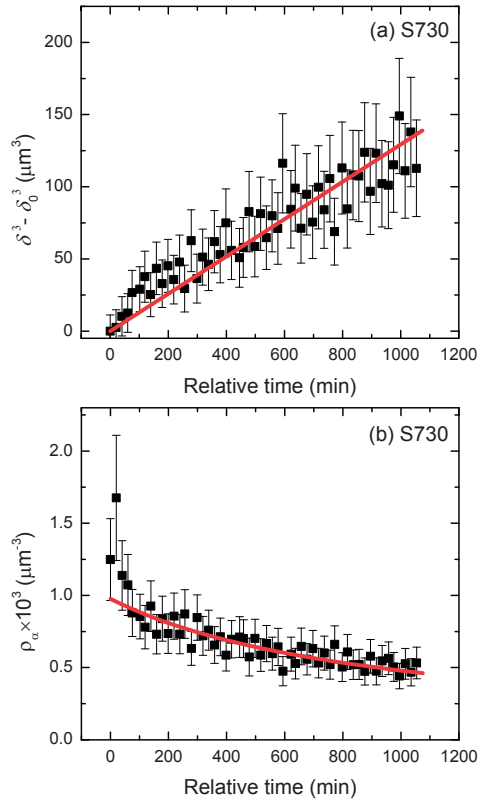


**Fig. 4.13.** (a) Evolution of  $\delta^3 - \delta_0^3$  ('0' denotes the starting moment of cycling) as a function of time  $t$ , showing a fit to  $\delta^3 - \delta_0^3 = kt$  with a slope of  $k = 0.129(4) \mu\text{m}^3\text{min}^{-1}$  for cycling between 993 and 1013 K (720 and 740 °C, S730). (b) The corresponding number of ferrite grain as a function of time  $t$ , which can be fitted to  $\rho_\alpha = \frac{\rho_0}{1+\beta t}$  with  $\rho_0 = 9.8(4)\times 10^{-4} \mu\text{m}^{-3}$  and  $\beta = 1.0(1)\times 10^{-4} \text{min}^{-1}$ .

**Table 4.4.** The average values of ferrite grain spacing  $\rho_\alpha^{-1/3}$ , relative degree of transformation  $(f_\alpha^{eq} - f_\alpha)/f_\alpha^{eq}$  and *bcc* iron bulk diffusivity  $D_{bulk}^{Fe,\alpha}$  and grain-boundary diffusivity  $D_{GB}^{Fe,\alpha}$  calculated according to [36].

Experiments	$\langle \rho_\alpha^{-1/3} \rangle$ ( $\mu\text{m}$ )	$\langle (f_\alpha^{eq} - f_\alpha)/f_\alpha^{eq} \rangle$ (-)	$\langle D_{bulk}^{Fe,\alpha} \rangle$ ( $\text{m}^2\text{s}^{-1}$ )	$\langle D_{GB}^{Fe,\alpha} \rangle$ ( $\text{m}^2\text{s}^{-1}$ )
S720A	11.1(9)	0.26	$1.25\times 10^{-17}$	$5.68\times 10^{-12}$
S730	9.5(7)	0.29	$1.77\times 10^{-17}$	$6.34\times 10^{-12}$
S740	6(2)	0.47	$2.51\times 10^{-17}$	$7.06\times 10^{-12}$
S745	6(2)	0.46	$2.97\times 10^{-17}$	$7.45\times 10^{-12}$

These parameters are now given in Table 4.4 for the cycling experiments. For cycling at the highest temperatures (S740 and S745) no considerable coarsening is found due to the large difference between the formed ferrite fraction and the equilibrium fraction ( $(f_{\alpha}^{eq} - f_{\alpha})/f_{\alpha}^{eq} > 0.45$ ), although the grain spacing is smaller. For cycling at the lowest temperatures (S720A) the reason for a negligible coarsening is probably due to the larger spacing between ferrite grains and a decrease in diffusivities at lower temperature, which slows down the coarsening kinetics.

#### 4.4.2. Interface migration during cycling

The partial cyclic approach, now experimentally proven to occur in the absence of new nucleation, provides a direct insight into the interaction between the interface migration and the substitutional elements. In the present 3DND study of Fe-0.25C-2.1Mn (wt.%), the interface migrates slowly back and forth with a net increase in both the ferrite fraction and the ferrite grain size over cycling. Ferrite is shown to be able to transform back from the austenite as a result of the diffusional flux balance of Mn between ferrite and austenite during each cycle, even though the ferrite fraction is far from equilibrium. This progressive migration into austenite over cycling, coupled with the cyclic interface migration, indicates that the migration of the interface is predominantly controlled by the Mn diffusion front that stays in contact with the moving interface. This situation differs from the cyclic behavior in Fe-0.023C-0.17Mn (wt.%) [11], where the interface can migrate by ‘cutting’ through the Mn diffusion spike and can leave that spike behind. The Mn diffusion spike in the present alloy always exists in the vicinity of the interface and its length scale is expected to be longer than the width of the interface. This interaction between the interface migration and Mn diffusion is controlled by three factors: i) the diffusivity of Mn in austenite  $D_{\gamma}^{Mn}$ , ii) the velocity of the interface  $v$ , iii) the interfacial concentrations. These three factors together control the length scale  $L$  of the Mn diffusion spike. In general,  $L$  can be expressed as [37]:

$$L = \frac{D_{Mn}}{v} / \frac{c_{Mn}^{\gamma*} - c_{Mn}^{\alpha*}}{c_{Mn}^{\gamma*} - c_{Mn}^{\alpha}}, \quad (4.6)$$

where  $c_{Mn}^{\alpha}$  is the nominal concentration of Mn. For isothermal transformations, Coates [38] showed that  $L = 2D/v$  and analyzed that interface migrates under LE condition for  $L > 5$  nm whilst the diffusion zone becomes part of the interface for  $L < 5$  nm. Hillert [39] similarly pointed out that the interfacial condition is close to LE for  $D/v > 10d$  where  $d$  is the atomic distance, whereas interface migrates under PE for  $D/v < 0.4d$ . As listed in Table 4.3 we calculated the average values of  $D_{\gamma}^{int}/v$  in the cycling stage, where

$D_{Mn}^{int} = \sqrt{D_{Mn}^{\alpha} D_{Mn}^{\gamma}}$  with  $D_{Mn}^{\alpha} = 0.756 \times 10^{-4} \exp(-224.5 \times 10^3/RT)$  and  $D_{Mn}^{\gamma} = 0.178 \times 10^{-4} \exp(-264 \times 10^3/RT)$  [40]. The calculated value of  $L$  obtained from Eq. 4.6 by assuming a LE interfacial condition is also given. The results suggest that the interface migrates most likely in an intermediate conditions between LE and PE for a cycling rate of  $1 \text{ Kmin}^{-1}$  according to the criteria proposed by Coates [38] and Hillert [39]. This is fully in line with the experimental behavior for  $f_{\alpha}$ , which according to the simulations shows a behavior between the LE and the PE conditions (see Fig. 4.10).

The present study shows that the cyclic interface migration is coupled with a net increase in both  $f_a$  and  $\delta$  over cycling. The intrinsic cyclic behavior is weakened and is difficult to capture independently unless these two effects could be decoupled. We attempted to decouple these two effects by subtracting the average for each heating and cooling part from the individual cycles. As shown in Fig. 4.14, the transformation curves for  $f_a - \langle f_a \rangle$  form a closed loop for each cycle. The loops overlap and therefore reproduce for different cycles. This suggests that the cyclic interface mobility can be analyzed in more detail after the effect of progressing migration into austenite is decoupled from the cyclic effect. In Fig. 4.14 we can now also observe a stagnant stage where the interface is quasi immobile [11]. The formation of this stage is mainly due to Mn partitioning. How this stagnant phase is affected by the cycling rate and concentrations of substitutional elements has been analyzed computationally in detail for low substitutional element concentrations in [41]. According to [41], the length of the stagnant stage (measured by temperature difference  $\Delta T$  where interface is immobile) may become very small or can even disappear for the low heating and cooling rates of  $1 \text{ Kmin}^{-1}$  used in the present study. For the current 2.1 wt.% Mn steel the length of the stagnant stage appears to be  $\Delta T = 6 \text{ K}$  and  $3 \text{ K}$  for cycling experiments between 983 and 1003 K (710 and 730 °C, S720A) and 993 and 1013 K (720 and 740 °C, S730), respectively. For cycling experiment between 1003 and 1023 K (730 and 750 °C, S740) shown in Fig. 4.14c, the interface migrates more sluggish at the lower temperatures than at the higher temperatures compared to the cycling experiments shown in Fig. 4.14a-b. The area of the loop gives an indication of how strong the Mn partitioning can drag the interface migration. As shown in [41], the area of the cyclic loop increases with increasing Mn concentrations for the same carbon content, and correspondingly, the length of the stagnant stage increases with additions of substitutional elements such as Mn, Ni and Si. A detailed physical description of the cyclic loop requires further study.

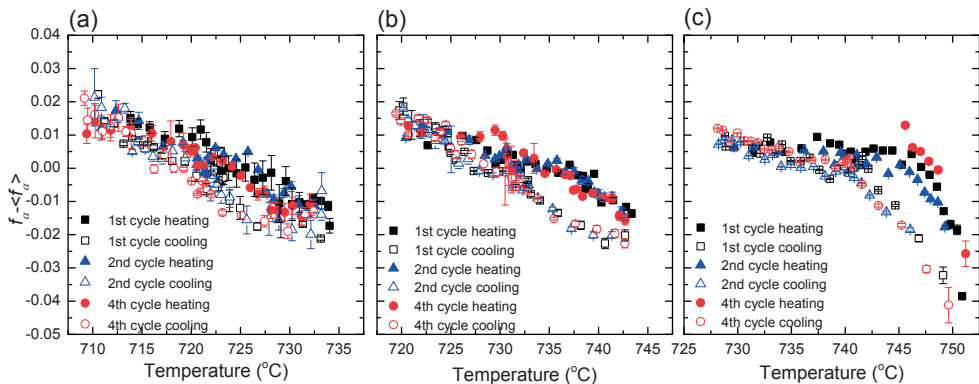


Fig. 4.14. Cyclic part of the ferrite phase fraction  $f_a - \langle f_a \rangle$  as a function of temperature for the first 4 cycles for (a) 983 and 1003 K (710 and 730 °C, S720A), (b) 993 and 1013 K (720 and 740 °C, S730) and (c) 1003 and 1023 K (730 and 750 °C, S740) at a cycling rate of  $1 \text{ Kmin}^{-1}$ .

It is widely accepted that the partitioning of substitutional elements like Mn could lead to a stagnant  $\gamma \rightarrow \alpha$  transformation upon switching from heating to cooling and *vice versa*. Modelling approaches that take into account the energy dissipation due to the trans-diffusion of substitutional elements inside the interface have been able to predict transformation stasis [5, 42-44]. However, as shown in the present study, the length scale of Mn diffusion spike can vary from 1 to 15 nm, which suggests that both the short-range and long-range diffusion of Mn play an important role in the slowing down of the interface migration. This provides a challenge to quantitatively address the effects of long-range Mn diffusion in the grain and local diffusion inside the interface. The concept of an effective interface mobility [13] may still remain a useful approach to account for the long-range of Mn diffusion together with the solute drag theory [44-46] to describe the energy dissipation due to the diffusion inside the interface.

My ongoing research suggests that the combination of the solute drag theory and my new 3D model for the evolution of the microstructure during the austenite-ferrite and ferrite-austenite transformation is capable of predicting the unique features as observed during cyclic partial transformations of C-Mn steels and to even predict their Mn-concentration dependence, without the need to make additional phenomenological assumptions. These early results still require a deeper and more extensive analysis and will be reported in a separate publication. They are therefore not included in this thesis.

#### 4.5. Conclusions

The evolution of the ferrite fraction and the ferrite grain size during slow partial cyclic austenite-ferrite phase transformations in Fe-0.25C-2.1Mn (wt.%) steel has been studied in detail with 3DND experiments. The number density of the ferrite grains was estimated and the results demonstrate that during cycling additional nucleation is proven to be negligible or even absent. Hence, the current work provides the experimental evidence that cyclic partial transformations indeed can yield direct information on the actual movement of the austenite-ferrite interface and can be free from the effects of simultaneous nucleation. During cycling, the austenite-ferrite interface migrates into the austenite region and back to the ferrite region in each cycle with a net increase in both ferrite fraction and ferrite grain size over multiple cycles; a feature which cannot be captured by 1D (or fixed geometry) simulations of interface mobility during solid state phase transformations. The interface migration velocity is of the order of  $10^{-3}$   $\mu\text{m/s}$  during cycling. This low value is attributed to Mn partitioning. The length of the Mn diffusion spike is estimated to be 1-15 nm, indicating a probable coexistence of short-range and long-range diffusion. The intrinsic cyclic behavior of the interface migration is visible after subtracting the effect of the progressive interfacial migration into austenite. The closing cyclic loops are reproducible and reveal a stagnant stage.

#### Acknowledgements

The authors are grateful to Dr. Astrid Perlade at Arcelor Mittal Marzières-lèts-Metz for providing the steel samples and Prof. Ekkes Brück for fruitful discussion. Haixing Fang acknowledges support by Hussein Farahani for providing access and guidance to

DICTRA software and the financial support provided by the China Scholarship Council (CSC).

## References

1. G. Purdy, J. Ågren, A. Borgenstam, Y. Bréchet, M. Enomoto, E. Gamsjager, M. Gouné, M. Hillert, C. Hutchinson, M. Militzer, H. Zurob, *ALEMI: Metall. Mater. Trans. A*, 2011, vol. 42, pp. 3703-18.
2. H.S. Zurob, C.R. Hutchinson, Y. Breché, H. Seyedrezai, G.R. Purdy: *Acta Mater.*, 2009, vol. 57, pp. 2781-92.
3. E. Novillo, D. Hernández, I. Gutiérrez, B. López: *Mater. Sci. Eng. A*, 2004, vol. 385, pp. 83-90.
4. A. Phillion, H.W. Zurob, C.R. Hutchinson, H. Guo, D.V. Malakhov, J. Nakano, G.R. Purdy: *Metall. Mater. Trans. A*, 2004, vol.35, pp. 1237-42.
5. H. Chen and S. van der Zwaag: *Acta Mater.*, 2014, vol. 72, pp. 1-12.
6. S.E. Offerman, N.H. van Dijk, J. Sietsma, S. Grigull, E.M. Lauridsen, L. Margulies, H.F. Poulsen, M.T. Rekveldt, S. van der Zwaag: *Science*, 2002, vol. 298, pp. 1003-5.
7. H. Guo, G.R. Purdy, M. Enomoto, H.I. Aaronson: *Metall. Mater. Trans. A*, 2006, vol. 37, pp. 1721-9.
8. Z.Q. Liu, G. Miyamoto, Z.G. Yang, T. Furuhashi: *Acta Mater.*, 2013, vol. 61, pp. 3120-9.
9. C.R. Hutchinson, A. Fuchsmann, Y. Bréchet: *Metall. Mater. Trans. A*, 2004, vol. 35, pp. 1211-21.
10. M. Gouné, F. Danoix, J. Ågren, Y. Bréchet, C.R. Hutchinson, M. Militzer, G. Purdy, S. van der Zwaag, H. Zurob: *Mater. Sci. Eng. R*, 2015, vol. 92, pp. 1-38.
11. H. Chen, B. Appolaire, S. van der Zwaag: *Acta Mater.*, 2011, vol. 59, pp. 6751-60.
12. H. Chen, S. van der Zwaag: *Metall. Mater. Trans. A*, 2017, vol. 48, pp. 2720-9.
13. E. Gamsjäger, M. Wiessner, S. Schider, H. Chen, S. van der Zwaag: *Phil. Mag.*, 2015, vol. 95, pp. 2899-917.
14. M. Segawa, A. Yamanaka, S. Nomoto: *Comp. Mater. Sci.*, 2017, vol. 136, pp. 67-75.
15. H. Chen, B. Zhu, M. Militzer: *Metall. Mater. Trans. A*, 2016, vol. 47, pp. 3873-81.
16. R. Rosman, M.T. Rekveldt: *Phys. Rev. B*, 1991, vol. 43, pp. 8437.
17. M.T. Rekveldt, N.H. van Dijk, S.V. Grigoriev, W.G. Bouwman: *Rev. Sci. Instr.*, 2006, vol. 77, pp. 073902.
18. S.G.E. te Velthuis, N.H. van Dijk, M.T. Rekveldt, J. Sietsma, S. van der Zwaag: *J. Appl. Phys.*, 2001, vol. 89, pp. 1275-80.
19. H. Fang, S. van der Zwaag, N.H. van Dijk: *Philos. Mag.*, 2018, vol. 98, pp. 1884-99.
20. S.G.E. te Velthuis, N.H. van Dijk, M.T. Rekveldt, J. Sietsma, S. van der Zwaag: *Acta Mater.*, 2000, vol. 48, pp. 1105-14.
21. S.E. Offerman, L.J.G.W. van Wilderen, N.H. van Dijk, M.T. Rekveldt, J. Sietsma, S. van der Zwaag: *Acta Mater.*, 2003, vol. 51, pp. 3927-38.
22. R. Rosman, M.T. Rekveldt: *J. Mag. Mag. Mater.*, 1991, vol.95, pp. 319-40.
23. A.S. Arrott and B. Heinrich: *J. Appl. Phys.*, 1981, vol. 52, pp. 2113-5.
24. S. Sakarya, N.H. van Dijk, E. Brück: *Phys. Rev. B*, 2005, vol. 71, pp. 174417.
25. M. Kumar, R. Sasikumar, P.K. Nair: *Acta Mater.*, 1998, vol. 46, pp. 6291-303.

26. H. Chen and S. van der Zwaag: *Comp. Mater. Sci.*, 2010, vol. 49, pp. 801-13.
27. J.R. Bradley and H.I. Aaronson: *Metall. Mater. Trans. A*, 1981, vol. 12, pp. 1729-41.
28. K. Oi, C. Lux, G.R. Purdy: *Acta Mater.*, 2000, vol. 48, pp. 2147-55.
29. C. Capdevila, J. Cornide, K. Tanaka, K. Nakanishi, E. Urones-Garrote: *Metall. Mater. Trans. A*, 2011, vol. 42, pp. 3719-28.
30. A. Borgenstam, L. Höglund, J. Ågren, A. Engström: *J. Phase Equil.*, 2000, vol. 21, pp. 269-80.
31. G.H. Zhang, R. Wei, M. Enomoto, D.W. Suh: *Metall. Mater. Trans. A*, 2012, vol. 43, pp. 833-42.
32. F. Danoix, X. Sauvage, D. Huin, L. Germain, M. Gouné: *Scrip. Mater.*, 2016, vol. 121, pp. 61-5.
33. J.M. Vitek, S.S. Babu., E. Kozeschnik: *Symposium on the thermodynamics, kinetics, characterization and modeling of austenite formation and decomposition, Materials Science and Technology Meeting*, 2003, pp. 139-48.
34. E. Cotrina, A. Iza-Mendia, B. López, I. Gutiérrez: *Metall. Mater. Trans. A*, 2004, vol. 35, pp. 93-102.
35. R. Bengochea, B. López, I. Gutiérrez: *Metall. Mater. Trans. A*, 1998, vol. 29, pp. 417-26.
36. H. Hänsel, L. Stratmann, H. Keller, H.J. Grabke: *Acta Metall.*, 1985, vol. 33, pp. 659-65.
37. J. Sietsma, S. van der Zwaag: *Acta Mater.*, 2004, vol. 52, pp. 4143-52.
38. D.E. Coates: *Metall. Mater. Trans. B*, 1972, vol. 3, pp. 1203-12.
39. M. Hillert: *Scripta Mater.*, 2002, vol. 46, pp. 447-53.
40. H. Oikawa: *Technol. Rep. Tohoku Univ.*, 1982, vol. 47, pp. 215-24.
41. H. Chen, M. Gouné, S. van der Zwaag: *Comp. Mater. Sci.*, 2012, vol. 55, pp. 34-43.
42. J. Odqvist, M. Hillert, J. Ågren: *Acta Mater.*, 2002, vol. 50, pp. 3213-27.
43. H.S. Zurob, D. Panahi, C.R. Hutchinson, Y. Brechet, G.R. Purdy: *Metall. Mater. Trans. A*, 2013, vol. 44, pp. 3456-71.
44. W.W. Sun, H.S. Zurob, C.R. Hutchinson: *Acta Mater.*, 2017, vol. 139, pp. 62-74.
45. G.R. Purdy, Y.J.M. Brechet: *Acta Metall. Mater.*, 1995, vol. 43, pp. 3763-74.
46. M. Hillert: *Acta Mater.*, 1999, vol. 47, pp. 4481-505.





---

# Chapter 5

## **Autonomous filling of creep cavities in Fe-Au alloys studied by synchrotron X-ray nano-tomography**

The autonomous filling of creep-loading induced grain-boundary cavities by gold-rich precipitates at a temperature of 550 °C has been studied as a function of the applied load for Fe-Au alloys using synchrotron X-ray nano-tomography. The alloy serves as a model alloy for future self-healing creep resistant steels. The size, shape and spatial distribution of cavities and precipitates are analyzed quantitatively in 3D at a nanometer resolution scale. The filling ratios for individual cavities are determined and thus a map of the filling ratio evolution is obtained. It is found that the gold-rich precipitates only form at cavity surfaces and thereby repair the creep cavity. The shape of the cavities changes from equiaxed to planar crack like morphologies as the cavities grow. The time evolution of the filling ratio is explained by a simple model considering isolated cavities as well as linked cavities. The model predictions are in good agreement with the measurements.

## 5.1. Introduction

Creep damage in steels occurs during long-term use at high temperatures and arises from the nucleation, growth and coalescence of grain-boundary cavities, which ultimately leads to catastrophic failure of the entire structure [1-2]. To date, most strategies [3-6] have aimed to tune the composition and microstructures of creep-resistant steels in such a way that the formation of creep damage is postponed, if not avoided. In the last two decades an alternative strategy has been explored to extend the lifetime of materials and structures via their ability to self-heal the early damage by the material themselves [7]. By now, this approach has been demonstrated to significantly enhance the component lifetime for a wide range of materials, including polymers, concrete, composite materials, aluminum alloys and steels [8-10].

Restricting the development of self healing materials to that of self healing metals, Laha and coworkers [11-13] observed a significant increase in creep lifetime in Cu and B enriched austenitic stainless steels, which was attributed to the healing of creep damage due to dynamic precipitation of either Cu or BN at the creep cavity surface. However, in more recent studies [14-15] on Fe-Cu and Fe-Cu-B-N model alloys, it was found that Cu precipitates do not only form in the grain boundaries, but to a larger extent also throughout the matrix. In order to enhance the defect-induced precipitation, while suppressing the undesired precipitation in the matrix at the same time, a high nucleation energy barrier for precipitation in the matrix and a strong driving force for segregation to cavity surface is required. Previous studies [16-17] showed that Au atoms in Fe-Au alloys have a strong preference to segregate and combine with Fe atoms to form Au-rich precipitates. This makes Au an excellent healing agent for the creep damage in ferrous alloys. Fe-Au alloys are therefore an ideal model system to study the self healing of creep damage. A detailed understanding will provide essential input to design future self-healing creep resistant steels. Extensive research [18-19] has been carried out subsequently to investigate the autonomous repair mechanism of the Fe-Au alloys during creep. Scanning electron microscopy (SEM) and X-ray photoelectron spectroscopy (XPS) observations confirmed the strong tendency of Au atoms to segregate on a free surface. Transmission electron microscopy (TEM) and small-angle neutron scattering (SANS) identified that the gold precipitation was induced and accelerated by the defects in the Fe-Au alloys. Electron probe micro-analysis (EPMA) and atom probe tomography (APT) quantified the local chemical compositions and thus indicated the diffusion pathways of Au atoms. However, all these measurements were limited to characterization of two-dimensional (2D) cross sections or a small three-dimensional (3D) region with a length size of several nanometers. In order to build a more comprehensive understanding of the repair mechanism of creep damage in Fe-Au alloys, the 3D microstructure needs to be resolved and studied at both nanometer and micrometer length scales.

Synchrotron X-ray tomography has developed into a powerful 3D imaging technique for non-invasive characterization of materials [20,21]. The high penetration power, high spatial resolution, as well as the multiple-contrast mechanisms make it an appealing method for the study of internal structures in metals. It has been employed

for investigating the size and shape of phases in metals such as aluminum alloys [22-24] and steels [25-26].

In the present study, synchrotron X-ray holotomography with a voxel size down to 25 nm was successfully employed to resolve the 3D structure of un-healed and healed creep damage in an Fe-Au (1 at.% Au) alloy. We determined and analyzed the size, shape and spatial distribution of the cavities and precipitates in creep-failed samples submitted to creep at various constant loads and a fixed temperature of 550 °C. From this we derived a model for the creep cavity filling and obtained a better insight in the mechanisms responsible for the formation and healing of creep cavities.

## 5.2. Materials and methods

### 5.2.1. Sample preparation and creep tests

The chemical composition of the Fe-Au alloy studied is listed in Table 5.1. The rolled sheet material was produced by Goodfellow. Miniature tensile test samples with a conventional dog-bone shape (a gauge length of 12.5 mm, a width of 6 mm and a thickness of 0.5 mm) were machined by spark erosion. These samples were then annealed at 868 °C for 5 h in an evacuated and sealed quartz tube filled with 200 mbar ultra-high purity argon and quenched in water. Subsequently, creep tests were carried out in vacuum on the as-quenched samples at a temperature of 550 °C and constant loads corresponding to initial stress levels of 60, 80, 100 and 117 MPa [18-19]. Bar-shaped samples with a square cross section of 200×200  $\mu\text{m}^2$  and a length of around 6 mm were cut by spark erosion from the uniform gauge section of the creep-failed samples for tomography experiments. The long axis of the bar-shaped samples was aligned with the stress axis in the creep experiments. The sample was taken such that the region to be characterized was between 2 and 4 mm away from the fracture surface. In addition to the X-ray tomography, the 2D microstructure of the samples was analyzed by a scanning electron microscope (JEOL JSM 6500F) equipped with an Autrata back-scattered electron detector. A detailed 2D characterization of the microstructure of these samples by electron microscopy and atom-probe tomography has been reported previously [18-19].

Table 5.1. The chemical composition of the Fe-Au alloy sample (wt.%).

Au	B	N	C	Ce	Fe
2.87	< 0.01	0.0085	0.0008	0.015	balanced

### 5.2.2. Synchrotron X-ray nano-tomography

For the morphological study of both the nano and micro-scale structures in the Fe-Au alloys, synchrotron hard X-ray tomography based on phase contrast with high spatial resolution was adopted. Holotomography measurements of the samples were conducted at the ID16A-NI nano-imaging beamline of the European Synchrotron

Radiation Facility (ESRF) in Grenoble, France [27]. This new beamline offers a unique combination of nanofocus ( $\approx 20$  nm) and a very high photon flux (up to  $10^{12}$  photons/s at  $\Delta E/E \approx 1\%$ ). Two pairs of multilayer coated Kirkpatrick-Baez (KB) optics are used to focus the X-rays at 17 and 33.6 keV, respectively. The higher energy of 33.6 keV was chosen in this experiment to optimize the transmission through the samples. Besides the benefits of the ability to perform nano-tomography with a high energy, the magnifying geometry of the cone beam also allows the switch between a large field of view (FOV) with 100 nm voxel size, and a finer FOV at a voxel size of 25 nm.

Due to the free space propagation of the X-ray beam the contrast in the images is dominated by phase contrast, related to the real part of the complex refractive index, which is determined by the electron density of the material. By measuring the Fresnel diffraction patterns at different effective propagation distances, the phase maps of the sample can be retrieved via holographic reconstruction, the so called phase retrieval procedure [28] implemented using GNU Octave software.

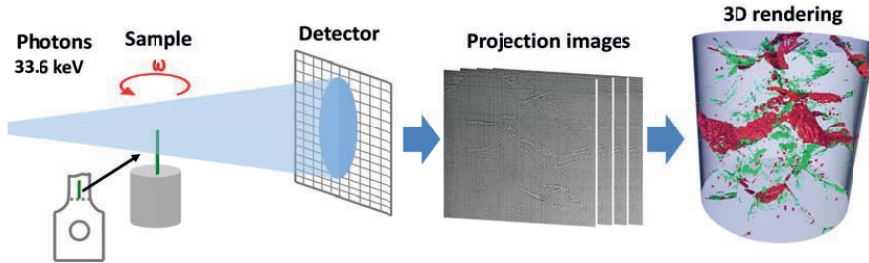


**Fig. 5.1.** Schematic diagram of the synchrotron X-ray holotomography imaging process. In the 3D rendering the precipitates and cavities are labelled in green and red, respectively, while the iron matrix is in transparent light grey.

As shown in Fig. 5.1, the bar-shaped sample was mounted on the rotation stage of the tomography setup. During the scan, it was placed downstream of the KB focus and magnified radiographs were recorded onto an X-ray detector using a FReLoN charged-coupled device (CCD) with a  $2048 \times 2048$  binned pixels array. For one tomography scan, 1500 projections were acquired with an exposure time of 1.00 s for a resolution of 100 nm and 1.25 s for the higher resolutions of 25 and 50 nm. Tomographies at four different focus-to-sample distances were acquired to complete one holotomography scan, which were subsequently used for phase retrieval. The 2D phase maps retrieved from the angular projections were then used as input for a tomographic reconstruction based on the filtered back projection (FBP) algorithm method (ESRF PyHST software package) [29]. The reconstructed 3D volumes were visualized and rendered with 3D visualization software Avizo 8.1 (FEI).

The phases present in the creep-failed samples have previously been characterized as: (i) the Fe-Au alloy matrix (with a *bcc* structure), (ii) empty creep

cavities and (iii) Au-rich precipitates (containing 80 at.% Au and 20 at.% Fe) [19]. In the present study, only the creep cavities and gold precipitates are of interest because they directly affect the self-healing of creep damage by site-selective precipitation of Au-rich precipitates at the creep cavity surface. Since the electron density of Au is much higher than that of Fe and that of vacuum is much smaller than that of Fe, the contrast difference between an empty cavity and an Au-rich precipitate is very large. Hence we can clearly recognize the Au-rich precipitates as dark features and creep cavities as bright features. Both the precipitates and the creep cavities can be segmented by applying a threshold value for the local density variations (grey scale) in the 3D image. It should be noted that the quality of the segmentation strongly depends on the threshold value. The value was extensively tested to achieve an optimal contrast for the precipitates and the creep cavities. The segmentation provided binary images of the precipitate and the creep cavities for further analysis. In order to study the filling mechanism of the creep cavities in more detail we not only identified cavities and gold precipitates, but also determined the degree of pore filling by examining the co-location of pores and precipitates.

### 5.2.3. Data analysis

A quantitative analysis of both the creep cavities and the Au-rich precipitates, identified in the binary images, was performed using a MATLAB program with the DIPImage toolbox [30]. The shape of the objects can be characterized by several parameters. The shape complexity  $\Omega_d$  (where  $d$  is the dimensionality of the object) is a dimensionless parameter in which the surface area of the object  $A$  is normalized by the surface area of a sphere with the same volume as the object  $V$  [31]. This parameter quantifies the irregularity of the shape. For three-dimensional objects ( $d = 3$ ), the complexity corresponds to:

$$\Omega_3 \equiv \frac{A}{\pi^{1/3}(6V)^{2/3}}. \quad (5.1)$$

The value of the shape complexity varies between  $\Omega_3 = 1$  for a sphere and  $\Omega_3 \rightarrow \infty$  for objects with a finite area  $A$  and a negligible volume ( $V \rightarrow 0$ ). The reciprocal value of the three-dimensional shape complexity is also known as the sphericity  $\Psi = 1/\Omega_3$  (where  $0 \leq \Psi \leq 1$ ) [32].

An additional shape characterization is obtained by approximating the shape of the object by an equivalent ellipsoid with the same moment of inertia as the real object [33]. Assuming the composition of the particle to be uniform, the semi-axes of the ellipsoid  $a_j$  can be determined from the eigenvalues of  $I_j$  of the moment of inertia tensor  $\mathbf{I}$ :

$$a_j = \sqrt{\frac{5(\text{Tr}(\mathbf{I}) - 2I_j)}{2V}}, \quad j = 1, 2, 3 \quad (5.2)$$

where  $\text{Tr}(\mathbf{I}) = I_{11} + I_{22} + I_{33}$  is the sum of the elements along the main diagonal of the moment of inertia tensor  $\mathbf{I}$ . The corresponding eigenvectors  $\mathbf{B}_j$  representing the spatial

orientation of the semi-axes can be calculated by solving  $(\mathbf{I} - a_j \mathbf{1})\mathbf{B}_j = \mathbf{0}$ , where  $\mathbf{1}$  is the unit matrix. In the present work the major, intermediate and minor semi-axes ( $a_j$ ) are expressed as  $a$ ,  $b$  and  $c$ , respectively. Using these parameters the elongation  $E$  and flatness  $F$  are defined as [34]:

$$E = \frac{2a}{b+c}, \quad (5.3)$$

$$F = \frac{b}{c}. \quad (5.4)$$

For a sphere all axes are equal ( $a = b = c$ ), resulting in an elongation of  $E = 1$  and a flatness of  $F = 1$ . For a rod-shaped ellipsoid of revolution ( $b = c$ ) with one long axis ( $a$ ) one finds  $E = a/c$  and  $F = 1$ , while for a sheet-shaped ellipsoid of revolution ( $a = b$ ) with one short axis ( $c$ ) one finds  $E = 2a/(a+c)$  and  $F = a/c$  (and thus  $E = 2F/(F+1)$ ).

It is found that the combination of the complexity  $\Omega_3$ , the elongation  $E$  and the flatness  $F$  provides an unambiguous quantitative approach to monitor the morphologic evolution of both the creep cavities and the precipitates. Based on these three combined descriptors the shape of both the cavities and the precipitates are classified as: (1) spheres, (2) equiaxed shapes, (3) rods, (4) sheets and (5) complex objects.

In order to determine the filling ratio of the creep cavities (*i.e.* the volume of connected Au precipitation over the volume of the original creep cavity) it is necessary to check for each open cavity how many precipitates are in direct contact with it and to determine the location of outer boundary of the pore-precipitate ensemble with the Fe-rich matrix. This was performed by dilating the particles by a predefined number of pixels in orthogonal directions and identifying the intersection. In this way, for each cavity the filling ratio ( $FR$ ) by precipitation can be calculated:

$$FR = \frac{V_{precipitate}}{V_{cavity} + V_{precipitate}}, \quad (5.5)$$

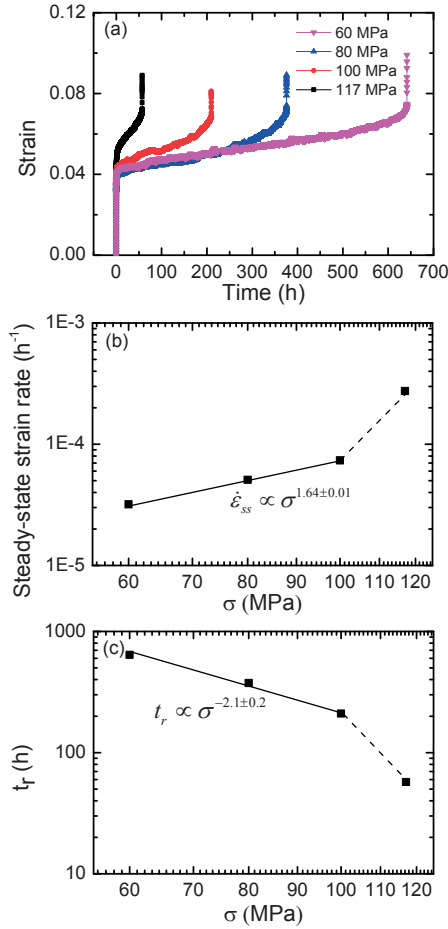
where  $V_{precipitate}$  is the total volume of precipitates in contact with the cavity and  $V_{cavity}$  is the volume of the open cavity.

## 5.3. Results

### 5.3.1. Creep behavior and electron microscopy

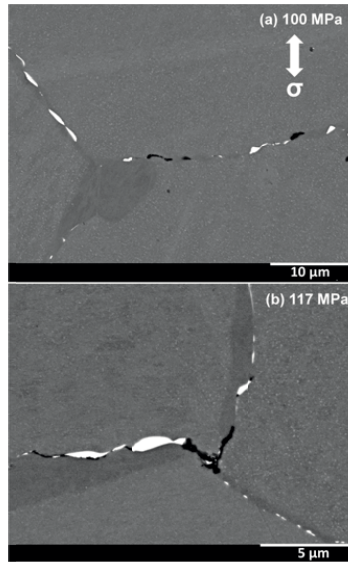
The strain-time curves of the Fe-Au samples under different loads are shown in Fig. 5.2a and the derived stress dependent steady-state strain rate and rupture time are given in Fig. 5.2b and Fig. 5.2c, respectively [18-19]. All creep curves show the usual rapid strain increase in the initial stage (stage I) followed by a stage with an approximately constant strain rate (stage II) before the strain accelerated in the failure regime (stage III). The creep failure strain is about 0.10 for all samples. The creep lifetime is mainly controlled by the steady-state strain rate  $\dot{\epsilon}_{ss}$  in the secondary stage. It is found that  $\dot{\epsilon}_{ss}$  depends on the applied stress and fulfills a Sherby-Dorn

relationship [35] with  $\dot{\epsilon}_{ss} \propto \sigma^{1.64}$  in the low stress region ( $\leq 100$  MPa), while at a higher stress the stress exponent increases. This low stress exponent suggests the creep deformation is controlled by the combination of diffusion and dislocation motion [36]. The stress exponent for the lifetime is derived to be about -2 and becomes more negative at the highest stress. The change in the stress exponent of both the steady-state strain rate and the lifetime for a stress above 100 MPa suggests that there is a different creep mechanism at higher stresses.



**Fig. 5.2.** (a) Creep curves of the Fe-Au samples creep loaded at 550 °C and 60, 80, 100 and 117 MPa and the derived stress dependence of (b) the steady-state strain rate and (c) the rupture time [18-19].





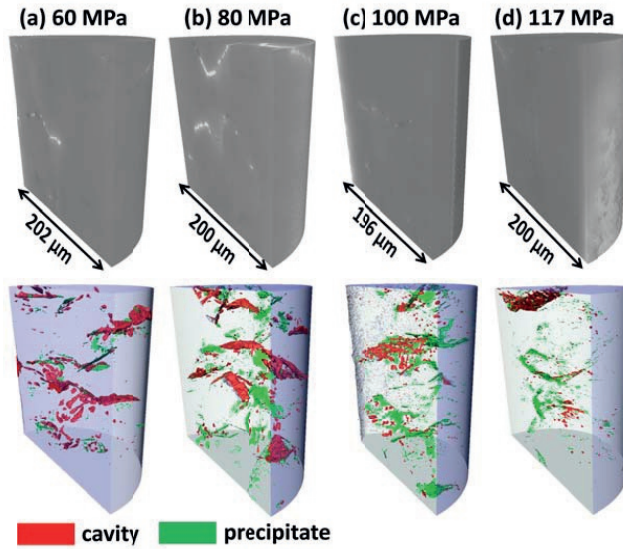
**Fig. 5.3.** Back-scattered scanning electron microscopy images of the Fe-Au alloy after creep at a temperature of 550 °C and a stress of (a) 100 MPa and (b) 117 MPa. Note that the white features are gold precipitates and the black features are creep cavities. The direction of the applied stress is indicated in (a).

Fig. 5.3 shows back-scattered SEM images of 2D cross-sections for the Fe-Au alloy samples after creep at a temperature of 550 °C and a stress of 100 and 117 MPa, respectively. White features are gold precipitates and black features are creep cavities. It can be seen in Fig. 5.3a and 5.3b that the gold precipitates are formed inside the grain-boundary cavities and have an irregular shape that matches the morphology of the creep cavities. Fully filled cavities are observed along inclined grain boundaries, as shown in Fig. 5.3a. Partially filled cavities along grain boundaries that are oriented perpendicular to the applied stress are found in both Fig. 5.3a and 5.3b. Fig. 5.3b also shows an unfilled cavity at a grain-boundary junction. Gold depletion zones are indicated by darker regions in Fig. 5.3 and form close to the grain boundaries where gold precipitates have formed. More details of the 2D characterization of the microstructure can be found in [18-19]. As these observations are limited to 2D images it is difficult to establish how the cavity is filled by gold precipitation.

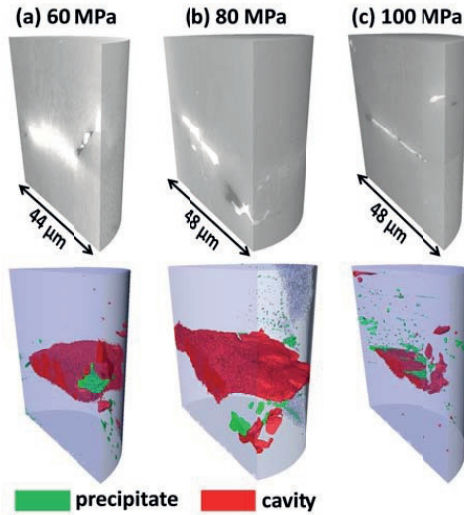
### 5.3.2. Tomographic rendering

Fig. 5.4 shows the 3D tomographic renderings with a voxel size of 100 nm for the four creep-loaded samples. For these lower resolution imaging settings, the minimum size of identified cavities and precipitates is 0.3 μm (3 times the 100 nm voxel size). Objects with a smaller size are regarded as noise and ignored. It is shown in Fig. 5.4 that the spatial distribution of cavities and precipitates is heterogeneous. Most of the cavities are close to precipitates except for some small ones. The precipitates range

from small isolated spherical or equiaxed particles to large coalesced objects with complicated shapes that follow the profile of the cavities. The big cavities are approximately oriented perpendicular to the stress direction. As the field of view (FOV) is around 200  $\mu\text{m}$  high with a transverse cross section of  $200 \times 200 \mu\text{m}^2$ , the probed 3D volume contains about 60 grains for an average grain size of  $57 \pm 8 \mu\text{m}$ . This indicates that the dataset with a voxel size of 100 nm provides meaningful quantitative statistics.



**Fig. 5.4.** Overview of the 3D tomographic renderings before (upper part) and after (bottom part) phase segmentation with a voxel size of 100 nm for samples after creep at a temperature of 550  $^{\circ}\text{C}$  and a load of (a) 60 MPa, (b) 80 MPa, (c) 100 MPa and (d) 117 MPa. The applied stress is along the vertical direction.



**Fig. 5.5.** Overview of the 3D tomographic renderings before (upper part) and after (bottom part) phase segmentation with a voxel size of 25 nm for samples after creep at a temperature of 550 °C and a load of (a) 60 MPa, (b) 80 MPa and (c) 100 MPa. The applied stress is along the vertical direction.

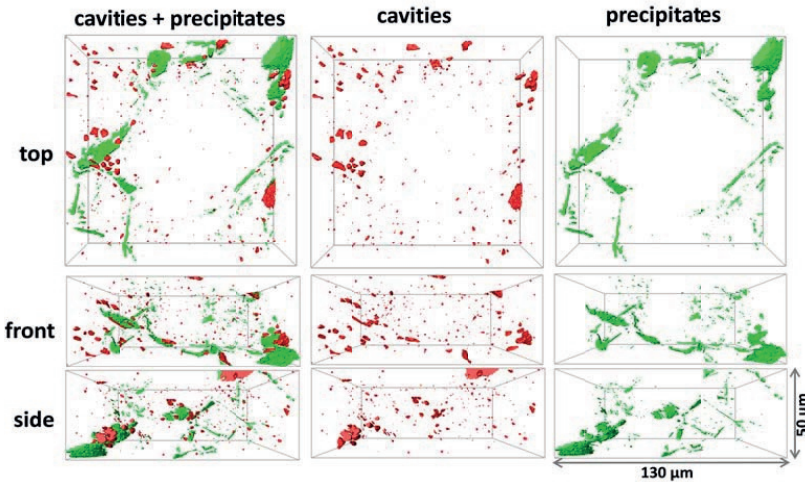


**Fig. 5.6.** A ROI with a size of  $130 \times 130 \times 50 \mu\text{m}^3$  revealing the microstructure of the Fe-Au alloy after creep failure at 550 °C and 80 MPa. The applied stress is normal to the top view.

Of particular interest are also the details of large transverse grain boundary cavities shown in Fig. 5.5 recorded with the smaller voxel of 25 nm. At the lower loads, *i.e.*, for the longer failure times, the grain boundary cavity has enough time to grow

and ultimately covers an entire grain-boundary facet. The figure also shows that parts of the grain-boundary cavity surfaces are covered by precipitates. As the smallest characterized particle size is 75 nm (3 times the 25 nm voxel size), we can probe the early growth stage of the cavities and the centers of these small particles could be regarded as nucleation sites. The average spacing between the smallest cavities is estimated to be around 4  $\mu\text{m}$ .

To better understand the spatial distribution of the cavities and precipitates, the region of interest (ROI) shown in Fig. 5.6 is extracted from the creep-failed sample at 80 MPa and 550 °C (see in the Supplementary Material Fig. S5.1-S5.3 for the results at a stress of 60, 100 and 117 MPa and movie S4 for a 3D angular view on the results for a stress of 80 MPa). By projecting this microstructure from different angles, it is found that the positions of the precipitates clearly delineate the grain boundaries as shown best in the top view. This is in agreement with the previous SEM studies which showed that the precipitates in the Fe-Au alloy are formed exclusively at grain boundaries and at pre-formed cavities [18-19]. With the grain boundary positions identified, it is found that most of cavities are indeed located on the grain boundaries, while some small cavities appear in the matrix. This suggests that not all cavities nucleate on the grain boundary. However, only the grain boundary cavities are able to grow into larger sizes. Fig. 5.6 also reveals that the particles formed at different locations have different shapes: particles dispersively distributed on the grain boundaries and within the matrix are mainly spherical or equiaxed; particles on the inclined grain boundaries are more elongated or flattened, while particles located on the grain junctions have a relatively complicated shape.

### 5.3.3. Shape classification of cavities and precipitates

In order to understand the fine details of the healing reaction and the interaction between damage formation and cavity filling, the particles morphologies as determined by tomography are based on their elongation  $E$ , flatness ( $F$ ) and complexity values ( $\Omega_3$ ) classified in 5 categories: (a) spherical, (b) equiaxed, (c) rods, (d) sheets and (e) complex shapes. The criteria for the classifications are listed in Table 5.2. In Fig. 5.7 examples are shown for the classified cavity and precipitate shapes (with their particle volume).

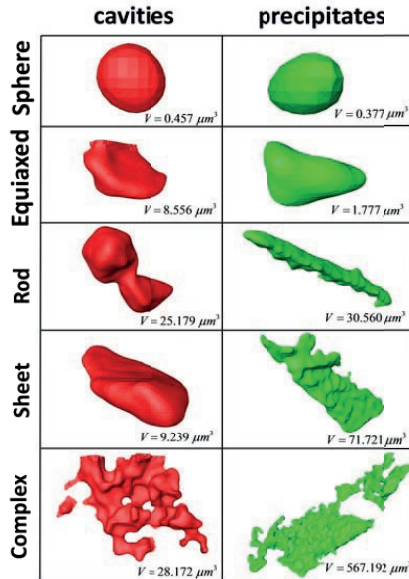


**Fig. 5.7.** Examples of classified cavity and precipitate shapes for the Fe-Au alloy after creep at 550 °C and 80 MPa (top view projections extracted from Fig. 5.6). The particle volumes are also indicated.

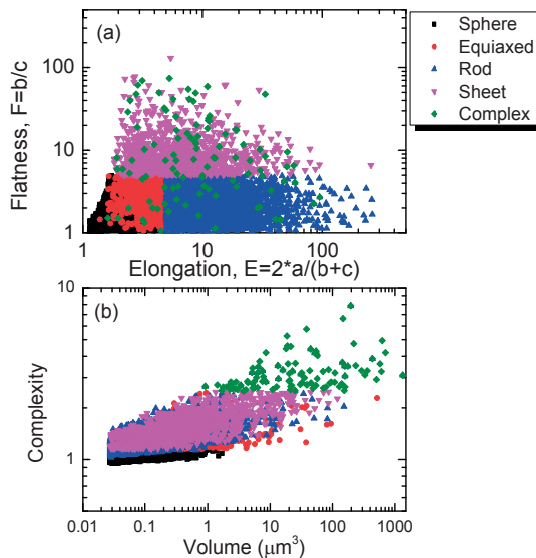


**Fig. 5.8.** (a) Flatness  $F$  as a function of the elongation  $E$  and (b) the complexity as a function of the particle volume for 8139 precipitates identified from the probed volume of the Fe-Au alloy after creep at 550 °C and 80 MPa.

**Table 5.2.** Classifications of different shapes based on the elongation ( $E$ ), flatness ( $F$ ) and complexity ( $\Omega_3$ ) of the objects.

	$E$	$F$	$\Omega_3$
Sphere	-	-	$\Omega_3 \leq 1.15$
Equiaxed	$< 5$	$< 5$	$1.15 < \Omega_3 < 2.5$
Rod	$\geq 5$	$< 5$	$1.15 < \Omega_3 < 2.5$
Sheet	-	$\geq 5$	$1.15 < \Omega_3 < 2.5$
Complex	-	-	$\Omega_3 \geq 2.5$

Fig. 5.8a and 5.8b respectively show the flatness versus the elongation and the complexity as a function of the volume for over 8000 individual precipitates in the sample loaded at 80 MPa. In Fig. 5.8a the spherical particles occupy the left bottom corner, as they are characterized by  $F \approx E \approx 1$ . Next are the equiaxed particles which show slightly higher, yet comparable values of  $E$  and  $F$ . The rod-like particles are more elongated, while the sheet particles are more flattened. Therefore, the rod-like particles are located in the right bottom region while the sheet-like particles are located in the top region in Fig. 5.8a. The complex particles are distinguished by their complexity ( $\Omega_3$ ) and as can be seen in Fig. 5.8a they may have a more randomly relationship between  $E$  and  $F$ . In Fig. 5.8b the spherical particles with the lowest  $\Omega_3$  have small volumes, the complex ones have large volumes, while the equiaxed, rod and sheet types fall in between. For the precipitate population of other samples a similar behavior was observed. This demonstrates that the proposed classification is a reliable way to identify different types of particles.

### 5.3.4. Size distribution

Fig. 5.9a and 5.9b show the number distribution  $D_N$  versus the equivalent diameter for the cavities and the precipitates, respectively. The corresponding volume distributions  $D_V$  are shown in Fig. 5.9c and 5.9d. The equivalent particle diameter (EqDiameter)  $d$  is the diameter of a sphere with the same volume as the particle. As shown in Fig. 5.9a and 5.9b, the number distribution of the cavities and precipitates can be fitted to a log-normal distribution:

$$D_N(d) = \frac{N_0}{dw\sqrt{2\pi}} \exp\left(-\frac{\{\ln(d) - \ln(\bar{d})\}^2}{2w^2}\right), \quad (5.6)$$

where  $N_0$  is the number density,  $\bar{d}$  the mean value and  $w$  the relative distribution width of the equivalent diameter. The fitted values are listed in Table 5.3.

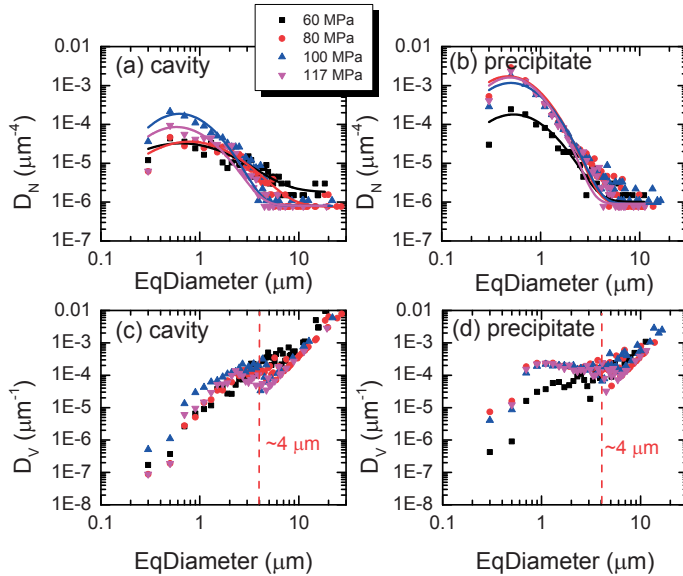


**Fig. 5.9.** Number distribution  $D_N$  of (a) cavities and (b) precipitates and the volume distribution  $D_V$  of (c) cavities and (d) precipitates as a function of the equivalent diameter  $d$  for the Fe-Au alloy after creep at 550 °C. The data points are tomographic result with a voxel size of 100 nm per voxel and the solid curves are the log-normal fittings.

**Table 5.3.** Fitted parameters  $N_0$ ,  $\bar{d}$  and  $w$  for the log-normal size distribution of cavities and precipitates after creep at an applied stress of  $\sigma = 60, 80, 100$  and  $117$  MPa. In between brackets is the error in the last digit. The volume fraction  $f_V$  is obtained directly from the 3D tomographic volumes.

Phase	$\sigma$ (MPa)	$N_0$ ( $\mu\text{m}^{-3}$ )	$\bar{d}$ ( $\mu\text{m}$ )	$w$	$f_V$ (%)
Cavities	60	$7.0(5) \times 10^{-5}$	1.5(1)	0.92(8)	0.64
	80	$7.6(3) \times 10^{-5}$	1.50(6)	0.80(3)	0.76
	100	$1.94(6) \times 10^{-4}$	0.86(2)	0.57(2)	0.24
	117	$9.2(5) \times 10^{-5}$	0.85(4)	0.62(4)	0.11
Precipitates	60	$1.7(1) \times 10^{-4}$	0.76(4)	0.60(5)	0.098
	80	$1.3(1) \times 10^{-3}$	0.63(4)	0.54(6)	0.24
	100	$9.3(6) \times 10^{-4}$	0.67(3)	0.55(4)	0.35
	117	$1.11(7) \times 10^{-3}$	0.63(3)	0.50(4)	0.14

The fits indicate that the average diameter  $\bar{d}$  of the cavities is about 1.50  $\mu\text{m}$  for the samples loaded at 60 and 80 MPa and about 0.85  $\mu\text{m}$  for the samples loaded at 100 and 117 MPa. The width of the cavity size distribution increases with decreasing applied stress, as indicated by the  $w$  value reported in Table 5.3. As the average growth time is increased with increasing lifetime (*i.e.* decreasing applied stress), the coalescence of cavities is more enhanced at low stresses. The coarsening of the cavities in the later creep stages could occur by merging small cavities, which leads to both a decrease of the cavity number and an increase of the cavity size. In Table 5.3 it is indicated that the number density of cavities in the samples loaded at 60 and 80 MPa is smaller than at 100 and 117 MPa. For precipitates both  $\bar{d}$  and  $w$  remain nearly constant, except for the sample loaded at 60 MPa, which has a slightly larger  $\bar{d}$  value. This is mainly attributed to the fact that there are much fewer spherical precipitates in the sample loaded at 60 MPa compared to the other samples. As there are more coalesced cavities in the sample loaded at 60 MPa, the precipitates grow continuously at the large cavity surface with less chance to nucleate at small cavities, which leads to much less spherical precipitates and a greater value of  $\bar{d}$ .

The volume distributions  $D_V$  of both cavities and precipitates show two different regions with a cross-over around  $d \approx 4 \mu\text{m}$ , as shown in Fig. 5.9c and 5.9d. This value is similar to the average spacing between cavities derived from Fig. 5.5. When  $d < 4 \mu\text{m}$ , the cavities and precipitates show a peak in  $D_V$  around 2.2 and 1.5  $\mu\text{m}$ , respectively. In contrast, when  $d > 4 \mu\text{m}$ , the particles are more likely to have coalesced to form large volume objects, resulting in a continuous increase in  $D_V$ .

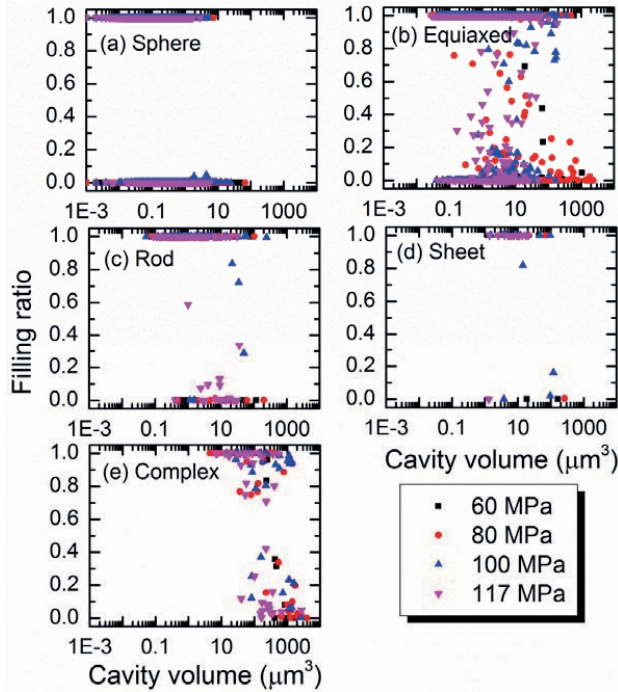
### 5.3.5. Filling ratio of the creep cavities

Fig. 5.10 shows the degree of filling for each creep cavity as a function of their volume for the four different applied stress levels. The obtained filling ratios (defined in Eq. 5.5) are presented with a subdivision into the identified shape types. Unfilled cavities correspond to  $FR = 0$ , completely filled cavities to  $FR = 1$  and partially filled cavities to  $0 < FR < 1$ . The resolution limit for the volume in the determination of the filling ratio corresponds to 5 times the resolution ( $V_{min} = (5 \times 0.1 \mu\text{m})^3 = 0.125 \mu\text{m}^3$ ). Therefore, for all cavities or precipitates smaller than  $0.1 \mu\text{m}^3$  the filling ratio can only be 0 or 1.

Fig. 5.10a shows that the spherical cavities ( $n = 1474$ ) span the volume range of  $10^{-3}$  to  $100 \mu\text{m}^3$ , while the spherical precipitates ( $n = 9690$ ) span the volume range  $10^{-3}$  to  $10 \mu\text{m}^3$ . This suggests that cavities form prior to the precipitates, which supports the viewpoint that the precipitates are induced by the cavities. Somewhat surprisingly, no partially filled spherical cavities were observed. In the case of equiaxed cavities ( $n = 591$ ) and precipitates ( $n = 1779$ ), the largest volume of such an (unfilled) cavity was  $3000 \mu\text{m}^3$ , while that of the largest fully filled precipitate was  $800 \mu\text{m}^3$ . Again, the largest cavity volume well exceeded the largest precipitate volume. Unlike the case of the well-defined spherical particles, in the case of equiaxed particles partial filling was frequently observed ( $n = 249$ ) over the volume range of 0.1 to  $100 \mu\text{m}^3$ . Partial filling was particularly obvious for the sample tested at the highest load level. Low level



partial filling of the largest cavities was manifest for the sample loaded at a stress of 80 MPa.



**Fig. 5.10.** Filling ratio of individual creep cavities as a function of the cavity volume in the Fe-Au alloy after creep at a temperature of 550 °C and a load of 60, 80, 100 and 117 MPa classified into: (a) spherical cavities, (b) equiaxed cavities, (c) rod-like shaped cavities, (d) sheet-shaped cavities and (e) complex cavities. The cavities were identified from the data obtained for a voxel size of 100 nm.

In the case of rod-like cavities ( $n = 26$ ) and precipitates ( $n = 336$ ) (Fig. 5.10c), the maximum size of the cavities and that of the precipitates are about equal. Furthermore, the fraction of partially filled (large) cavities is very low. This suggests that rod like cavities remain empty for a relatively long time, but once the deposition process has been triggered the filling of the cavities proceeds rather quickly. A similar conclusion can be drawn in the case of sheet like cavities (Fig. 5.10d), which occurred less frequently ( $n = 45$ ). In this case most of the sheet structures are fully filled ( $n = 38$ ), which is not surprising if the nucleation density of a gold-rich precipitate is surface area determined.

Finally, Fig. 5.10e shows the filling fractions for complex shaped cavities. The figure shows that such (relatively large) defects occur primarily at higher stress levels. At a nominal stress level of 80 MPa all such cavities are fully filled. At higher stress

levels primarily partially filled structures are observed, which confirms the notion that the complex shaped structures reflect the merging of local damage sites just prior to catastrophic failure of the sample.

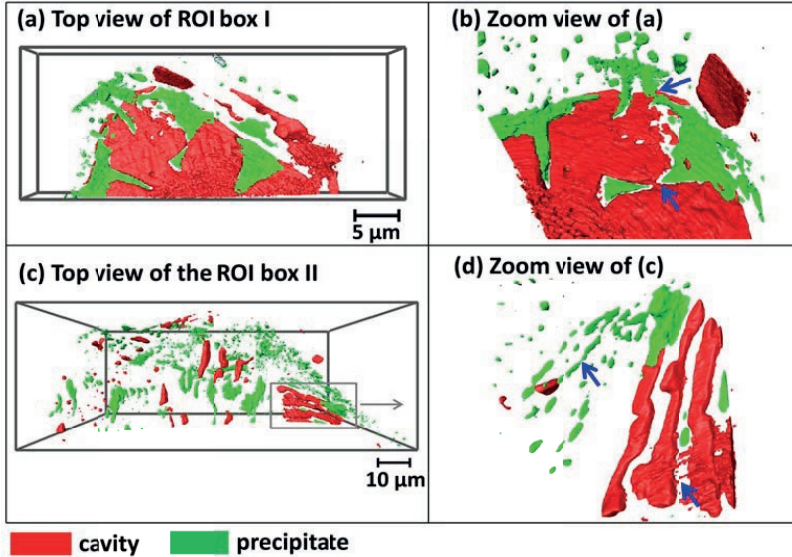


**Fig. 5.11.** Examples of creep cavities partially filled by precipitates. The ROI is extracted from the tomographic 3D rendering of the Fe-Au alloy after creep at a temperature of 550 °C and a load of (a, b) 100 MPa and (c, d) 117 MPa, respectively. The blue arrows in the figure show the linkage of cavities or precipitates.

We will now focus in more detail on the filling of cavities at the grain boundaries. Fig. 5.11a and 5.11b show a big transverse grain boundary cavity partially filled by several precipitates. Due to the filling by precipitation at the cavity surface, this cavity cannot develop to cover the whole transverse grain boundary. Instead this cavity extends into the locations where less precipitates are formed and was linked up to generate a large cavity with a complex shape. This suggests that the precipitation could impede the growth of the large cavity although the linkage of the cavity is unstoppable. Smaller grain-boundary cavities are shown in Fig. 5.11c and 5.11d. A nearly identical spacing of about 4  $\mu\text{m}$  is observed between the small cavities (unfilled and filled) at the transverse grain boundary. As the cavities have not coalesced significantly in this stage, the precipitates are able to completely fill some of them. Fig. 5.11d shows three rod-like cavities formed at the inclined grain boundary with a spacing of about 2  $\mu\text{m}$  between them. It is interesting to note that the orientations of the cavities are identical to the grain boundary sliding (GBS) direction, which suggests that GBS favors the elongation of the cavities. In the meantime the linkage between these cavities proceeds, which is indicated by the arrow in Fig. 5.11d. From this

detailed observation we can conclude that the cavities nucleate with a certain spacing between them at either transverse or inclined grain boundaries. The precipitates can fill small cavities efficiently, whereas once the cavities link together to form large ones it is too late to fill them completely.

Fig. 5.12 shows several examples of partially filled creep cavities produced at different stress levels. The observed structures indicate that the filling process generally starts from one location and develops until the cavity is completely filled. The necking in Fig. 5.12a suggests that this rod type cavity, which is located on the inclined grain boundary with respect to the applied stress, is the result of the coalescence of two equiaxed cavities. The resulting topology results in a small  $FR$  value for rod like structures. This situation is comparable to that of Fig. 5.12b, in which the linkage of neighbouring cavities results in a big open cavity, but a low value of  $FR$ . In contrast, when the precipitation is induced soon after the nucleation of the cavity the cavity filling by the precipitate can accommodate the growth of the cavity leading to the high  $FR$  values found for the cavities shown in Fig. 5.12d-f. Fig. 5.12c shows that a rod-like cavity is nearly half filled ( $FR = 0.47$ ) by the precipitate from one side. It is interesting to note in Fig. 5.12f that the open cavity has been fully encapsulated. This further demonstrates that the precipitate is filling the cavity rather than inducing the formation of the cavity.

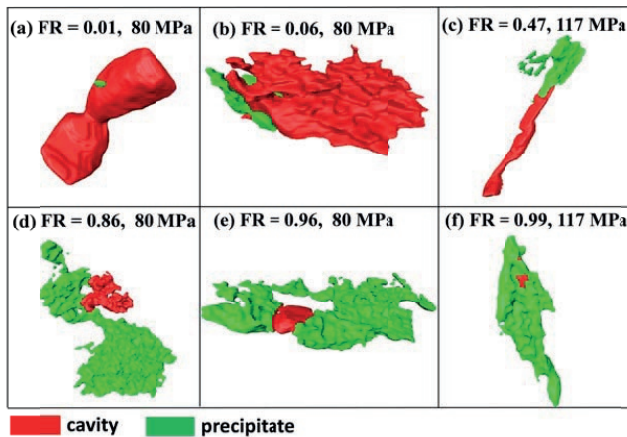


**Fig. 5.12.** Examples (top view) showing cavities with different filling ratios ( $FR$ ). The applied stress is normal to the top view.

## 5.4. Discussion

### 5.4.1. Growth modes of the creep cavities

The development of a creep cavity consists of nucleation, growth and coalescence processes. As these processes can happen simultaneously over the whole creep lifetime,

it is difficult to analyze each process separately. However, combining an analysis of the locations and the different types of cavities can provide an insight into the cavity evolution.

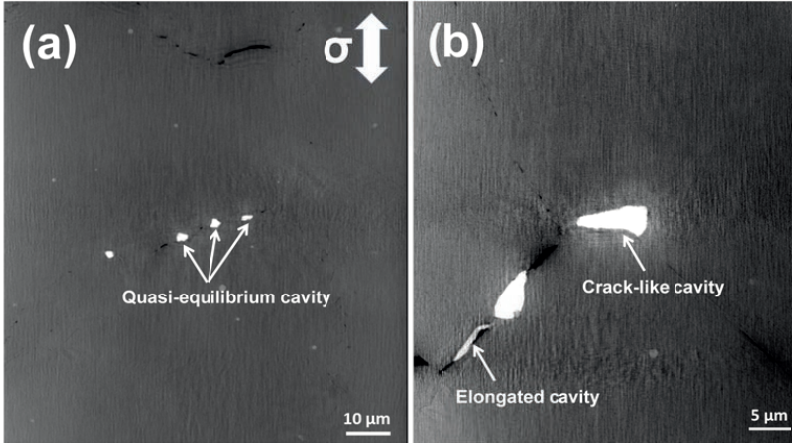


**Fig. 5.13.** Two tomography slices parallel to the applied stress show different growth modes of the creep cavities in the Fe-Au alloy sample after creep at (a) 117 MPa and (b) 60 MPa. Quasi-equilibrium cavities, crack-like cavities at a transverse grain boundary and an elongated cavity at an inclined grain boundary are indicated by the arrows.

As the resolution limit ( $\approx 3$  times the voxel size, *i.e.* 75 nm) is close to the predicted size of the critical nucleus of about 50 nm [37], the cavities with a size  $d < 1 \mu\text{m}$  illustrate the early growth stage and preferred nucleation sites of the cavities. The location of the creep cavities shown in the 3D tomographic renderings indicates that grain boundaries are the preferred positions for the nucleation of cavities. A cavity may nucleate on a transverse grain boundary by the accumulation of the vacancies, while a cavity at an inclined grain boundary or triple point (partially) may be the result of grain boundary sliding (GBS). Once a cavity has nucleated on the grain boundary, the subsequent growth involves the vacancies diffusion along the cavity surface (surface diffusion), followed by diffusion along the grain boundary (grain-boundary diffusion), which finally causes the grain displacement leading to matrix creep [38]. When the surface diffusion is rapid enough, the cavity is able to maintain its quasi-equilibrium shape, as shown in Fig. 5.13a. Normally this quasi-equilibrium shape is lens-shaped with an angle of  $\psi \approx 75^\circ$  between the tangent to the cavity surface and the plane of the grain boundary. However, when the surface diffusion is not much faster than the grain-boundary diffusion, the cavity cannot attain the equilibrium shape and develops into a crack-like cavity [39]. A cavity located at an inclined grain boundary may be distorted and elongated due to GBS [40], as shown in Fig. 5.13b. In conclusion, the tomography data suggest that both the grain-boundary diffusion and GBS play a role in the cavity growth in the Fe-Au alloy samples.

Different growth mechanisms of creep cavities have been analyzed extensively in previous studies [37-45]. Several parameters have been proposed to define the growth mode. The evolution of cavity shape depends on the diffusivity ratio  $\Delta$  [39] defined as:

$$\Delta = \frac{D_s \delta_s}{D_{GB} \delta_{GB}}, \quad (5.7)$$

where  $D_s$  and  $D_{GB}$  are the surface diffusivity and grain boundary diffusivity, respectively. The diffusivity corresponds to  $D = D_0 \exp(-Q/RT)$  with a constant pre-factor  $D_0$ , an activation energy  $Q$ , the gas constant  $R$  and the absolute temperature  $T$ . The variables  $\delta_s$  and  $\delta_{GB}$  are the surface and grain-boundary diffusion thickness, respectively. The surface diffusion layer thickness is estimated by  $\delta_s = \Omega^{1/3}$ , where  $\Omega$  is the volume per atom [39]. The grain boundary diffusion layer thickness is assumed to be two atomic layers ( $\delta_{GB} \approx 2\delta_s \approx 5 \times 10^{-10}$  m) [46]. In the present work, a value for  $\Delta$  of 1.3 was estimated based on the values reported in the literature [38]. This suggests the surface diffusion is comparable to the grain boundary diffusion. According to [39], the cavity growth takes place maintaining a quasi-equilibrium shape as long as

$$\sigma < 1.9 \left( \frac{\gamma_s}{r} \right) \left( 1 + 1.3 \frac{\Delta \lambda}{r} \right), \quad (5.8)$$

and transfers into a crack-like shape when

$$\sigma > 3.5 \left( \frac{\gamma_s}{r} \right) \left( 1 + 1.2 \frac{\Delta \lambda}{r} \right), \quad (5.9)$$

where  $\sigma$  is the applied stress,  $\gamma_s$  the interfacial energy,  $r$  the cavity radius and  $\lambda$  the cavity spacing (center-to-center distance between the cavities). Assuming  $\gamma_s = 1.95$  J/m<sup>2</sup>,  $\Delta = 1.3$  and  $\lambda = 4$   $\mu$ m, the cavity can attain the equilibrium shape when the cavity radius  $r$  is less than 0.68, 0.58, 0.52 and 0.48  $\mu$ m at  $\sigma = 60, 80, 100$  and 117 MPa, respectively. The cavity would develop into crack-like shape when  $r$  is larger than 0.90, 0.77, 0.69 and 0.63  $\mu$ m at  $\sigma = 60, 80, 100$  and 117 MPa, respectively. It is estimated that the shape of the cavity shows a transition when  $0.48 < r < 0.90$   $\mu$ m from the equilibrium shape to the crack-like shape as the cavity growth proceeds. This is reflected in the examples of Fig. 5.13.

To address the influence of the creep flow on the diffusive cavity growth, Needleman and Rice proposed to estimate the diffusion length  $\Lambda$  [38] from:

$$\Lambda = \left( \frac{D_{GB} \delta_{GB} \Omega \sigma}{kT \dot{\epsilon}} \right)^{1/3}, \quad (5.10)$$

where  $\dot{\epsilon}$  the strain rate,  $k$  Boltzmann's constant and  $T$  the absolute temperature. The diffusion length is calculated to be  $\Lambda = 2.60, 2.41, 2.36$  and 1.65  $\mu$ m for  $\sigma = 60, 80, 100$  and 117 MPa, respectively. The value of  $\Lambda$  is comparable to half of the average cavity spacing  $\lambda$  and slightly increases with decreasing applied stress. This indicates that both diffusion and creep flow control the cavity growth. As the vacancies diffuse from

the cavity surface to the tip and then along the grain boundary, matrix creep flow is allowed to occur, resulting in a deformation of the grains. This accommodates and favors the cavity growth by transporting vacancies over shorter distances. Therefore, it is suggested that the growth of the creep cavities in this Fe-Au alloy occurs in a coupled diffusion and creep-flow mode. The numerical description of this sort of creep behavior has been presented by Chen and Argon [47].

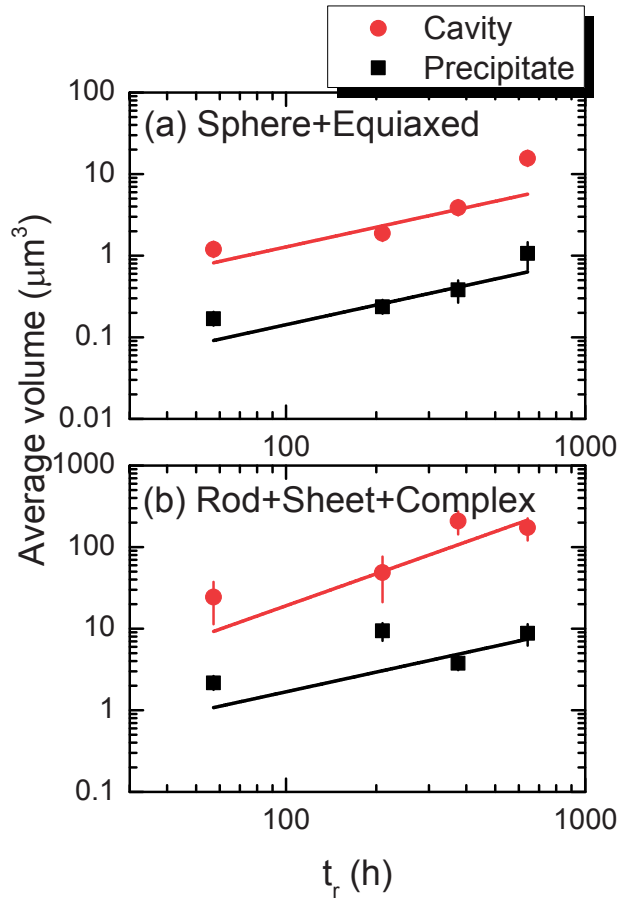


**Fig. 5.14.** Average volume of the precipitates and cavities grouped into (a) spherical and equiaxed shaped and (b) rod, sheet and complex shaped particles as a function of the rupture time.



**Table 5.4.** The derived parameters from a fit of the average volume  $V$  versus the rupture time  $t$  to a power law dependence of the form  $V = k t^n$  for the creep cavities and precipitates subdivided into two different shape groups. For cavities the pre-factor  $k$  is assumed to be proportional to the applied stress. Listed is the value at a reference stress of  $\sigma = 100$  MPa. For the precipitates the pre-factor  $k$  is independent of stress. In between brackets is the error in the last digit.

Shape	Cavities		Precipitates	
	$k$ (100 MPa)	$n$	$k$	$n$
	( $\mu\text{m}^3\text{h}^{-n}$ )		( $\mu\text{m}^3\text{h}^{-n}$ )	
Sphere + Equiaxed	0.033(6)	0.8	0.0036(5)	0.8
Rod+Sheet+Complex	0.05(1)	1.3	0.04(1)	0.8

In Fig. 5.14 the relationship between the average volume of the creep cavities and precipitates is shown for two shape groups as a function of the rupture time. The fitting curves indicate that the average volume has a power-law dependence on the rupture time, expressed as  $V = k t^n$ . The derived values of the pre-factor  $k$  and time exponent  $n$  are summarized in Table 5.4. As the creep cavity growth is controlled by both diffusion and creep flow (the strain rate that is related to the applied stress), the pre-factor for cavity growth  $k_{cav}$  is expected to be proportional to the applied stress  $\sigma$  and can be expressed as  $k_{cav} = k_0(\sigma / \sigma_0)$  where  $k_0$  is a temperature dependent constant at a reference stress  $\sigma_0$  ( $\sigma_0 = 100$  MPa in Table 5.4). It is shown that the time exponent for the growth of cavities with spherical and equiaxed shapes is similar to the value for the growth of precipitates. The time exponent of cavities in rod, sheet and complex shapes increases, while the time exponent of precipitates in these shapes remains the same. Based on the previous analysis of the cavity growth mechanism, it is postulated that the spherical and equiaxed shaped cavities correspond to the early growth stage before coalescence, while the rod, sheet and complex types are most likely formed by coalescence in the later growth stage. This suggests that the coalescence of cavities accelerates the cavity growth, resulting in an increase of the time exponent. In contrast, the growth of precipitates is mainly controlled by the bulk diffusion of gold, which is insensitive to the stress, and therefore its time exponent for growth does not change.

#### 5.4.2. Filling mechanism of the creep cavities

Previous studies [16-19] have shown that the gold precipitates can only form at defect sites due to the high energy barrier for their nucleation in the matrix. It is found that the Au atoms first segregate on the cavity surface and then form Au-rich precipitates (with about 20 at.% Fe at  $T = 550$  °C). These observations are further clarified by the present tomography measurements that show a close correlation between the size, shape and spatial distribution of the cavities and precipitates. Furthermore, the degree of filling of each cavity has been deduced by this 3D nano-imaging technique, which allows a more detailed evaluation of the pore filling behavior.

Essentially the self-healing kinetics is controlled by the relative rates of the damage (creep cavity) formation and healing (gold precipitation). Depending on the local conditions, the gold precipitation is triggered by the nucleation of creep cavities and becomes active when the cavities reach a characteristic size  $V_0$ . It is found in Fig. 5.10 that  $V_0$  can vary between 0.1 and 100  $\mu\text{m}^3$ . In order to evaluate the self-healing kinetics for a single cavity, we propose two different cases: (i) the cavity growth associated with the filling by the precipitates takes place without linkage with other cavities (coalescence); (ii) the growing cavity links with other cavities after it reaches a specific size  $V_1$ .

For the first case, it is assumed that the filling starts for a cavity volume  $V_0$ . After that, the cavity volume  $V_{cav}$  (including the filled and unfilled part) follows a power law with a constant time exponent  $m$ . Simultaneously, the gold atoms diffuse to the cavity surface and form a gold precipitate with a volume  $V_{prec}$  that follows a power law with a constant time exponent  $n$ :

$$V_{cav} = V_0 + k_{cav} t^m, \quad (5.11)$$

$$V_{prec} = k_{prec} t^n, \quad (5.12)$$

where  $k_{cav}$  and  $k_{prec}$  quantify the combined effects of stress and local conditions (e.g. the grain size and local grain-boundary orientation) on the growth of the creep cavity and precipitate, respectively. By taking the ratio of their volumes, the filling ratio  $FR$  is obtained:

$$FR = \frac{V_{prec}}{V_{cav}} = \frac{k_{prec}}{k_{cav}} \left( \frac{V_{cav} - V_0}{k_{cav}} \right)^{\frac{n}{m}}. \quad (5.13)$$

Without linkage the time exponents  $m$  and  $n$  are expected to be equal as they are both diffusion controlled. This is in agreement with the parallel slopes for the time evolution of the average volume for spherical and equiaxed shaped objects, as shown in Fig. 5.14a and supported by previous studies [19,48-49]. Therefore, Eq. 5.13 can be simplified to:

$$FR = \frac{k_{prec}}{k_{cav}} \left( 1 - \frac{V_0}{V_{cav}} \right), \quad (5.14)$$

where the filling ratio is purely controlled by the ratio  $k_{prec}/k_{cav}$  and the characteristic volume  $V_0$ . For  $k_{prec} > k_{cav}$  complete filling ( $FR = 1$ ) is achieved for  $V_{cav} = V_0[k_{prec}/(k_{prec} - k_{cav})]$  at  $t = [V_0/(k_{prec} - k_{cav})]^{1/m}$ .

However, if the cavity links with other cavities then the self-healing kinetics would change. The cavity volume  $V_{cav}$  can in this case be described by an increase in the growth exponent of the cavity to  $m + \Delta m > m$  after a critical time  $t_{link}$  when linkage starts to take place (or equivalently, beyond a critical volume  $V_{cav} > V_1$  for  $t > t_{link}$ ). For  $t > t_{link}$  the cavity volume then corresponds to:



$$V_{cav} = V_1 + k_{cav,link} (t - t_{link})^{m+\Delta m} \quad (V_{cav} > V_1), \quad (5.15)$$

$$V_{prec} = k_{prec} t^n, \quad (5.16)$$

with  $V_1 = V_0 + k_{cav} t_{link}^m$ . The filling ratio after linkage can now be formulated as:

$$FR = \frac{k_{prec}}{V_{cav}} \left[ \left( \frac{V_1 - V_0}{k_{cav}} \right)^{\frac{1}{m}} + \left( \frac{V_{cav} - V_1}{k_{cav,link}} \right)^{\frac{1}{m+\Delta m}} \right]^n \quad (V_{cav} > V_1). \quad (5.17)$$

Before linkage,  $FR$  is still described by Eq. 5.14. For  $t > t_{link}$  the value of  $FR$  will decrease with time as the exponent for the cavity growth has increased ( $\Delta m > 0$ ).

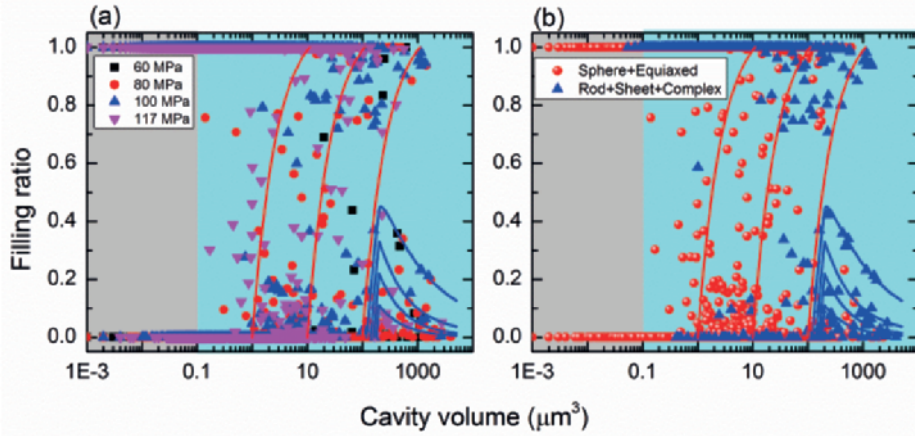


**Fig. 5.15.** The comparison between the predictions of the filling model for the cavities without (red curves) and with linkage (blue curves) and the observed filling ratios of all cavities present in the samples after creep at different loads. (a) Cavities were grouped according to different loads. (b) Cavities were grouped into two shape categories (spherical and equiaxed shaped cavities; rod, sheet and complex shaped cavities). The solid red curves based on a non-linkage model are displayed for model parameters  $n = m = 0.8$ ,  $k_{prec}/k_{cav} = 1.1$  and  $V_0 = 1, 10$  and  $100 \mu\text{m}^3$ . The solid blue curves are displayed for the linkage model using the following parameter values  $n = m = 0.8$ ,  $m+\Delta m = 1.3$ ,  $k_{prec}/k_{cav} = 1.1$ ,  $V_1 = 200 \mu\text{m}^3$  and  $V_0 = 120, 140, 160$  and  $180 \mu\text{m}^3$  (with  $k_{cav,link}/k_{cav} = 0.01, 0.1, 1$ , and  $10 \text{ h}^{-0.5}$ , respectively). Note that in the grey shaded region it is experimentally not possible to determine partial filling.

In Fig. 5.15 the evolution of the filling ratio is calculated for several cases with and without linkage. It can be seen that the two different routes for the evolution of the filling ratio shown in Fig. 5.10 are in good agreement with the model predictions in the absence and presence of linkage for creep cavities. It is clarified that  $FR$  can continuously increase with increasing cavity volume until the cavity is fully filled when there is no linkage. As the initial cavity volume required to induce precipitation  $V_0$

varies, the cases without linkage form a band and cover a wide range of cavity volumes from 0.1 to 100  $\mu\text{m}^3$ . However, the filling ratio decreases sharply when a linkage of creep cavities starts to occur. This hypothesis is supported by the data in Fig. 5.15b where the filling ratios for most of the spherical and equiaxed shaped cavities are located in the predicted filling ratio regimes assuming no pore linkage. In contrast, half of the cavities with rod, sheet and complex shapes, for which a coalescence of cavities is expected, are located in the region of a decreasing filling ratio. The remaining partially filled cavities are yet in the increasing region because they are nearly fully filled before the linkage takes place. From the present work we estimate a critical linkage volume of  $V_1 \approx 200 \mu\text{m}^3$  at which point the filling ratio of the linked cavities starts to decrease. The observed behavior for the filling ratio of individual creep cavities is in good agreement with the predictions of this simple model.

## 5.5. Conclusions

Synchrotron X-ray phase nano-tomography experiments were carried out successfully on creep-failed Fe-Au alloy samples after creep at 550 °C for several constant loads. 3D images of the microstructure of the Fe-Au alloy samples at nanometer length scale were obtained and analyzed. Different stages in the filling process of individual creep cavities by gold precipitation were identified to characterize the self-healing mechanism in creep-resistant steels. The following conclusions can be drawn from this study:

- 1) The creep cavities are predominately formed at stress-affected grain boundaries. The precipitates nucleate exclusively on grain faces and preferentially on the free cavity surface formed on these grain faces.
- 2) By classifying the precipitates and cavities into spherical, equiaxed, rod, sheet and complex shaped objects, it is possible to clarify their nucleation, growth and coalescence in a qualitative way. The spheres denote the smallest volume objects and reveal the nucleation sites. The equiaxed objects mainly reflect the early growth stage before coalescence, while the rod, sheet and complex objects are considered to be formed in the later growth stage and potentially influenced by coalescence.
- 3) The quantitative analysis of the size, shape and spatial distribution for the creep cavities and the precipitates demonstrates strong correlation between the morphology of the cavities and precipitates. It is demonstrated that the gold precipitates form preferentially at cavity surfaces and act as healing agents rather than cavitation sites for creep cavities. The self-healing character of added Au in Fe-based alloys is fully supported by this study.
- 4) The creep cavities develop in a coupled diffusion (both surface diffusion and grain boundary diffusion) and creep flow mode. It is derived that the shape of the cavity shows a transition from the quasi-equilibrium shape to the crack-like shape for a cavity radius in the range of  $0.48 < r < 0.90 \mu\text{m}$  as the cavity proceeds to grow. Elongated cavities at inclined grain boundaries are probably generated by grain-boundary sliding.

- 5) Two different time evolutions for the filling ratio of individual creep cavities are observed from the tomography results. This observation can be explained by a simple model considering the absence and presence of linkage for neighboring creep cavities. The filling ratio increases continuously for increasing cavity volumes until complete filling is achieved when there is no linkage of cavities. In contrast, the filling ratio decreases sharply once linkage between creep cavities becomes the main microstructural evolution mode.

### Acknowledgements

This research is financially supported by the innovation-oriented research program (IOP) on self-healing materials of the Dutch Ministry of Economic Affairs, Agriculture and Innovation (Project SHM01017 and SHM012011) and a grant from the China Scholarship Council (CSC). The authors thank Lu Shen for her help during the synchrotron experiment. We thank Wim Verwaal and Joost van Meel at the Faculty of Civil Engineering and Geosciences, Delft University of Technology for providing the image analysis environment. We acknowledge the European Synchrotron Radiation Facility for provision of synchrotron radiation facilities and thank the beamline staff for assistance in using beamline ID16A-NI.

### References

1. J. Lemaitre, R. Desmorat: *Engineering damage mechanics: ductile, creep, fatigue and brittle failures*, Springer-Verlag, Berlin, 2005.
2. M.F. Ashby, C. Gandhi, D.M.R. Taplin: *Acta Metall.*, 1979, vol. 27, pp. 699-729.
3. M. Taneike, F. Abe, K. Sawada: *Nature*, 2003, vol. 424, pp. 294-6.
4. P.J. Ennis, A. Zielinska-Lipiec, O. Wachter, A. Czyrska-Filemonowicz: *Acta Mater.*, 1997, vol. 45, pp. 4901-7.
5. K. Maruyama, K. Sawada, J. Koike: *ISIJ Int.*, 2001, vol. 41, pp. 641-53.
6. A. Aghajani, C. Somsen, G. Eggeler: *Acta Mater.*, 2009, vol. 57, pp. 5093-106.
7. S.R. White, N.R. Sottos, P.H. Geubelle, J.S. Moore, M.R. Kessler, S.R. Sriram, E.N. Brown, S. Viswanathan: *Nature*, 2001, vol. 409, pp. 794-7.
8. M.D. Hager, P. Greil, C. Leyens, S. van der Zwaag, U.S. Schubert: *Adv. Mater.*, 2010, vol. 22, pp. 5424-30.
9. G.Q. Xu, M.J. Demkowicz: *Phys. Rev. Lett.*, 2013, vol. 111, pp. 145501.
10. S. van der Zwaag, E. Brinkman, eds., *Self healing materials: pioneering research in the Netherlands*, IOS Press, Amsterdam, 2015.
11. K. Laha, J. Kyono, S. Kishimoto, N. Shinya: *Scr. Mater.*, 2005, vol. 52, pp. 675-8.
12. K. Laha, J. Kyono, N. Shinya: *Scr. Mater.*, 2007, vol. 56, pp. 915-8.
13. K. Laha, J. Kyono, T. Sasaki, N. Shinya: *Metall. Mater. Trans. A*, 2005, vol. 36, pp. 399-409.
14. S.M. He, N.H. van Dijk, M. Paladugu, H. Schut, J. Kohlbrecher, F.D. Tichelaar, S. van der Zwaag: *Phys. Rev. B*, 2010, vol. 82, pp. 174111.
15. S.M. He, N.H. van Dijk, H. Schut, E.R. Peekstok, S. van der Zwaag: *Phys. Rev. B*, 2010, vol. 81, pp. 094103.

16. S. Zhang, G. Langelaan, J.C. Brouwer, W.G. Sloof, E. Brück, S. van der Zwaag, N.H. van Dijk: *J. Alloy. Compd.*, 2014, vol. 584, pp. 425-9.
17. S. Zhang, J. Kohlbrecher, F.D. Tichelaar, G. Langelaan, E. Brück, S. van der Zwaag, N.H. van Dijk: *Acta Mater.*, 2013, vol. 61, pp. 7009-19.
18. S. Zhang, C. Kwakernaak, W.G. Sloof, E. Brück, S. van der Zwaag, N.H. van Dijk: *Adv. Eng. Mater.*, 2015, vol. 17, pp. 598-603.
19. S. Zhang, C. Kwakernaak, F.D. Tichelaar, W.G. Sloof, M. Kuzmina, M. Herbig, D. Raabe, E. Brück, S. van der Zwaag, N.H. van Dijk: *Metall. Mater. Trans. A*, 2015, vol. 46, pp. 5656-70.
20. A. Pyzalla, B. Camin, T. Buslaps, M. Di Michiel, H. Kaminski, A. Kottar, A. Pernack, W. Reimers: *Science*, 2005, vol. 308, pp. 92-5.
21. E. Maire, P.J. Withers: *Int. Mater. Rev.*, 2014, vol. 59, pp. 1-43.
22. E. Nizery, H. Proudhon, J.Y. Buffiere, P. Cloetens, T.F. Morgeneyer, S. Forest: *Philos. Mag.*, 2015, vol. 95, pp. 2731-46.
23. H. Toda, S. Yamamoto, M. Kobayashi, K. Uesugi, H. Zhang: *Acta Mater.*, 2008, vol. 56, pp. 6027-39.
24. D. Kurumlu, E.J. Payton, M.L. Young, M. Schöbel, G. Requena, G. Eggeler: *Acta Mater.*, 2012, vol. 60, pp. 67-78.
25. E. Maire, O. Bouaziz, M. Di Michiel, C. Verdu: *Acta Mater.*, 2008, vol. 56, pp. 4954-64.
26. C. Landron, E. Maire, J. Adrien, H. Suhonen, P. Cloetens, O. Bouaziz: *Scr. Mater.*, 2012, vol. 66, pp. 1077-80.
27. A. Pacureanu, Y. Yang, J.C. da Silva, R. Baker, R. Barrett, S. Bohic, Y. Dabin, F. Fus, E. Gagliardini, C. Guilloud, O. Hignette, M. Hubert, M. Langer, J. Meyer, C. Morawe, J. Morse, R. Tachoueres, P. van der Linden, F. Villar, L. Weber, P. Cloetens: *The ESRF Upgrade nanoprobe beamline ID16A-NI for hard X-ray coherent imaging and fluorescence microscopy*, manuscript under preparation for J. Synchrotron Radiation.
28. P. Cloetens, W. Ludwig, J. Baruchel, D. van Dyck, J. van Landuyt, J.P. Guigay, M. Schlenker: *Appl. Phys. Lett.*, 1999, vol. 75, pp. 2912-4.
29. A. Mirone, E. Brun, E. Gouillart, P. Tafforeau, J. Kieffer: *Nucl. Instrum. Meth. B*, 2014, vol. 324, pp. 41-8.
30. <http://www.diplib.org/>.
31. H.J. Catrakis, P.E. Dimotakis: *Phys. Rev. Lett.*, 1998, vol. 80, pp. 968.
32. H. Wadell: *J. Geol.*, 1935, vol. 43, pp. 250-80.
33. A. Borbély, F.F. Csikor, S. Zabler, P. Cloetens, H. Biermann: *Mater. Sci. Eng. A*, 2004, vol. 367, pp. 40-50.
34. A. Isaac, F. Sket, W. Reimers, B. Camin, G. Sauthoff, A.R. Pyzalla: *Mater. Sci. Eng. A*, 2008, vol. 478, pp. 108-18.
35. O.D. Sherby: *Acta Metall.*, 1962, vol. 10, pp. 135-47.
36. J. Cadek: *Creep in metallic materials*, Elsevier Science Publishers B.V., Amsterdam, 1988.
37. R. Raj, M.F. Ashby: *Acta Metall.*, 1975, vol. 23, pp. 653-66.
38. A. Needleman, J.R. Rice: *Acta Metall.*, 1980, vol. 28, pp. 1315-32.
39. T.J. Chuang, K.I. Kagawa, J.R. Rice, L.B. Sills: *Acta Metall.*, 1979, vol. 27, pp. 265-84.

40. I.W. Chen: *Metall. Trans. A*, 1983, vol. 14, pp. 2289-93.
41. G.H. Edward, M.F. Ashby: *Acta Metall.*, 1979, vol. 27, pp. 1505-18.
42. M.E. Kassner, T.A. Hayes: *Int. J. Plasticity*, 2003, vol. 19, pp. 1715-48.
43. M. Vöse, B. Fedelich, J. Owen: *Comp. Mater. Sci.*, 2012, vol. 58, pp. 201-13.
44. T. Shrestha, M. Basirat, I. Charit, G.P. Potirniche, K.K. Rink: *Mater. Sci. Eng. A*, 2013, vol. 565, pp. 382-91.
45. A. Das, N. Roy, A.K. Ray: *Mater. Sci. Eng. A*, 2014, vol. 598, pp. 28-33.
46. J.C. Fisher: *J. Appl. Phys.*, 1951, vol. 22, pp. 74-7.
47. I.W. Chen, A.S. Argon: *Acta Metall.*, 1981, vol. 29, pp. 1759-68.
48. H.B. Aaron, H.I. Aaronson: *Acta Metall.*, 1968, vol. 16, pp. 789-98.
49. W.D. Nix, K.S. Yu, J.S. Wang: *Metall. Trans. A*, 1983, vol. 14, pp. 563-70.

## Supplementary Material for Chapter 5

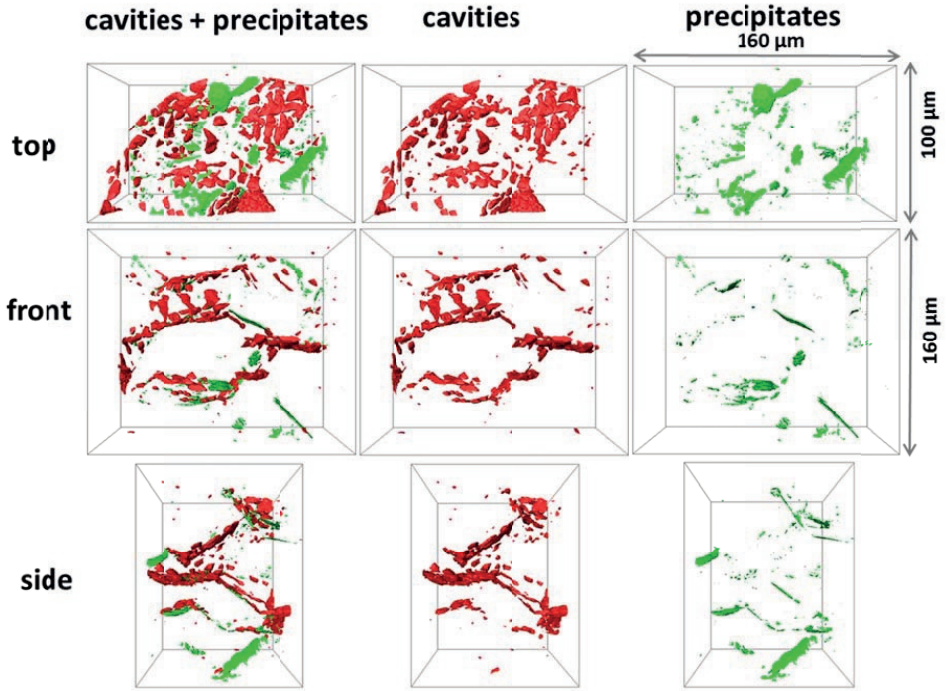


**Figure S1.** Spatial distribution of cavities and precipitates in a ROI of the Fe-Au sample after creep at 550 °C and 60 MPa. The applied stress is normal to the top view.



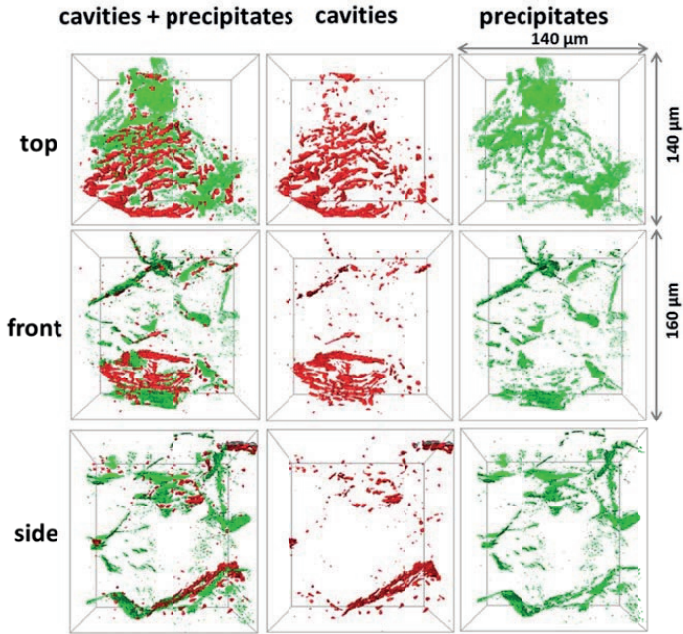


**Figure S2.** Spatial distribution of cavities and precipitates in a ROI of the Fe-Au sample after creep at 550 °C and 100 MPa. The applied stress is normal to the top view.

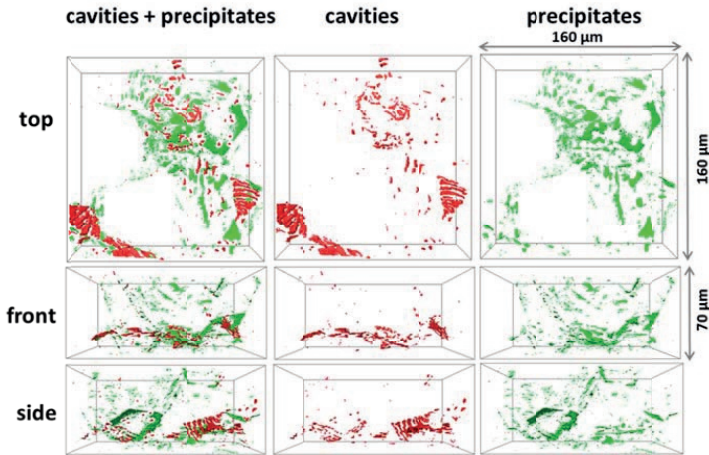


**Figure S3.** Spatial distribution of cavities and precipitates in a ROI of the Fe-Au sample after creep at 550 °C and 117 MPa. The applied stress is normal to the top view.

**Movie S4.** 3D visualization indicating the segmentation and spatial distribution of cavities and precipitates in the Fe-Au sample after creep at 550 °C and 80 MPa.

Filename: Movie\_S4\_3D\_visualization\_FeAu\_80MPa\_100nm.mpg (available at <https://ars.els-cdn.com/content/image/1-s2.0-S135964541630711X-mmc2.mp4>)

File description: This movie shows the correspondence between the original 3D volume image (grey value) and segmented 3D volume image (color) by clipping a slice from the bottom to the top and from the front to the back side. In the grey valued 3D volume image the bright and dark features are cavities and precipitates, respectively (see main text of the manuscript for details). After segmentation the cavities and precipitates are denoted in red and green colors, respectively. The iron matrix is in transparent light grey. It should be noted that the edge part of the slices are not in the sample volume. After the clipping, the segmented 3D volume image is rotated to show the spatial distribution of the cavities and precipitates from different angles. The length scale bar is given along the horizontal direction. The applied stress is along the vertical direction.





---

# Chapter 6

## **Autonomous filling of grain boundary cavities during creep loading in Fe-Mo alloys**

We have investigated the autonomous repair of creep damage by site-selective precipitation in a binary Fe-Mo alloy (6.2 wt.% Mo) during constant-stress creep tests at temperatures of 813, 823 and 838 K (540, 550 and 565 °C). Scanning electron microscopy studies on the morphology of the creep failed samples reveal irregularly formed deposits that show a close spatial correlation with the creep cavities, indicating the filling of creep cavities at grain boundaries by precipitation of the Fe<sub>2</sub>Mo Laves phase. Complementary transmission-electron microscopy and atom probe tomography have been used to characterize the precipitation mechanism and the segregation at grain boundaries in detail.

## 6.1. Introduction

Molybdenum is an important alloying element for high performance steel grades to be deployed at elevated temperatures. It is mainly used to improve the creep properties by solid-solution strengthening [1-3]. For binary Fe-Mo alloys several studies have been performed to determine the effect of the Mo concentration on the creep behavior at elevated temperatures [4-7], but only limited data are available on the formation of Mo-containing precipitates in these model alloys [8,9]. In high-Cr steels containing Mo and/or W, the precipitation of the  $(\text{Fe,Cr})_2(\text{Mo,W})$  Laves phase occurs during long term exposure at higher temperatures. The influence of Mo on the creep properties has been interpreted exclusively in terms of solid-solution strengthening and precipitation hardening [10,11], without considering its role in mediating local creep damage in the form of grain boundary pores.

Recently, Laha and co-workers [12-15] have reported that creep damage can be self healed in compositionally-modified austenitic stainless steels. They attributed the enhanced creep resistance to dynamic precipitation of Cu and BN at the crack surface, preventing further growth of the creep damage. In our previous work on Fe-Cu and Fe-Cu-B-N model alloys Cu precipitation at deformation-induced structural defects was indeed found to take place [16,17]. However, the preference for Cu and BN to precipitate at open deformation-induced defects was found to be relatively weak and a high concentration of spherical Cu precipitates was formed homogeneously in the matrix, greatly reducing the healing potential of the Cu atoms initially brought into a supersaturated state.

Based on these results we subsequently explored the self-healing potential in Fe-Au and Fe-Au-B-N model alloys [18-22]. The choice for Au as the active solute was based on the fact that the solute Au atoms are appreciably larger than the matrix Fe atoms (in contrast to solute Cu atoms), resulting in a high nucleation barrier for precipitation within the matrix. As a result, the Au atoms show a strong preference to exclusively segregate at dislocations and creep-cavity surfaces. We have demonstrated that Fe-Au is an excellent model system for the self healing of creep cavities. However, the use of Au as a healing agent in large scale steel structures is unlikely due to economic reasons.

In the present study the use of a technologically more relevant alloying element, Mo, to autonomously fill creep deformation induced grain boundary cavities is examined for a high purity Fe-6.2 wt.% Mo model alloy. Like Au, Mo has a larger atomic radius compared to Fe ( $r_{\text{Mo}}/r_{\text{Fe}} = 1.09$ ) and satisfies the key requirements for an efficient healing agent: (i) the solutionized Mo atoms are mobile and tend to segregate from the matrix at aging temperatures around 823 K (550 °C); (ii) there is a high energy barrier for nucleation of Mo-rich precipitates ( $\text{Fe}_2\text{Mo}$ ) in the matrix due to a large atomic misfit with respect to the bcc iron lattice.

To this aim Mo precipitation at microscopic defect sites at grain boundaries in solutionized Fe-Mo alloys is studied by creep experiments at constant loads at temperatures of 813, 823 and 838 K (540, 550 and 565 °C). The resulting

microstructure of the creep-failed samples was studied in detail by electron microscopy and atom probe tomography in order to evaluate the deposition process and the mass transport to the damage sites.

## 6.2. Experimental

The composition of the studied high-purity Fe-Mo alloy (produced by Goodfellow) is listed in Table 6.1. The samples of dog-bone shape were cut from sheet material by spark erosion and solution treated at 1173 K (900 °C) for 5 h in evacuated silica tubes filled with 200 mbar ultrahigh purity argon. The silica tubes were subsequently dropped into water at room temperature. The average grain size before creep was 19  $\mu\text{m}$ . According to thermodynamic calculations (THERMOCALC), the Mo is fully dissolved in the iron matrix above 1111 K (838 °C).

**Table 6.1.** The chemical composition of Fe-Mo alloy (in wt.%) with balance iron.

Mo	N	C	S
6.207	0.0047	0.0183	<0.001

Creep tests were performed using an Instron testing machine (5560 series with a 1 kN load cell) equipped with a home-built creep test module operating at high temperatures. To avoid surface oxidation of the samples, the miniature creep tester works under high vacuum conditions ( $<1 \times 10^{-4}$  mbar). The dog-bone shaped samples had a gauge length of 12.5 mm and a cross section of 3 mm<sup>2</sup> (thickness of 0.5 mm and width of 6 mm). The creep tests were conducted at a constant temperature of 813, 823 and 838 K (540, 550 and 565 °C) and at constant creep loads. During the experiment the force on the sample was controlled at a constant level. The corresponding stress therefore refers to the initial stress. The homogenized solute concentration of about 6.2 wt.% (i.e. 3.7 at.%) Mo provides a strong chemical driving force for segregation as the equilibrium concentration of solute Mo in the matrix phase amounts to 1.4 wt.% (i.e. 0.8 at.%) Mo at a testing temperature of 823 K (550 °C). The super-saturation corresponds to 4.8 wt.% (i.e. 2.9 at.%) Mo.

Microstructures were analyzed with a scanning electron microscope (JEOL JSM 6500F) equipped with an AuTrata back-scattered electron detector and an electron back-scattering diffraction (EBSD) system employing an Oxford - HKL Nordlys II detector. Micrographs were taken with an electron beam energy of 15 keV. The EBSD patterns were acquired with an electron beam energy of 20 keV and a beam current of 600 pA. Except for the analysis of the fracture surface the microstructure analysis was performed in the uniform elongation part of the samples. Transmission electron microscopy (TEM) measurements were performed using a Tecnai F20ST/STEM instrument operating at 200 kV. Bright Field (BF), lattice images (without objective aperture) and Annular Dark Field (ADF) in STEM (Scanning Transmission Electron Microscopy) mode were obtained. ADF images show the heavier parts of the sample as

bright (*Z*-contrast). For elemental analysis Energy Dispersive Spectroscopy was performed using the attached EDAX CM-200ST system (30 mm<sup>2</sup>, ultrathin window).

The Mo enrichment at the grain boundary and the accompanying matrix depletion was studied by atom probe tomography (APT). The target preparation of specific grain boundaries into the apex of the atom probe specimens was conducted using a FEI Helios NanoLab 600i dual-beam FIB/SEM instrument. Grain boundaries that showed the features of interest were first identified by means of a 2D EBSD scan and then extracted from the surface of the bulk material by standard FIB lift-out procedures. The selected areas of interest were deposited on a commercial Si tip array and then sharpened to tip radii of <100 nm. After a cleaning procedure as described by Thompson [23] the samples were analyzed by APT. The APT characterization was conducted on a LEAP 3000X HR instrument (Cameca), operated in laser-pulsed mode at a base temperature of 60 K, a laser frequency of 250 kHz and a 0.4 nJ pulse energy. The reconstruction was carried out using commercial software (Cameca IVAS®) following the protocol introduced by Geiser and co-workers [24].

### 6.3. Results

The creep results for the as-quenched (solutionized) Fe-Mo alloy loaded at different constant stress levels at a fixed temperature of 823 K (550 °C) are presented in Fig. 6.1. The strain-time curves in Fig. 6.1a indicate that this alloy shows a considerable ductility, which leads to high creep strains (> 50%) upon fracture. The corresponding strain rate as a function of strain (Fig. 6.1b) indicates a short primary creep regime where the creep rate rapidly decreases, until a more steady-state creep starts at a strain of about 0.08. From the strain versus time (Fig. 6.1a) and the strain rate versus strain (Fig. 6.1b) it can be seen the primary creep stage extends until a strain of about 0.08 is reached. The primary creep is followed by an oscillating creep rate before the minimum strain rate is observed. The strain rate oscillation is expected to be attributed to continuous dynamic recrystallization [25-27]. After the steady-state creep regime, a gradual increase in creep rate takes place, which marks the start of the tertiary creep regime. The fraction of the creep lifetime occupied by the quasi steady-state creep regime with a minimum creep rate decreases at higher stress levels.

The quasi steady-state strain rate and the creep lifetime as a function of the applied stress at a temperature of 823 K (550 °C) are shown Fig. 6.1c and 6.1d. As expected, the creep rate increases with increasing stress. The stress exponent is deduced from the Sherby-Dorn equation for the steady-state strain rate [28]:

$$\dot{\epsilon}_s = Ad^m \sigma^n \exp\left(-\frac{Q}{RT}\right), \quad (6.1)$$

where  $A$  is a structure-dependent constant,  $Q$  is an apparent activation energy,  $d$  is the grain size,  $m$  is the grain size exponent,  $\sigma$  is the stress and  $n$  is the stress exponent. The deduced stress exponent of  $n \approx 15$  is relatively high and is related to the interaction between the solute Mo atoms and the high dislocation density generated at these high strain levels [9,29]. The creep lifetime decreases for increasing stress with a

maximum lifetime until fracture of 849 h at the lowest applied stress of 180 MPa. In Fig. 6.1e and 6.1f the corresponding area fraction of Fe<sub>2</sub>Mo Laves phase precipitates, obtained from an image analysis of the SEM data (described in the next section), is shown as a function of stress and lifetime, respectively. The precipitate fraction increases with the creep life time and is still relatively low compared to the equilibrium fraction of 9.8 vol.% Fe<sub>2</sub>Mo.

The results of temperature-dependent creep tests on the solutionized Fe-Mo alloy performed at a stress of 200 MPa and temperatures of 813, 823 and 838 K (540, 550 and 565 °C) are shown in Fig. 6.2. Using Eq. 6.1 an experimental activation energy of  $Q = 319 \pm 14$  kJ/mol was obtained, which is consistent with the activation energy for the diffusion of Mo in *bcc* iron [30]. In Fig. 6.2e and 6.2f the corresponding area fraction of Fe<sub>2</sub>Mo Laves phase precipitates, obtained from an image analysis of the SEM data (described in the next section), is shown as a function of temperature and lifetime, respectively. The precipitate fraction increases with temperature.

**Table 6.2.** A summary of the creep results for the Fe-Mo alloy with the creep temperature  $T$  the creep stress  $\sigma$ , the average grain diameter  $d$  of the alloy, the time to rupture  $t_r$ , the minimum strain rate  $\dot{\epsilon}_{\min}$  and the area fraction of Fe<sub>2</sub>Mo precipitates  $f_p$ .

$T$ K (°C)	$\sigma$ (MPa)	$d$ ( $\mu\text{m}$ )	$t_r$ (h)	$\dot{\epsilon}_{\min}$ ( $\times 10^{-4} \text{ h}^{-1}$ )	$f_p$ (%)
	180	19	849.2	3.52	0.11 $\pm$ 0.03
823 (550)	190		311.6	8.04	0.079 $\pm$ 0.034
	200		117.0	25.1	0.036 $\pm$ 0.011
	160	28	715.6	5.47	0.84 $\pm$ 0.14
838 (565)	200		62.4	31.8	0.31 $\pm$ 0.11
	237		2.1	836	0.16 $\pm$ 0.06
813 (540)	200	28	318.1	7.81	0.017 $\pm$ 0.005
823 (550)			201.8	13.1	0.027 $\pm$ 0.008
838 (565)			62.4	31.8	0.31 $\pm$ 0.11

An additional set of creep tests on the same alloy, but with a different average grain size ( $d = 28 \mu\text{m}$ ), was conducted at a temperature of 838 K (565 °C) for an applied stress of 160, 200 and 237 MPa. From these experiments the same stress exponent of  $n \approx 15$  was obtained. In Table 6.2 the quantitative results of the creep tests have been summarized.

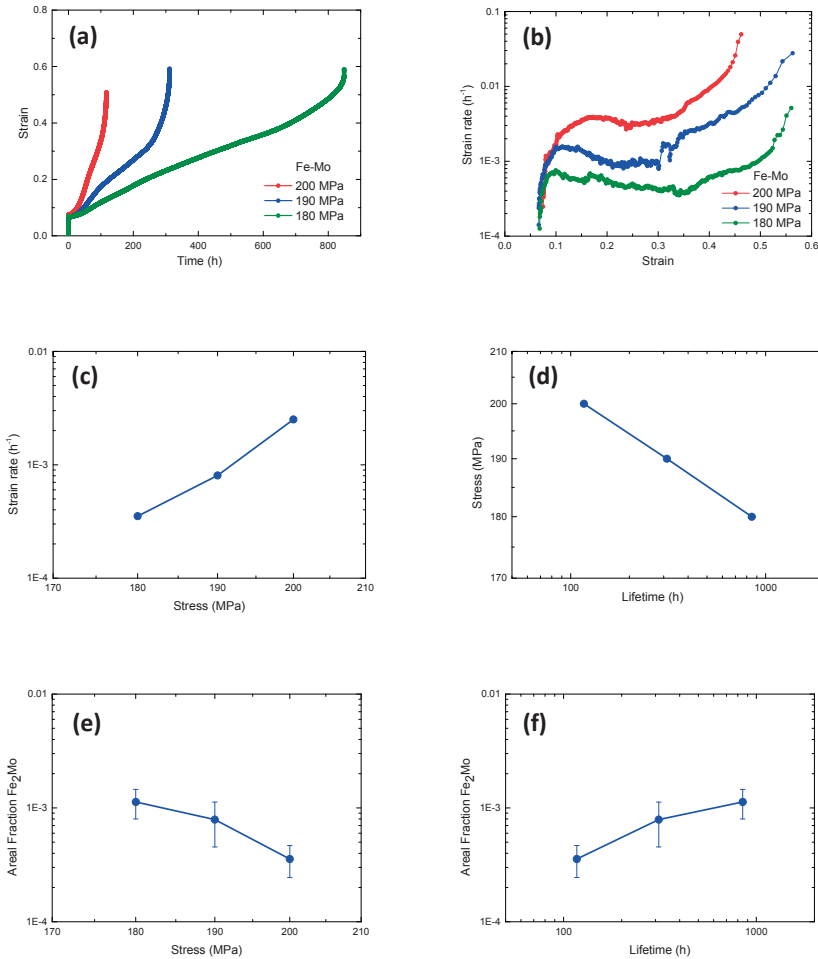


**Fig. 6.1.** (a) Creep curves for the Fe-Mo alloy for constant stress at a temperature of 823 K (550 °C) and (b) the corresponding strain rate as a function of strain. From these, (c) the steady-state strain rate and (d) the creep lifetime as a function of applied stress are determined. From an image analysis of the SEM data the area fraction of the Fe<sub>2</sub>Mo Laves phase is deduced as a function of (e) stress and (f) lifetime.

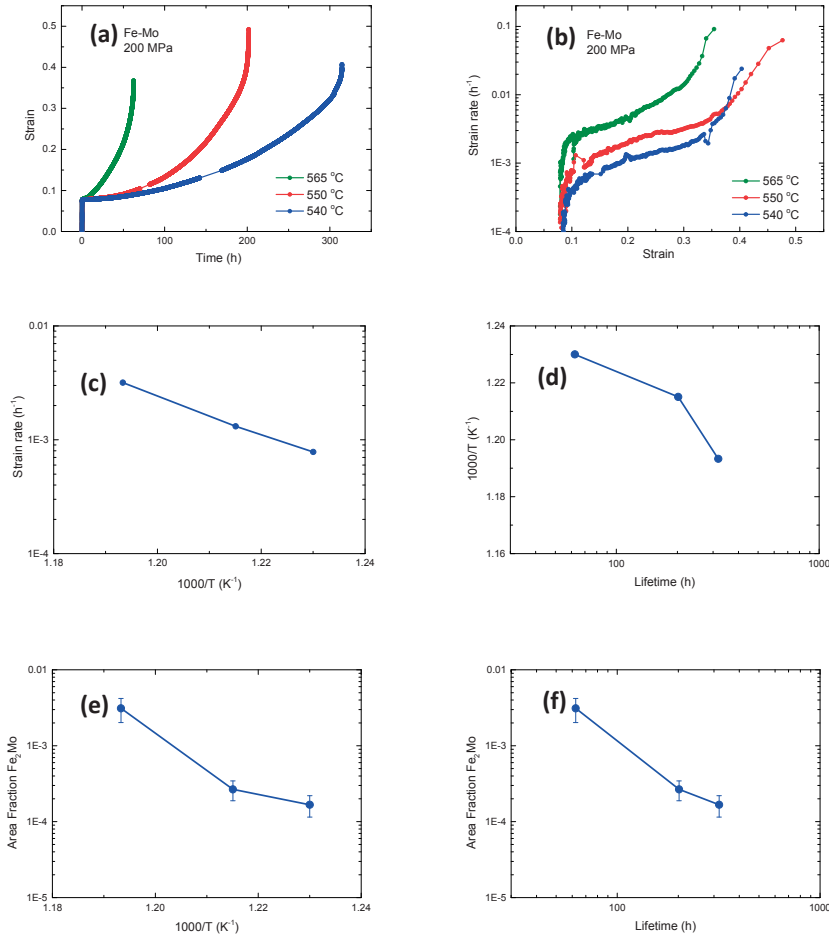


**Fig. 6.2.** (a) Creep curves and (b) strain rate as a function of strain at different temperatures for the Fe-Mo alloy at a stress of 200 MPa. (c) Arrhenius plot illustrating the temperature dependence of the strain rate. From an image analysis of the SEM data the area fraction of the Fe<sub>2</sub>Mo Laves phase is deduced as a function of (e) temperature and (f) lifetime.

### 6.3.2. Scanning electron microscopy

The fracture surface after creep failure for a stress of 200 MPa and a temperature of 823 K (550 °C) is shown in Fig. 6.3 and indicates a ductile fracture mode. Mo-rich precipitates are observed on the fracture surface, as indicated by the arrows. The phase composition was analyzed by EDS (a quantitative analysis of the phase composition will be presented with the TEM and atom probe measurements).



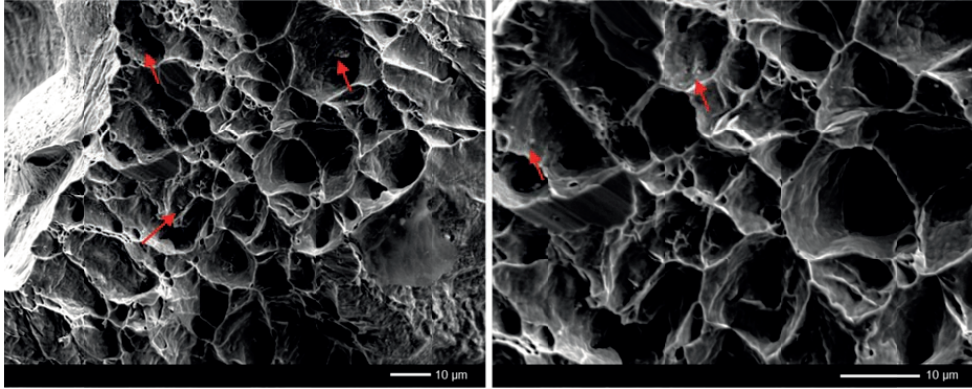


**Fig. 6.3.** Fracture surfaces of the Fe-Mo alloy after creep for an applied stress of 200 MPa at a temperature of 823 K (550 °C). Red arrows mark the Mo-rich precipitates.

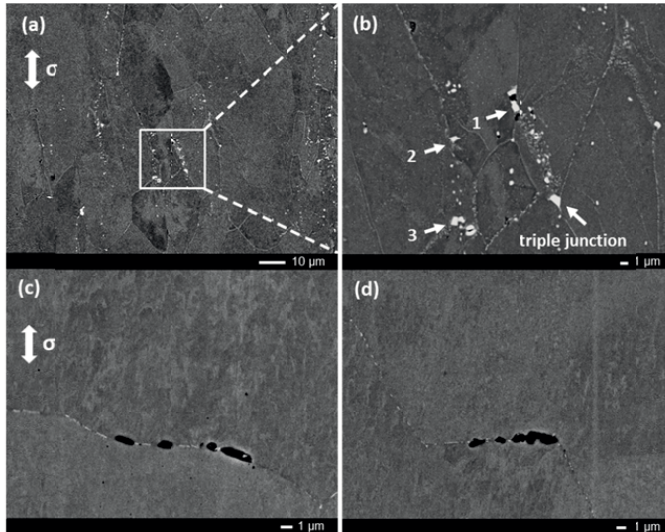


**Fig. 6.4.** Micrographs of the Fe-Mo alloy after creep for (a-b) a stress of 180 MPa at a temperature of 823 K (550 °C), (c-d) a stress of 200 MPa at a temperature of 838 K (565 °C).

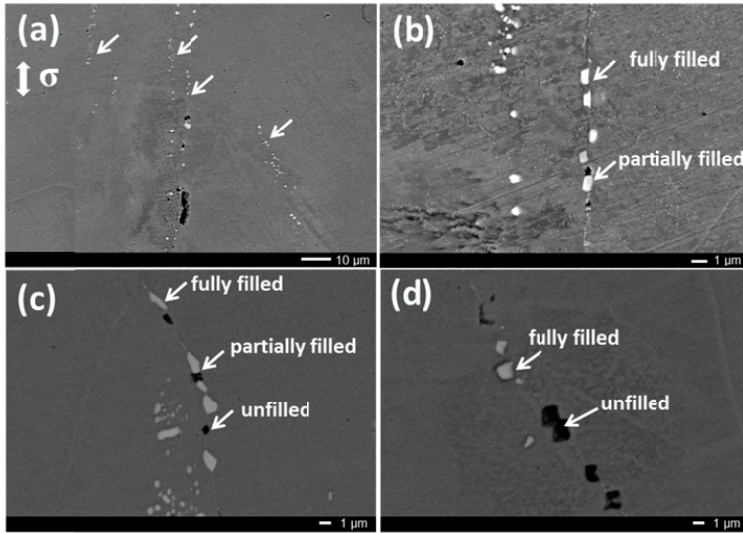


**Fig. 6.5.** Micrographs of the Fe-Mo alloy after creep for a stress of 160 MPa at a temperature of 838 K (565 °C) demonstrating cavities and precipitation at grain boundaries parallel to the loading direction.

Fig. 6.4 shows the SEM morphology of the Fe-Mo alloy after creep failure. In Fig 6.4a and 6.4b the microstructure after creep at a stress of 180 MPa and a temperature of 823 K (550 °C) is shown. The direction of the applied stress is indicated in the upper left hand corner. In the SEM picture of Fig. 6.4a the majority of grains is elongated along the stress direction. Such a grain deformation is expected for a fracture strain of about 60%. Mo-rich deposits are formed heterogeneously along the grain boundaries. The largest precipitates are formed at triple junctions, which are also the preferential nucleation sites for creep cavities. At high magnification (Fig. 6.4b) the microstructure shows a partial filling of a microscopic defect site (1), as well as irregular-shaped precipitates that are not connected to a pore, marked by (2) and (3). These observations are explained by a preferential Mo segregation on the creep cavity surface and a continuous growth of the formed precipitates until a complete filling of the creep cavities is achieved. Fig. 6.4c-d shows the microstructure after creep at a higher temperature of 838 K (565 °C) for a stress of 200 MPa. Again, heterogeneous precipitation along grain boundaries is clearly visible. Creep cavities are mainly formed along grain boundaries perpendicular to the stress direction, which are the favorite sites for cavity nucleation. However, the growth and coalescence of these cavities is relatively fast, so that the Mo may not have had sufficient time to precipitate at the cavity surface and fill the damage site completely.

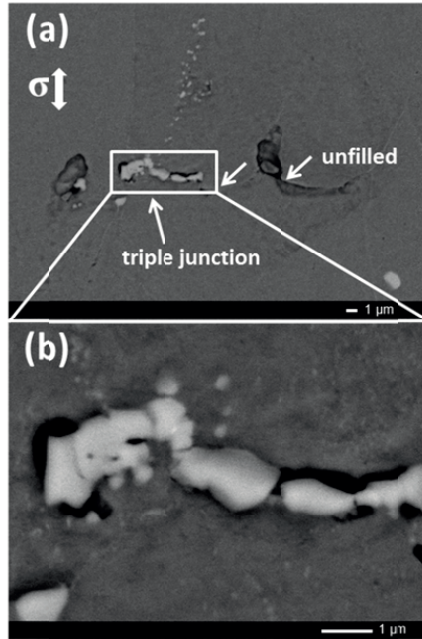


**Fig. 6.6.** Micrographs of the Fe-Mo alloy after creep for a stress of 160 MPa at a temperature of 838 K (565 °C) demonstrating cavities and precipitation at grain boundaries perpendicular to the loading direction.

In order to observe a more pronounced interaction between the creep damage and the site-selective Mo precipitation at the free cavity surface a lower load of 160 MPa was applied at the higher temperature of 838 K (565 °C). The strain at rupture reaches a relatively high value of about 60% for which damage is observed at: (i) grain boundaries oriented perpendicular to the loading direction, at (ii) triple points and (iii) at sliding grain boundaries oriented at a shallow angle to the loading direction. Fig. 6.5 depicts SEM images of creep damage and site-selective Mo precipitation along parallel grain boundaries. Examples of (i) unfilled cavities, (ii) partially filled cavities and (iii) fully filled cavities can clearly be observed. Creep damage and site-selective Mo precipitation is not restricted to parallel grain boundaries, but also seems to occur in some localized deformation bands within the grains, as marked by the white arrows in Fig. 6.5a.

In Fig. 6.6 a SEM image illustrates the creep damage and Mo precipitation observed at grain boundaries oriented perpendicular to the loading direction. The partially filled triple junction reveals a complex precipitate phase comprised of several individual crystallites. By combining a series of SEM images the area fraction of Fe<sub>2</sub>Mo precipitates was obtained for the studied creep conditions. The obtained results are shown in Figs. 6.1 and 6.2 and summarized in Table 6.2.

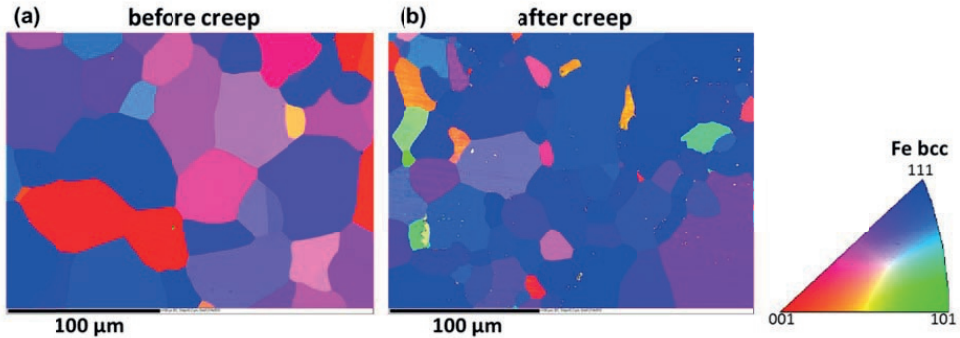


**Fig. 6.7.** Orientation maps for the solutionized Fe-Mo alloy (a) before and (b) after creep for a stress of 160 MPa at a temperature of 838 K (565 °C). The colors correspond to the inverse pole figure with respect to the sample surface normal. The white areas in the creep-failed sample correspond to the Laves phase  $\text{Fe}_2\text{Mo}$ .

To obtain more insight into the microstructure evolution during creep EBSD experiments were performed. In Fig. 6.7 orientation maps for the solutionized Fe-Mo alloy are shown (a) before and (b) after creep at a stress of 160 MPa and a temperature of 838 K (565 °C). In contrast to earlier measurements on creep-loaded solutionized Fe-Au alloys [22] no indications for an extensive sub-grain formation were observed. However, the average grain size for the Fe-rich *bcc* matrix phase derived from the EBSD figures was reduced from 33 μm before creep (Fig. 6.7a) to 22 μm after creep (Fig. 6.7b). A comparison of the orientation maps before and after creep suggest that some  $\langle 111 \rangle$  micro-texture has formed during the creep tests. The white areas in the creep-failed sample correspond to the Laves phase  $\text{Fe}_2\text{Mo}$ .

### 6.3.3. Transmission electron microscopy

TEM measurements were performed on the Fe-Mo alloy after creep at 180 MPa and 823 K (550 °C) to characterize the structure and composition of the precipitates formed in the grain interior and the precipitates formed at the grain-boundary cavities. As shown in Fig. 6.8, nanoscale precipitates are formed in the matrix after creep. A high dislocation density is present due to the extensive plastic deformation during creep (Figs. 6.8a and 6.8b). Previous TEM studies on similar model alloys (Fe-Cu, Fe-Cu-B-N, Fe-Au, Fe-Au-B-N) did not reveal a high dislocation density for undeformed specimens that were heated to 823 K (550 °C) [16,17,18,22].



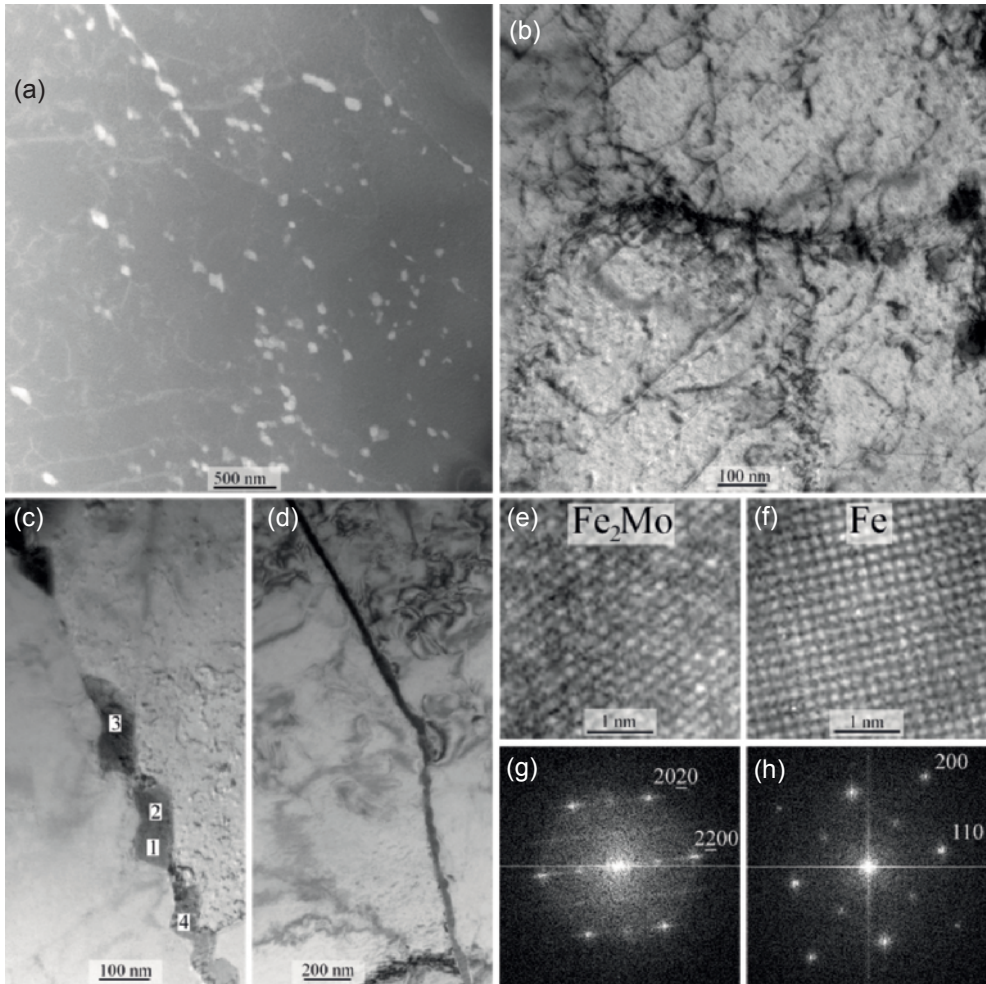


**Fig. 6.8.** TEM images of the Fe-Mo alloy after creep at 180 MPa and 823 K (550 °C). (a) STEM annular dark field showing matrix precipitates. (b) BF showing matrix dislocations. (c,d) BF showing grain-boundary precipitates. (e,f) HREM taken from areas near position 4 in (c) in the precipitates and the matrix respectively. The associated Fourier transforms in (g) and (h) were taken from a larger area than shown in (e) and (f).

Precipitates are also present along grain boundaries, as shown in Fig. 6.8c. Some grain boundary are completely covered with a thin film of the  $\text{Fe}_2\text{Mo}$  phase (see Fig. 6.8d). The nature of the precipitates and film was identified by EDS and by lattice imaging. For example, the Fe and Mo composition was measured with the electron beam on 4 different positions on the precipitates in Fig. 6.8c (see numbers) as  $33(\pm 1)$ ,  $33(\pm 1)$ ,  $32(\pm 2)$  and  $31(\pm 2)$  at.% Mo, consistent with a  $\text{Fe}_2\text{Mo}$  type precipitate. Several lattice images were obtained from different precipitates that showed lattice spacings and lattice-plane angles consistent with an hexagonal  $\text{Fe}_2\text{Mo}$  lattice structure with  $a =$

0.472 nm and  $c = 0.772$  nm. In thermodynamic equilibrium the presence of the  $\text{Fe}_2\text{Mo}$  phase in combination with the Fe-rich *bcc* matrix phase is expected for our binary Fe-Mo alloy at a temperature of 823 K (550 °C) [31]. One of the lattice images covers an area of Fig. 6.8c that contains precipitate number 4 and the neighboring matrix. The associated Fourier transform in Fig. 6.8g shows that the electron beam was aligned along the [0001] axis of the hexagonal structure for precipitate number 4. Part of the same lattice image of the matrix neighboring precipitate number 4 is shown in Fig. 6.8f. The associated Fourier transform (of a larger area) in Fig. 6.8h shows the electron beam direction in the Fe matrix is [100]. The indices in the Fourier transforms further indicate that within a few degrees the orientation relation  $(\underline{2}\underline{2}00)_{\text{Fe}_2\text{Mo}} \parallel (110)_{\text{Fe}}$  is found. Hence, for this precipitate an orientation relationship with one of the Fe grains is approximately:

$$\begin{aligned} [0001]_{\text{Fe}_2\text{Mo}} &\parallel [100]_{\text{Fe}} \\ (\underline{2}\underline{2}00)_{\text{Fe}_2\text{Mo}} &\parallel (110)_{\text{Fe}}. \end{aligned}$$

Other orientation relationships exist as well, as expected for precipitates at a grain boundary.

#### 6.3.4. Atom probe tomography

APT was employed to quantify grain boundary segregation, the chemical composition of the Mo-rich precipitates at the grain boundaries, the matrix composition in direct contact to the grain-boundary precipitates and the matrix composition far away from the grain boundaries. In total six tips with a total volume of  $3.5 \times 10^6 \text{ nm}^3$  were measured. The tips were prepared from two lift-outs, one at the grain boundary and the other in the matrix.

According to thermodynamic calculations two phases are in equilibrium at 823 K (550 °C) in the Fe-Mo alloy investigated here: the Laves phase  $\text{Fe}_2\text{Mo}$  with 33 at.% Mo and the  $\alpha$ -iron matrix with 0.8 at.% Mo. Our APT results summarized in Fig. 6.9 indicate that the Mo concentration in the grain boundary precipitates, in the  $\alpha$ -iron matrix close to the grain-boundary precipitates and in the  $\alpha$ -iron matrix far away from the grain boundaries amount to 36 at.%, 2.0 at.% and 3.5 at.% Mo, respectively. The measured composition of the precipitates and the adjacent matrix is in close agreement with the predicted equilibrium values. However, the composition of the matrix further away from the grain boundaries is still close to the nominal alloy composition of 3.7 at.% Mo, and thus far from thermodynamic equilibrium (this was also found from EDS in TEM). It can be concluded that although the system is close to local equilibrium at the precipitates, the overall system is still far away from thermodynamic equilibrium. Mo is thus still supersaturated in the matrix and available for further healing of creep defects.

Two different grain boundaries were measured and the amount of segregated solutes was analyzed by means of a 1-D concentration profile and ladder diagrams [32]. As indicated in Fig. 6.10, the crystallographic character of the interfaces was analyzed

based on the crystallographic information contained in the detector event histograms of the atom probe runs by means of atom-probe crystallography [33]. Both measured grain boundaries were identified as high-angle grain boundaries. At a grain boundary with a disorientation angle of about  $16^\circ$  a Mo solute excess of  $3.15 \text{ at/nm}^2$  was measured (Figs. 6.9a and 6.9b), while at a grain boundary with a disorientation angle of about  $35^\circ$  a Mo excess value of  $3.37 \text{ at/nm}^2$  was measured (Fig. 6.10). Such a variation in the solute excess between two different grain boundaries is normal, as the enrichment of solutes at grain boundaries is highly dependent on their crystallographic character [34,35].

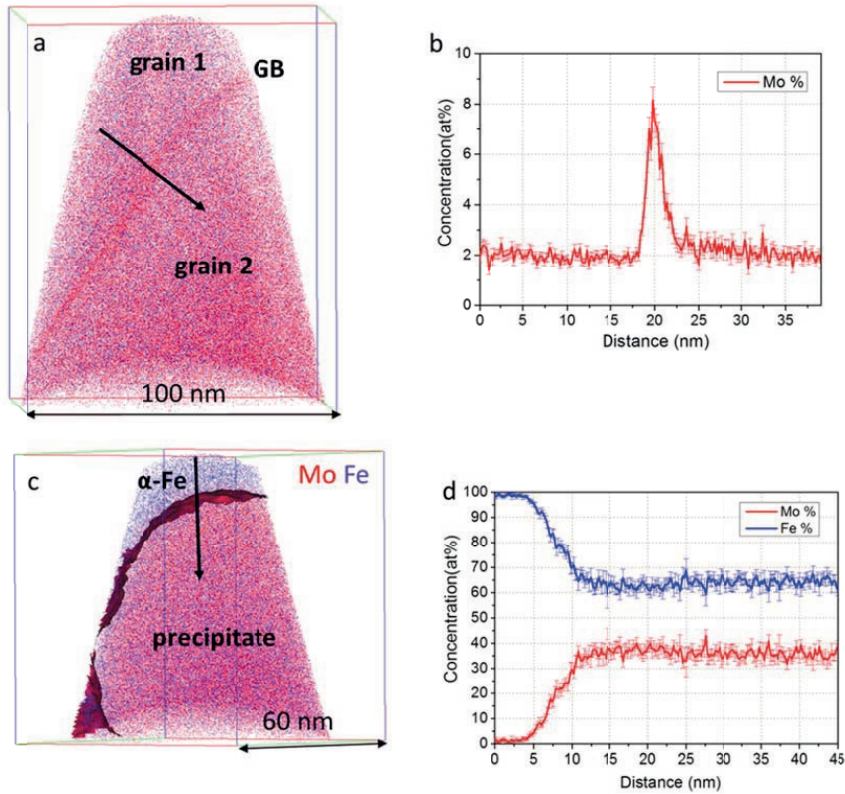


**Fig. 6.9.** Atom probe tomography data on the Fe-Mo alloy after creep at a stress of 180 MPa at a temperature of 823 K (550 °C), showing (a) a grain boundary (GB) with a Mo segregation of up to 8 at.% (b) and (c) a Mo-rich particle at a grain boundary with a concentration of 36 at.% Mo (d). All elements except Fe (blue) and Mo (red) are removed for clarity.

## 6.4. Discussion

### 6.4.1. Autonomous repair of creep damage

The fractographs of the creep rupture surface in Fig. 6.3 indicate that intergranular failure is the dominant failure mode for this material. As indicated in Figs. 6.1 and 6.2, creep failure occurs at a relatively high strain of about 60%. The electron microscopy images of Figs. 6.4-6 indicate that creep damage forms at (i) grain boundaries oriented perpendicular to the loading direction, (ii) grain boundaries oriented along the loading direction, (iii) grain-boundary triple points and finally, to a lower extent, at (iv) localized deformation bands inside the grains. The shape of the larger Mo-rich deposits clearly reflects the morphology of the creep cavities, demonstrating that site-selective deposition of the Mo-rich phase at free creep cavity surfaces.

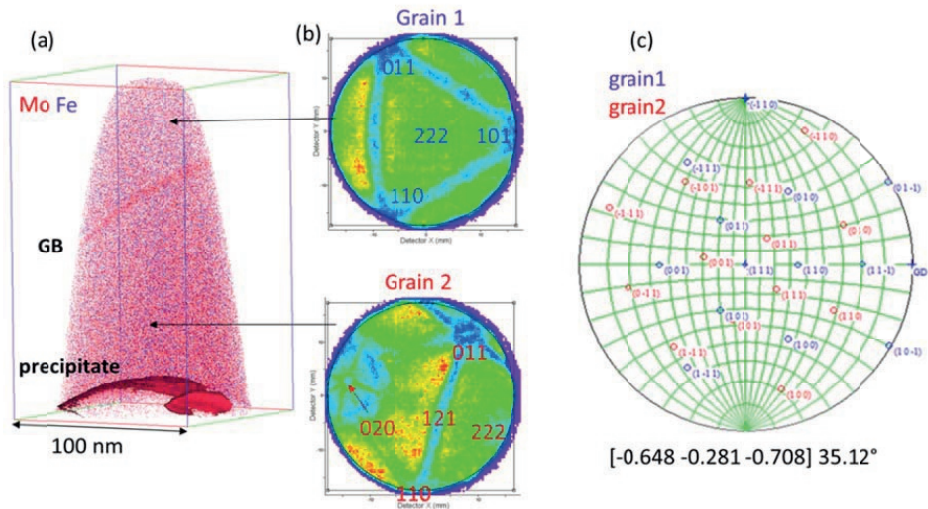


**Fig. 6.10.** Atom probe crystallographic analysis of a grain boundary (GB); (a) an ion map, containing a grain boundary and a Mo-rich precipitate, highlighted by a 13 at.% Mo isosurface; (b) detector event histogram of the upper and lower grain with labelled crystallographic poles; (c) standard stereographic projection, showing the poles of both grains. The grain boundary disorientation was calculated using the TOCA software (Tools for Orientation Determination and Crystallographic Analysis) [39,40].

In order to evaluate the kinetics of the self-healing process it is essential to obtain the effective grain-boundary and volume diffusion coefficient for Mo in the Fe matrix. As no information is available for the grain-boundary diffusion coefficient of Mo in pure iron, the Fe self diffusion along grain boundaries is applied. At 823 K (550 °C), which is in the middle of the explored temperature regime, the grain



boundary diffusivity in iron amounts to  $D_{GB} = 2.4 \times 10^{-14} \text{ m}^2\text{s}^{-1}$  [36], while the volume diffusivity of Mo in iron is estimated to be  $D_V = 2.8 \times 10^{-21} \text{ m}^2\text{s}^{-1}$  [30]. Using the literature value for the volume diffusion coefficient of Mo in an iron matrix at 823 K (550 °C) and a time to failure of 800 h the estimated diffusion length amounts to  $2\sqrt{D_V t} \approx 0.2 \text{ }\mu\text{m}$  for volume diffusion and  $2\sqrt{D_{GB} t} \approx 500 \text{ }\mu\text{m}$  for grain-boundary diffusion. The large difference between the diffusion length and the Mo-depletion distance indicates that only a thin layer close to the grain boundaries will be solute depleted. This is supported by the current atom probe results which indicate that the  $\alpha$ -Fe matrix further away from the grain boundaries still has the nominal composition. In previous experiments on Fe-Au alloys [21,22] it was found that the value of the effective volume diffusion coefficient was three orders of magnitude larger than expected as a result of an extensive subgrain formation during creep loading. For the Fe-Mo alloy the EBSD experiments did not show experimental evidence for extensive subgrain formation (Fig. 6.7). The observed distance between the deformation bands in the Fe-Mo alloy is of the order of the grain size (see Fig. 6.4), and therefore, the generated diffusion pathways are macroscopically spaced in Fe-Mo (rather than microscopically in Fe-Au). As a result, these deformation bands are not expected to contribute significantly to the effective volume diffusion and the solute depleted regions remain relatively narrow in the vicinity of the grain boundaries that act as fast diffusion pathways.

#### 6.4.2. Requirements for the healing of creep damage

Our current experiments on the self-healing behavior of creep damage in Fe-Mo alloys are in qualitative agreement with those obtained for the Fe-Au alloy system [21,22]. From these studies the following requirements to achieve an efficient autonomous repair of creep damage can be formulated [37]:

- 1) Mobile *healing agent*: high mobility of the segregating solute element.
- 2) *Driving force* towards the damage site:
  - a) Chemical potential provided by super-saturation of the chosen solute.
  - b) Gain in strain and surface energy for precipitates located at creep cavities.
- 3) Damage formation acts as a *trigger* for precipitation at the free surface of a damage site.
- 4) *Site-selective precipitation*: a high energy barrier for nucleation at non-damage sites.
- 5) Sufficient *interfacial bonding* between matrix and precipitate.
- 6) A high *healing rate* compared to the rate of damage formation.
- 7) Sufficiently large *reservoir of healing agents* within the matrix to heal the damage volume.

In the following the estimation of the healing potential of local creep damage (i.e. open pores at grain boundaries) is discussed, given the available reservoir of healing

agents (supersaturated solute). Furthermore, we will discuss the relative healing efficiency.

### 6.4.3. Solute reservoir for the healing of creep damage

If the filling (i.e. autonomous repair) of creep cavities is purely driven by the supersaturation of the solute Mo atoms, then it can easily be estimated how much damage can potentially be healed by balancing the volume fraction of grain-boundary creep cavities  $f_D$ , with the volume fraction that can maximally be filled by the deposit formed by the supersaturated solute  $f_H$ .

The volume fraction of creep damage can be estimated as  $f_D = N_C V_C / V_G$ , where  $N_C$  is the average number of grain-boundary creep cavities per grain,  $V_C$  is the average volume of a single creep cavity and  $V_G$  is the average grain volume. For a lens-shaped creep cavity one finds  $V_C = \pi \psi d_C^3 / 6$ , where  $d_C$  is the cavity diameter and  $\psi = (2 - 3 \cos \alpha + \cos^3 \alpha) / 2 \sin^3 \alpha \approx 0.69$  a geometrical factor that is defined by the opening angle  $\alpha \approx 75^\circ$  of the creep cavity [38]. Assuming a spherical grain shape, the grain volume amounts to  $V_G = \pi d_G^3 / 6$ , where  $d_G$  is the grain diameter. Combining these relations leads to:

$$f_D = \psi N_C (d_C / d_G)^3. \quad (6.2)$$

The volume fraction of creep damage that can maximally be healed by the supersaturated solute  $f_H$  can be evaluated from the initially homogeneously distributed nominal solute concentration  $x_0$  (= 3.7 at.% Mo for this alloy), the equilibrium solute concentration in the matrix  $x_m$  (= 0.8 at.% Mo at  $T = 823$  K (550 °C)) and a scaling factor  $R \approx 1$  for the effective volume occupied by the solute atom in the precipitate compared to its volume occupied in the solute:

$$f_H = R(x_0 - x_m). \quad (6.3)$$

The scaling factor  $R$  can be approximated by the difference in atomic volume occupied by the solute Mo relative to Fe:  $R \approx v_{Mo} / v_{Fe} = 1.30$ . The maximum phase fraction of grain-boundary precipitates depends on the solute concentration in the precipitate  $x_p$  (= 33.3 at.% Mo for the Fe<sub>2</sub>Mo precipitates) and amounts to  $f_p = (x_0 - x_m) / x_p = 9.3\%$ .

The consumed fraction of the healing reservoir  $\chi$  can now be defined as:

$$\chi = \frac{f_D}{f_H} = \left( \frac{\psi}{R} \right) \left( \frac{N_C}{x_0 - x_m} \right) \left( \frac{d_C}{d_G} \right)^3 \leq 1. \quad (6.4)$$

Initially there is no damage, and therefore  $\chi = 0$ . During creep this value increases until the reservoir of supersaturated solute is depleted when a critical value of  $\chi = 1$  is reached. From Eq. 6.4 it can be seen that for a given type of healing precipitate the critical value for which the solute reservoir is depleted is reached later when: (i) the grains are larger, (ii) the supersaturation is higher, (iii) the creep cavities are smaller and (iv) the number of creep cavities per grain is lower. As expected, the

grain size and cavity size are the dominant contributions. For an average grain size of  $d_G = 20 \mu\text{m}$ , a cavity size of  $d_c = 1 \mu\text{m}$  and a supersaturation of  $\Delta x = x_0 - x_m = 3 \text{ at.}\%$  Mo about 450 cavities ( $N_C$ ) can be filled at the grain boundary of a single grain before the supersaturation is exhausted ( $\chi = 1$ ).

It should however be noted that the above discussion is only valid for long time scales. For creep experiments with a finite time, not all supersaturated solute may have had the time to diffuse towards the grain boundaries and contribute to the filling of the creep cavities. As discussed before, the estimated diffusion length within the grain amounts to  $2\sqrt{D_V t}$ . The diffusion-limited volume fraction that can maximally be healed  $f_H^{\text{kin}}$  is reduced to the fraction of the grain that is located within a diffusion length of the grain boundary:

$$f_H^{\text{kin}} = f_H \left\{ 1 - \left( 1 - \frac{4\sqrt{D_V t}}{d_G} \right)^3 \right\} \approx f_H \left( \frac{12\sqrt{D_V t}}{d_G} \right). \quad (6.5)$$

Only when the diffusion length  $2\sqrt{D_V t}$  is larger than the grain radius  $d_G/2$ , all available solute reserves can contribute to pore filling, resulting in  $f_H^{\text{kin}} = f_H$ . This situation is reached after a characteristic time of  $t_0 = d_G^2/16D_V$ . Using the literature value for volume diffusion coefficient of Mo in bcc Fe of  $D_V = 2.8 \times 10^{-21} \text{ m}^2\text{s}^{-1}$  at 823 K (550 °C) [30] and a time to failure of 800 h the estimated diffusion length amounts to  $2\sqrt{D_V t} \approx 0.2 \mu\text{m}$ . For a grain size of  $d_G = 20 \mu\text{m}$  the available solute is reduced by a factor  $f_H^{\text{kin}} / f_H \approx 12\sqrt{D_V t} / d_G = 6\%$ , which means that the quoted maximum number of cavities per grain ( $N_C$ ) that can be healed reduces from 450 to about 30 under the given conditions.

For the kinetically limited regime the maximum number of cavities that can be healed now scales as  $N_C^{\text{max}}(t) \propto \sqrt{t}$ . For steady-state creep the number of cavities per grain  $N_C(t) = \dot{N}_C t$  however scales linearly with time. As a result, the part of the reservoir accessible by diffusion may potentially run out (when  $t_1 < t_0$ ) before all supersaturated solute is consumed, which then provides a limit on the maximum allowed strain rate to provide efficient filling of the cavities.

#### 6.4.4. Healing efficiency of creep damage

The previously developed model for the filling of creep cavities [22] will be used to estimate the average filling ratio  $\eta$  of creep cavities as a function of (increasing) applied stress (or decreasing failure time). It is assumed that the site-selective precipitation at the cavities starts immediately after the nucleation of creep cavities. The lifetime generally scales with the applied stress  $\sigma$  as:  $t_f = k\sigma^{-n}$ , where  $k$  is a temperature-dependent constant and, as discussed in section 3, the stress exponent amounts to  $n \approx 15$  for the Mo alloy.

The healing time  $t_h$  can be evaluated by assuming a time-dependent creep cavity volume of  $V_c(t) = V^* + a\sigma t$  and a precipitate volume of  $V_p(t) = bt$ . The time to fill an individual creep cavity  $t_h = (V^* / b) / \{1 - \sigma / \sigma_c\}$  now strongly depends on the applied stress, where  $\sigma_c = b/a$  is the critical stress beyond which the cavity grows faster than the filling takes place [22]. The corresponding volume of the filled cavity is  $V_h = bt_h = V^* / \{1 - \sigma / \sigma_c\}$ . The fraction of filled cavities now amounts to:

$$\eta \approx \frac{t_f - t_h}{t_f} = 1 - \left( \frac{V^*}{bk} \right) \frac{\sigma^n}{1 - \sigma / \sigma_c}. \quad (6.6)$$

Although the critical stress is expected to be beyond 200 MPa, the high value for the stress exponent  $n \approx 15$  clearly limits the expected stress range for which filling of the creep cavities by Mo precipitates is effective at a given temperature.

#### 6.4.5. Effect of autonomous creep cavity filling on the macroscopic creep behavior

It is not straightforward to quantify the effect of healing on the overall creep behavior experimentally. The best would be to have a reference sample that is not self healing, but has comparable creep properties. In a previous paper we established that self healing extends the lifetime by using both solutionized and solution-depleted Fe-Cu alloys as reference system for the studied Fe-Au alloys [21,22]. In these experiments it was found that the filling of creep cavities significantly reduces the strain rate. The same mechanisms are expected to apply for creep in Fe-Mo alloys. More experimental and modeling studies are required to establish the link between the microscopic creep-cavity filling and the macroscopic creep rate in detail.

### 6.5. Conclusions

We have studied the self-healing potential of creep-induced defects in a high-purity Fe-Mo alloy (6.2 wt.% Mo) at temperatures of 813, 823 and 838 K (540, 550 and 565 °C). The creep curves at different constant stresses indicate a ductile fracture mode with maximum strains up to 60%. Electron microscopy measurements after creep clearly indicate a filling of creep cavities by Fe<sub>2</sub>Mo precipitates. In some cases a partial filling of the creep cavities is observed, while in most cases a complete filling is found. The presence of relatively large precipitates with irregular shapes indicates a filling of the creep cavities. The density of generated cavities and the formed precipitates strongly increases with temperature. As a result of the relatively large strain at rupture creep cavities are formed not only at grain boundaries oriented perpendicular to the loading direction and at triple points, but also at sliding grain boundaries oriented along the loading direction.

The demonstrated site-selective Fe<sub>2</sub>Mo precipitation at creep cavity surfaces provides the opportunity to incorporate self-healing capabilities in high-temperature creep steels that often already contain Mo for solid-solution strengthening.

Supersaturation of Mo in the alloy can provide a desirable self-healing healing potential to further extend the creep lifetime. Achieving this requires a careful design of the alloy composition and heat treatment. Considering the solubility of 1.4 wt.% Mo for binary Fe-Mo at 823 K (550 °C), the Mo concentration can probably be reduced to about 3 wt.% Mo (about 1 at.% supersaturation) without sacrificing the healing capabilities.

### Acknowledgements

This research was financially supported by the innovation-oriented research program (IOP) on self-healing materials of the Dutch Ministry of Economic Affairs, Agriculture and Innovation (IOP project SHM01017). We thank Marcel Sluiter and Casper Versteyleen for fruitful discussions and Gijs Langelaan for assistance with the development of the creep tester.

### References

1. R.L. Klueh: *Mater. Sci. Eng.*, 1978, vol. 35, pp. 239-53.
2. R.L. Klueh: *Nucl. Eng. Des.*, 1982, vol. 72, pp. 329-44.
3. T. Sourmail: *Mater. Sci. Techn.*, 2001, vol. 17, pp. 1-14.
4. A. Fuchs and B. Ilschner: *Acta Metall.*, 1969, vol. 17, pp. 701-10.
5. H. Oikawa, D. Mizukoshi, and S. Karashima: *Metall. Trans. A*, 1978, vol. 9A, pp. 1281-5.
6. H. Oikawa, K. Kaneko, and S. Hasegawa: *Scripta Metall.*, 1984, vol. 18, pp. 393-6.
7. S. Nanba and H. Oikawa: *Mater. Sci. Eng. A*, 1988, vol. 101, pp. 31-7.
8. E. Hornbogen: *J. Appl. Phys.*, 1961, vol. 32, pp. 135-9.
9. D. Isheim: *Acta Mater.*, 2000, vol. 48, pp. 2873-83.
10. J. Hald: *Int. J. Pres. Vessels Pip.*, 2008, vol. 85, pp. 30-7.
11. S. Zhu, M. Yang, X.L. Song, Z. Zhang, L.B. Wang, S. Tang, and Z.D. Xiang: *Mater. Sci. Eng. A*, 2014, vol. 619, pp. 47-56.
12. K. Laha, J. Kyono, S. Kishimoto, and N. Shinya: *Scripta Mater.*, 2005, vol. 52, pp. 675-8.
13. K. Laha, J. Kyono, and N. Shinya: *Scripta Mater.*, 2007, vol. 56, pp. 915-8.
14. K. Laha, J. Kyono, and N. Shinya: *Philos. Mag.*, 2007, vol. 87, pp. 2483-505.
15. K. Laha, J. Kyono, and N. Shinya: *Metall. Mater. Trans. A*, 2011, vol. 43A, pp. 1187-97.
16. S.M. He, N.H. van Dijk, H. Schut, E.R. Peekstok, and S. van der Zwaag: *Phys. Rev. B*, 2010, vol. 81, p. 094103.
17. S.M. He, N.H. van Dijk, M. Paladugu, H. Schut, J. Kohlbrecher, F.D. Tichelaar, and S. van der Zwaag: *Phys. Rev. B*, 2010, vol. 82, p. 174111.
18. S. Zhang, J. Kohlbrecher, F. D. Tichelaar, G. Langelaan, E. Brück, S. van der Zwaag, and N. H. van Dijk: *Acta Mater.*, 2013, vol. 61, pp. 7009-19.
19. S. Zhang, H. Schut, J. Čížek, F.D. Tichelaar, E. Brück, S. van der Zwaag, and N.H. van Dijk: *J. Mater. Sci.*, 2014, vol. 49, pp. 2509-18.

20. S. Zhang, G. Langelaan, J.C. Brouwer, W.G. Sloof, E. Brück, S. van der Zwaag, and N.H. van Dijk: *J. Alloys Comp.*, 2014, vol. 584, pp. 425-9.
21. S. Zhang, C. Kwakernaak, W. G. Sloof, E. Brück, S. van der Zwaag, and N.H. van Dijk: *Adv. Eng. Mater.*, 2015, vol. 17, pp. 598-603.
22. S. Zhang, C. Kwakernaak, F. D. Tichelaar, W.G. Sloof, M. Kuzmina, M. Herbig, D. Raabe, E. Brück, S. van der Zwaag, and N.H. van Dijk: *Metall. Mater. Trans. A*, 2015, vol. 46A, pp. 5656-70.
23. K. Thompson, B. Gorman, D.J. Larson, B. van Leer, and L. Hong: *Microsc. Microanal.*, 2006, vol. 12, pp. 1736-7.
24. B.P. Geiser, D.J. Larson, E. Oltman, S. Gerstl, D. Reinhard, T.F. Kelly, and T.J. Prosa: *Microsc. Microanal.*, 2009, vol. 15 pp. 292-3.
25. M.J. Luton and C.M. Sellars: *Acta Metall.*, 1969, vol. 17, pp. 1033-43.
26. T. Sakai and J.J. Jonas: *Acta Metall.*, 1984, vol. 32, pp. 189-209.
27. F. Otto, G.B. Viswanathan, E.J. Payton, J. Frenzel, and G. Eggeler: *Acta Mater.*, 2012, vol. 60, pp. 2982-98.
28. O.D. Sherby: *Acta Metall.*, 1962, vol. 10, pp. 135-47.
29. S. Spigarelli, L. Kloc, and P. Bontempi: *Scripta Mater.*, 1997, vol. 37, pp. 399-404.
30. H. Nitta, T. Yamamoto, R. Kanno, K. Takasawa, T. Iida, Y. Yamazaki, S. Ogu, and Y. Iijima: *Acta Mater.*, 2002, vol. 50, pp. 4117-25.
31. T.B. Massalski, H. Okamoto, P.R. Subramanian, and L. Kaeprzak: *Binary Alloy Phase Diagrams*, 2nd ed., ASM International, Materials Park, 1990.
32. B.W. Krakauer and D.N. Seidman: *Phys. Rev. B*, 1993, vol. 48, pp. 6724-7.
33. M.P. Moody, F. Tang, B. Gault, S.P. Ringer, and J.M. Cairney: *Ultramicroscopy*, 2011, vol. 111, pp. 493-9.
34. P. Lejček, S. Hofmann, and V. Paidar: *Acta Mater.*, 2003, vol. 51, pp. 3951-3963.
35. M. Herbig, D. Raabe, Y. J. Li, P. Choi, S. Zaeferrer, and S. Goto: *Phys. Rev. Lett.*, 2014, vol. 112, pp. 126103.
36. G. Stechauner and E. Kozeschnik: *J. Mater. Eng. Perform.*, 2014, vol. 23, pp. 1576-9.
37. S. van der Zwaag and E. Brinkman: *Self Healing Materials: Pioneering research in the Netherlands*, IOS Press, Amsterdam, 2015.
38. R. Raj and M.F. Ashby: *Acta Metall.*, 1975, vol. 23, pp. 653-66.
39. S. Zaeferrer: *Adv. Imag. Electron Phys.*, 2002, vol. 125, pp. 355-415.
40. S. Zaeferrer: *J. Appl. Crystallogr.*, 2000, vol. 33, pp. 10-25.



---

# Chapter 7

## **Autonomous filling of creep cavities by dynamic precipitation in Fe-W alloys studied by synchrotron X-ray nanotomography**

We have studied the self-healing of creep damage of a high-purity Fe-3.8 wt.% W binary alloy at a temperature of 550 °C and for several constant loads. The simultaneous evolution of creep cavities and precipitates was studied in 3D in a broad size range from the nanometer to the micron scale using synchrotron X-ray nanotomography. The 3D images with a resolution down to 30 nm demonstrate an autonomous filling of the creep cavities by Fe<sub>2</sub>W precipitation in the binary Fe-W alloy. The combined input of a shape classification and the spatial distribution provides an effective approach to identify isolated and linked objects. The degree of filling by precipitation for individual creep cavities was determined for all partially filled cavities. Two clearly different types of behavior are observed for isolated and linked cavities. The isolated cavities can be filled completely, while for the linked cavities the filling the cavities continue to grow. The filling kinetics is analyzed resulting in an estimate for the filling time. The demonstrated self-healing potential of supersaturated W atoms in *bcc* iron provides a new perspective on the role of W in high-temperature creep-resistant steels.



## 7.1. Introduction

Creep failure in steels occurs when a constant load is applied at an elevated temperature (normally above 450 °C) via the formation of isolated grain-boundary cavities, followed by their coalescence, ultimately leading to the formation of a catastrophic crack. To improve the creep resistance and prolong the creep lifetime for the steel components subject to external stress and high temperature, abundant efforts have been paid to optimize the chemical composition and the microstructure of the steels by combining various strengthening routes such as solid solution strengthening, precipitation hardening and work hardening to increase the initial strength and postpone the damage as long as possible [1-5]. Once the creep cavity nucleates, its growth cannot be stopped and coalescence with neighboring cavities eventually leads to failure.

Different from postponing the damage initiation, a novel approach was proposed in which the damage is self healed by the material itself resulting a significant prolongation of the lifetime [6-8]. For austenitic (*fcc* structure) stainless steels Laha and coworkers [9-11] and Shinya [12] observed that the precipitation of either Cu or BN at the creep cavity surface resulted in a significant increase in the creep lifetime. Subsequently, Zhang and coworkers [13-16] demonstrated that the creep cavities in Fe-Au and Fe-Mo alloys can be filled by second-phase precipitation driven by the diffusion of supersaturated solute atoms in the ferritic (*bcc* structure) iron-rich matrix. Based on these studies on Fe-X binary alloys, the key requirements for an element X to be an efficient self-healing agent can be summarized: i) the element X can be solutionized into Fe matrix at high temperature, and be brought to an adequate degree of supersaturation at the creep temperature to provide appreciable driving force for precipitation; ii) the atomic size of X is considerably larger than that of the matrix Fe, resulting in high nucleation barrier for precipitation in the matrix and a strong preference to precipitate at the free surface of the damage site; iii) the diffusivity of the element X must be larger than that of Fe to ensure that the filling of the cavity (controlled by solute diffusion) can catch up with the cavity growth (controlled by vacancy diffusion).

Tungsten is highly appreciated as an important alloying element in high-performance creep-resistant steels, like high chromium (9-12 wt.% Cr) ferritic/martensitic steels, because of its excellent solid-solution strengthening and precipitation hardening. For the currently most advanced creep-resistant high-chromium steels, W is added to replace part of the Mo to improve the creep-resistance at higher temperatures and to reduce neutron activation for potential applications in Generation IV nuclear reactors [17-19]. Although a lot of work [20-24] has been done to study the effect of W on the creep properties, only the solid-solution strengthening and the precipitation hardening have been investigated without considering the interaction of solute W with the creep cavities and the cavity filling by  $(\text{Fe,Cr})_2(\text{Mo,W})$  Laves phase precipitates. Similar to Au and Mo, solute W can also be tuned into a supersaturated state in binary Fe-X alloys at the creep temperature. Due to the larger atomic radius ( $r_{\text{W}}/r_{\text{Fe}} \approx 1.10$ ) and the large solute diffusivity [25] compared to that of Fe in the *bcc* iron-rich matrix, W satisfies the key requirements to be an efficient healing agent in

Fe-based alloys. It is the aim of the present study to experimentally clarify whether the supersaturated W can indeed act as an effective healing agent in Fe-W alloys by monitoring to what extent Fe<sub>2</sub>W Laves phase precipitates fill the creep cavities as a function of the creep time.

To this aim creep tests were performed on solutionized Fe-W alloys for constant loads at a temperature of 550 °C. Following a detailed synchrotron X-ray nanotomography study demonstrating self healing of creep damage in Fe-Au alloys [26], we use this powerful 3D imaging tool to characterize the evolution of both the creep cavities and the precipitation inside these cavities at different stages of the creep life with a spatial resolution down to 30 nm. Electron microscopy was used to obtain complementary information on the composition and the crystal structure of the precipitates formed during creep.

## 7.2. Experimental methods

### 7.2.1. Samples and creep tests

Rolled sheets of high-purity Fe-W binary alloy sample were produced by Goodfellow. The chemical composition of the Fe-W alloy is 3.800 wt.% W, 0.020 wt.% Si, 0.026 wt.% S, 0.0014 wt.% N, 0.0024 wt.% C and balance Fe. Dog-bone shaped creep test samples (with a gauge length of 12.5 mm, a width of 6 mm and a thickness of 0.5 mm) were cut from the as-received sheet material by spark erosion. These samples were then annealed at 900 °C for 24 h in an evacuated and sealed quartz tube filled with 200 mbar ultra-high purity argon and subsequently quenched in water. Electron microscopy was used to observe the quenched samples and confirmed that the alloy was in a fully solutionized state and there were no grain-boundary precipitates in the samples after the heat treatment. The average grain diameter of the quenched samples was determined from the electron microscopy images and amounted to 127 µm. Creep tests were performed in vacuum on the solutionized alloy samples at a temperature of 550 °C and initial loads of 140 and 160 MPa. Creep tests until sample rupture were carried out first to determine the rupture time  $t_R$  for a specific creep condition. Then creep tests for the same creep condition were performed that were interrupted after a selected fraction of the expected rupture time (e.g.  $t/t_R = 0.25, 0.50$  and  $0.75$ ). For the tomography experiments bar-shaped samples with a cross section of  $250 \times 250 \mu\text{m}^2$  and a length of about 6 mm were cut by spark erosion from the uniform gauge section of the samples after the creep tests. The long axis of the tomography samples was oriented along the direction of the applied stress during the creep tests. The 2D microstructure of the samples after creep was analyzed by a scanning electron microscope (JEOL JSM 6500F). The grain-boundary precipitates were characterized with transmission electron microscopy (TEM) using a Tecnai F20ST/STEM instrument operating at 200 kV. The composition in the vicinity of the grain boundary was measured with atom probe tomography (APT). The APT analysis was conducted on a LEAP 3000X HR instrument, operated in laser-pulsed mode at a base temperature of 60 K, a laser frequency of 250 kHz, and a 0.4 nJ pulse energy.

### 7.2.2. Synchrotron X-ray nano-tomography

Phase contrast tomography with nanometer resolution using coherent X-rays from a synchrotron source was adopted to quantify the 3D structure of the Fe-W alloy samples after the creep tests. Holotomography measurements on the bar-shaped Fe-W samples were performed at the ID16A-NI nano-imaging beamline of the European Synchrotron Radiation Facility (ESRF) in Grenoble, France [27]. This beamline offers an extremely high spatial resolution down to 13 nm [27-28] by a unique combination of nanofocusing and a very high brilliance. A detailed description of this unique instrument can be found elsewhere [28-29].

The maximum photon energy of 33.6 keV available at this beamline was used to optimize the transmission through the sample. The bar-shaped Fe-W sample was mounted on the rotational stage of the tomography setup. Two resolutions of 100 and 30 nm per voxel were used. The field of view (FOV) at a voxel size of 100 nm was taken from a sample region with a distance between 0.5 and 3.0 mm away from the fracture surface for creep ruptured sample and from the middle of the sample length for the interrupted creep sample. The field of view (FOV) at a voxel size of 30 nm was then a selected region of the FOV rendered at the voxel size of 100 nm. During the tomography scan, the nano-focused beam illuminated the sample and magnified radiographs were recorded using a charge-coupled device (CCD) with a 2048×2048 binned pixel array. In total 1800 projections were acquired with an exposure time of 1.00 s for both resolutions, while the sample was rotated over 180 degrees. Scans at four different focus-to-sample distances were performed for subsequent phase retrieval. The holotomographic reconstruction using the retrieved 2D phase maps [30] was implemented using the ESRF PyHST software package [31] by employing the filtered back projection (FBP) algorithm. For each scan, 3216 slices were reconstructed that correspond to a sample volume of  $321.6 \times 321.6 \times 321.6 \mu\text{m}^3$  for the 100 nm resolution and  $96.48 \times 96.48 \times 96.48 \mu\text{m}^3$  for the 30 nm resolution. The reconstructed 3D volumes were rendered and visualized with the FEI Avizo 8.1 software. The general procedure of data rendering is illustrated in Fig. S7.1.

As characterized with scanning electron microscopy (Fig. S7.2), the Fe-W alloy samples after the creep tests constitute of three phases: (i) the *bcc* iron-rich matrix with supersaturated tungsten, (ii) empty creep cavities and (iii) precipitates of the Fe<sub>2</sub>W Laves phase. In the grain interior of the as-received material a limited number of FeWO<sub>4</sub> precipitates were observed. These stable particles are not expected to affect the precipitation at free creep cavity surfaces. We will only be interested in creep cavities and precipitates because they are directly related to the autonomous filling of creep damage by precipitation at the free surface of creep cavities. Since the electron densities of the Laves phase ( $3.352 e/\text{\AA}^3$ ), Fe ( $2.208 e/\text{\AA}^3$ ) and vacuum are distinctly different, the contrast between these three phases is significant. Therefore, we can recognize the near-black features as precipitates and bright features as creep cavities in the reconstructed grey-valued slices. Both phases were segmented by applying a threshold value in grey scale of the 3D images. The threshold values were carefully chosen and extensively tested to obtain an optimal contrast between the creep cavities and precipitates. It should be noted that the minimum size of identified object for both

resolutions is 8 voxels, that is  $8 \times 10^{-3} \mu\text{m}^3$  for the 100 nm resolution and  $2.16 \times 10^{-4} \mu\text{m}^3$  for the 30 nm resolution. Objects with a smaller size are regarded as noise and ignored. After the phase segmentation binary images were obtained and exported for further analysis.

### 7.2.3. Quantitative analysis

We not only identified different phases in the Fe-W alloy samples but also quantitatively described their shapes and determined the filling ratio of each individual cavity by examining the co-location of pores and precipitates. The quantitative analysis was employed on the binary images exported from Avizo using a MATLAB program with the DIPimage toolbox [32]. The shape of an object was characterized by shape complexity  $\Omega_3$  in 3D and three semi-axes of an equivalent ellipsoid that was used to approximate the real object by having the same moments of inertia. Thus the major, intermediate and minor semi-axes (expressed as  $a$ ,  $b$  and  $c$ , respectively) can be used to calculate the elongation  $E$  and the flatness  $F$  of the object. By using the three parameters  $\Omega_3$ ,  $E$  and  $F$ , we can unambiguously classify all objects into five different shapes: sphere, equiaxed, rod-like, sheet and complex. A detailed description and criteria for shape classification can be found in our previous work [26].

To quantify the spacing between objects, we calculated the distance for each object to its nearest neighbor based on the coordinates of their centers of mass in 3D. By checking the contact between the cavity and the precipitate, we determined how many precipitates deposited on each cavity and how much of the original cavity volume occupied by the precipitates. As previously defined [26], we can determine the filling ratio  $FR$  of each cavity by precipitation:

$$FR = \frac{V_{prec}}{V_{cav} + V_{prec}}, \quad (7.1)$$

where  $V_{prec}$  is the total volume of precipitates in contact with the cavity and  $V_{cav}$  is the volume of the open cavity. In this paper, an individual object consisted of cavities and precipitates in contact with each other will be referred to particle. The sum of  $V_{cav}$  and  $V_{prec}$  in Eq. 7.1 will be referred to as the particle volume in the subsequent discussion unless specified otherwise.

## 7.3. Results

### 7.3.1. Creep results

Fig. 7.1 shows the strain-time curves of the Fe-W alloy samples until rupture, as well as those for the samples interrupted at a selected fraction of expected rupture time, at a temperature of 550 °C and a constant stress of 140 and 160 MPa. Details regarding the creep conditions and resulting creep time  $t$ , strain  $\varepsilon$  and strain rate  $\dot{\varepsilon}$  are given in Table 7.1. The creep curves of the interrupted creep tests reproduced very well with the creep curves up to rupture under the same load. This assures the reliability of the analysis of the microstructure evolution as a function of the creep time in the different tomography samples. The creep curve at 160 MPa shows a usual creep curve, in which strain rapidly increases in the primary stage (stage I), goes to a steady

increasing stage (stage II) until accelerates to rupture (stage III). The creep curve at 140 MPa shows a somewhat unusual stage II creep behavior with a weak transition in creep rate.

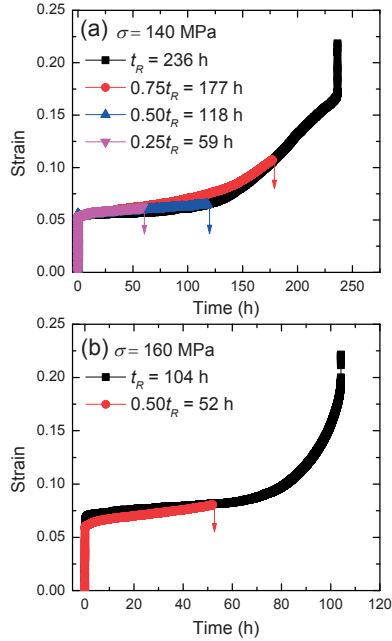


**Fig. 7.1.** Creep curves of the Fe-W alloy samples at a temperature of 550 °C and a constant stress of (a) 140 MPa and (b) 160 MPa. The arrows indicate the interrupted creep tests.

**Table 7.1.** Creep parameters of the Fe-W alloy samples indicating the temperature  $T$ , the applied stress  $\sigma$ , the creep time  $t$ , the creep time relative to the rupture time  $t/t_R$ , the strain  $\epsilon$  and the strain rate  $\dot{\epsilon}$ .

Sample	$T$ (°C)	$\sigma$ (MPa)	$t$ (h)	$t/t_R$ (-)	$\epsilon$ (-)	$\dot{\epsilon}$ (h <sup>-1</sup> )
S1	550	140	236	1	0.218	$8.7(3) \times 10^{-5}$
S2	550	140	177	0.75	0.107	$1.7(6) \times 10^{-4}$
S3	550	140	118	0.50	0.065	$7.6(2) \times 10^{-5}$
S4	550	140	59	0.25	0.062	$1.3(2) \times 10^{-4}$
S5	550	160	104	1	0.222	$2.0(5) \times 10^{-4}$
S6	550	160	52	0.50	0.081	$3.1(8) \times 10^{-5}$

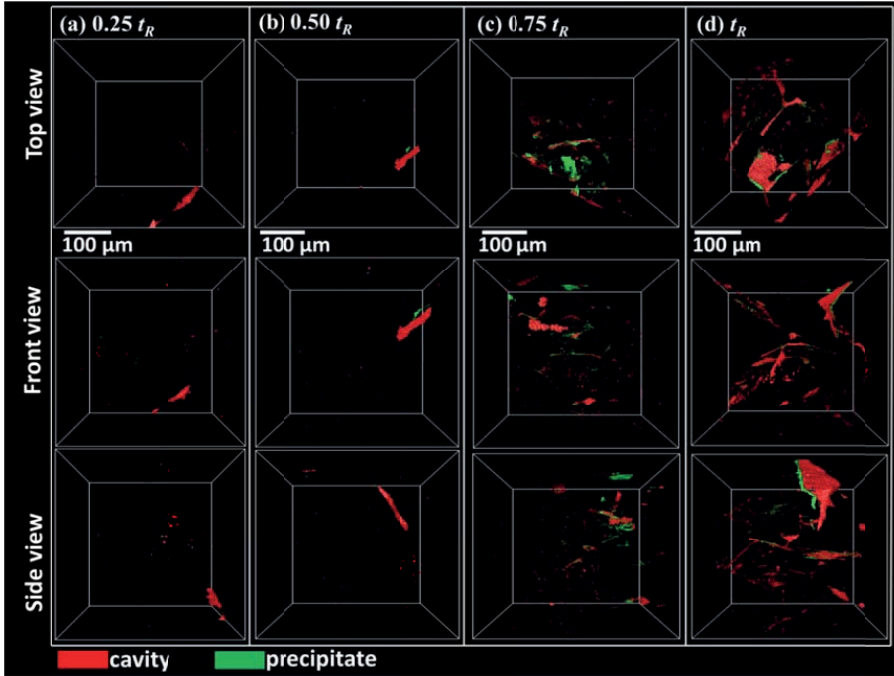
### 7.3.2. Tomographic rendering

Fig. 7.2 shows the 3D tomographic renderings with a field of view (FOV) of  $321 \times 321 \times 321 \mu\text{m}^3$  (with a voxel size of 100 nm) for the samples after creep at 550 °C and 140 MPa for different times relative to the rupture time  $t_R$ . Cavities and precipitates were segmented and labelled in red and green, respectively. Fig. 7.2 clearly shows that the number of cavities increases with increasing creep time. In the early interrupted creep samples ( $0.25t_R$  and  $0.50t_R$ ), most of the cavities and precipitates are very small with an average equivalent diameter of about 0.55  $\mu\text{m}$ . In both samples only three cavities are elongated with equivalent diameter  $> 4 \mu\text{m}$ . In the creep sample interrupted at  $0.75t_R$  and the ruptured sample, more cavities and precipitates grow to bigger size with a larger variety in shapes ranging from small isolated spherical or equiaxed shapes to more extended and complex shapes. It can also be seen from Fig. 7.2c and Fig. 7.2d that the grain boundaries are clearly delineated by the spatial distribution of cavities and precipitates. This heterogeneous distribution of cavities and precipitates at grain boundaries is in line with our previous observations on the Fe-Au alloy samples [7].

Given a large length scale range (from 0.1 to 321  $\mu\text{m}$  for a voxel size of 100 nm) covered with the tomography in one volumetric dataset, we have a broad view on the co-locations of cavities and precipitates. Figs. 7.2a and 7.2b indicate that a lot of cavities are connected to one or more precipitates. In Fig. 7.2c and Fig. 7.2d the largest cavities at transverse grain boundaries, as well as inclined grain boundaries, are linked and often partly filled by precipitates. Fig. 7.2d also shows that complex cavities located at inclined and transverse grain boundaries join at grain corners and with a partial filling by precipitates. All these features indirectly demonstrate that the precipitates occupy space that was originally inside a cavity.

More detailed views of the subvolume from the FOV presented in Fig. 7.2 are obtained by additional measurements with a voxel size of 30 nm. For an applied stress of 140 MPa the results are shown in Fig. 7.3. For the samples after creep at a load of 160 MPa, the 3D views are shown in Figs. S7.3 (100 nm resolution) and S4 (30 nm resolution). The 3D volume with the enhanced resolution of 30 nm covers a length scale ranging from 60 nm to 96  $\mu\text{m}$ . With the higher resolution, we can see finer details that are invisible in the lower resolution datasets. For example, in Fig. 7.2a it is hard to see that several individual precipitates are connected to the same cavity. However, in Fig. 7.3a it is clearly visible that two cavities are filled with more than one precipitate with different sizes and different orientations. A similar case can be found for the ruptured sample. Comparing Fig. 7.2d to Fig. 7.3d, we found that many small isolated cavities close to the large complex grain-corner cavity are empty from any precipitate in Fig. 7.2d, whereas in Fig. 7.3d these cavities are surrounded by tiny precipitates. The enhanced resolution may also affect the shape of the same object. One of the examples is shown in Fig. 7.3a where the cavity shapes have gained in complexity compared to the more spherical shapes observed in Fig. 7.2a. Similar examples can also be found for samples after interrupted creep for  $0.50t_R$  (Fig. 7.3b) and  $0.75t_R$  (Fig. 7.3c). There are two reasons for the differences appeared for these two resolutions. One is that the edge of an object is less blurred and better visible at a higher resolution.

The other is that the contrast between the precipitate and the cavity is enhanced in the grey scale images at a higher resolution. A direct comparison of rendered images for the same FOV between 100 and 30 nm resolutions is presented in Figs. S7.5-S7.8 for different samples.



**Fig. 7.2.** 3D tomographic volume ( $321 \times 321 \times 321 \mu\text{m}^3$ ) with a voxel size of 100 nm after phase segmentation showing cavities and precipitates in Fe-W alloy samples after creep at a temperature of 550 °C and a stress of 140 MPa for a time relative to rupture  $t/t_R$  of (a) 0.25, (b) 0.50, (c) 0.75 and (d) 1.00, where  $t_R$  is the rupture time. The applied stress is normal to the top view.

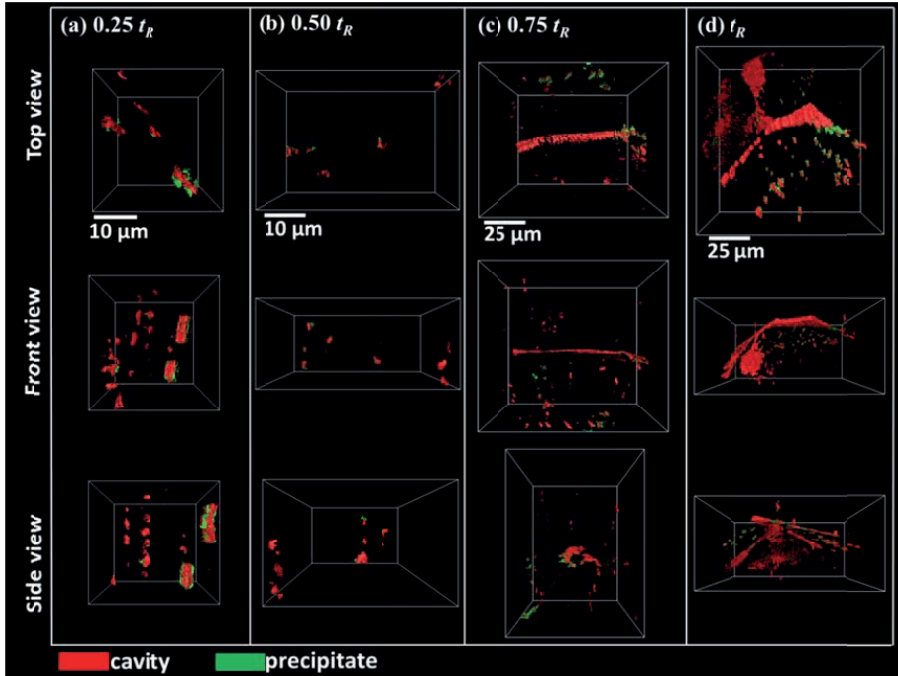


**Fig. 7.3.** 3D tomographic volume renderings with a voxel size of 30 nm after phase segmentation showing cavities and precipitates in Fe-W alloy samples after creep at a temperature of 550 °C and a stress of 140 MPa for a time relative to rupture  $t/t_R$  of (a) 0.25, (b) 0.50, (c) 0.75 and (d) 1.00, where  $t_R$  is the rupture time. The ROI size is (a)  $30 \times 26 \times 26 \mu\text{m}^3$ , (b)  $75 \times 96 \times 96 \mu\text{m}^3$ , (c)  $96 \times 80 \times 96 \mu\text{m}^3$  and (d)  $96 \times 96 \times 48 \mu\text{m}^3$ . The applied stress is normal to the top view.

Although some fine features may not have been characterized in the FOVs with 100 nm resolution, the larger rendered sample volume (compared to that with 30 nm resolution) provides a better overview and is thereby statistically more significant for the determination of the number and volume distributions of different shape classes for the cavities and the precipitates. Therefore, we derived the statistical information from images with a 100 nm resolution, while we used images with a 30 nm resolution to focus on features that better represent the early growth stage of objects (the sensitivity extends down to sizes that are expected to be found just after nucleation). Figs. S7.9 and S7.10 show the number and volume distributions of particles for different samples, respectively. All number distributions show lognormal distributions and fitted parameters are shown in Table S7.1. It is found that both the number density  $N_0$  and the average diameter  $\bar{d}$  of the cavities increase with increasing creep time for samples loaded at 140 and 160 MPa. However, for the precipitates there is no evident monotonic change as a function of creep time. For the samples loaded at 140 MPa, the number density of precipitates first stays low for the shortest creep times ( $0.25t_R$  and  $0.50t_R$ ) and then increases by about 20 times for  $0.75t_R$ , followed by a decrease in ruptured sample ( $t_R$ ). For the sample loaded at 160 MPa, we only see the increase in



number densities of precipitates from the creep time of  $0.50t_R$  to  $t_R$ . The average diameter of precipitates is in all case slightly smaller than that of cavities, indicating that the precipitates are lagging behind in their development compared to the cavities, as expected for the damage-induced precipitation in self-healing alloys.

### 7.3.3. Identification of isolated and linked cavities

Previous studies [26, 33] have shown that the growth behavior of isolated and linked cavities is very different. Therefore, it is very important to distinguish isolated cavities from linked cavities and analyze them separately. In the present study it is not possible to know the history of an individual cavity. However, an effective method to identify these two types of cavities is by analyzing their shape and their size relative to the cavity spacing.

Using the previously defined shape classification [26] the following cavity shapes are defined: spherical, equiaxed, rod-like, sheet and complex. Fig. 7.4 shows the 3D spatial distribution of cavities for creep samples loaded at 140 MPa for creep times of  $0.25t_R$  (top row) and  $t_R$  (bottom row) with examples for each shape. The rod-like, sheet and complex cavities are more likely to form by linking neighboring cavities as indicated by the frequently observed necking in the 3D shapes, which is not observed for spherical and equiaxed cavities. In addition to the shape classification, we add a second criterion to identify isolated and linked cavities by comparing the cavity size to the cavity spacing. If the major axes (*i.e.*  $2a$ ) of a cavity with a rod-like, sheet or complex shape is larger than the average cavity spacing  $\langle \lambda_{\text{cavity}} \rangle$ , this cavity is regarded as a linked cavity. All other cavities (including the cavities with a spherical or equiaxed shape) are regarded as isolated.

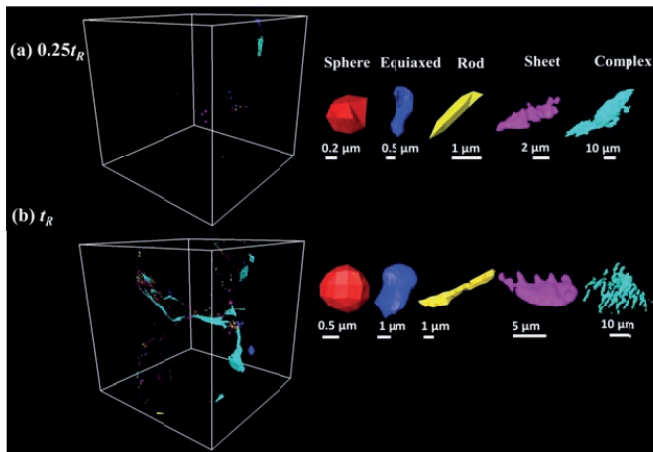


**Fig. 7.4.** 3D view of cavities in the sample after creep at a temperature of 550 °C and a stress of 140 MPa for a creep time relative to rupture of (a)  $0.25t_R$  and (b)  $t_R$ . The cavities in the sample volume (left image) are classified in different shapes: sphere, equiaxed, rod, sheet and complex. Extracted examples of classified cavities in different shapes are also shown.

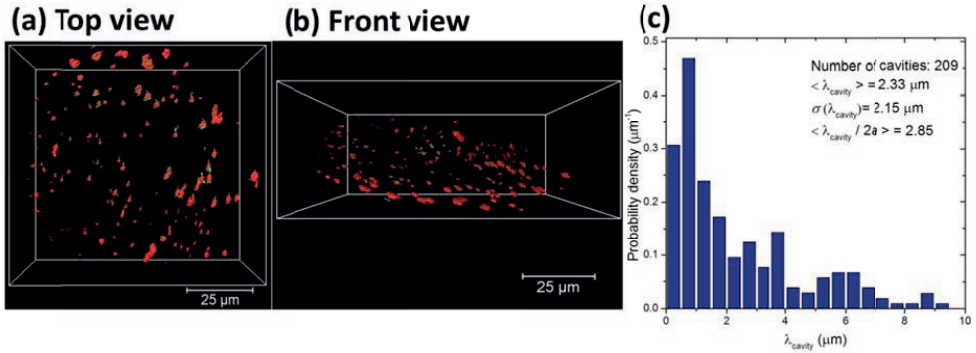


**Fig. 7.5.** (a) Top view and (b) front view of a region of interest extracted from the Fe-W sample after creep at a temperature of 550 °C and a stress of 160 MPa after rupture ( $t = t_R$ ) showing the spatial distribution of the cavities. (c) Distribution of the spacing  $\lambda_{\text{cavity}}$  between the cavities. The distribution indicates an average cavity spacing of  $\langle \lambda_{\text{cavity}} \rangle = 2.33 \mu\text{m}$ . With an equivalent cavity diameter on the grain boundary plane of  $\langle d_{\text{GB}} \rangle = 1.06 \mu\text{m}$  the ratio between the cavity spacing and the cavity size is  $\langle \lambda_{\text{cavity}} / d_{\text{GB}} \rangle = 2.85$ .

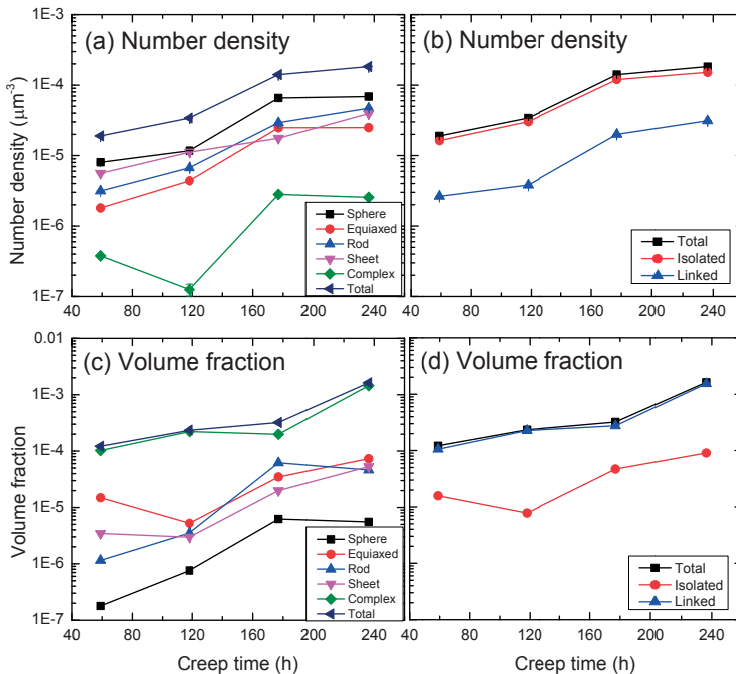


**Fig. 7.6.** Number density (a, b) and volume fraction (c, d) of cavities of the Fe-W alloy samples after creep at a temperature of 550 °C and a stress of 140 MPa for different time times with (a, c) cavities classified by shape and (b, d) cavities classified as isolated or linked.

To derive an accurate estimate for  $\langle \lambda_{\text{cavity}} \rangle$  a FOV was selected in the Fe-W sample creep loaded at 160 MPa until rupture ( $t = t_{\text{R}}$ ) shown in Fig. 7.5 with a grain boundary plane oriented with an angle of about 70 degrees to the applied stress. There are 285 cavities in total located at this plane and 73% of these (209 cavities) have a size smaller than  $0.5 \mu\text{m}^3$ . Since these 209 cavities have a narrow size distribution, it is believed that these creep cavities are in their early growth stage of without any linkage with neighboring cavities. Fig. 7.5c shows the distribution of  $\lambda_{\text{cavity}}$ , indicating an average value of  $\langle \lambda_{\text{cavity}} \rangle = 2.33 \mu\text{m}$  and the standard deviation of  $\sigma(\lambda_{\text{cavity}}) = 2.15 \mu\text{m}$ . The equivalent diameter of each cavity in the grain boundary plane is calculated as  $d_{\text{GB}} = 2\sqrt{ab}$ . The estimated ratio of the cavity spacing to the equivalent cavity diameter on the grain boundary plane is then  $\langle \lambda_{\text{cavity}}/d_{\text{GB}} \rangle = 2.85$ .

By quantifying the cavity shapes and comparing their major axes to  $\langle \lambda_{\text{cavity}} \rangle$ , we can now explicitly separate the isolated and linked cavities. Fig. 7.6 shows the number density and volume fraction of cavities classified into shapes (a, c) and classified into isolated and linked cavities (b, d) as a function of creep time at a temperature of 550 °C and a stress of 140 MPa. The number density of creep cavities is dominated by the spherical cavities, while complex cavities are relatively rare in number. In contrast, the volume fraction of cavities is dominated by complex cavities, whereas spherical cavities contribute very little to the volume fraction (as the complex cavities are generally much larger than spherical cavities). Similarly, as shown in Fig. 7.6b and 7.6d the isolated cavities contribute most to the number density, while linked cavities are the dominant contribution in the volume fraction.

### 7.3.4. Filling ratio of individual cavity by precipitation

The filling ratio  $FR$  (as defined in Eq. 7.1) of each creep cavity is plotted as a function of its volume in Fig. 7.7 for samples loaded at 140 MPa and in Fig. 7.8 for samples loaded at 160 MPa. The obtained filling ratios of the partly filled creep cavities are separated into isolated and linked cavities for samples after creep times relative to the rupture time  $t_{\text{R}}$ . For an unfilled particle  $FR = 0$ , for a fully filled particle  $FR = 1$  and for a partially filled particle  $0 < FR < 1$ . In 3D images the resolution limit to identify a partially filled cavity is two pixels in all directions, corresponding to a volume of  $0.008 \mu\text{m}^3$  for a voxel size of 100 nm. This resolution limit applies for both the unfilled and the filled part of the cavity, resulting in an inaccessible area marked in grey in Figs. 7.7 and 7.8. Below this limit only fully unfilled or fully filled cavities can be identified.

Fig. 7.7a-d show that the number of cavities and the distribution in volume and filling ratio of unfilled, partially filled and fully filled cavities are changing with the creep time. The volume of the fully filled particles spans from  $10^{-3} \mu\text{m}^3$  to a maximum of about 1.3, 2.4, 190 and  $71 \mu\text{m}^3$  for a relative creep time  $t/t_{\text{R}}$  of 0.25, 0.50, 0.75 and 1.00, respectively. The volume of the unfilled particles spans from  $10^{-3} \mu\text{m}^3$  to a maximum of about 2272, 4467, 1133 and  $15813 \mu\text{m}^3$  for a relative creep time  $t/t_{\text{R}}$  of 0.25, 0.50, 0.75 and 1.00, respectively. It can be seen that the volume of the unfilled cavities spans a wider range than the volume of the fully filled cavities and that the volume of the largest unfilled cavities are several orders of magnitude bigger than the largest

fully filled cavities. This suggests that the precipitates form at a later stage than the cavities, which is fully in line with the proposed self-healing mechanism where the formation of precipitates is induced by the free surface generated by the formation of the creep cavities. The volume range covered by the partially filled particles also expands with increasing creep time. For the sample with a creep time of  $0.25t_R$ , in total 49 partially filled cavities are observed with a volume between  $0.1$  and  $25 \mu\text{m}^3$ . For a creep time of  $0.50t_R$  a similar distribution is observed (27 partially filled cavities with a volume ranging from  $0.1$  to  $30 \mu\text{m}^3$ ). When the creep time increases to  $0.75t_R$  and  $t_R$ , the number of partially filled cavities increases (713 for  $0.75t_R$  and 521 for  $t_R$ ) and the volume range of the partially filled particles expands significantly (from  $0.01$  to  $10^4 \mu\text{m}^3$ ). Although there are less partially filled cavities present in the samples with shorter creep times ( $0.25t_R$  and  $0.50t_R$ ), the observed filling ratios span over the whole range from 0 to 1, indicating that the lowest creep time of  $0.25t_R$  is already sufficient to fill the earliest nucleated creep cavities at this stress level. As expected, the linked cavities are predominantly observed in the later creep stages and are generally the largest in size.

For the samples loaded at a higher stress of 160 MPa shown in Fig. 7.8, the maximum volume is again much larger for the unfilled cavities than for the fully filled cavities. A significant number of partially filled cavities is observed in both samples (299 for  $0.50t_R$  and 268 for  $t_R$ ). Unlike the sample loaded at 140 MPa, for a creep time of  $0.50t_R$  the filling ratio of most of the partially filled cavities for the sample loaded at 160 MPa only ranges up to 0.6 (see Fig. 7.8a). Interestingly, no fully filled cavities are observed with a volume beyond  $0.6 \mu\text{m}^3$ . In the ruptured sample loaded at 160 MPa the filling ratio of the partially filled cavities occupy the whole range from 0 to 1 (see Fig. 7.8b).

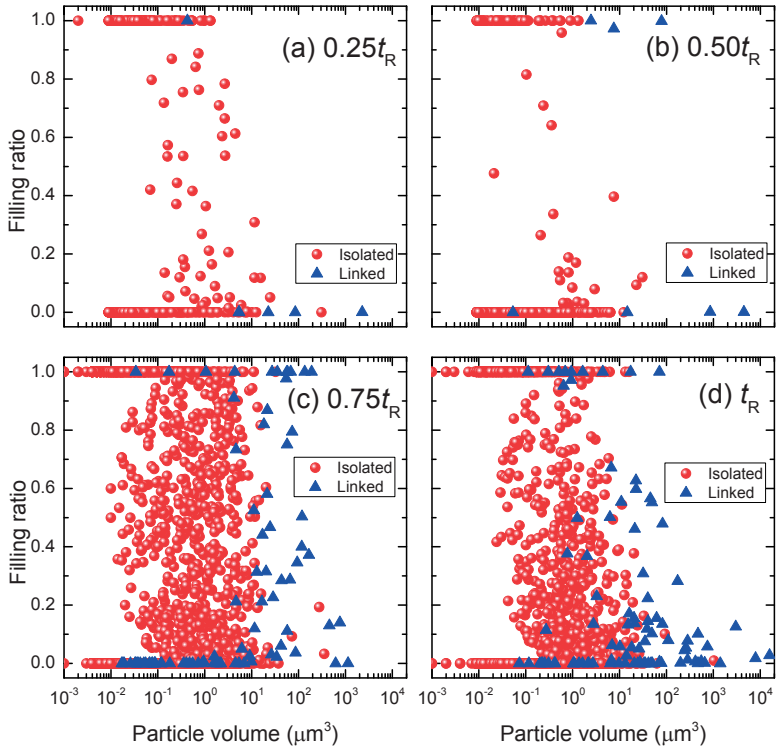


**Fig. 7.7.** Filling ratio of individual creep cavities as a function of the cavity volume (sum of the unfilled cavity and the precipitation in the cavity) in the Fe-W alloy samples after creep at a temperature of 550 °C and a stress of 140 MPa for different creep times relative to the rupture time  $t_R$ . The creep cavities were identified from the data obtained for a voxel size of 100 nm. The red spheres correspond to isolated cavities and the blue triangles to linked cavities. Note that the grey shaded region is experimental not accessible for partially filled cavities.

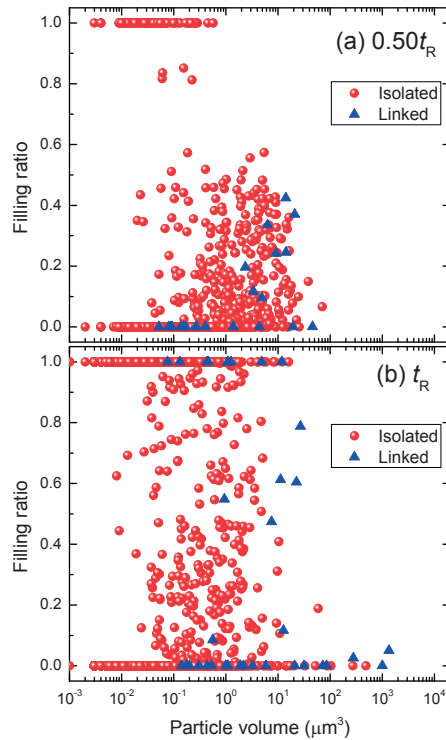


**Fig. 7.8.** Filling ratio of individual creep cavities as a function of the cavity volume (sum of the unfilled cavity and the precipitation inside the cavity) in the Fe-W alloy samples after creep at a temperature of 550 °C and a stress of 160 MPa for different creep times relative to the rupture time  $t_R$ . The creep cavities were identified from the data obtained for a voxel size of 100 nm. The red spheres correspond to isolated cavities and the blue triangles to linked cavities. Note that the grey shaded region is experimental not accessible for partially filled cavities.

Examples of partially filled cavities in the Fe-W sample loaded at 140 MPa for  $0.25t_R$  and  $t_R$  are shown in Figs. 7.9 and 7.10, respectively. The four partially filled cavities in Fig. 7.9 resolved from the high resolution data (30 nm voxel size) for a creep time of  $0.25 t_R$  all show rich details in shape with local precipitation on one location of the cavity surface. The data suggest that the precipitate first forms at a local area of the cavity and then grows along one particular side thereby blocking the growth of the cavity in this direction, while the cavity may continue to grow in other directions.

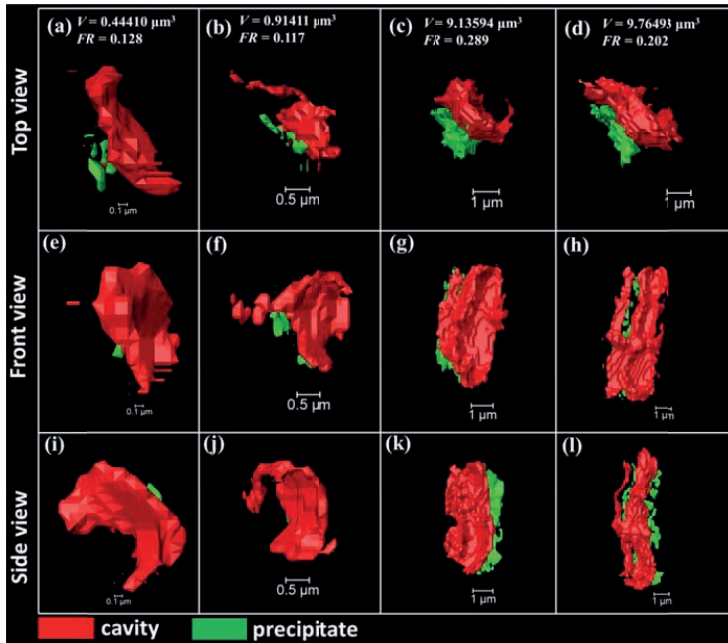


**Fig. 7.9.** Examples of partially filled creep cavities in Fe-W alloy samples after creep at a temperature of 550 °C and a stress of 140 MPa for a creep time of  $0.25t_R$ . The figure shows representations of four partially filled creep cavities from different angles rendered from high-resolution data with a voxel size of 30 nm. The applied stress is normal to the top view.

In Fig. 7.10 the cavity filling by precipitation is investigated for the final creep stage at rupture. Fig. 7.10a shows that a small particle is partially filled by two precipitates from two opposite sides. In Fig. 7.10b and 7.10c the particles are decorated with several precipitates in different locations. These precipitates are forming a chain to encapsulate the creep cavities. This chain-like precipitation on the cavity surface is also present in Fig. 7.10d, for a large creep cavity formed by linking cavities at one transverse and two inclined grain boundaries. On the long-end of this cavity the precipitates are encapsulating the linkage area. In other necking parts of this cavity precipitates are also present. All these observations support the idea that the formation of precipitates is filling the cavity from the cavity surface inwards. Similar features are also observed in the Fe-W alloy sample loaded at 160 MPa for creep times of  $0.50t_R$  and  $t_R$  as shown in Fig. S7.11 and S7.12, respectively.

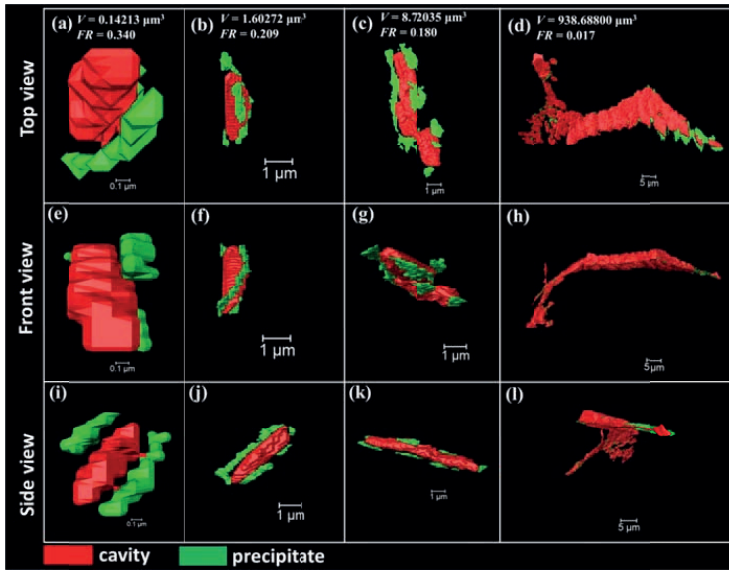


**Fig. 7.10.** Examples of partially filled creep cavities in Fe-W alloy samples after creep at a temperature of 550 °C and a stress of 140 MPa for creep up to rupture ( $t = t_R$ ). The figure shows representations of four partially filled cavities from different angles rendered from high-resolution data with a voxel size of 30 nm. The applied stress is normal to the top view.

## 7.4. Discussion

### 7.4.1. Autonomous filling of creep cavities by precipitation

Extensive evidence from the tomographic characterization demonstrates that the precipitates form at the cavity free surface, *i.e.* the precipitation is filling the cavity during the entire creep process. As shown in Figs. 7.2 and 7.3, the cavities form at transverse, inclined grain boundaries and grain corners. For the precipitates that are co-located with open cavities, they always adapt their morphologies to match the remaining open cavity from one end or from one side edge. Detailed views on the co-located examples in Figs. 7.9 and 7.10 clearly show that multiple precipitates can form at different sites on the same cavity, decorating the surface, and even form a chain encapsulating the cavity resulting in a continuous growth and linkage of the precipitates. The morphologies of the precipitates linked to small cavities in the very early growth stage are irregular and reflect the morphologies of the cavities. This is illustrated in Figs. 7.7 and 7.8. The filling ratio maps for different creep times show that there are more unfilled cavities with sizes ranging up to much larger volumes than those of the fully filled and partially filled cavities, suggesting that the filling can only be triggered after the cavity has been formed. Figs. 7.7 and 7.8 also show that the maximum size of the partially filled cavities is always bigger than that of the fully filled cavities.



According to our previous studies [16, 26], the filling starts after the cavity reaches a certain volume  $V_{0,cav}$ , which depends on the local grain boundary conditions, *e.g.* orientation to the applied stress, and thereby could span a wide size range. For the filling of one single cavity by precipitation the filling ratio would continuously increase to reach full filling ( $FR = 1$ ) as the supersaturated W atoms diffuse towards the cavity surface and combine with the Fe atoms to form  $Fe_2W$  precipitates at the cavity surface. However, the growth of the cavities can be accelerated by linkage with neighboring cavities. If this is the case, the filling ratio would continuously drop after linkage. Although we did not monitor the filling of individual cavities over the creep process in this study, the experimental filling ratios of such a large number of cavities illustrates the different stages of the filling process and map out the different filling routes. These trends obtained for the Fe-W alloy are in line with those observed for the Fe-Au alloy [26].

#### 7.4.2. Nucleation and growth of creep cavities and precipitates

The healing kinetics of the cavities is controlled by the balance between the cavity growth rate and the precipitation rate inside the cavity. To analyze the filling kinetics it is essential to study the nucleation and growth of both the cavity and the precipitates. Since the resolution limit of the tomographic image ( $\approx 2$  times of the voxel size, *i.e.* 60 nm) is close to the predicted size of the critical nucleus of about 50 nm for a creep cavity [34], we can be confident that all the formed cavities are observed in the 3D images. The number of observed cavities is lower than the number of formed cavities as a result of linkage. By assuming that the linked cavities contain an estimated number of  $2a/\langle \lambda_{cav} \rangle$  of formed cavities the effect of linkage on the cavity number can be estimated. As shown in Figs. 7.11a and 7.11b, this analysis provides a lower bound (observed) and an upper bound (corrected) for the cavity number. The slope of the linear fits in Fig. 7.11a for the average cavity number per grain as a function of the creep time indicates that the cavity nucleation takes place continuously at a rate of about one cavity per grain per hour at a temperature of 550 °C and a stress of 140 MPa. This steady-state nucleation is consistent with the expectations for stage II creep.

Once the grain-boundary creep cavity nucleates and starts to grow, the supersaturated W atoms in the iron matrix experiences a driving force towards the free creep cavity surface. Since the energy barrier for the nucleation of a  $Fe_2W$  precipitate is significantly reduced at the free cavity surface compared to the matrix (as a result of the strain energy) the precipitation is strongly site selective.

The number of precipitates formed at each cavity was also determined from the 3D tomography images. In Fig. 7.11c the average number of precipitates in each cavity is plotted as a function of the creep time and in Fig. 7.11d the number of precipitates per cavity surface area versus creep time is shown. The data clearly show that the number of precipitates per cavity or per cavity area is more or less constant over the entire creep process. This suggests that the number of precipitates correlates with dislocation density, which is expected to be relatively constant due to the balance between the formation and annihilation of dislocations during secondary creep stage.

Fig. 7.11c and 7.11d also show that the number of precipitates for  $\sigma = 160$  MPa is slightly higher than that for  $\sigma = 140$  MPa, implying that higher dislocation density enhances the precipitation.

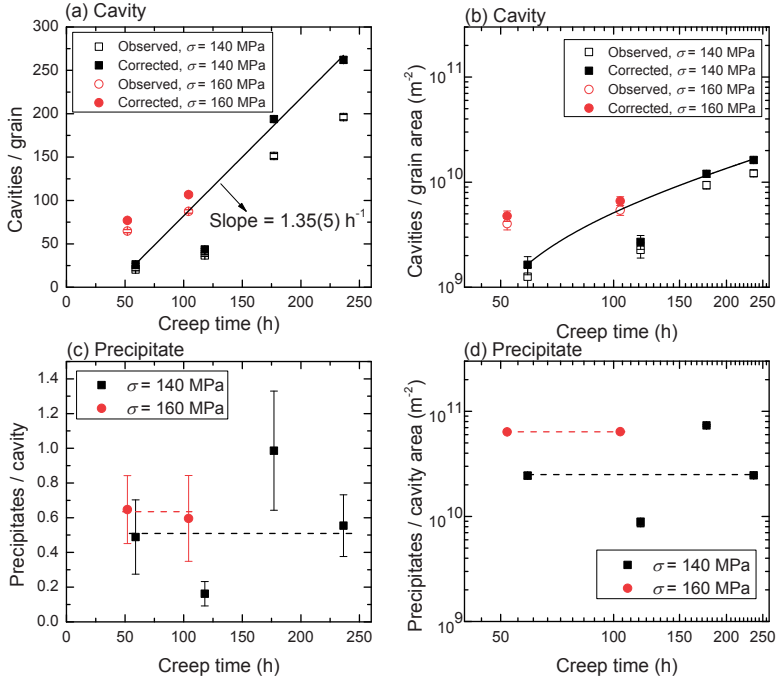


**Fig. 7.11.** Number of cavities and precipitates as a function of creep time. Number of cavities (a) per grain and (b) per grain area (amounts to  $\langle d_{\text{grain}} \rangle^{-2}$ , where  $\langle d_{\text{grain}} \rangle$  is the average grain diameter of 127  $\mu\text{m}$ ) as a function of creep time. The curves in (a) and (b) are linear fits of the corrected cavity number versus creep time for the sample creep at a stress of 140 MPa. Number of precipitates (c) per cavity and (d) per cavity area indicating a constant value over creep time. The lines in (c) and (d) are a guide to the eye.

In-situ studies on cavity growth during creep in brass [35-36] and copper [37] show a large variety in growth behavior for single cavities. An average volumetric growth rate  $\dot{V}$  is thus required to describe the overall growth behavior. To analyze the growth rates of both the cavities and precipitates, their average volumes are shown in Fig. 7.12 divided into isolated and linked cavities and precipitates. The fitting curves in Fig. 7.12 indicate that the average volume as a function of the creep time  $t$  follows a power law, expressed as  $\langle V \rangle = kt^n$ , for both cavities and precipitates. The fitting parameters of  $k$  and  $n$  are given in Table 7.2. For isolated cavities and precipitates, the power law exponents are identical and equal to  $n = 0.8$ . For linked cavities the power law exponent increases to  $n = 1.3$ , whereas it remains  $n = 0.8$  for the linked precipitates. This growth behavior is consistent with that observed in the Fe-Au alloy.

For comparison, we also listed the fitting parameters of the power law growth for the Fe-Au alloy in Table 7.2. Compared to the Fe-Au alloy, the pre-factor  $k$  for both the isolated and linked cavities are smaller than for the Fe-W alloy, which indicates a slower cavity growth rate (as the time exponents are equal). Besides the differences in materials properties and the applied load the average grain size of the Fe-W alloy samples ( $\approx 127 \mu\text{m}$ ) is much larger than that of the Fe-Au alloy samples ( $\approx 57 \mu\text{m}$ ). The pre-factors for the precipitate growth in the Fe-W alloy are also found to be smaller than those in the Fe-Au alloy. This difference is mainly attributed to a much slower volume diffusivity of W compared to Au in *bcc* iron ( $D_{\text{Au}}/D_{\text{W}} \approx 10^3$  at  $550 \text{ }^\circ\text{C}$  [25]).

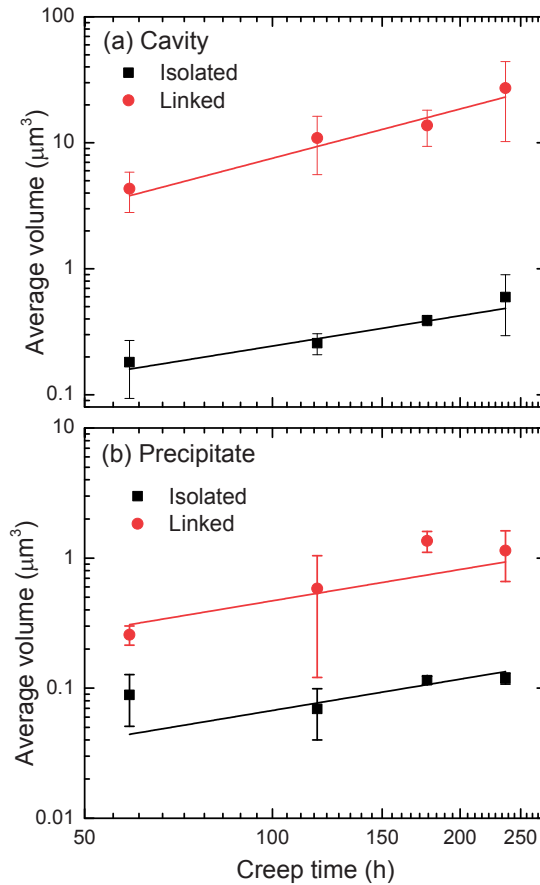


**Fig. 7.12.** Average volume  $\langle V \rangle$  of isolated and linked (a) cavities and (b) precipitates as a function of the creep time  $t$ . The lines show a fit to  $\langle V \rangle = kt^n$ .

**Table 7.2.** Fit parameters of the average volume  $\langle V \rangle$  versus the creep time  $t$  to a power law dependence of the form  $\langle V \rangle = kt^n$  for the Fe-W alloy. For comparison, the fit parameters from a previous study for the Fe-Au alloy [26] are listed.

Sample	Particle type	Cavities		Precipitates	
		$k$	$n$	$k$	$n$
		( $\mu\text{m}^3\text{h}^{-n}$ )		( $\mu\text{m}^3\text{h}^{-n}$ )	
Fe-4W	Isolated	0.0061(2)	0.8	0.0017(1)	0.8
	Linked	0.019(2)	1.3	0.012(2)	0.8
Fe-3Au	Isolated	0.033(6)	0.8	0.0036(5)	0.8
	Linked	0.05(1)	1.3	0.04(1)	0.8

The time exponent  $n = 0.8$  for precipitate growth is consistent with results from modeling. Aaron and Aaronson [38] experimentally observed that the time exponent for the volumetric growth of precipitates at grain boundaries is between 0.66 and 1 with an average of 0.81. A recent study by Versteylen and coworkers [39] showed that the time exponent for the filling of a grain-boundary cavity by diffusional precipitation can range from 0.5 to 1 and strongly depends on (i) the ratio between the cavity spacing and the cavity radius and (ii) the ratio between the grain-boundary diffusivity and bulk diffusivity of the supersaturated solute atoms. For isolated cavities a similar diffusional character of vacancies (the reverse diffusion of Fe) is expected resulting in the same growth exponent of 0.8. However, the linkage of cavities significantly accelerates the cavity growth resulting in an increase of the time exponent to 1.3 (see Fig. 7.12a).

### 7.4.3. Filling time for creep cavities

In a previous work [26] we analyzed the filling ratio as a function of the cavity volume. Without linkage with neighboring cavities the filling ratio  $FR$  can continuously increase to reach 1 at complete filling. However, for cavity growth with linkage to neighboring cavities the filling ratio initially increases and is then expected to continuously decrease after linkage occurs as this accelerates the cavity growth. In the present study of the Fe-W alloy, we also find these two trends in the maps of the filling ratio as a function of the cavity volume in Figs. 7.7 and 7.8 for the isolated and linked cavities.

The time-dependent measurements now allow us to estimate the filling time for the creep cavities. Fig. 7.7 shows that filling ratios for an initial cavity volume of  $V_0 > 0.1 \mu\text{m}^3$  are distributed over the full range between 0 and 1 at all four creep stages, indicating a complete filling could be achieved within  $0.25t_R$  ( $= 59$  h) at a stress of 140 MPa. At 160 MPa, the filling ratios for  $V_0 > 0.1 \mu\text{m}^3$  however only range up to 0.6, indicating that complete filling has not been achieved within  $0.5t_R$  ( $= 52$  h). The average filling ratio  $\langle FR \rangle$  for the partially filled cavities that do not show a linkage

with neighboring cavities is plotted in in Fig. 7.13a. It clearly shows that for  $\sigma = 140$  MPa the value of  $\langle FR \rangle$  saturates at about 0.35 after 59 h, whereas for  $\sigma = 160$  MPa the value of  $\langle FR \rangle$  increases to the same saturation level after 52 h. This indicates that for  $\sigma = 140$  MPa a creep time of 59 h is long enough to completely fill a creep cavity with an initial volume of about  $0.1 \mu\text{m}^3$ . On the other hand, the shortest filling time at  $\sigma = 160$  MPa can be used to estimate the lower limit of the filling time at a lower load of 140 MPa. Assuming that the filling time shows the same stress dependence as the strain rate (see Fig. S7.2), a lower limit for the filling time of a cavity of 33 h is obtained for  $\sigma = 140$  MPa. Therefore, the time for complete filling of a cavity with an initial size of  $V_0 \approx 0.1 \mu\text{m}^3$  is between 33 and 59 h for creep at a temperature of  $550 \text{ }^\circ\text{C}$  and a stress of 140 MPa, whereas the filling time at a stress of 160 MPa is longer than 52 h (and expected to be shorter than 104 h).

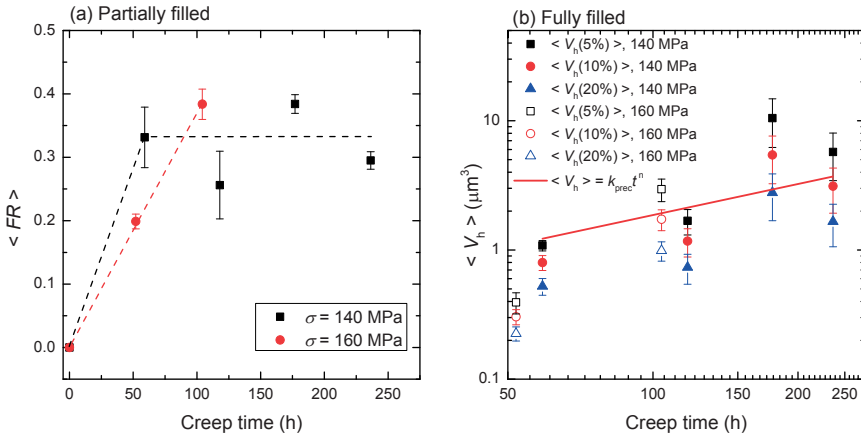


**Fig. 7.13.** (a) Average filling ratio  $\langle FR \rangle$  of partially filled cavities and (b) average volume of the 5%, 10% and 20% largest fully filled cavities, denoted as  $\langle V_h(5\%) \rangle$ ,  $\langle V_h(10\%) \rangle$  and  $\langle V_h(20\%) \rangle$ , as a function of creep time for creep at  $550 \text{ }^\circ\text{C}$  and constant loads of 140 MPa and 160 MPa. The curves in (a) are guide lines for the eye and the curve in (b) is a fit of data for creep at 140 MPa with  $\langle V_h \rangle = k_{prec} t_h^n$  where  $k_{prec} = 0.0468 \mu\text{m}^3\text{h}^{-0.8}$  and  $n = 0.8$ .

The largest volume of the fully filled cavity also reflects the kinetics of filling. Fig. 7.13b shows that at a stress of 140 MPa the average volume of the 5%, 10% and 20% largest fully filled cavities increases with the same slope for increasing creep times. As expected, for the higher stress of 160 MPa the largest healed volume is smaller compared to that for 140 MPa. According to our previous work [26], the healing time  $t_h$  can be estimated by  $t_h = \left( \frac{V_0}{k_{prec} - k_{cav}} \right)^{1/n}$ , where  $k_{prec}$  and  $k_{cav}$  account for the growth dependence of precipitates and cavities, respectively. The healed volume in this model corresponds to  $V_h = k_{prec} t_h^n$ . An estimate of the healing time is made by averaging the lower and upper limits as  $t_h = 46$  h for an initial cavity  $V_0 \approx 0.1 \mu\text{m}^3$ , which results in

$V_h \approx 1 \mu\text{m}^3$  for creep at 140 MPa. Assuming  $n = 0.8$  (consistent with the growth exponent shown in Fig. 7.12), prefactors of  $k_{\text{prec}} \approx 0.0468 \mu\text{m}^3\text{h}^{-0.8}$  and  $k_{\text{cav}} \approx 0.0421 \mu\text{m}^3\text{h}^{-0.8}$  are obtained respectively. The derived value of  $k_{\text{prec}}$  is in good agreement with the tomography data for the maximum healed cavity shown in Fig. 13b. This indicates that the estimate for the filling time of a creep cavity at a temperature of 550 °C and a stress of 140 MPa is realistic and fully supported by our tomographic observations.

## 7.5. Conclusions

We have studied the self-healing of creep damage in a high-purity binary Fe-3.8 wt.% W alloy at a temperature of 550 °C and several constant applied stresses. The spatial distribution and the morphology of both the precipitates and the cavities were monitored by synchrotron X-ray nano-tomography. The nature of the creep cavities and the precipitates indicate the autonomous filling of creep cavities by precipitation of the Fe<sub>2</sub>W Laves phase in the Fe-W alloy. The 3D images obtained at a resolution of 100 nm provide detailed statistics on the creep cavities, while the 3D images obtained at a resolution of 30 nm allow a detailed view on the morphology of the partially filled cavities. Two different trends for the cavity filling are observed for isolated and linked cavities, respectively. The filling ratio of the isolated cavity increases continuously until complete filling is achieved, whilst the filling ratio of the linked cavities first increases, but then continuously decreases after linkage has occurred. This is mainly attributed to different growth mechanisms for isolated and linked cavities as indicated by different power law exponents for cavity growth. The parameters responsible for the filling are identified and the characteristic filling time is estimated. The results show that for our Fe-W alloy about 46 h are required to completely fill a creep cavity with an initial volume of 0.1  $\mu\text{m}^3$  which reaches a volume of about  $V_h \approx 1 \mu\text{m}^3$  at complete filling under creep conditions at a temperature of 550 °C and a constant stress of 140 MPa.

The demonstrated self-healing potential of supersaturated W atoms in *bcc* iron provides a new perspective on the role of W for high-temperature creep-resistant steels. The self-healing mechanism in Fe-W alloys operates in parallel to the solid solution strengthening. This study shows a promising future for the control of creep damage by the addition of affordable alloying elements that enable the self-healing of creep damage.

## Acknowledgements

This research is financially supported by the innovation-oriented research program (IOP) on self-healing materials of the Dutch Ministry of Economic Affairs, Agriculture and Innovation (Project SHM012011) and a grant from the China Scholarship Council (CSC). We thank Joost van Meel and Dr. Dominique Ngan-Tillard at the Faculty of Civil Engineering and Geosciences, Delft University of Technology for providing the access to FEI Avizo. We acknowledge the European Synchrotron Radiation Facility for provision of synchrotron radiation facilities and thank the beamline staff for assistance in using beamline ID16A-NI.

## References

1. M. Taneike, F. Abe, K. Sawada: *Nature*, 2003, vol. 424, pp. 294-6.
2. H.K.D.H. Bhadeshia: *ISIJ Int.*, 2001, vol. 41, pp. 626-40.
3. K. Maruyama, K. Sawada, J. Koike: *ISIJ Int.*, 2001, vol. 41, pp. 641-53.
4. Q. Lu, W. Xu, S. van der Zwaag: *Acta Mater.*, 2014, vol. 77, pp. 310-23.
5. L. Sun, T.H. Simm, T.L. Martin, S. McAdam, D.R. Galvin, K.M. Perkins, P.A.J. Bagot, M.P. Moody, S.W. Ooi, P. Hill, M.J. Rawson, H.K.D.H. Bhadeshia: *Acta Mater.*, 2018, vol. 149, pp. 285-301.
6. M.D. Hager, P. Greil, C. Leyens, S. van der Zwaag, U.S. Schubert: *Adv. Mater.*, 2010, vol. 22, pp. 5424-30.
7. S. van der Zwaag, E. Brinkman, eds., *Self healing materials: pioneering research in the Netherlands*, IOS Press, Amsterdam, 2015.
8. N.H. van Dijk, S. van der Zwaag: *Adv. Mater. Interfaces*, 2018, p. 1800226.
9. K. Laha, J. Kyono, S. Kishimoto, N. Shinya: *Scr. Mater.*, 2005, vol. 52, pp. 675-8.
10. K. Laha, J. Kyono, N. Shinya: *Scr. Mater.*, 2007, vol. 56, pp. 915-8.
11. K. Laha, J. Kyono, T. Sasaki, N. Shinya: *Metall. Mater. Trans. A*, 2005, vol. 36, pp. 399-409.
12. N. Shinya: *Adv. Sci. Tech.*, 2008, vol. 54, pp. 152-7.
13. S. Zhang, J. Kohlbrecher, F.D. Tichelaar, G. Langelaan, E. Brück, S. van der Zwaag, N.H. van Dijk: *Acta Mater.*, 2013, vol. 61, pp. 7009-19.
14. S. Zhang, C. Kwakernaak, W.G. Sloof, E. Brück, S. van der Zwaag, N.H. van Dijk: *Adv. Eng. Mater.*, 2015, vol. 17, pp. 598-603.
15. S. Zhang, C. Kwakernaak, F.D. Tichelaar, W.G. Sloof, M. Kuzmina, M. Herbig, D. Raabe, E. Brück, S. van der Zwaag, N.H. van Dijk: *Metall. Mater. Trans. A*, 2015, vol. 46, pp. 5656-70.
16. S. Zhang, H. Fang, M.E. Gramsma, C. Kwakernaak, W.G. Sloof, F.D. Tichelaar, M. Kuzmina, M. Herbig, D. Raabe, E. Brück, S. van der Zwaag, N.H. van Dijk: *Metall. Mater. Trans. A*, 2016, vol. 47, pp. 4831-44.
17. R.L. Klueh: *Int. Mater. Rev.*, 2005, vol. 50, pp. 287-310.
18. A. Puype, L. Malerba, N. De Wispelaere, R. Petrov, J. Sietsma: *J. Nuc. Mater.*, 2018, vol. 502, pp. 282-8.
19. T. Sakthivel, S.P. Selvi, K. Laha: *Mater. Sci. Eng. A*, 2015, vol. 640, pp. 61-71.
20. C.S. Smith: *J. Appl. Phys.*, 1941, vol. 12, pp. 817-22.
21. P.J. Ennis, A. Zielinska-Lipiec, O. Wachter, A. Czyrska-Filemonowicz: *Acta Mater.*, 1997, vol. 45, pp. 4901-7.
22. K. Sawada, M. Takeda, K. Maruyama, R. Ishii, M. Yamada, Y. Nagae, R. Komine: *Mater. Sci. Eng. A*, 1999, vol. 267, pp. 19-25.
23. D. Rojas, J. Garcia, O. Prat, G. Sauthoff, A.R. Kaysser-Pyzalla: *Mater Sci Eng A*, 2011, vol. 528, pp. 5164-76.
24. A. Aghajani, C. Somsen, G. Eggeler: *Acta Mater.*, 2009, vol. 57, pp. 5093-106.
25. C.D. Versteyleen, N.H. van Dijk, M.H.F. Sluiter: *Phys. Rev. B*, 2017, vol. 96, p. 094105.
26. H. Fang, C.D. Versteyleen, S. Zhang, Y. Yang, P. Cloetens, D. Ngan-Tillard, E. Brück, S. van der Zwaag, N.H. van Dijk: *Acta Mater.*, 2016, vol. 121, pp. 352-64.

27. J.C. da Silva, A. Pacureanu, Y. Yang, F. Fus, M. Hubert, L. Bloch, M. Salome, S. Bohic, P. Cloentens, *High-energy cryo X-ray nano-imaging at the ID16A beamline of ESRF*, Proc. SPIE 10389, X-Ray Nanoimaging: Instruments and Methods III, 2017, p. 103890F.
28. J.C. da Silva, A. Pacureanu, Y. Yang, S. Bohic, C. Morawe, R. Barrett, P. Cloentens: *Optica*, 2017, vol. 4, pp. 492-5.
29. C. Gramaccioni, Y. Yang, A. Procopio, A. Pacureanu, S. Bohic, E. Malucelli, S. Lotti, G. Farruggia, I. Bukreeva, A. Notargiacomo, M. Fratini, P. Valenti, L. Rosa, F. Berlutti, P. Cloentens, S. Lagomarsino: *Appl. Phys. Lett.*, 2018, vol. 112, p. 053701.
30. P. Cloentens, W. Ludwig, J. Baruchel, D. van Dyck, J. van Landuyt, J.P. Guigay, M. Schlenker: *Appl. Phys. Lett.*, 1999, vol. 75, pp. 2912-4.
31. A. Mirone, B. Brun, E. Gouillart, P. Tafforeau, J. Kieffer: *Nucl. Instrum. Meth. B*, 2014, vol. 324, pp. 41-8.
32. <http://www.diplib.org/>.
33. M.E. Kassner, T.A. Hayes: *Int. J. Plasticity*, 2003, vol. 19, pp. 1715-48.
34. R. Raj, M.F. Ashby: *Acta Metall.*, 1975, vol. 23, pp. 653-66.
35. A. Pyzalla, B. Camin, T. Buslaps, M. Di Michiel, H. Kaminski, A. Kottar, A. Pernack, W. Reimers: *Science*, 2005, vol. 308, pp. 92-5.
36. A. Isaac, K. Dzieciol, F. Sket A. Borbély: *Metall. Mater. Trans. A*, 2011, vol. 42, pp. 3022-30.
37. A. Isaac, F. Sket, W. Reimers, B. Camin, G. Sauthoff, A.R. Pyzalla: *Mater. Sci. Eng. A*, 2008, vol. 478, pp. 108-118.
38. H.B. Aaron, H.I. Aaronson: *Acta Metall.*, 1968, vol. 16, pp. 789-98.
39. C.D. Versteyleen, N.K. Szymański, M.H.F. Sluiter, N.H. van Dijk: *Philos. Mag.*, 2018, vol. 98, pp. 864-77.



## Supplementary Material for Chapter 7

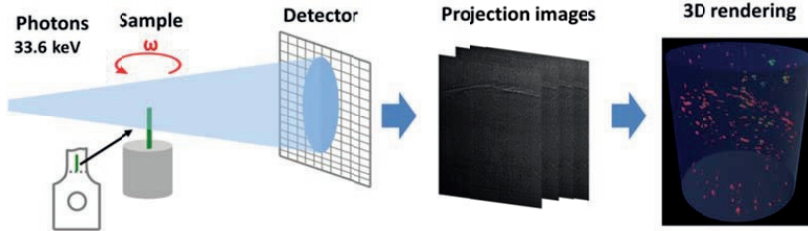


**Fig. S7.1.** Schematic diagram of the synchrotron X-ray holotomography imaging process. In the 3D rendering the precipitates and cavities are labelled in green and red, respectively, while the iron matrix is in transparent light blue.

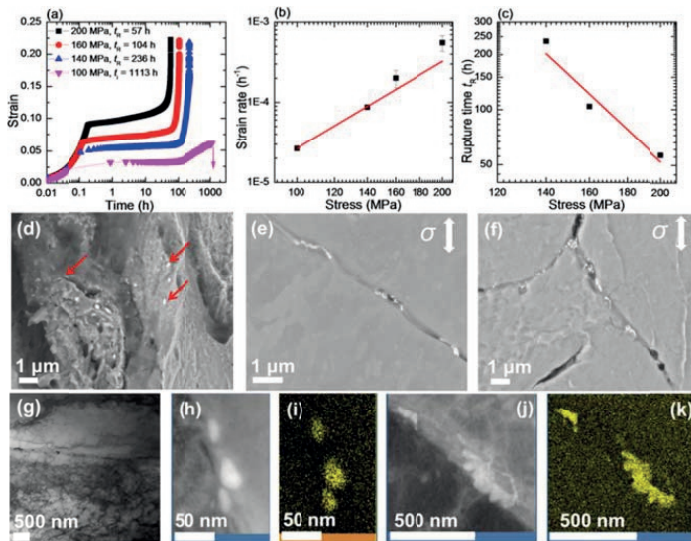


**Fig. S7.2.** (a) Creep curves of Fe-W alloy sample creep at 550 °C and different constant loads, where  $t_R$  indicates the rupture time and  $t_i$  the interruption time. (b) Strain rate and (c) rupture time as a function of the applied stress both showing a power law dependence. (d) SEM of the fracture surface after creep rupture revealing precipitates (indicated by arrows) attached to creep cavities. (e) and (f) show the filling of creep cavities by precipitation at inclined grain boundary and grain junction, respectively. (g) TEM dark field images showing precipitates at a grain boundary. (h) TEM bright field images of isolated precipitates (taken from (g)) and (i) corresponding W mapping. (j) TEM bright field images of linked precipitates (taken from (g)) and (k) corresponding W mapping.

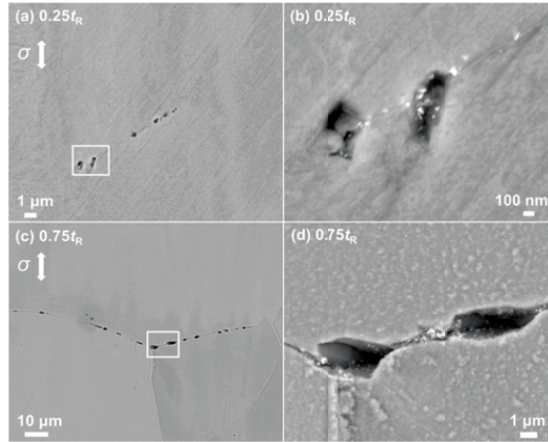


**Fig. S7.3.** SEM images showing precipitation at grain-boundary cavities in Fe-W alloy sample after creep at a temperature of 550 °C and a stress of 160 MPa for a time relative to rupture  $t/t_R$  of (a, b) 0.25 and (c, d) 0.75. (b) and (d) show the zoom view of the region in (a) and (c), respectively, marked with rectangle boxes. The direction of the applied stress is indicated in (a) and (c).

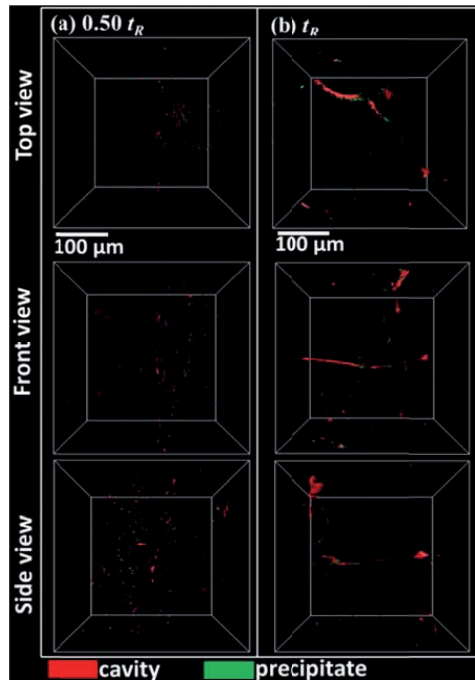


**Fig. S7.4.** 3D tomographic volume ( $321 \times 321 \times 321 \mu\text{m}^3$ ) with a voxel size of 100 nm after phase segmentation showing cavities and precipitates in Fe-W alloy samples after creep at a temperature of 550 °C and a stress of 160 MPa for a time relative to rupture  $t/t_R$  of (a) 0.50 and (b) 1.00, where  $t_R$  is the rupture time. The applied stress is normal to the top view.

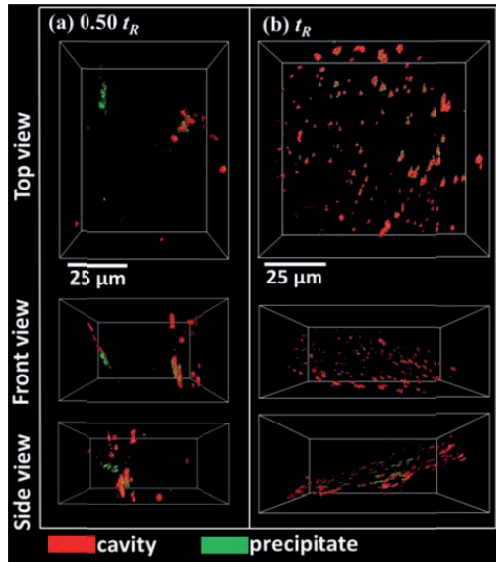


**Fig. S7.5.** 3D tomographic volume for a voxel size of 30 nm after phase segmentation showing cavities and precipitates in Fe-W alloy samples after creep at a temperature of 550 °C and a stress of 160 MPa for a time relative to rupture  $t/t_R$  of (a) 0.50 and (d) 1.00, where  $t_R$  is the rupture time. The region of interest (ROI) is (a)  $70 \times 96 \times 39 \mu\text{m}^3$  and (b)  $96 \times 96 \times 36 \mu\text{m}^3$ . The applied stress is normal to the top view.

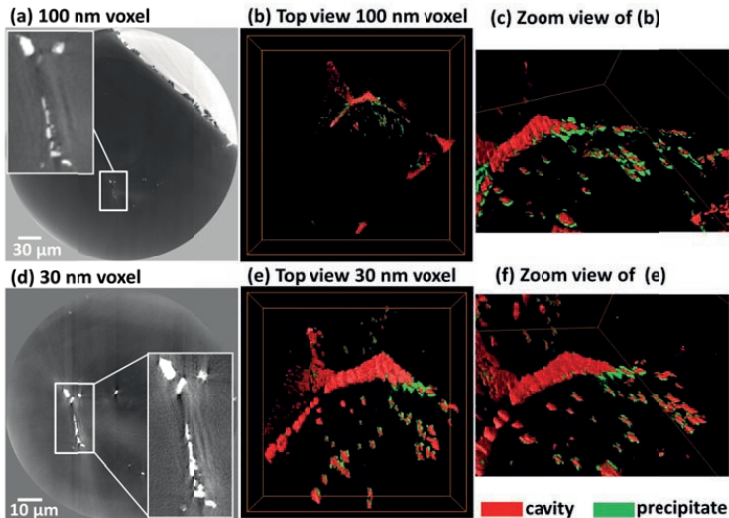


**Fig. S7.6.** Comparison of the same sample region in a (a, d) 2D slice and (b, c, e, f) 3D segmentation after creep at a temperature of 550 °C and a stress of 140 MPa at rupture ( $t = t_R$ ), resolved voxel sizes of (b, e) 100 nm and (c, f) 30 nm. The applied stress is normal to the top view.

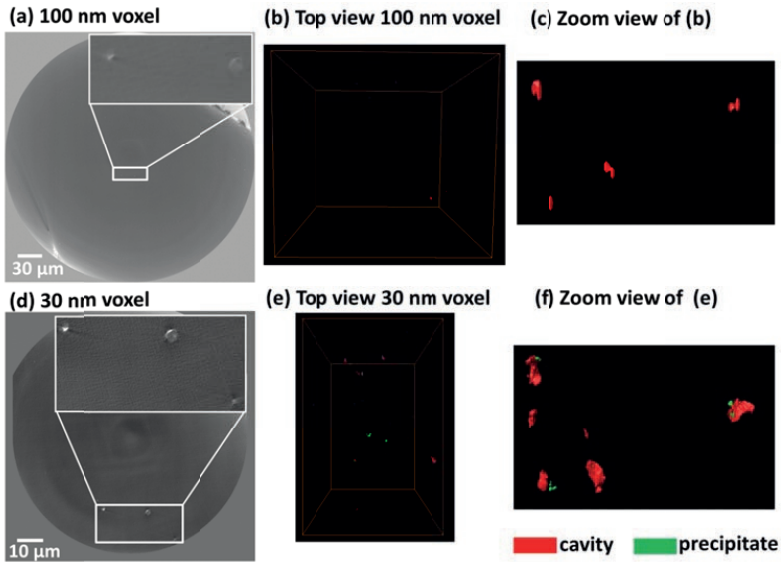


**Fig. S7.7.** Comparison of the same sample region in a (a, d) 2D slice and (b, c, e, f) 3D segmentation after creep at a temperature of 550 °C and a stress of 140 MPa for a creep time of  $t = 0.5t_R$  (where  $t_R$  is the time to rupture) resolved at voxel sizes of (b, c) 100 nm and (e, f) 30 nm. The applied stress is normal to the top view.

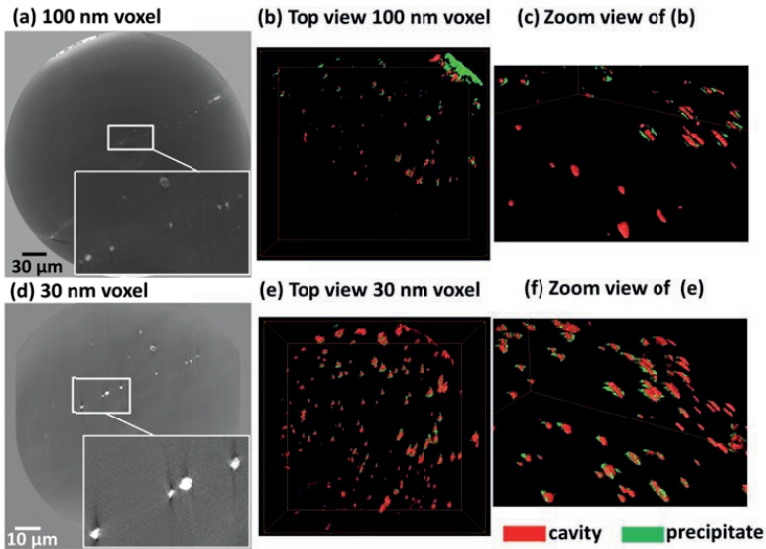


**Fig. S7.8.** Comparison of the same sample region in a (a, d) 2D slice and (b, c, e, f) 3D segmentation after creep at a temperature of 550 °C and a stress of 160 MPa at rupture ( $t = t_R$ ) resolved at voxel sizes of (b, c) 100 nm and (e, f) 30 nm. The applied stress is normal to the top view.

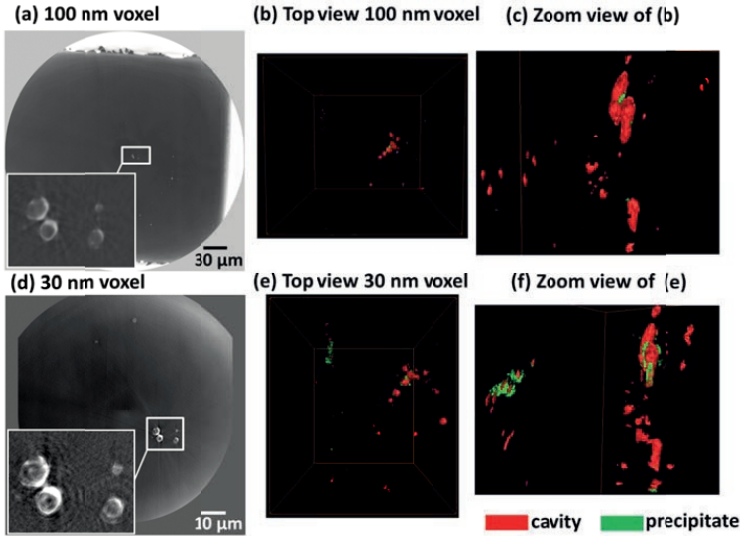


**Fig. S7.9.** Comparison of the same sample region of a (a, d) 2D slice and (b, c, e, f) 3D segmentation after creep at a temperature of 550 °C and a stress of 160 MPa for a creep time of  $t = 0.5t_R$  (where  $t_R$  is the rupture time) resolved at voxel sizes of (b, c) 100 nm and (e, f) 30 nm. The applied stress is normal to the top view.

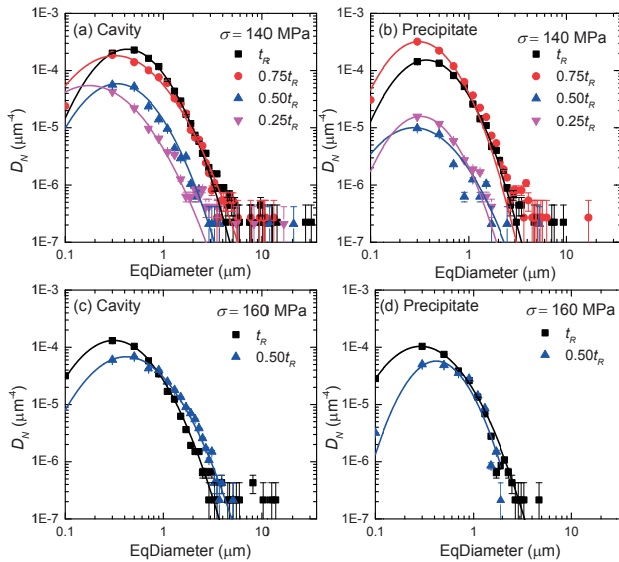


**Fig. S7.10.** Number distribution  $D_N$  of (a, c) cavities and (b, d) precipitates as a function of the equivalent diameter  $d$  for the Fe-W alloy samples after creep for specified fractions of the rupture time. The creep tests are performed at a stress of (a, b) 140 MPa and (c, d) 160 MPa.

**Table S7.1.** Fit parameters  $N_0$ ,  $\bar{d}$  and  $\omega$  for the log-normal size distribution of open cavities and precipitates after creep for a selected fraction  $t/t_R$  of ruptured time at an applied stress of  $\sigma$  of 140 and 160 MPa and a temperature of 550 °C. The number density  $N_p$  and volume fraction  $f_v$  are obtained directly from the 3D tomographic volume at a voxel size of 100 nm.

Phase	$\sigma$ (MPa)	$t/t_R$	Fit			Experiment	
			$N_0$	$\bar{d}$	$\omega$	$N_p$	$f_v$
			( $\mu\text{m}^{-3}$ )	( $\mu\text{m}$ )	(-)	( $\mu\text{m}^{-3}$ )	(%)
Cavities	140	0.25	$2.5(1)\times 10^{-5}$	0.32(1)	0.77(2)	$1.90\times 10^{-5}$	0.0122
		0.50	$3.9(1)\times 10^{-5}$	0.51(1)	0.64(1)	$3.41\times 10^{-5}$	0.0235
		0.75	$1.4(1)\times 10^{-4}$	0.55(1)	0.74(2)	$1.41\times 10^{-4}$	0.0322
		1	$1.9(1)\times 10^{-4}$	0.62(1)	0.61(1)	$1.83\times 10^{-4}$	0.1623
	160	0.50	$6.2(3)\times 10^{-5}$	0.66(2)	0.69(3)	$6.04\times 10^{-5}$	0.0063
		1	$8.3(1)\times 10^{-5}$	0.48(1)	0.65(1)	$8.15\times 10^{-5}$	0.0190
Precipitates	140	0.25	$8.4(3)\times 10^{-6}$	0.44(1)	0.56(3)	$8.12\times 10^{-6}$	0.0002
		0.50	$6.2(2)\times 10^{-6}$	0.45(2)	0.70(1)	$4.80\times 10^{-6}$	0.0005
		0.75	$1.7(1)\times 10^{-4}$	0.43(1)	0.57(1)	$1.72\times 10^{-4}$	0.0228
		1	$9.9(1)\times 10^{-5}$	0.52(1)	0.59(1)	$9.62\times 10^{-5}$	0.0082
	160	0.50	$3.6(2)\times 10^{-5}$	0.62(2)	0.55(2)	$3.82\times 10^{-5}$	0.0009
		1	$6.2(1)\times 10^{-5}$	0.45(1)	0.66(1)	$6.00\times 10^{-5}$	0.0017

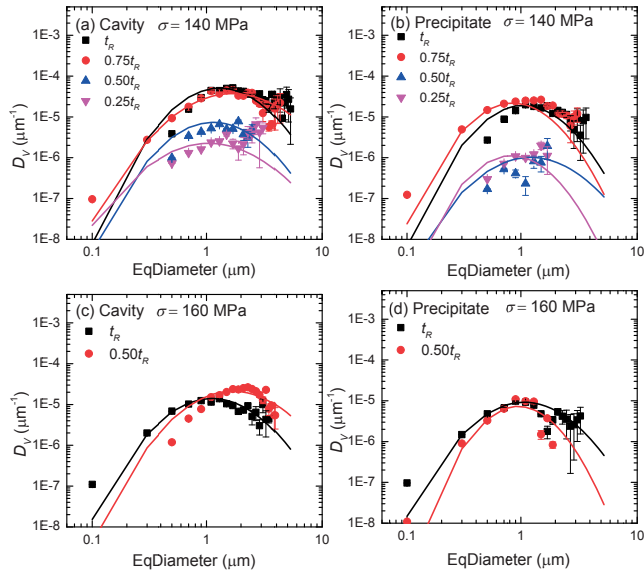


**Fig. S7.11.** Volume distribution  $D_V$  of (a, c) cavities and (b, d) precipitates as a function of the equivalent diameter  $d$  for the Fe-W alloy samples after creep for a specified fraction of the rupture time. The creep tests are performed at a stress of (a, b) 140 MPa and (c, d) 160 MPa. For clarity, the data points with  $d > 3 \mu\text{m}$  are not shown due to the large statistical uncertainty.

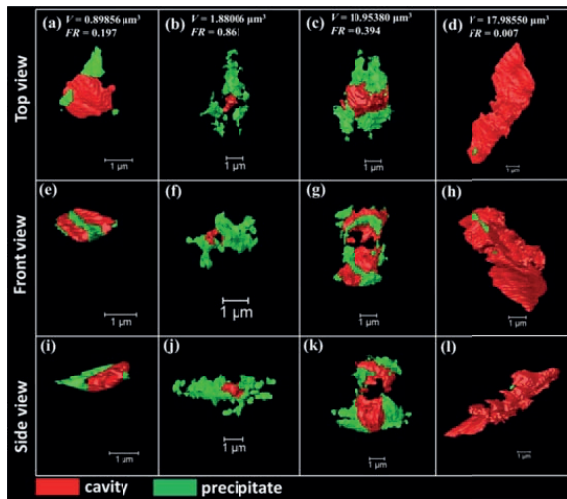


**Fig. S7.12.** Examples of partially filled particles in Fe-W alloy samples after creep at a temperature of 550 °C and a stress of 160 MPa for a creep time of  $t = 0.50t_R$  (where  $t_R$  is the rupture time) viewed from different angles and obtained for a voxel size of 30 nm. The applied stress is normal to the top view.



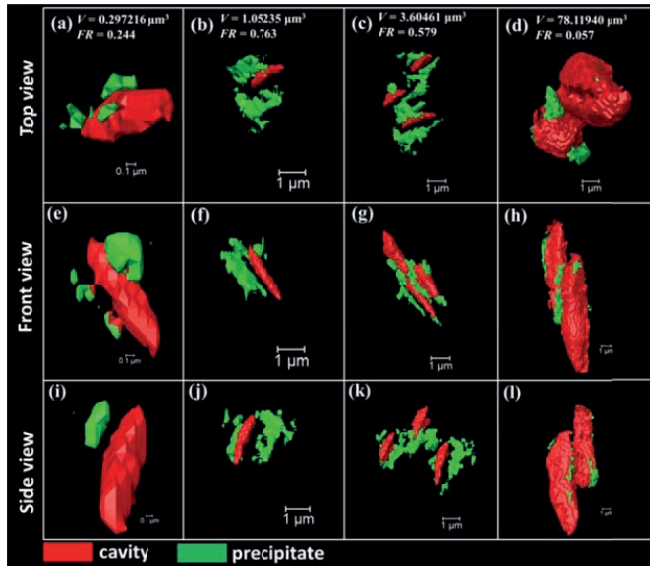


**Fig. S7.13.** Examples of partially filled particles in Fe-W alloy samples after creep at a temperature of 550 °C and a stress of 160 MPa at rupture ( $t = t_R$ ) viewed from different angles and obtained for a voxel size of 30 nm. The applied stress is normal to the top view.

**Movie S7.1.** 3D visualization with a voxel size of 100 nm indicating the segmentation and spatial distribution of cavities and precipitates in the Fe-W sample after creep at 550 °C and 140 MPa for a creep time of  $t = 0.75t_R$  (where  $t_R$  is the rupture time).

Filename: MovieS1\_S2\_Fe\_4W\_550C\_140MPa\_0\_75tR\_100nm.mpg

File description: This movie shows the correspondence between the original 3D volume image (grey value) and segmented 3D volume image (color) by clipping slices from three orthogonal directions. In the grey valued 3D volume image the bright and dark features are cavities and precipitates, respectively (see main text of the manuscript for details). After segmentation the cavities and precipitates are denoted in red and green colors, respectively. The iron matrix is in transparent light grey. It should be noted that the edge part of the slices are not in the sample volume. After the clipping, the segmented 3D volume image is rotated and zoomed inside into different regions of the sample volume to show the spatial distribution of the cavities and precipitates from different angles.

**Movie S7.2.** 3D visualization with a voxel size of 30 nm indicating the segmentation and spatial distribution of cavities and precipitates in the Fe-W sample after creep at 550 °C and 140 MPa for a creep time of  $t = 0.75t_R$  (where  $t_R$  is the rupture time).

Filename: MovieS2\_S2\_Fe\_4W\_550C\_140MPa\_0\_75tR\_30nm.mpg

File description: This movie shows the correspondence between the original 3D volume image (grey value) and segmented 3D volume image (color) by clipping slices from three orthogonal directions. In the grey valued 3D volume image the bright and dark features are cavities and



precipitates, respectively (see main text of the manuscript for details). After segmentation the cavities and precipitates are denoted in red and green colors, respectively. The iron matrix is in transparent light grey. It should be noted that the edge part of the slices are not in the sample volume. After the clipping, the segmented 3D volume image is rotated to show the spatial distribution of the cavities and precipitates from different angles.

**Movie S7.3.** 3D visualization with a voxel size of 100 nm indicating the spatial distribution of cavities classified into five different shapes (spherical, equiaxed, rod-like, sheet and complex) in the Fe-W sample after creep at 550 °C and 140 MPa for a creep time of  $t = t_R$  (where  $t_R$  is the rupture time).

Filename: MovieS3\_S1\_Fe\_4W\_550C\_140MPa\_tR\_100nm\_shape.mpg

File description: This movie shows the spatial distribution of the creep cavities labelled in different colors in the 3D volume image. First all the cavities are labeled in red. Then the identified spherical, equiaxed, rod-like, sheet and complex cavities are shown in order and labelled in red, blue, yellow, pink and light blue, respectively. Finally all cavities are shown and labelled in colors corresponding to their shape category.

---

# Summary

Solid-state phase transformations in steels cover a broad range of aspects. The underlying physics behind these phase transformations usually include nucleation, diffusion, lattice reconstruction and interactions between solutes and grain boundaries and interfaces. These features and the fact that the events take place at high temperatures, in the bulk, at time scales ranging from milliseconds to hours and at length scales ranging from atomic dimensions to millimeters make even the most widely studied phase transformation in steel, the austenite-ferrite phase transformation, only approximately understood and therefore an attractive topic for investigation. Quantitative data obtained by sophisticated physical characterization techniques in combination with supporting physical microstructural models addressing the relevant length and time scale are required to bring the field of ferrous physical metallurgy further.

This thesis focusses on two new approaches to orchestrate phase transformations in steels such that more physical insight is obtained or that new properties can be reached: (1) cyclic partial austenite-ferrite phase transformations that are designed to unravel the grain growth, and more specifically the interface mobility by avoiding concurrent nucleation of new phases. This topic is studied by computational studies and 3D neutron depolarization studies that are capable to in-situ monitor the ferrite grain size and fraction. (2) Self healing of creep damage by site selective precipitation of supersaturated iron-based alloys. A strong preference for precipitation at free creep cavity surfaces compared to that in the bulk can result in a filling of creep cavities and a significant extension of the creep life time. To make this self-healing mechanism applicable for creep-resistant steels, a search for an alternative healing agent for Au in Fe is to be executed and new design recipes need to be extracted on the basis of the experimental input from advanced characterization techniques such as electron microscopy and X-ray nanotomography.

In Chapters 2-4 the kinetics of the austenite-ferrite phase transformation is studied using 3D mixed-mode modelling and three dimensional neutron depolarization (3DND) for different processing conditions, *i.e.* continuous cooling, isothermal holding and thermal cycling. In Chapters 5-7 the self healing Fe-Au, Fe-Mo and Fe-W alloys have been studied in detail using creep tests and microstructure characterizations a.o. via nano-tomography using synchrotron radiation.

In Chapter 2 a 3D mixed-mode model that couples the classical nucleation theory and the interface mobility considering an intermediate case between diffusion-controlled and interface-controlled growth conditions is presented to predict the microstructure evolution in C-Mn steels during cooling from the austenitic state. This model has been validated by comparing the simulation results to those simulated with a phase-field model for identical parameters and dilatometry data for linear cooling of an Fe-0.10C-0.49Mn (wt.%) steel. The simulations show that the ferrite fractions during  $\gamma$ - $\alpha$  transformation can be reproduced by tuning the growth parameters. However, the evolution of the ferrite grain size distribution cannot be reproduced by a tuning of only these growth parameters. This suggests that analyzing grain size

distribution for different  $f_0$  levels is required to derive more accurate estimates of the key physical parameters, including the nucleation temperature interval and the effective interface mobility. Better estimates of both are essential for controlling the microstructure during steel production.

Given the fact that both the ferrite fraction and the ferrite grain size distribution are important to predict transformation kinetics, quantitative in-situ information on the ferrite grain size is indispensable. Three dimensional neutron depolarization (3DND) may be the only technique that is able to measure *in-situ* the ferrite fraction and ferrite grain size simultaneously within the bulk of transforming steel sample. In 3DND the rotation angle of the polarized neutron beam after passing through a magnetized sample corresponds to the fraction of ferromagnetic phase. The decrease in the degree of polarization measures the average variation in the local magnetic field, thereby providing a measure for the magnetic domain size. For austenite-ferrite phase transformations the 3DND can provide measurements of ferrite fraction and ferrite grain size as it is consistent with the magnetic configuration below the Curie temperature of ferrite. To extend the 3DND data analysis from its current level yielding only the average ferrite grain size to a state where also the ferrite grain size distribution is determined one needs to numerically compute the magnetic configuration and compare the resulting 3DND parameters to the steel microstructure, as is presented in Chapter 3. The results show that the magnetic particle size derived from 3DND data is in very good agreement with the computed microstructural particle size over a wide range of volume fractions and grain size distributions. Deviations in the estimated particle size from 3DND data are found to originate from the spread in particle size. A relationship between the field correlation function and the relative width of the particle size distribution has been proposed to accurately describe the deviations and extract the grain size distribution.

In Chapter 4 the evolution of the ferrite fraction and the ferrite grain size during slow partial cyclic austenite-ferrite phase transformations in an Fe-0.25C-2.1Mn (wt.%) steel has been studied with 3DND experiments. The number density of the ferrite grains was determined and the results demonstrate that during cycling nucleation is negligible or even absent. Hence, the current work provides the first experimental evidence that cyclic partial transformations indeed can yield direct information on the actual movement of the austenite-ferrite interface and can be free from the effects of simultaneous nucleation. The interface migration velocity was found to be of the order of  $10^{-3}$   $\mu\text{m/s}$  during cycling. This low value is attributed to Mn partitioning for which the width of the diffusion spike is estimated to be 1-15 nm. The intrinsic cyclic behavior of the interface migration is visible after subtracting the effect of the progressive interfacial migration into austenite. The closing loops of interface position are reproducible for multi cycles and a stagnant stage is revealed.

In Chapter 5 the microstructure of creep-failed Fe-Au samples is characterized using 3D with high-resolution X-ray nano-tomography based on a highly coherent and brilliant beam produced by a synchrotron source. The obtained 3D images of the microstructure of the Fe-Au alloy samples at nanometer length scale reveal different stages in the filling process of individual creep cavities by gold precipitation. The quantitative analysis of the size, shape and spatial distribution for the creep cavities and the gold precipitates demonstrates a strong correlation between the morphology of

the cavities and precipitates. It is demonstrated that the gold precipitates preferentially at the cavity surfaces and act as healing agents for creep cavities. The self-healing character in Fe-Au alloys is fully supported by this study. The filling ratio of individual creep cavities follow two distinct routes that are considered to correspond to the absence and presence of linkage for neighboring creep cavities.

The recipes to design a self healing Fe-X binary alloy can be extracted from these studies on the Fe-Au alloy. The key requirements for an element X to be an efficient self-healing agent can be summarized as follows: i) the element X can be solutionized into Fe matrix at high temperature, and be brought to an adequate degree of supersaturation at the creep temperature to provide appreciable driving force for precipitation; ii) the atomic size of X is considerably larger than that of the matrix Fe, resulting in high nucleation barrier for precipitation in the matrix and a strong preference to precipitate at the free surface of the damage site; iii) the diffusivity of the element X must be larger than that of Fe to ensure that the filling of the cavity (controlled by solute diffusion) can catch up with the cavity growth (controlled by vacancy diffusion). Both Fe-Mo and Fe-W alloys apply to these requirements. In Chapter 6 the self-healing of creep-induced defects in a high-purity Fe-Mo alloy (6.2 wt.% Mo) at temperatures of 813, 823 and 838 K has been studied. The electron microscopy measurements after creep clearly indicate a filling of creep cavities by Fe<sub>2</sub>Mo precipitates. In some cases a partial filling of the creep cavities is observed, while in most cases a complete filling is found. The demonstrated site-selective Fe<sub>2</sub>Mo precipitation at creep cavity surfaces suggest that self-healing in commercial high-temperature creep steels, which often already contain Mo for solid-solution strengthening, may be realized by adjusting the Mo level.

In Chapter 7 the self-healing of creep damage has been investigated for a high-purity binary Fe-3.8 wt.% W alloy at a temperature of 550 °C and several constant applied stresses. The spatial distribution and the morphology of both the precipitates and the cavities were monitored by synchrotron X-ray nano-tomography. The nature of the creep cavities and the precipitates indicate the autonomous filling of creep cavities by precipitation of the Fe<sub>2</sub>W Laves phase in the Fe-W alloy. The 3D images obtained at a resolution of 100 nm provide detailed statistics on the creep cavities, while the 3D images obtained at a resolution of 30 nm allow a detailed view on the morphology of the partially filled cavities. Two different trends for the cavity filling are observed for isolated and linked cavities, respectively. The filling ratio of the isolated cavity increases continuously until complete filling is achieved, whilst the filling ratio of the linked cavities first increases, but then continuously decreases after linkage has occurred. This is attributed to differences in growth behavior for isolated and linked cavities as indicated by different power law exponents for cavity growth. The characteristic filling time is estimated to be about 46 h for reaching a complete filling volume of about 1 μm<sup>3</sup> at a temperature of 550 °C and a constant stress of 140 MPa.

The demonstrated self-healing potential of supersaturated W atoms, together with Mo, in *bcc* iron provides new perspectives on the roles of Mo and W for high-temperature creep-resistant steels. The self-healing mechanism in such alloys operates in parallel to the solid-solution strengthening. These studies show a promising future for the control of creep damage by the tuning of more affordable alloying elements that enable the self-healing of creep damage.



---

# Samenvatting

Transformaties in de vaste fase van staal kunnen vanuit vele gezichtspunten beschouwd worden. Tot de onderliggende natuurkunde achter deze fasetransformaties behoren gewoonlijk nucleatie, diffusie, reconstructie van het rooster en wisselwerking tussen opgeloste stoffen en korrelgrenzen en grensvlakken. Deze aspecten en het feit, dat de gebeurtenissen plaats vinden bij hoge temperaturen, binnen in het materiaal, op tijdschalen van milliseconden tot uren en op lengteschalen van atomaire afmetingen tot millimeters zorgen er voor, dat zelfs de meest uitgebreid bestudeerde fasetransformatie in staal, die tussen austeniet en ferriet, maar bij benadering begrepen is en daarom een aantrekkelijk onderzoeksonderwerp blijft. Kwantitatieve data verkregen met geraffineerde technieken voor fysische karakterisatie ondersteund door fysische modellen voor de microstructuur op de relevante lengte- en tijdschalen zijn vereist om het onderzoeksveld van de fysische ijzermetallurgie verder te brengen.

Dit proefschrift legt zich toe op twee nieuwe methoden van aanpak om fasetransformaties in staallegeringen zo te orkestreren, dat meer fysisch inzicht wordt verkregen of dat nieuwe eigenschappen bereikbaar worden: (1) cyclische partiele austeniet-ferriet transformaties, die er op gericht zijn om de korrelgroei en meer specifiek de grensvlakmobiliteit te ontrafelen door gelijktijdige nucleatie van nieuwe fasen te vermijden. Dit onderwerp wordt bestudeerd met computerstudies en 3D neutronendepolarisatie studies, die in staat zijn om in-situ de ferrietkorrelgrootte en fractie ferriet te volgen. (2) Zelfherstel van kruipschade door locatieselectieve precipitatie van oververzadigde op ijzer gebaseerde legeringen. Een sterke voorkeur voor precipitatie op het vrije oppervlak van kruipholten vergeleken met precipitatie in de bulk kan resulteren in het vullen van kruipholten en een significante verlenging van de levensduur voor kruip. Om dit zelfherstelmechanisme bruikbaar te maken voor kruipresistente staallegeringen, is een zoektocht ondernomen naar een alternatief herstellmiddel voor Au in Fe en nieuwe ontwerpreecepten moeten afgeleid worden op basis van de experimentele input van geavanceerde karakterisatietechnieken zoals elektronenmicroscopie en Röntgentomografie.

In Hoofdstukken 2-4 wordt de kinetica van de austeniet-ferriet fasetransformatie bestudeerd met 3D mixed-mode modelleren en driedimensionale neutronendepolarisatie (3DND) voor verschillende verwerkingsomstandigheden, *d.w.z.* continue koeling, bij vaste temperatuur en thermische kringlopen. In Hoofdstukken 5-7 zijn de zelfherstellende Fe-Au, Fe-Mo en Fe-W legeringen in detail bestudeerd met kruiptesten en microstructuurkarakterisatie o.a. via nanotomografie met gebruik van synchrotronstraling.

In Hoofdstuk 2 wordt een 3D mixed-mode model gepresenteerd, dat de klassieke nucleatietheorie en de mobiliteit van het grensvlak koppelt in het intermediaire geval tussen diffusiebegrensde en grensvlakbegrensde omstandigheden om de evolutie van de microstructuur te voorspellen in C-Mn staal tijdens koelen vanuit de austenitische toestand. Dit model is gevalideerd door de simulatieresultaten te vergelijken met die gesimuleerd met een phase-field model voor dezelfde waarden van de parameters en dilatometriedata voor lineair koelen van een Fe-0.10C-0.49Mn staal (in gewichts%). De

simulaties tonen, dat de ferrietfracties gereproduceerd kunnen worden gedurende  $\gamma$ - $\alpha$  transformatie door de groeiparameters goed af te stemmen. De evolutie van de grootteverdeling van de ferrietkorrels kan echter niet gereproduceerd worden door alleen deze groeiparameters af te stemmen. Dit suggereert dat analyse van de korrelgrootteverdeling voor verschillende  $f_\alpha$  niveaus vereist is om nauwkeuriger schattingen van de belangrijkste fysische parameters af te leiden, inclusief het nucleatie temperatuur interval en de effectieve grensvlakmobiliteit. Schattingen van beide zijn essentieel om de microstructuur tijdens de staalproductie te sturen.

Gegeven het feit dat zowel de ferrietfractie als de grootteverdeling van de ferrietkorrels van belang zijn om de transformatiekinetiek te voorspellen, is het onontbeerlijk om kwantitatieve in-situ informatie over de ferrietkorrelgrootte te verkrijgen. Driedimensionale neutronendepolarisatie (3DND) is waarschijnlijk de enige techniek die in staat is om de ferrietfractie en de ferrietkorrelgrootte tegelijkertijd te meten in de bulk van een transformerend staalproefstuk. In 3DND correspondeert de rotatiehoek van de gepolariseerde neutronenbundel na passage door een gemagnetiseerd proefstuk met de fractie ferromagnetische fase. De afname in de polarisatiegraad meet de gemiddelde variatie in het lokale magnetische veld, waarmee het een maat geeft voor de magnetische domeingrootte. Voor austeniet-ferriet fasetransformaties kan 3DND metingen opleveren van ferrietfractie en ferriet korrelgrootte omdat het consistent is met de magnetische configuratie beneden de Curie temperatuur van ferriet. Om de 3DND data analyse te verheffen van zijn huidige niveau, waarin deze alleen de gemiddelde ferrietkorrelgrootte oplevert naar een toestand, waar ook de grootteverdeling van de ferrietkorrels wordt bepaald dient men de magnetische configuratie numeriek te berekenen en de resulterende 3DND parameters te vergelijken met de staal microstructuur, zoals gepresenteerd is in Hoofdstuk 3. De resultaten tonen dat de magnetische deeltjesgrootte afgeleid uit 3DND data in zeer goede overeenstemming is met de berekende microstructurele deeltjesgrootte over een breed bereik van volumefracties en verdelingen van korrelgrootten. Voor afwijkingen in de deeltjesgrootte geschat uit 3DND data wordt gevonden, dat zij voortkomen uit de spreiding in deeltjesgrootte. Een verband tussen de veldcorrelatiefunctie en de relatieve breedte van de deeltjesgrootteverdeling is voorgesteld om de afwijkingen nauwkeurig te beschrijven en daaruit de verdeling over de korrelgrootte af te leiden.

In Hoofdstuk 4 is de evolutie van de ferrietfractie en de ferrietkorrelgrootte gedurende langzame partiele cyclische austeniet-ferriet fasetransformaties in een Fe-0.25C-2.1Mn (gewichts%) staal bestudeerd met 3DND experimenten. De getalsdichtheid aan ferrietkorrels werd bepaald en de resultaten tonen aan, dat tijdens de cycli nucleatie verwaarloosbaar of zelfs afwezig is. Daarom geeft dit werk het eerste experimentele bewijs dat cyclische partiele transformaties inderdaad directe informatie kunnen opleveren over de actuele beweging van het austeniet-ferriet grensvlak en vrij kunnen zijn van de effecten van gelijktijdige nucleatie. Voor de migratiesnelheid van het grensvlak werd gevonden, dat die tijdens cycli van de orde van  $10^{-3}$   $\mu\text{m/s}$  is. Deze lage waarde wordt toegeschreven aan Mn partitionering waarvoor de breedte van de diffusie piek geschat wordt op 1-15 nm. Het 3D mixed-mode model gepresenteerd in Hoofdstuk 2 is nu uitgebreid voor cyclische fasetransformaties. Dit nieuwe model incorporeert meesleuren van opgeloste stof en

vindt automatisch de verandering van de transformatierichting voor niet-monotone thermische profielen. De modelresultaten werden eerst geïjkt voor continue koeling en bij vaste temperatuur in een reeks Fe-C-Mn ternaire legeringen. Daarna is dit model toegepast om de transformatiekinetiek tijdens partiele faseformatiecycli te beschrijven. Voor de stagnerende fase wordt gevonden dat die geïnduceerd wordt door het meesleuren van opgelost Mn. Voor een significant effect van de korrelgrootteverdeling wordt ook gevonden, dat het gedrag onder cycli beïnvloedt. Dit model, dat rekentechnisch goedkoop is, verschaft een veelzijdig en flexibel hulpmiddel om austeniet-ferriet faseformaties in laag-gelegeerd staal met een minimale hoeveelheid aanpasbare parameters te beschrijven en voorspellen.

In Hoofdstuk 5 wordt de microstructuur van Fe-Au proefstukken, die door kruip gefaald hebben, gekarakteriseerd met behulp van 3D hoge-resolutie Röntgen nanotomografie gebaseerd op een sterk coherente intense bundel geproduceerd door een synchrotron. De verkregen 3D beelden van de microstructuur van de proefstukken van Fe-Au legeringen onthullen op de lengteschaal van nanometers verschillende stadia in het vulproces van individuele kruipholten door goudprecipitatie. De kwantitatieve analyse van de grootte, vorm en verdeling over de ruimte van de kruipholten en de goudprecipitatie toont een sterke correlatie aan tussen de morfologie van de holten en precipitaten. Er is aangetoond, dat goud bij voorkeur neerslaat op het oppervlak van de holten en zich veeleer gedraagt als herstellend middel dan als nucleatiepunt voor kruipholten. Het zelf herstellend karakter van Fe-Au legeringen wordt volledig ondersteund door deze studie. De vulfactor van individuele kruipholten kan twee verschillende wegen volgen, die worden beschouwd te corresponderen met de afwezigheid en aanwezigheid van verbindingsmogelijkheid met naburige kruipholten.

De recepten om een zelf herstellende Fe-X binaire legering te ontwerpen kunnen afgeleid worden uit deze studies aan de Fe-Au legering. De cruciale vereisten om element X een efficiënt zelfherstellend middel te laten zijn kunnen als volgt samengevat worden: i) element X kan opgelost worden in de Fe matrix bij hoge temperatuur en tot een adequate mate van oververzadiging gebracht worden op de kruiptemperatuur om een aanmerkelijke drijvende kracht voor precipitatie te verschaffen; ii) de atoomgrootte van X is aanzienlijk groter dan die van de matrix Fe, resulterend in een hoge nucleatiedrempel voor precipitatie in de matrix en een sterke voorkeur om neer te slaan op het vrije oppervlak van het defect; iii) de diffusiviteit van element X moet groter zijn dan die van Fe om te verzekeren dat het vullen van de holte (bepaald door diffusie van de opgeloste stof) de groei van de holte (bepaald door vacaturediffusie) kan inhalen. Voor zowel Fe-Mo als Fe-W legeringen zijn deze vereisten van toepassing. In Hoofdstuk 6 is het zelfherstel van kruipgeïnduceerde defecten in een Fe-Mo legering van hoge zuiverheid (6.2 gewichts% Mo) bij temperaturen van 813, 823 en 838 K bestudeerd. De elektronenmicroscopie metingen na kruip geven duidelijke aanwijzingen voor het opvullen van kruipholten door Fe<sub>2</sub>Mo precipitatie. In enkele gevallen wordt een partiele vulling van de kruipholten waargenomen, terwijl in de meeste gevallen een volledige vulling wordt gevonden. De aangetoonde selectieve Fe<sub>2</sub>Mo precipitatie op het oppervlak van kruipholten suggereert dat zelfherstel in commercieel hoge-temperatuur kruipstaal, dat vaak al Mo bevat voor versterking door oplossing, gerealiseerd kan worden door het Mo niveau aan te passen.



In Hoofdstuk 7 is het zelfherstel van kruipschade onderzocht in een binaire Fe-3.8 gewichts% W legering van hoge zuiverheid bij een temperatuur van 550 °C en verscheidene constante aangelegde spanningen. De ruimtelijke verdeling en de morfologie van zowel de precipitaten als de holten werden gevolgd met synchrotron Röntgen nanotomografie. De aard van de kruipholten en de precipitaten wijzen op de autonome vulling van kruipholten door precipitatie van de Fe<sub>2</sub>W Laves fase in de Fe-W legering. De 3D beelden verkregen met een resolutie van 100 nm leveren gedetailleerde statistiek op over de kruipholten, terwijl de 3D beelden verkregen met een resolutie van 30 nm een gedetailleerd beeld geven van de morfologie van de gedeeltelijk gevulde holten. Twee verschillende trends voor de opvulling van de holten worden waargenomen voor geïsoleerde en verbonden holten, respectievelijk. De vulgraad van de geïsoleerde holte neemt continu toe tot volledige vulling wordt bereikt, terwijl de vulgraad van de verbonden holten eerst toeneemt, maar daarna continu afneemt, nadat verbinding is opgetreden. Dit wordt toegeschreven aan verschillen in groeigedrag voor geïsoleerde en verbonden holten, zoals aangegeven door verschillende exponenten in de machtsverband voor holtegroei.

De karakteristieke vultijd wordt geschat op ongeveer 46 uur om een volume van ongeveer 1 μm<sup>3</sup> bij een temperatuur van 550 °C en een constante spanning van 140 MPa volledig te vullen. Het aangetoonde zelfherstelpotentieel van oververzadigde W atomen, samen met Mo, in *bcc* ijzer opent nieuwe perspectieven voor de rol van Mo en W in hoge-temperatuur kruipresistente staallegeringen. Het zelfherstel mechanisme in zulke legeringen werkt parallel aan de versterking door de opgeloste atomen zelf. Deze studies tonen een veelbelovende toekomst voor de beheersing van kruipschade door de toevoeging van meer betaalbare legeringselementen, die het zelfherstel van kruipschade mogelijk maken.

---

# Acknowledgements

It is a pleasant and unforgettable journey for me to have my four-year PhD study in Delft with a lot of support and help from many fantastic people, to whom I would like to sincerely express my gratitude.

First of all, I would like to thank my corresponding promotor, Sybrand van der Zwaag, not only for his continuous support, inspiring discussions and forward-looking visions, but also for his encouragement and advice on my daily life and my future career. You are a superman in working and scientific thinking. Not only just being efficient in correcting manuscripts, you are also thinking very fast, and your brain is always full of fantastic ideas which I deeply admire. I still remember the moments that you gave feedbacks on my research progress while being treated in the hospital after you had a bad bike accident, and that you joined for our progress meeting in a raining morning after you drove over night. Feel lucky to have such a promotor who takes the responsibility of supervising students as the priority. Thank you, Sybrand.

A deep thanks goes to my daily supervisor, Niels van Dijk, for his every detail in research and his physics-based way of both thinking and supervising that shaped me and surely be beneficial to my future career. Niels, you are not just a good supervisor to discuss all details that we encountered in X-rays, neutrons, phase transformations etc., but also a good friend with whom I can share my upset. You are always optimistic and you always have plenty interesting stories, scientifically or not it does not matter, that cheer us up and sometimes inspire me on my own research. I deeply admire your thoughtful thinking, planning and predicting. You always come up with solutions that seemed to be 'simple' at first thought, while later they are very often shown to be very effective and very elegant. I wish I have learned a bit from you.

A special thanks goes to my another promotor, Ekkes Brück, for his kind support and fruitful discussions during my every progress meeting, mostly held in his office. While you gave comments relatively less than Niels and Sybrand, you gave stimulating feedbacks when you did. I also benefit a lot from your expertise in magnetism and your corrections on some of my papers.

This thesis would not be in the current form without collaborations with people outside TU Delft, to whom I would like to express my gratitude. Firstly I would like to thank Dr. Peter Cloetens and his colleagues at ESRF beamline ID-16A that provides the highest spatial resolution for X-ray tomography. I was lucky to use this beamline twice and got a bunch of data with the help of Peter and Yang Yang. Then I would like to thank Dr. Michael Herbig, Dr. Shanoob, Dr. Kuzmina and Prof. Dierk Raabe at Max-Planck-Institut für Eisenforschung for their beautiful atom probe measurements on Fe-Mo and Fe-W alloys. I would also like to thank Dr. Joachim Kohlbrecher at PSI for support with the SANS experiments. Thanks also goes to Dr. Astrid Perlade for supplying the steel sample for neutron depolarization experiments. Thanks to Dr. Kangying Zhu for organizing the Martensite/bainite Theses Day at Arcelor Mittal in Metz where I enjoyed a lot with the stimulating discussions.

I also received a lot of support and help from colleagues across several Faculties of TU Delft. I would like to thank Dr. Wim Sloof and Kees Kwakernaak for their

support in using SEM and EBSD, which enables the basic characterization on microstructures. Thanks to Hans Brouwer for help with heat treatments and Sander for support with sample preparation. Thanks to Dr. Frans Tichelaar for TEM measurements. Thanks to Dr. Dominique Ngan-Tillard for teaching me how to use Avizo. Thanks to Joost van Meel and Wim Verwaal for giving me the access to a powerful computer that was able to process the synchrotron tomographic dataset with a size up to 32 GB. A special thanks goes to Bert for sealing countless samples in quartz tubes.

In the first three years of my PhD research, one of my main tasks was to build furnaces for neutron depolarization experiments or to modify furnace for creep testing. Building instruments truly requires a lot of inputs from technicians with different expertise. Thanks to Piet for helping me a lot with designing, machining and lending good mechanical stuff. Thanks to Martijn for help with sorting out a lot of problems with vacuum. Thanks to Ernst van der Wal for taking care of metal cutting and machining components. Thanks to Ernst Born for designing and making the compact furnace for neutron depolarization experiments. Thanks to Youp van Goozen and Ruud van Tol for building new parts for the creep tester. Thanks to William for machining some mechanical parts for the big furnace for PANDA. I would also like to thank all other people at DEMO workshop who helped me.

I would also like to express my gratitude to Prof. Wolfgang Ludwig at ESRF, Prof. Annika Borgenstam at KTH, Prof. Bart Kooi at University of Groningen, Prof. Jilt Sietsma and Prof. Katia Pappas at TU Delft for serving on the committee for my PhD defense.

My sincere acknowledgement goes to people across different research groups for stimulating discussions on self healing steels. Thanks goes to Dr. Shasha Zhang for introducing self healing to me in the very beginning. Thanks to Dr. Casper Versteyleen for discussions on *ab initio* and self healing modeling. Thanks to Nikodem for carrying out experiments on Fe-W alloys together with me. At the later stage, Hao Yu and Yifan joined in to design the self healing steels. Very happy to see that self healing creep steel is evolving to be more and more industrially relevant. I would also like to thank Dr. Marcel Sluiter for stimulating discussions during our progress meetings. To extend self healing metals to other self healing materials, I very much enjoyed the discussions with Dr. Garcia Santiago, Nan, Wouter, Arijana, Paul, Vincenzo and many others I met in self healing lunch meetings or conferences. Thank you all.

I would also like to thank people who helped me a lot with my research on steel phase transformations. Thanks to Dr. Theo Rekveldt for sharing knowledge on neutron depolarization and SESANS. Thanks to Kees de Vroege for help with the PANDA software. Thanks to Hussein for help with dilatometer and providing access to DICTRA simulations. Thanks to Pina for simulation results by phase-field modeling. Thanks to Dr. Zenan Yang for friendship and a lot of discussions when we shared our living apartment in the first year. Thanks to Dr. Xiaojun Xu and Dr. Qi Lu for many suggestions at the early stage of my PhD study. Thanks to Dr. Hao Chen for encouragement and support. Thank to Dr. Wei Xu for suggestions in the very beginning of my stay in Delft. Thanks to Dr. Shuai Tang and Dr. Huifang Lan for help and discussions on metallography and dilatometer experiments. Thanks to Dr. Lie Zhao for discussions in the very beginning of my PhD study. Thanks to John at

Sheffield for discussions on in-situ neutron depolarization and in-situ TEM experiments.

My sincere acknowledgements go to friends and colleagues at groups FAME, NPM2, NovAM and within TU Delft. Thanks to Anton, Kees Goubitz, Michel Steenvoorden, Dr. Henk Schut, Piet, Kees de Vroege, Michel Thijs, Fred, and Marlies for their daily technical help. Thanks to Shanta, Nicole and Ilse for administrative support. Thanks to Dr. Jouke Heringa for software support and help with translating the Summary into Samenvatting in Dutch. Thanks to Zhou Zhou, Wenqin, Maurits, Yifan, Hao, Daniëlla, Ranjita, Nan, Jimmy, Atsushi, Hussein, Tian, Jiawei, Bowei, Xinmin, Xuefei, Yibole, Stephan, Michael, Steven, Dimitris, Ivan, Jun, Fengqi, Prasad, Thang, Maik, Bert, Ben, Lian, Maxim, Paul, Lars, Ankit, Lambert, Jeroen, Paul, Bei, Fengjiao, Chris, Evgenii, Zhaolong, Xiaoyu, Yaolin, Chuang, Shasha Lv, Zhu, Ming, Kun, Chao, Tomas, Swapna, Hongde, Tiantian, Beien, Zheng, Huanhuan, Shi, Yanqing, Tianshi, Guoping, Laobing, Hao, Jiayi and many others for interesting talks, help, pingpong, lunch and dinner.

I would like to deeply thank my parents. You raised me up and shaped me by going through a lot of tough moments, while you never ask me for anything in return. I was very selfish to pursue my own career while you are always selfless to give me sufficient freedom. I have never said thanks to you face to face. I owe you too much.

Last but not the least, I would like to specially thank my wife, Zhifang Hu, for your endless love and support since 2006. We together have got through a lot of happiness as well as difficult times. Now we have established our small family by having our little Wendy. Thank you with my love.

Haixing Fang,  
Delft, September, 2018



---

# List of publications

## Journal articles related to the PhD study

8. **H. Fang**, S. van der Zwaag, N.H. van Dijk, *Modelling on the cyclic partial austenite-ferrite phase transformations in Fe-C-Mn alloys using a 3D mixed-mode model coupled with solute drag*, in preparation.
7. **H. Fang**, N. Szymanski, C.D. Versteyleen, P. Cloetens, C. Kwakernaak, W.G. Sloof, F.D. Tichelaar, S. Balachandran, M. Herbig, E. Brück, S. van der Zwaag, N.H. van Dijk, *Self healing of creep damage in iron-based alloys by supersaturated tungsten*, submitted.
6. **H. Fang**, S. van der Zwaag, N.H. van Dijk, *In-situ 3D neutron depolarization study of the transformation kinetics and grain size evolution during cyclic partial austenite-ferrite phase transformations in Fe-C-Mn steels*, Metallurgical and Materials Transactions A, 2018, 49, pp. 5962-5975.
5. **H. Fang**, S. van der Zwaag, N.H. van Dijk, *Modelling study on the three-dimensional neutron depolarization response of the evolving ferrite particle size distribution during the austenite-ferrite phase transformation in steels*, Philosophical Magazine, 2018, 98, pp. 1884-1899.
4. **H. Fang**, M.G. Mecozzi, E. Brück, S. van der Zwaag, N.H. van Dijk, *Analysis of the grain size evolution for ferrite formation in Fe-C-Mn steels using a 3D model under a mixed-mode interface condition*, Metallurgical and Materials Transactions A, 2018, 49, pp. 41-53.
3. W.W. Sun, **H. Fang**, N.H. van Dijk, S. van der Zwaag, C.R. Hutchinson, *Linking surface precipitation in Fe-Au alloys to its self-healing potential during creep loading*, Metallurgical and Materials Transactions A, 2017, 48, pp. 2109-2114.
2. **H. Fang**, C.D. Versteyleen, S. Zhang, Y. Yang, P. Cloetens, D. Ngan-Tillard, E. Brück, S. van der Zwaag, N.H. van Dijk, *Autonomous filling of creep cavities in Fe-Au alloys studied by synchrotron X-ray nano-tomography*, Acta Materialia, 2016, 121, pp. 352-364.
1. S. Zhang, **H. Fang**, M.E. Gramsma, C. Kwakernaak, W.G. Sloof, F.D. Tichelaar, M. Kuzmina, M. Herbig, D. Raabe, E. Brück, S. van der Zwaag, N.H. Van Dijk, *Autonomous filling of grain-boundary cavities during creep loading in Fe-Mo alloys*, Metallurgical and Materials Transactions A, 2016, 47, pp. 4831-4844.

## Conference proceedings related to the PhD study

1. S. van der Zwaag, S. Zhang, **H. Fang**, E. Brück, N.H. van Dijk, *Towards self-healing creep resistant steels*, CF-7: 7th International Conference on Creep, Fatigue and Creep-Fatigue Interaction, Tamil Nadu, India, 19-22 January 2016, pp. 85-90.

### Journal articles related to the Master study

3. Hong-Yi Li, **Hai-Xing Fang**, Kang Wang, Wang Zhou, Zhao Yang, Xiao-Man Yan, Wen-Sun Ge, Qian-Wen Li, Bing Xie, *Asynchronous extraction of vanadium and chromium from vanadium slag by stepwise sodium roasting–water leaching*, Hydrometallurgy, 2015, 156, pp. 124-135.
2. **Hai-Xing Fang**, Hong-Yi Li, Tao Zhang, Bao-Si Liu, Bing Xie, *Influence of CaO on existence form of vanadium-containing phase in vanadium slag*, ISIJ International, 2015, 55, pp. 200-206.
1. **Hai-Xing Fang**, Hong-Yi Li, Bing Xie, *Effective chromium extraction from chromium-containing vanadium slag by sodium roasting and water leaching*, ISIJ International, 2012, 52, pp.1958-1965.

### Conference presentations

9. **H. Fang** et al, *Direct view of self healing in creep alloys*, Dutch Materials 2018, Utrecht, The Netherlands. (Invited oral presentation)
8. **H. Fang** et al, *Self healing Fe-W alloys for creep application*, MSE 2018, Darmstadt, Germany. (Oral)
7. **H. Fang** et al, *Cyclic austenite-ferrite phase transformations in low-alloyed steels: polarized neutron experiments and modelling*, MSE 2018, Darmstadt, Germany. (Oral)
6. **H. Fang** et al, *Autonomous healing of creep damage in Fe-W alloys studied by synchrotron X-ray nanotomography*, THERMEC' 2018, Paris, France. (Poster)
5. **H. Fang** et al, *Autonomous healing of creep damage in Fe-X alloys: a nanotomographic study*, The 6<sup>th</sup> International Conference on Self-Healing Materials (ICSHM 2017), Friedrichshafen, Germany. (Oral)
4. **H. Fang** et al, *Cyclic austenite-ferrite transformations in steels studied by in-situ 3D neutron depolarization*, EUROMAT 2017, Thessaloniki, Greece. (Oral)
3. **H. Fang** et al, *Autonomous filling of creep cavities in Fe-X alloys: a nanotomographic study*, EUROMAT 2017, Thessaloniki, Greece. (Oral)
2. **H. Fang** et al, *Development of grain size distribution in Fe-C-Mn steels: modelling and neutron depolarization experiments*, Bainite/martensite Theses Day 2017, Metz, France. (Oral)
1. **H. Fang** et al, *In-situ neutron depolarization study of ferrite formation during thermal cycling in  $\gamma$ - $\alpha$  region*, Bainite/martensite Theses Day 2016, Metz, France. (Oral)

### Awards and Highlights

3. 2018 TMS-AIME Champion H. Mathewson Award by The Minerals, Metals & Materials Society (TMS).
2. 2017 ASM Henry Marion Howe Medal by the American Society of Metals (ASM).
1. **H. Fang**, C.D. Versteyleen, S. Zhang, Y. Yang, P. Cloetens, D. Ngan-Tillard, E. Brück, S. van der Zwaag, N.H. van Dijk, *Direct view of self healing in Fe-Au alloys by X-ray nanotomography*, 2016 ESRF highlights.

---

# Curriculum Vitae

## Haixing Fang

Born on July 9th, 1990  
Chenzhou, Hunan province, China

### **Sept. 2014 – Dec. 2018**

PhD candidate in the group Fundamental Aspects of Materials and Energy (FAME) and also the group Novel Aerospace Materials (NOVAM), Delft University of Technology, Delft, The Netherlands. His PhD thesis is on studying cyclic phase transformations in low-alloyed steels and self healing creep steels, under the supervision of Prof. Dr. Sybrand van der Zwaag, Prof. Dr. Ekkes Brück and Dr. Niels van Dijk.

### **Sept. 2011 – Jun. 2014**

Master of Engineering in Metallurgical Engineering, Chongqing University, Chongqing, China. His Master thesis is on studying the physical-chemical properties of chromium-containing vanadium slag and the efficient extractions of vanadium and chromium, under the supervision of Prof. Dr. Bing Xie.

### **Sept. 2007 – Jun. 2011**

Bachelor of Engineering in Metallurgical Engineering, Chongqing University, Chongqing, China.









ISBN 978-94-028-1285-5



9 789402 812855